Oxygen activation by novel nonheme diiron enzymes

A DISSERTATION
SUBMITTED TO THE FACULTY OF THE GRADUATE SCHOOL
OF THE UNIVERSITY OF MINNESOTA
BY

Van V. Vu

IN PARTIAL FULFILLMENT OF THE REQUIREMENTS
FOR THE DEGREE OF
DOCTOR OF PHYLOSOPHY

Professor Lawrence Que, Jr.

December 2011

Acknowledgments

First and foremost, I would like to thank my advisor, Prof. Larry Que, for giving me the opportunity to work in an excellent collaborative atmosphere of his lab. Six years ago, I was lucky when Larry read my email sent from a free Yahoo account that was often overlooked by others. I thought he just wanted to increase the diversity of the group when he announced enthusiastically "We have a Vietnamese for the first time" at group meeting. But I later found out that he is always enthusiastic and energetic like that in many aspects, even after the ever-lasting group meetings, which is very inspiring to me. In Larry's lab, in addition to learning spectroscopy and biochemistry from my own research projects, I was able to learn inorganic chemistry from many excellent synthetic bioinorganic chemists, which has proved invaluable for my professional development. I am also grateful for the flexibility that Larry gave me in the last five years. With a right amount of guidance, Larry allowed me to grow as an independent scientist. As a science editor, Larry has been overly patient with my typical Asian grammatical English errors.

I would also like to thank Prof. John Lipscomb, who I call my unofficial advisor, for the opportunity to be part of his group. John's doors were always open to me anytime I needed him. I was very fortunate to be able to learn about biochemistry and EPR spectroscopy from John and his group members, as well as to access their equipment. In addition, John and Larry, the two "old timers of the MPIG" as Larry said, together with Prof. Bill Tolman and other faculty members, created a very strong Metalloprotein Interest Group, in which I had the opportunity to interact with many bright bioinorganic chemists.

I am very grateful to work with Dr. Tom Makris in John's lab, a big brother as one of John's students said. Tom inspires me with his enormous knowledge of molecular biology and biochemistry, as well as EPR spectroscopy. He discovered new diiron enzymes and a novel intermediate, without which my spectroscopic studies would have been much less exciting. I also thank Tom for a lot of insightful discussion about research, as well as about world football, not the American football, in which Tom is a true expert.

My time in graduate school would not have started well if it were not for Dr. Erik Farquhar, the King of the Que group's biolab. I called him the magic man who would repair everything that I broke when I first joined the lab. Erik taught me, step by step from the very beginning, biochemical skills and X-ray absorption spectroscopy, which played an instrumental part in my thesis work. I relied a lot on his excellent editing skills and incredible literature knowledge in chemistry, XAS, sports, and many other subjects. I enjoyed his company going in all the EXAFS trips or doing crazy things in the lab.

Along these lines, the Que group biolab members have been my wonderful to me. Dr. Joe Emerson initiated the hDOHH project that became the main part of my thesis work. Andy Fielding helped me a lot with operating the EPR instrument. I enjoyed the sail boat rides or talking endlessly about a variety of subjects with Andy. I learned from Andy and Erik how one can achieve a lot by being consistent and patient with his work.

Other members in the Que and Lipscomb groups, one way or another, have contributed to my growth in graduate school with their insightful discussion and experimental assistance. I thank Dr. Erik Farquhar, Dr. Adam Fiedler, Dr. Kallol Ray, Dr. Matt Cranswick, Dr. Kathy Van Heuvelen, and Dr. Feifei Li for being very wonderful EXAFS team members. I especially thank Matt and Kathy for covering most of the work during my last trip, which was a very tough time for me. Matt, Kathy, together with Dr. Jonathan Frisch took care of the Raman instrument, on which I believe no one has spent more time than I did in the last few years.

My research would not have been nearly as successful without all the collaborations that I was fortunate to have in the last five years. Dr. Myung Hee Park at NIH generously provided proteins and plasmids, helped with some difficult biochemical assays, and spent hours discussing our results. Dr. Jack E. Folk at NIH kindly contributed significant amounts of chemicals, which are difficult to synthesize. Prof. Eckard Münck at Carnegie Mellon University and his group carried out the Mössbauer analysis of hDOHH samples. I received a large number of samples from my generous collaborators, Dr. Aidan McDonald, Dr. Anusree Mukherjee, Dr. Matt Cranswick, Dr. Dong Wang, Dr. Ken Xue, and Dr. Feifei Li., and especially Dr. Tom Makris and Dr. Johnathan Frisch.

XAS data were collected on Beamline X3B at the National Synchrotron Radiation Light Source (NSLS) and Beamlines 7-3 and 9-3 at the Stanford Synchrotron Radiation Lightsource (SSRL), all of which are supported by the U.S. DOE and NIH. Our XAS experiments were all successful with the kind help of the beamline staff, Dr. Matthew Latimer, Dr. Erik Nelson, and Dr. Allyson Soo Hoo at SSRL, as well as Dr. Mike Sullivan, Dr. Jen Bohon, and our former EXAFS team leader Dr. Erik Farquhar at NSLS.

I would like to thank the Vietnam Education Foundation for providing me with a fellowship during my first two years in graduate school and for suggesting me to go to Minnesota. I was also generously supported by fellowships from the Department of Chemistry and Graduate School at the University of Minnesota. My thesis work was supported by National Institutes of Health Grant GM38767 (to Prof. Larry Que).

I would not have grown to be the person I am today without my family, as well as my former advisor and colleagues. My mother and father have always been supportive. Growing up in our big family, I learned from you the values of hardworking, commitment, and leadership. You always let me choose what I like to do and support me to reach my best in it, for which I am ever grateful. It was Prof. Do D. Vu who brought bioinorganic chemistry to me. He and other members of the Division of Inorganic Chemistry, Faculty of Chemistry at Vietnam National University-Hanoi taught the right way to approach science from the very beginning, which has helped me to go this far.

Last but not least, I would like to thank “Nhoc” Tram Anh Do, my beloved wife for accepting me as a devoted graduate student, being always supportive and bringing joys to my PhD life. I am grateful that you have been a part of my family and it has been a real joy for me to be a part of your wonderful family. My time in Minnesota might have still been enjoyable with all the friendships I was fortunate to have at work and outside of the lab. But it could not have been nearly as joyful without your company. Because of you I did not become a nerd like those in PhD Comics. Thank you for being my lifetime friend.

Abstract

Enzymes that utilize nonheme diiron centers to activate dioxygen and carry out various chemical transformations are of great fundamental and practical interest. The mechanisms of these enzymes can be studied using various spectroscopic and biochemical methods, which are greatly aided by parallel studies on relevant model complexes. This thesis work employs this approach to investigate three non-cannonical diiron enzymes, human deoxyhypusine hydroxylase (hDOHH), as well as CmlA and CmlI, a pair of oxygenases on the biosynthesis pathway of the antibiotic chloramphenicol.

We first provide a summary of recent studies on enzymes that employ the canonical 4-helix-bundle motif to house a diiron cluster with a 2-His-4-carboxylate ligand set, as well as those that use a whole new range of structural motifs and/or exibit non-canonical reactivities (Chapter 1). We have successfully characterized an unusually stable, yet functional, peroxo intermediate of hDOHH (hDOHHperoxo), an enzyme which possesses a superhelical HEAT-repeat fold (Chapter 2). Detailed spectroscopic analysis of hDOHHperoxo and related model complexes reveals that hDOHHperoxo contains a (cis-μ-1,2-peroxo)diiron(III) unit (Chapter 2) with an additional μ-hydroxo ligand (Chapter 3). This μ-hydroxo ligand is proposed to contribute to the remarkable stability of hDOHHperoxo and its reactivity. The formation of hDOHHperoxo and its reaction with substrate are detailed in Chapter 4. hDOHH adopts various conformations in different forms, that significantly affect the formation and activation of

hDOHHperoxo. Notably, we have observed the epoxidation of one of the unsaturated analogues of the native deoxyhypusine-containing eIF5A substrate.

In line with the studies on the unusual hDOHHperoxo intermediate, we have also studied another unique and relatively stable peroxo intermediate of CmlI (CmlIperoxo). Resonance Raman spectroscopy suggests that CmlIperoxo possibly contains a (μ-η^1:η^2-peroxo)diiron(III) cluster instead of the more common (μ-1,2-peroxo)diiron(III) cluster found in canonical diiron enzymes and model complexes (Chapter 5). EXAFS analysis of as-isolated CmlI reveals that it contains about 3 His ligands, which is consistent with sequence homology analysis. The third His ligand in CmlI could be responsible for the shift in the peroxo binding geometry of CmlIperoxo. Finally, resonance Raman and EXAFS analysis of CmlA, a β-hydroxylase, shows that this enzyme contains a (μ-oxo)(μ-1,3-carboxylato)diiron(III) cluster with about 4 His ligands, a feature similar to diiron reductases and hydrolases. As found for CmlI, the extra His ligands in CmlA may lead to alternative reactive oxygen species as opposed to those found for methane monooxygenase and other canonical diiron enzymes.

To my beloved wife and family

Table of Contents

Acknowledgments……i
Abstract……...iv
Table of Contents……vi
List of Tables……...x
List of Figures……xi
Lists of Schemes……xii

Chapter 1 The versatility of diiron clusters in biology: structures, reactivities, mechanisms, and biological roles of oxygen-activating diiron enzymes that turnover organic substrates.....1

1.1. The canonical oxygen-activating diiron enzymes that oxidize organic substrates.....3
1.1.1. The conserved 4-helix bundle and 2-His-4-carboxylate structural motifs.....3
1.1.2. General mechanism.....6
1.1.3. The peroxo intermediates.....8
1.2. New reactivities of the canonical motif: regioselective aromatic ring epoxidation of CoA-tethered substrates by PaaA and BoxB.....12
1.3. New reactivity of the canonical motif: alkane synthesis by aldehyde decarbonylase.....15
1.4. An additional His ligand and a new reactive species: Substrate oxidizing peroxo intermediates in AurF and CmlI.....18
1.5. A new reactive species: Substrate oxidizing superoxo intermediate in MIOX.....23
1.6. A new structural motif for hydroxylase: DOHH, the first human diiron hydroxylase.....25
1.7. A new structural motif for hydroxylase: CmlA, a hydroxylase with a β-lactamase fold.....28
1.8. Summary.....30
1.9. Scope and aims of thesis.....32

Chapter 2 Human deoxyhypusine hydroxylase, an enzyme involved in regulating cell growth, is an oxygen-activating nonheme diiron enzyme.....33

2.1. Introduction.....34
2.2. Experimental.....36
2.2.1. Protein expression and purification.....36

2.2.2. Reduction and Re-oxidation of hDOHH....36
2.2.3. Activity assay....37
2.2.4. Spectroscopic Studies....37
2.3. Results....44
2.3.1. Evidence for an O_2-activating diiron cluster in hDOHH....44
2.3.2. Evidence for a (μ-peroxo)diiron(III) unit in hDOHH....47
2.3.3. Long-lived hDOHHperoxo can hydroxylate the deoxyhypusine residue in eIF5A....53
2.4. Discussion....54
2.5. Supporting information....60
Chapter 3 The bridging structure of hDOHHperoxo....62
3.1. Introduction....63
3.2. Experimental....65
3.2.1. Sample preparation....65
3.2.2. X-ray absorption spectroscopy....66
3.2.3. Cryo-reduction of hDOHHperoxo using X-ray beam or ^{60}Co γ rays....68
3.3. Results....69
3.3.1. XANES analysis....69
3.3.3. EXAFS analysis....73
3.3.4. EPR analysis of cryo-reduced hDOHHperoxo (pH 8.2) and oxyhemerythrin....81
3.4. Discussion....82
3.5. Supporting Information....88
Chapter 4 Formation and reaction of hDOHHperoxo....92
4.1. Introduction....93
4.2. Experimental....94
4.2.1. hDOHH purification....94
4.2.2. Stopped-flow experiments....95
4.2.3. pH-dependent reaction of hDOHHperoxo....95
4.2.4. Analytical size exclusion chromatography....96
4.2.5. Reaction of hDOHHperoxo with eIF5A(Dhp) substrate and its analogues....96
4.2.6. Mössbauer spectroscopy....98
4.3. Results....98
4.3.1. Formation of hDOHHperoxo....98
4.3.2. pH-Dependent reaction of hDOHHperoxo....102
4.3.3. Analytical size-exclusion chromatography....106
4.3.4. Reaction of hDOHHperoxo with substrate analogues....108

4.4. Discussion 112

Chapter 5 Characterization of a novel peroxodiiron(III) intermediate of an amine N-oxygenase in the biosynthesis pathway of chloramphenicol 115

5.1. Introduction 116

5.2. Experimental 118
5.2.1. X-ray absorption spectroscopy of oxidized CmlI at pH 7.0 118
5.2.2. Resonance Raman spectroscopy 118

5.3. Results and Discussion 120

5.5. Supporting Information 130

Chapter 6 Active site structure of a β-hydroxylase in antibiotic biosynthesis 136

6.1. Introduction 137

6.2. Experimental 138
6.2.1. Resonance Raman spectroscopy 138
6.2.2. X-ray absorption spectroscopy 139

6.3. Results 142
6.3.1. Resonance Raman spectroscopy 142
6.3.2. XANES analysis 143
6.3.3. EXAFS analysis 144

6.4. Discussion 150

References 157

List of Tables

Table 1.1. Diiron enzymes 3
Table 1.2. Properties of diiron(III)-peroxo units in enzymes and related model complexes 11
Table 2.1. Photoreduction yields (PY) at different *k* values of first scan data, assuming photoreduction rate is proportional to exposure time (t).[153] PY = 49×t/1340 (%). 43
Table 2.2. Properties of diiron(III)-peroxo units in enzymes and related model complexes 48
Table 2.3. Parameters for fits to unfiltered k^3-weighted EXAFS data of photoreduced $hDOHH_{phr}$ and hDOHHperoxo. 52
Table 2.4. Representative best fits to k^3-weighted EXAFS data of hDOHH and related diiron enzymes 55
Table 3.1. Model complexes used in this study 67
Table 3.2. XANES parameters for various hDOHH forms and model complexes 72
Table 3.3. EXAFS fitting results for hDOHHperoxo 74
Table 3.4. EXAFS fitting result for 1, 2, and 8 77
Table 3.5. EXAFS fitting result for N-Et-HPTB model complexes 79
Table 3.6. Correlation of the bridging structure of (μ-1,2-peroxo)diiron(III) with its Fe---Fe distance 83
Table 4.1. Ion exchange HPLC and HILIC LC/MS analysis of DHS and DOHH products digested with 6 N HCl at 110 ^{o}C 110
Table 5.1. Gaussian peak fitting results for CmlIperoxo 122
Table S.5.1. Pre-edge parameters for CmlI at pH 7.0 131
Table S.5.2. EXAFS fitting results for CmlI at pH 7.0 134
Table 6.1. Pre-edge parameters for CmlA obtained with EDG_FIT 143
Table 6.2. Results of EXAFS fitting to the first shell for CmlA 146
Table 6.3. Results of EXAFS fitting to first and second shells for CmlA 147
Table 6.4. EXAFS fitting results to unfiltered data for CmlA 149

List of Schemes

Scheme 1.1. Simplified generally accepted mechanisms for canonical oxygen-activating diiron enzymes 7
Scheme 1.2. Phenylacetyl-CoA and benzoyl-CoA metabolism.[46, 47] 12
Scheme 1.3. Synthesis pathway of alkane or alkene from fatty acids with possible C1 co-products.[19-22] N/F/FR = NADPH, ferredoxin, and ferredoxin reductase system. N/P = NADH and 5-methylphenazinium methylsulfate system. 16
Scheme 1.4. Oxygenation of *p*-aminobenzoic acid (PABA) by AurF as a step in the aureothin PKS synthesis pathway (left) and its proposed mechanisms. 19
Scheme 1.5. Reaction of MIOX and formation of the proposed C-H bond cleaving superoxo intermediate G. 23
Scheme 1.6. Post-translational (+)-hypusine biosynthesis. DHS = deoxyhypusine synthase 25
Scheme 1.7. The biosynthetic pathway of chloramphenicol 28
Scheme 2.1. Biosynthesis of hypusine on eIF5A 34
Scheme 3.1. Proposed cryo-reduction of hDOHHperoxo. 86
Scheme 4.1. Reaction of deoxyhypusine synthase (DHS) (left) and deoxyhypusine hydroxylase (DOHH) (right). 94
Scheme 4.2. Proposed working model for hDOHH. 112
Scheme 4.3. Proposed mechanism that leads to the stereospecificity of hDOHH. 114
Scheme 5.1. The biosynthesis pathway of chloramphenicol 117
Scheme 5.2. Two possible mechanisms involving the putative (μ-η^1:η^2-peroxo)diiron(III) intermediate of CmlI. 127
Scheme 5.3. Two possible peroxo-exchange mechanisms for CmlIperoxo 129
Scheme 6.1. The biosynthetic pathway of chloramphenicol 137

List of Figures

Figure 1.1. Overall protein scaffold of MMOH with the 4-helix bundle highlighted (1FYZ). 4

Figure 1.2. Crystal structures of BoxB.[44] A: oxidized form at 2.5 Å resolution. B: NADPH-reduced form with bound substrate at 2.3 Å resolution from views perperdicular to or along the Fe---Fe vector. The benzoyl substrate moiety is shown in grey. Glu 150 residue shifts away from bridging mode (shown in light blue-green). Sequence motif: $E_{120}X_{30}E_{150}X_2H_{153}$ and $D_{211}X_{29}E_{240}X_2H_{243}$....13

Figure 1.3. Crystal structure of fatty acid decarbonylase from from *P. marinus* MIT9313 (2OC5). Fe-μO = 1.940, 2.007 Å, ∠Fe-O-Fe = 109.9°, Fe---Fe = 3.232 Å. Sequence motif: $E^{45}X_{28}E^{73}X_2H^{75}$ and $E^{128}X_{29}E^{157}X_2H^{160}$ 15

Figure 1.4. Active site structure of AurF from *Streptomyces thioluteus* (3CHU). Sequence motif: $E^{101}X_{34}E^{136}$ X_2H^{139}, $E^{196}X_{26}H^{223}X_3E^{227}$ X_2H^{230} 19

Figure 1.5. Crystal structure of mouse MIOX with bound substrate (2HUO). 23

Figure 1.6. Hypothetical structure of hDOHH and a proposed structure of its (μ-1,2-peroxo)diiron(III) intermediate....26

Figure 1.7. A dinuclear metalloprotein with $\alpha\beta\beta\alpha$ (β-lactamase fold) and a proposed core structure of CmlA....29

Figure 1.8. The diverse functions, structural motifs, reactivities, and mechanisms of diiron enzymes....31

Figure 2.1. Models for FEFF calculation, generated by ChemBioDraw Ultra 11.0, which differs in the Fe-O and Fe···Fe distances. The Fe-O distance and Fe···Fe distance vary 0.1 Å steps from 1.9 to 2.1 Å and from 3.0 to 3.8 Å, respectively....41

Figure 2.2. Energy-dependence of exposure time. Exposure time after 1st scan (15 $Å^{-1}$) is 1200 s, at 0 $Å^{-1}$ (edge) is 140 s. Total exposure time at the edge of 2nd scan is 1340 s....42

Figure 2.3. XANES linear combination fitting using Athena program.[152] A linear combination fit (linear combo) to a second scan was obtained using a 1st scan and fully photoreduced data as standards. E_0 values, determined as the first inflection points of the edges using derivative plots, are ~ 7126.3, 7125.5, and 7124.5 eV for 1st scan, 2nd scan and photoreduced data, respectively. Fit range = E_0-20 – E_0+30 eV. The weight of photoreduced data in the linear combination is ~ 49 %, which is assigned as photoreduction yield at 1340 seconds exposure. 42

Figure 2.4. EXAFS data ($k^3\chi(k)$) photoreduced sample ($hDOHH_{phr}$) and the average data of first scans on 5 different fresh sample spots are shown in the top panel, while Fourier transforms at different k ranges are presented in the bottom panel. The k range of first scans data reflects the exposure time, which in turn reflects the photoreduction yield (see Table 2.1). Upon photoreduction, the inner shell $r' \sim 1.5 - 1.6$ Å clearly shifts to a longer distance, but there is no apparent change in the position of the $r' = 3$ Å peak. The first scans data in the k range = 2 – 12 $Å^{-1}$ is then assigned to hDOHHperoxo. 43

Figure 2.5. The UV-Visible spectra of hDOHH at room temparature. Conversion of as-isolated hDOHH (—) by 2.2 equiv. dithionite to reduced hDOHH (···) and its regeneration upon exposure to air after 180 minutes of anaerobic incubation (---). Inset: Change of A_{630} with time. 44

Figure 2.6. Mössbauer studies of hDOHH. 4.2 K zero field Mössbauer spectra of as-isolated hDOHH (A) and reduced with dithionite (B). The solid line in (A) is a simulation assuming two nested doublets as described in the text. (B) The solid line is a simulation of $hDOHH_{red}$ assuming two equally intense doublets representing ~ 75% of Fe. Details of data reduction and analyses are given in Supporting Information. 8.0 T Mössbauer spectra of as-isolated hDOHH recorded at 4.2 K (C) and 50 K (D). The solid lines are spectral simulations for an antiferromagnetically coupled diiron(III) center containing two high-spin (S = 5/2) Fe(III) sites. For the simulation of the 50 K spectrum we used J = 70 cm^{-1}. At 50 K the central features of the 8.0 T spectrum contain contributions from the mononuclear Fe(III) contaminant (see Mössbauer spectroscopy section in Supporting Information). 46

Figure 2.7. Resonance Raman spectra of hDOHH samples. A: as-isolated hDOHH. B-D: reduced hDOHH exposed to $^{16}O_2$, $^{18}O_2$, and mixed-labeled O_2 ($^{16}O_2$, $^{18}O_2$ and $^{16}O^{18}O$). Background features due to the protein itself have been subtracted using the spectrum of fully-reduced hDOHH collected under the same conditions. Experimental data are presented with thick lines and fits are presented with thin lines. 47

Figure 2.8. X-ray absorption spectroscopic analysis of hDOHH. A: XANES spectra of hDOHHperoxo first scans (—), $hDOHH_{phr}$ (---), and $hDOHH_{red}$ (···). B and C: Fe K-edge EXAFS data $k^3\chi(k)$ of $hDOHH_{phr}$ and hDOHHperoxo and their Fourier transforms (thin lines) in k range = 2 – 14 $Å^{-1}$ and 2 – 11.8 $Å^{-1}$, respectively. Best fits are represented by the thick lines. Details of the fitting protocols are provided in Table 2.3. 50

Figure 2.9. Reaction of hDOHHperoxo with ~ 1 equiv. of substrate, deoxyhypusine-containing eIF5A. Left: The decay of hDOHHperoxo was monitored by following the change in A_{630} at different incubation times in the absence of eIF5A(Dhp) (◇) and in the presence of eIF5A(Dhp) (■).Yields of hypusine (●) are calculated based on the observed amounts of hypusine (Hpu) and deoxyhypusine (Dhp); % Hpu = (Hpu×100)/(Hpu+Dhp). Right: UV/Vis spectra of hDOHHperoxo (blue) incubated with substrate for 24 hours at room temperature (yellow). After 24 hour incubation, the reaction mixture was cloudy and the precipitate was removed using centrifugation before the yellow spectrum was recorded. 53

Figure 2.10. Proposed core structure of hDOHHperoxo 57

Figure S.2.1. 4.2 K spectrum of hDOHH as isolated recorded in an external field of 8.0 T applied parallel to the observed γ-radiation; same conditions as in Fig. 2.6C but wider velocity scan. The red line is a spectral simulation, using A_o = -21.7 T for the magnetic hyperfine constant, of the mononuclear high-spin ferric contaminant. 60

Figure S.2.2. (A) 4.2 K zero field spectrum of $DOHH_{red}$ (raw data). The red curve outlines the remnant (5% of Fe) oxidized hDOHH. Subtraction of the oxidized fraction from (A) yields the "data" in (B). The red line in (B) indicates a high-spin ferrous species; as this species accounts for ~20% of the Fe, it is reasonable to assume that it represents the ferrous form of the mononuclear ferric contaminant (18%) of Fig. S.2.1. Subtraction of this contaminant yields (C) which is the spectrum shown in Fig. 2.6B. 61

Figure 3.1. (μ-1,2-Peroxo)diiron(III) complexes for XAS study or discussed in this chapter. 64

Figure 3.2. Fe K-edge XAS pre-edge features of hDOHHperoxo at pH 6.5 and model complexes. Index: 0: hDOHHperoxo; 1: 8; 2: 1; 3: 2;4: 3; 5: 4; 6: 5; 7: 6; 8: 7; 9: 10. 70

Figure 3.3. XANES spectra of hDOHHperoxo at pH 6.5 (——), 9.5 (——), 8.2 (— —) (partially photoreduced, photoreduced hDOHHperoxo at pH 8.2 (— • —), and chemically reduced hDOHH at pH 8.2 (••••). 71

Figure 3.4. Fitting of the pre-edge feature of hDOHH. A: hDOHHperoxo at pH 9.5; B: reduced hDOHH at pH 8.2; C: hDOHHperoxo at pH 8.2, partially photoreduced (see Fig. 3.3); D: photoreduced hDOHHperoxo at pH 8.2. Legend: data (ooo), fit (——), background (••••), pre-edge peaks (— — —). 71

Figure 3.5. Fourier transforms (left) and unfiltered Fe K-edge k^3-weighted EXAFS data (right) of hDOHHperoxo at pH 6.5 (top traces) and pH 9.5 (bottom traces). 74

Figure 3.6. Fourier transforms (left) of the Fourier-filtered Fe K-edge k^3-weighted EXAFS data (right) of hDOHHperoxo and model complexes. Data and fit parameters are shown bold in Tables 3.3 – 3.5. The red lines indicate the peaks corresponding to Fe---Fe paths in the Fourier transform spectra. 80
Figure 3.7. EPR spectra of hDOHHperoxo (left) and oxyHr (right) after cryo-radiolysis with ^{60}Co γ source. The spectra were collected in perpendicular mode, at ~ 12 K, and 10 mW power, 5G modulation amplitude. The cryo-reduced hDOHHperoxo samples were annealed at ~ 150 – 170 K for 10 mins. The cryo-reduced oxyHr samples were photoannealed at 77 K. The estimated g values for the cryo-reduced $^{16}O_2$-hDOHHperoxo sample are 1.909 and 1.947. The estimated g values for the $^{16}O_2$-oxyHr are 1.924 and 1.943.....81
Figure S.3.1. Resonance Raman spectrum of holo hDOHHperoxo prepared with 70 % enriched $^{17}O_2$ (647.1 nm excitation, 200 mW, 0 ^oC).....88
Figure S.3.2. Resonance Raman spectra of oxyHr prepared with 60 % enriched $^{17}O_2$ (––) and decayed Hr after exposed to 488 nm excitation laser (300 mW at ~ 0 ^oC). 88
Figure S.3.3. Annealing profile for cryo-reduced $^{16}O_2$-hDOHHperoxo.....89
Figure S.3.4. Annealing profile for cryo-reduced $^{17}O_2$-hDOHHperoxo.....89
Figure S.3.5. Annealing profile for cryo-reduced ^{57}Fe-hDOHHperoxo.....90
Figure S.3.6. EPR spectra of hDOHHperoxo before and after cryo-reduction with X-ray beam at the XAS beamline X3B of the National Synchrotron Light Source. The cryo-reduced sample was not annealed. 90
Figure S.3.7. Annealing profile for cryo-reduced $^{16}O_2$-oxyHr 91
Figure S.3.8. Annealing profile for cryo-reduced $^{17}O_2$-oxyHr 91
Figure 4.1. Purification of hDOHH with GSH-Sepharose affinity resin. Columns 1 and 2 were washed with air-saturated buffer, while column 3 and 4 were first washed with anaerobic buffer (left panel) followed by air-saturated buffer (right panel).....99
Figure 4.2. UV/vis spectra of hDOHHperoxo in various forms at pH 8.2. Left panel: ~ 0.1 mM holo hDOHHperoxo (——) was reduced with 2 equivalents of dithionite (——), which was then completely reacted with O_2 (– –) before 5 mM ascorbate was added (----). A solution containing ~0.36 mM $Fe(NH_4)_2(SO_4)_2$ and 5 mM ascorbate was exposed to the air ~ 1 minute (—••—). Right panel: ~ as-isolated hDOHH solution containing ~ 0.2 mM hDOHHperoxo (——) was mixed with 5 mM ascorbate (----). An $FeCl_3$ solution was mixed with 5 mM ascorbate 1 minute (—••—). 100

Figure 4.3. Formation kinetics of hDOHHperoxo from the reaction of reduced hDOHH with O_2-saturated buffer solution (1:1 mixing) at 4 ^oC, pH 7.5. Data is displayed with red diamonds, fit with blue line, and residual with black line. Fits to the data with two and three exponential growth step are shown on the left and right, respectively. 101

Figure 4.4. pH dependent self-decay of hDOHHperoxo at 37 ^oC. pH was measured at 37 ^oC. k_{obs} is displayed with open diamonds (◇) and $t_{1/2}$ with filled red circles (●). 102

Figure 4.5. Self-decay and reaction of hDOHHperoxo with 1 equivalent of eIF5A(Dhp) at 22 ^oC and pH's 6.0 and 7.5. 103

Figure 4.6. Mössbauer spectrum of hDOHHperoxo reacted with ~ 1 equivalent of eIF5A(Dhp). 105

Figure 4.7. Size-exclusion chromatographic analysis of hDOHH in various forms. All traces are aligned to the peak of the internal standard phthalic acid at t_R = 6.56 minutes (see Fig. 4.8). 106

Figure 4.8. Size-exclusion chromatographic analysis of the self-decay of hDOHHperoxo at pH 9.5 (left) and pH 6.5 (right). The peak at t_R = 6.56 minutes correspond to the phthalate standard. 107

Figure 4.9. Reaction of hDOHHperoxo with ~ 1 equivalent of eI5A(Lys), eIF5A(Dhp), and eIF5A(Dhp) analogues (shown on the right). Legends: self-decay (──), reaction with eIF5A(Lys) (──), eIF5A(HomoDhp) (----), eIF5A(8Me-Dhp) (──), eIF5A(cis=Dhp) (──), eIF5A(trans=Dhp) (●), eIF5A(d8-Dhp) (▲), and eIF5A(Dhp) (◇). 109

Figure 4.10. ESI-MS spectra of eIF5A(trans=Dhp) synthesized from the DHS reaction and its DOHH-oxidized product. 110

Figure 5.1. Fourier filtered k^3-weighted EXAFS spectrum of CmlI at pH 7.0 and its Fourier transform. k range = 2 – 12 $Å^{-1}$, back transform range = 0.85 – 4.00 Å, resolution = 0.16 Å. Best fit parameters :1 Fe-O at 1.89 Å, 4 Fe-N/O at 2.06 Å, 2 Fe---C at 3.01 Å, 0.5 Fe at 3.34 Å, 0.5 Fe at 3.59 Å, and 3.5 Fe---His multiple scattering paths at ~ 4.3 Å. See Table S.5.2 for more details. 120

Figure 5.2. Resonance Raman spectra of CmlIperoxo samples prepared with $^{16}O_2$, $^{18}O_2$, 1:2:1 mixture of $^{16}O_2$, $^{16}O^{18}O$, and $^{18}O_2$, respectively, as well as a peroxo decay sample. Spectra were obtained with ~ 200 – 300 mW laser power and subjected to two-point baseline subtraction. No smoothing or zapping was required. Spectra were aligned and normalized based on the sharp peak at 1005 cm^{-1} that arises from phenylalanine residues of the protein. Peak fitting results are provided in Table 5.1. 122

Figure 5.3. ν(O-O) values reported for various mononuclear iron, binuclear copper or iron, and heterobinuclear copper(II)/iron(III) peroxo complexes.[16, 77, 78, 81, 83, 108, 109 133, 177, 179, 181, 184, 185] 123
Figure 5.4. Proposed structure of CmlIperoxo (right) built based on the crystal structure of oxidized AurF–4-nitrobenzoate complex (3CHT) (left). Fe, O, C, N, and H atoms are shown in orange, red, dark grey, blue, and light grey, respectively. The green lines and numbers indicate the distances (in Å). Based on these distances, as well as to balance the charges on each iron center, the peroxo moiety is expected to bind η^2 to the Fe center on the left. In this proposed structure, the peroxo moiety is *cis* to both His ligands, a feature previously found in the crystal structure of the ternary enzyme–substrate–O_2 complex of naphthalene dioxygenase.[196] 125
Figure S.5.1. FEFF model and important scattering paths that were considered in the fitting procedure. The single scattering path from A_2 is associated with double and triple scattering paths involving A_1. Two double scattering paths are indistinguishable. A_1 = N at ~ 2.0 – 2.2 Å , A_2 = C or N at ~ 4.1 – 4.4 Å for imidazole moiety. 130
Figure S.5.2. Pre-edge feature of CmlI at pH 7.0. Peak parameters are provided in Table S.5.1. 131
Figure S.5.3. Fourier filtered k^5-weighted EXAFS spectrum of CmlI at pH 7.0 and its Fourier transform. See Table S.5.2 footnote for other data parameters. Best fit parameter are provided in Table S.5.2 (Fit 14). 132
Figure S.5.4. Resonance Raman spectra of CmlIperoxo. From top to bottom: $^{16}O_2$, 1:2:1 $^{16}O_2$, $^{16}O^{18}O$ (mixed label), $^{18}O_2$; $^{18}O_2$, and mixed label decay. Two-point baseline subtraction was applied. No smoothing or zapping was required. 135
Figure S.5.5. Gaussian peak fitting result to the mixed label 2 sample (Table 5.1). 135
Figure 6.1. Comparison of the edges of normalized first scan, second scan, and photoreduced data. 141
Figure 6.2. FEFF model and important scattering paths that were considered in the fitting procedure. The single scattering path from A_2 is associated with double and triple scattering paths involving A_1. Two double scattering paths are indistinguishable. A_1 = C at ~ 2.5 Å , A_2 = C at ~ 4.0 Å for bidentate carboxylate moiety. A_1 = N at ~ 2.0 – 2.2 Å , A_2 = C or N at ~ 4.1 – 4.4 Å for imidazole moiety. 141
Figure 6.3. Resonance Raman spectra of CmlA in $H_2{}^{16}O$, > 85 % $H_2{}^{18}O$, and > 85 % D_2O buffer solutions. All spectra were subjected to polynomial baseline correction and 2 points binomial smoothing. The sharp phenylalanine signal at 1005 cm^{-1} was used to align the data. Asterisks indicate the laser plasma lines. 142

Figure 6.4. Pre-edge quantification for first scan data with one peak (left) and two peaks (right). Parameters are provided in Table 5.1. Legend: Data (o), fit (—), background (–·–·), peaks (— —), and residual (·····). 144
Figure 6.5. Left: Unfiltered (black) and filtered (green) EXAFS data for CmlA. Right: Fourier transform of unfiltered data with *k* range = 2 – 13 $Å^{-1}$. 145
Figure 6.6. Fits to the first shell filtered data. Fit parameters are provided in Table 6.2. 146
Figure 6.7. Fits to the first and second shell filtered data. Fit parameters are provided in Table 6.3. 148
Figure 6.8. Fits to the unfiltered EXAFS data for CmlA. Both Fits 27 and 28 are lower in quality compared to Fit 29. 150
Figure 6.9. Best fit to unfiltered EXAFS data for CmlA (Fit 29). Fit parameters are provided in Table 6.4. 150
Figure 6.10. Comparison of the diiron(III) clusters of CmlA and related diiron proteins. 153

Chapter 1

The versatility of diiron clusters in biology: structures, reactivities, mechanisms, and biological roles of oxygen-activating diiron enzymes that turnover organic substrates

In the past three decades, the number of proteins containing non-heme non-sulfur carboxylate-bridged diiron active sites, so-called nonheme diiron enzymes, has increased rapidly.[1-23] These enzymes catalyze a wide range of chemical reactions, mainly oxidoreductive and some hydrolytic. They play various important roles in biology, including: (i) oxygen transport and/or sensing,[1, 24-26] (ii) O_2 and NO scavenging,[10] (iii) oxidative stress responses,[7, 27] (iv) iron storage and transport,[28] (v) biosynthesis of important biomolecules (DNAs,[8] lipids,[6] and proteins[16]) and bioactive products (antibiotics,[12, 14, 15, 18, 22] ubiquinone,[17] etc.), and (vi) metabolisms of hydrocarbons[4, 5] and other organic compounds.[11, 13, 20, 21] Of great fundamental and practical interest are the diiron enzymes that activate dioxygen to selectively oxidize organic substrates (roles v and vi). These enzymes are linked to a number of diseases including cancer, malaria, HIV, diabetes, obesity and aging.[6, 11, 17, 29-31] The conversion of organic substrates such as the selective functionalization of C-H bonds or small alkane synthesis would be relevant to chemical, pharmaceutical and energy industries. Understanding the molecular details of how these enzymes work would augment our knowledge of how Nature works that can potentially lead to practical applications. While recent reviews for specific types of diiron enzymes are available,[6, 8, 9, 32] the last excellent reviews on the entire class of diiron enzymes in general were published about 15 years ago.[2, 3] This chapter is devoted to a review of recent studies of both well characterized and recently found diiron enzymes that convert organic substrates. The first section will summarize the past and recent studies of canonical substrate-converting diiron enzymes. The subsequent sections will describe studies that expand the reactivities of the canonical enzymes as well as those

with new structural motifs catalyzing both old and new chemistries, including those that are included in this thesis.

1.1. The canonical oxygen-activating diiron enzymes that oxidize organic substrates

1.1.1. The conserved 4-helix bundle and 2-His-4-carboxylate structural motifs

Table 1.1. Diiron enzymes

Enzymes	Fold	Ligands	Function	Ref.
Canonical enzymes				
BMMs	α_4	2 H, 4 E/D	Hydrocarbon hydroxylation Alkene epoxidation	4, 5, 9
Desaturases	α_4	2 H, 4 E/D	Hydrocarbon desaturation	6
R2	α_4	2 H, 4 E/D	Tyrosine oxidation	8
Ferritin H-chain	α_4	1-2 H, 4 E/D	Ferroxidase	28
Rubrerythrin family	α_4	1-2 H, 5-6 D/E	Peroxidase	7, 27
Hemerythrin family	α_4	5 H, 2 D/E	O_2 carrier or sensor	1, 24-26
Fe-Urease	--	4H, 1D, 1K, ?	Urea hydrolysis	40
Uterroferin	$\alpha\beta\beta\alpha$	3 H, 1 Y, 2 D, 1 N	Phosphoric acid ester hydrolysis	41-43
Flavo-diiron proteins	$\alpha\beta\beta\alpha$	3-4 H, 3 D/E	NO and O_2 reduction	10
Recently found enzymes				
BoxB and PaaA	α_4	2 H, 4 E/D	Aromatic ring epoxidation	44-47
AD	α_4	2 H, 4 E/D	Aldehyde decarbonylation	19-21, 23
AurF	α_4	3 H, 4 E/D	Arylamine *N*-oxygenation	12, 14, 15
MIOX	--	4H, 2 D	4-electron oxidation of MI to DG	11, 13, 48-55
DOHH	HEAT	4H, 2E ?	C-H bond hydroxylation	16, 56-58
CmlA	$\alpha\beta\beta\alpha$	3-4 H, 3-4 E/D	C-H bond hydroxylation	18

The canonical organic substrate-oxidizing diiron enzymes belong to the multicomponent bacterial monooxygenase (BMMs) family, fatty acid desaturases family, and class Ia ribonucleotide reductase subunit R2 (R2). As found for most of other diiron enzymes, BMMs, desaturases, and R2 utilize a 4-helix-bundle protein fold to house their

diiron active sites.[3] A ligand set consisting of two His and four carboxylate (Glu and/or Asp) residues in the conserved sequence motif (**E/D**)X_n**E**X_2**H** (n = 29 – 37) is found to be unique for BMMs, desaturases, and R2s (Figure 1).[2, 3, 9, 33-39] Diiron enzymes that deviate from having either the 4-helix-bundle motif or a 2-His-4-carboxylate ligand set were not previously known to oxidize organic substrates (Table 1.1).

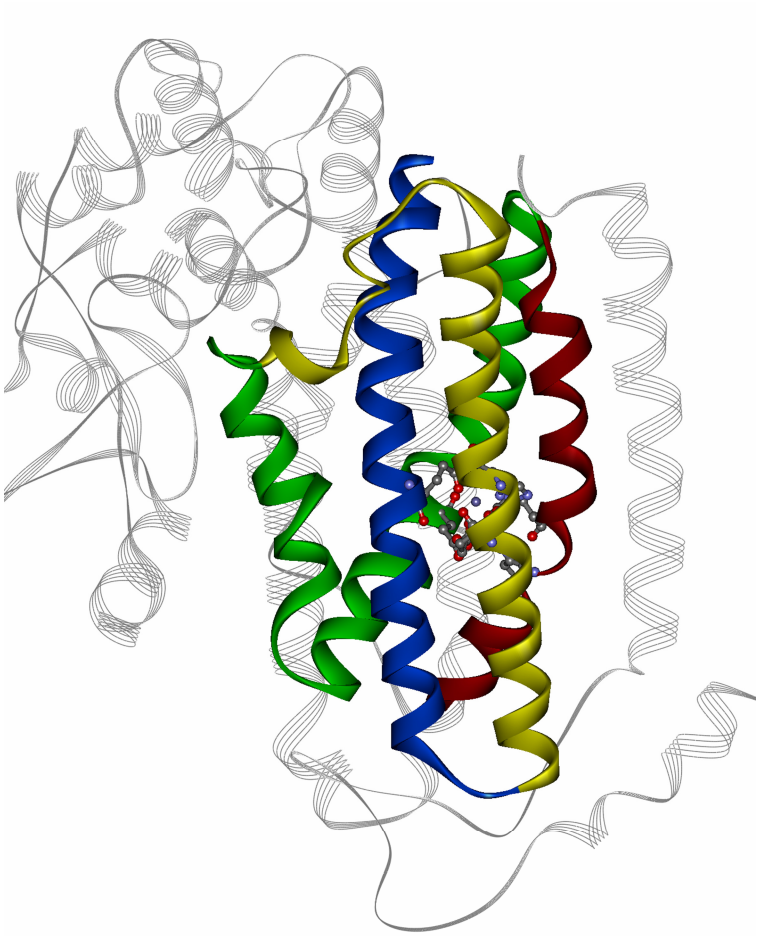

Figure 1.1. Overall protein scaffold of MMOH with the 4-helix bundle highlighted (1FYZ).

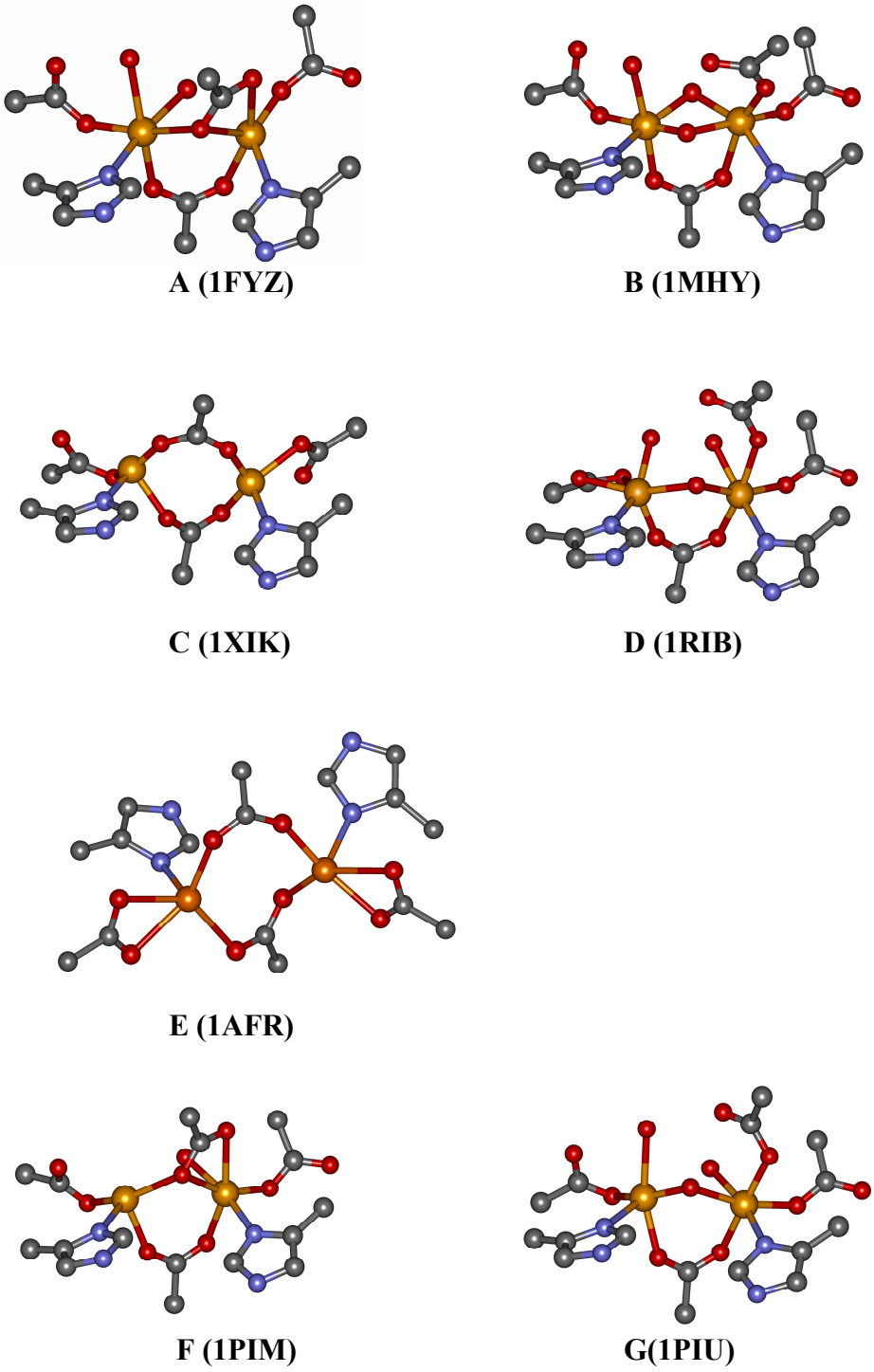

Figure 1.1. (Cont.). The diiron active sites with 2-His-4-carboxylate ligand sets of reduced MMOH (A), oxidized MMOH (B), reduced R2 (C), oxidized R2 (D), reduced Δ9D (E), reduced D84E R2 (F), and oxidized D84E R2 (G).

Among organic substrate oxidizing diiron enzymes, the structures of BMMs appear to be further conserved.[9, 39] The active site ligand arrangement of methane monooxygenase,[33-36] toluene/o-xylene monooxygenase,[37,38] and toluene 4-monooxygense[39] are homologous in both reduced and oxidized states (Fig. 1A and B, respectively), which are distinct from those of R2 (Fig. 1C and D), desaturases (Fig. 1E), and other diiron enzymes that do not exhibit oxygen atom transfer chemistry. Interestingly, having similar structures to those of BMMs in both oxidized and reduced forms (Fig. 1F and G), the mutant W48F/D84E R2 also exhibits monooxygenase chemistry instead of tyrosine oxidation as observed in wild type R2.[59, 60]

1.1.2. General mechanism

The general mechanism of diiron enzymes is shown in Scheme 1.1 based on the extensive studies of R2, MMO, and Δ^9D. In addition to the diiron-containing subunits, reductases are required for these enzymes in multiple turnover reaction. Furthermore, a small and cofactorless protein component that plays important regulatory role is found for BMMs. Of great interest are the oxygen activation steps, which involve the binding of O_2 to the diiron(II) center to form a peroxo intermediate that then undergoes O-O bond cleavage to form oxygenated high valent iron species. A mixed valent diiron(III/IV) (**X**) and a diiron(IV) (**Q**) intermediates have been trapped and characterized for R2 and MMO, respectively. A 2.5 Å Fe---Fe distance is found by EXAFS analysis for both of these intermediates.[61, 62] This distance could only be achieved in diamond core structures,

bis(μ-oxo)diiron(IV) for **Q** or (μ-1,1-carboxylato)(μ-oxo)diiron(III/IV) for **X** (Scheme 1.1), as observed in several model complexes.[63, 64]

Scheme 1.1. Simplified generally accepted mechanisms for canonical oxygen-activating diiron enzymes

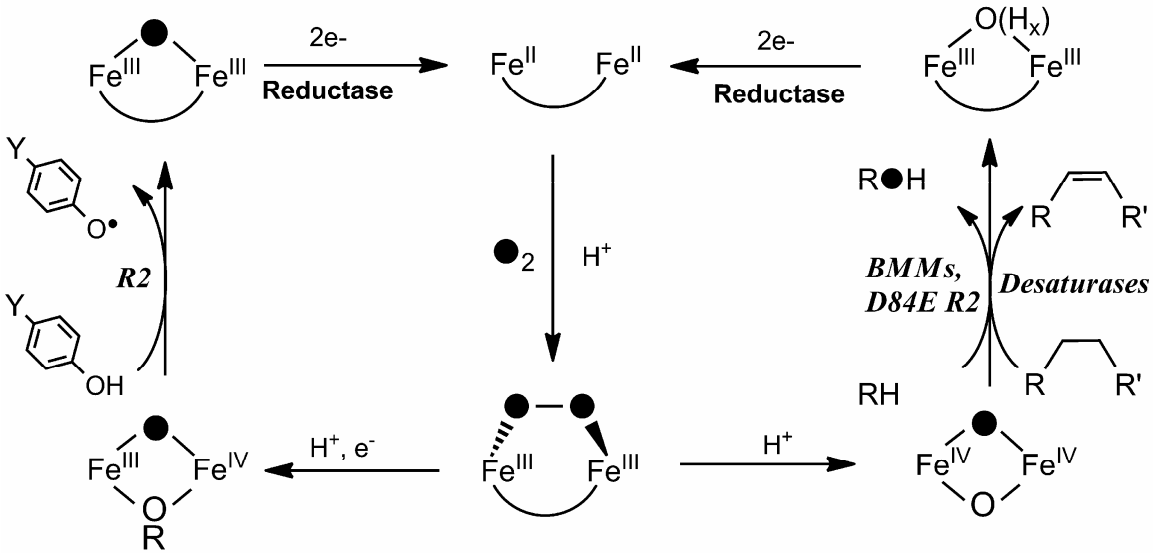

Q hydroxylates methane and other aliphatic hydrocarbons in a radical pathway involving the rate-determining homolytic cleavage of strong C-H bonds as evidenced by a very large substrate H/D KIE.[65, 66] On the other hand, **X** performs 1-electron oxidation of a nearby tyrosine residue (Y120) in R2 to form a diiron(III)-tyrosyl radical species[67-69] that is involved in a long range proton coupled electron transfer (PCET) to the catalytic subunit of RNR (R1). Oxygenated high valent species like **Q** and **X** are implicated in other diiron enzymes and observed in some synthetic model systems as the species responsible for substrate oxidation. Analogously, an iron(IV)-manganese(IV) has been observed in the O_2 activation by class Ic RNR from *Chlamydia trachomatis,* which is

then converted to a mixed valent iron(III)-manganese(IV) species functionally equivalent to the diiron(III)-tyrosyl radical system in class Ia R2.[70-72]

1.1.3. The peroxo intermediates

The peroxo intermediates of several canonical organic substrate-oxidizing diiron enzymes have been characterized by UV/Vis-detected stopped-flow techniques and rapid-freeze quench Mossbauer spectroscopy.[2, 73-80] Vibrational data of the O-O and Fe-O bonds have only been obtained for the peroxo intermediates of Δ^9D and D84E-R2, which unambiguously reveal a Fe-O-O-Fe (μ-1,2-peroxo) binding goemetry.[77, 78] A similar μ-1,2-peroxo intermediate has also been observed for the diiron ferroxidase site of frog ferritin.[81] While Δ^9Dperoxo is off pathway as it decays to a diferric state without desaturating its bound substrate,[6] the formation of **X** is the dominant decay pathway of D84E-R2peroxo, making it the only catalytically relevant peroxo intermediate of orgainic substrate oxidizing diiron enzymes that bears direct evidence for the peroxo moiety. Most of other peroxo intermediates of diiron enzymes have UV/Vis and Mössbauer spectroscopic properties similar to those of Δ^9Dperoxo, D84E-R2peroxo, and their model complexes and are thus believed to also have the μ-1,2-peroxo geometry. Furthermore, the Mössbauer parameters of these peroxo species differ from those of (μ-1,2-peroxo)diiron(III) complexes with an additional oxo/hydroxo/alkoxo ligand. [82, 83]

R2peroxo converts to **X** upon injection of an exogeneous electron via an electron transfer pathway involving the W48 residue near the surface of the protein. Blocking this electron transfer pathway to the diiron active site by replacing the W48 residue with an Ala or Phe residue of D84E-R2 allows the accumulation of the peroxo intermediate to a

yield suitable for structural analysis with EXAFS. A 2.5 Å Fe---Fe distance was derived by EXAFS for W48A/D82E-R2peroxo, leading to a proposed diamond core structure with two μ-1,1-carboxylato ligands in additional to the μ-1,2-peroxo moiety.[84] The same structure is also proposed for the peroxo intermediate of the ferroxidase subunit of frog ferritin that decays to a diferric cluster and H_2O_2 without O-O bond cleavage.[85] A closely related structure has been found only observed for a synthetic dimanganese peroxo complex,[86] but not yet found for any peroxo diiron model compound. The significantly large disorder parameter (10×10^{-3} Å^2) required by the EXAFS analysis for the 2.5 Å Fe---Fe path of W48A/D84E-R2peroxo at a small coordination number (0.6) [84] contradicts the proposed rigid structure consisting of two monoatomic and one diatomic bridging ligands. Indeed, in a later combined spectroscopic and computational study, the authors of this work proposed a ~ 3.6 Å Fe---Fe distance for W48F/D84E-R2peroxo, which is presumably identical to W48A/D84E-R2peroxo.[87] These contradicting results cast doubt on the precise structures of the peroxo intermediates of oxygen-activating diiron enzymes remains ambiguous.

The formation and activation of MMOperoxo has been extensively studied. The reaction of reduced hydroxylase subunit MMOH with O_2 is enhanced by 1000-fold in the presence of 1 – 2 equivalents of the regulatory subunit MMOB, allowing the accumulation of transient intermediates that are not observed in the absence of MMOB. Lipscomb and coworkers found evidence for two intermediates, designated as **O** and **P***, prior to the formation of MMOperoxo from *Methylosinus trichosporium*.[88] **O** is an oxygen adduct forming upon the addition of O_2 to reduced MMOH, in which the diiron center remains in the reduced state as evidenced by the characteristic g = 16 signal. **P***

forms after **O** with the lost of the g = 16 signal and decays to MMOperoxo. Subsequent conversion of MMOperoxo to **Q** is a single exponential step. Both the formation of MMOperoxo from $\mathbf{P}^*$ and its conversion to **Q** are pH-dependent with KSIE of 1.3 and 1.4, respectively.[88] Proton inventory measurements reveal that one proton is delivered in each of these steps.[88] Lippard and coworkers later also found KSIE of 2.0 and 1.8 for the formation and activation, respectively, of MMOperoxo from *Methylococcus capsulatus.*[89] They also proposed that proton transfer to an active site carboxylate residue in $\mathbf{P}^*$ leads to the isomerization of this intermediate to MMOperoxo.

Interestingly, Lippard and co-worker observed a "colorless" peroxodiiron(III) intermediate in ToMO (ToMOperoxo) with Mössbauer parameters distinct from the usually colored μ-1,2-peroxo intermediate (Table 1.2).[90] When the T201 residue, which is critical for the active site hydrogen bonding network, is mutated to several other residues, a colored peroxo species (T201Xperoxo) with UV/Vis and Mössbauer parameters typical of (μ-1,2-peroxo)diiron(III) species is observed in addition to ToMOperoxo (Table 1.2).[73, 91] Detailed kinetic analysis reveals that T201Xperoxo rapidly and reversibly isomerizes to ToMOperoxo involving a proton transfer event.[92] ToMOperoxo is then proposed to proceed on the reaction pathway as the aromatic ring attacking species. Whether ToMOperoxo is truly the substrate-oxidizing intermediate requires further investigation, both on the enzymatic and model systems. Nevertheless, the observation of multiple inter-converting peroxo species for ToMO, in line with that observed earlier for MMO, is an important insight toward understanding the oxygen activation mechanism by diiron enzymes.

Table 1.2. Properties of diiron(III)-peroxo units in enzymes and related model complexes

Peroxo Species	λ (nm) (ε ($M^{-1}cm^{-1}$))	δ (mm/s)	ΔE_Q (mm/s)	J (cm^{-1})	ν(O-O) (cm^{-1})	r(Fe···Fe) (Å)	$t_{1/2}$ (T (^oC)) formation	$t_{1/2}$ (T (^oC)) decay	Ref.
hDOHH	630 (2800)	0.55, 0.58 *(0.49, 0.63)*	1.16, 0.88 *(1.05, 0.99)*	50-70	855	3.44	~ 1 min (4)	Stable	16, Chapters 3 and 4
***Mt* MMOH**	725 (2500)	0.67	1.51	-	-	-	77 ms (4)	270 ms (4)	88
***Mc* MMOH**	720 (1350)	0.66	1.51	-	-	-	1 s (4)	2 s (4)	89
R2 mutants	700 (1500)	0.63	1.58	50	868	2.50	<130 ms (5)	<120 ms (5)	77, 79, 93
Mouse R2	700 (1500)	0.63	1.73	-	-	-	<1 ms (10)	11 ms (10)	74
Δ^9D	700 (1200)	0.68, 0.64	1.90, 1.06	-	898	-	15 ms (6)	30 min (25)	76, 78
Frog M Ferritin	650 (1000)	0.62	1.08	70	851	2.53	< 70 ms	< 1 s	85, 93, 94
ToMOH T201S	675 (1500)	0.67	1.51	-	-	-	8 ms (4)	0.23 s (4)	73
ToMOH	†	0.54	0.66	-	-	-	26 ms (4)	15 s (4)	90
OxyHr	500 (2000)	0.51, 0.54	1.09, 1.92	154	844	3.23	< 3 ms (6)	-	1, 95-102
AurF	500 (500)	0.54 (49%) 0.61 (33%)	0.66 0.35	-	-	-	<10 ms (20)	7 min (20)	103
CmlI	500 (500)	-	-	-	791	-	-	30 min (25) 3 hrs (4)	104, Chapter 5
OxyHr models	470 (2600)	0.53, 0.53	0.99, 1.57	-	843	-	-	-	105
Models type 1[a]	484 (2350)	0.53, 0.49	1.76, 1.15	-	841	-	-	-	
	682 (3450)	-	-	-	876	3.65	-	-	106
	694 (2650)	0.66	1.40	-	888	4.00	-	-	107
Models type 2[b]	560-750 (1200-3200)	0.53-0.56	0.52-1.26	57-60	845-908	3.05-3.47	-	-	83, 108, 109

† No chromophore observed. [a] bis(μ-1,3-carboxylato)(μ-1,2-peroxo)diiron(III) cores.[b](μ-1,2-peroxo)diiron(III) cores with an additional μ-alkoxo, μ-hydroxo, or μ-oxo ligand.

1.2. New reactivities of the canonical motif: regioselective aromatic ring epoxidation of CoA-tethered substrates by PaaA and BoxB

Scheme 1.2. Phenylacetyl-CoA and benzoyl-CoA metabolism.[46, 47]

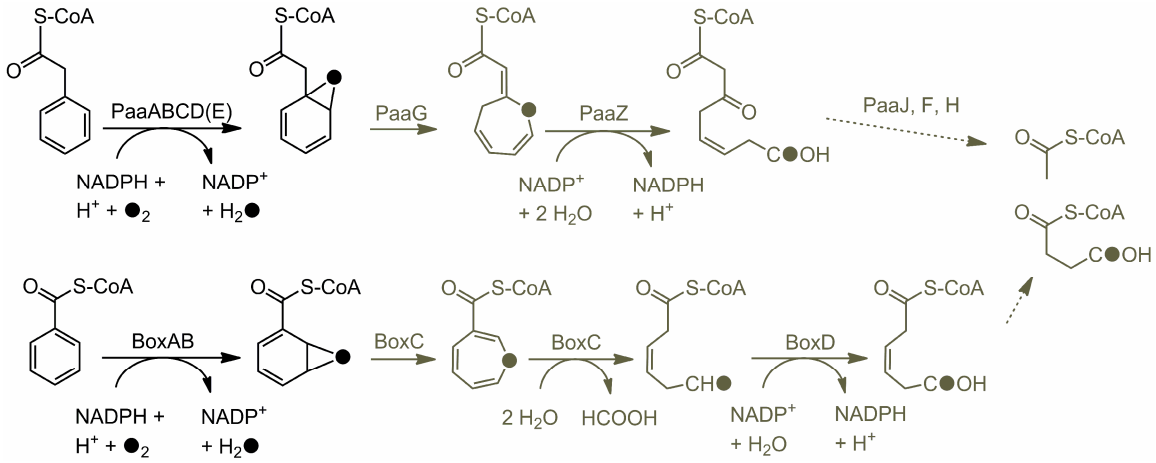

Aromatic compounds are among the major environmental pollutants[110] as well as the second most abundant class of organic growth substrate, next to carbohydrates, for microorganisms. Microorganisms overcome the stabilizing aromatic resonance energy with several strategies depending on the availability of oxygen. In aerobic pathways, the aromatic compounds are hydroxylated and ring cleaved by oxygenases using oxygen as the oxidant.[111, 112] In the absence of oxygen, aromatic compounds are usually converted to benzoyl-CoA that undergoes reductive dearomatization and ring cleavage.[113] A hybrid pathway occurs under semi-aerobic conditions, where CoA-tethered benzoate and phenylacetate have recently been shown to be first epoxidized by a monooxygenase and subsequently undergo oxygen-independent ring rearrangement and cleavage (Scheme 1.2).[46, 47] Among the enzymes involved in the epoxidation step, PaaA and BoxB are

identified as the monooxygenase subunits, whereas other components are reductase (PaaE and BoxA) or regulatory and structural subunits.

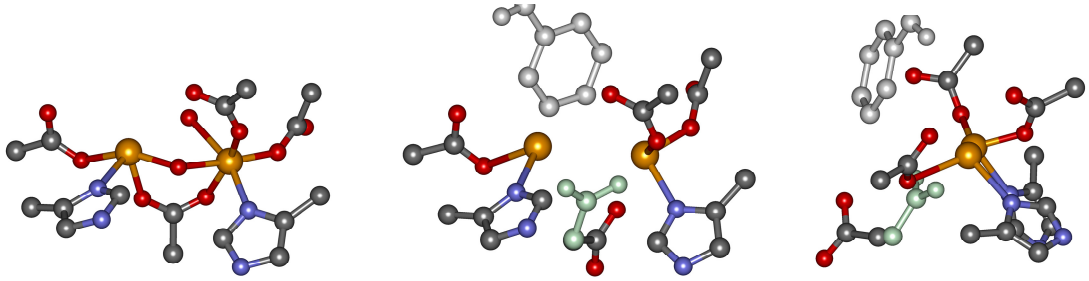

A (3Q1G) **B** (3PM5)

Figure 1.2. Crystal structures of BoxB.[44] A: oxidized form at 2.5 Å resolution. B: NADPH-reduced form with bound substrate at 2.3 Å resolution from views perperdicular to or along the Fe---Fe vector. The benzoyl substrate moiety is shown in grey. Glu 150 residue shifts away from bridging mode (shown in light blue-green). Sequence motif: $E_{120}X_{30}E_{150}X_2H_{153}$ and $D_{211}X_{29}E_{240}X_2H_{243}$

Recent studies show that PaaA and BoxB belong to a new branch of BMMs.[44, 45] Sequences of both enzymes contain the conserved diiron binding motifs (**D/E**)$X_{29\text{-}30}$**E**X_2**H** found for the canonical oxygen activating diiron enzymes.[3] The 2-His-4-carboxylate ligand set of BoxB has been confirmed by the crystal structure of its oxidized form. Although none of the iron-loaded forms of PaaA has been crystallized, superimposing the crystal structures of apo PaaA and oxidized ToMO reveals that 2 His and 4 carboxylate residues are located in a putative diiron binding site of PaaA in a similar fashion as in ToMO.[45]

In the oxidized form of BoxB, the 2-His-4-carboxylate ligand set arranges around the diiron active site in a way closely resembling that found for previously known BMMs (Fig. 2A). There is a well defined water-derived bridging ligand with Fe-O distances of 2.00 and 2.04 Å, an ∠Fe-O-Fe bond angle of 119.3°, and an Fe---Fe distance of ~ 3.5 Å.

Mössbauer spectroscopy shows that the oxidized form of BoxB contains a diiron(III) cluster with a quadruple splitting of 0.69 mm/s. This small ΔE_Q value is indicative of octahedral electronic geometry, which is smaller than values of 0.9 – 2.4 mm/s found for oxo-bridged diiron clusters with distorted electronic geometry.[114-116] The ΔE_Q value and structural parameters of the Fe-O-Fe unit are consistent with a μ-hydroxo bridged structure rather than a μ-oxo-bridged core as found in desaturases and R2 (Fig. 1.1), consistent with the 3.5 Å Fe---Fe distance. A second water molecule is found near a bridging position, which possibly leads to a bis(μ-hydroxo)diiron(III) core for oxidized BoxB, which is simlar to those in BMMs.

The crystal structure of a complex of BoxB with benzoyl-CoA has been obtained under anaerobic conditions in the presence of both BoxA and NADPH. The identity of the reduced diiron cluster is unclear although EPR shows that *in vitro* reduction of oxidized BoxB in solution yielded a mixed valent diiron(II/III) form. In the absence of NADPH, benzoyl-CoA did not co-crystallize with BoxB. Complexes of apo PaaA-PaaC with several CoA derivatives have also been obtained. There is a significant active site rearrangement in the crystal structure of reduced BoxB with benzoyl-CoA compared to the structure of oxidized BoxB. One iron center is displaced by 0.7 Å and the μ-1,3 Glu residue switches away from the diiron site. The two iron centers of reduced BoxB:benzoyl-CoA complex are thus not bridged (Fig. 2B), a feature also observed for the mixed valent state of phenol hydroxylase.[117] It is likely that oxidized BoxB and PaaA have low affinity for their substrates and that the reduction of the diferric state is necessary for the conformational change to occur upon substrate binding.

Complexes of PaaA and the NADPH-reduced form of BoxB with their substrates are the first examples of monooxygenase-substrate complexes that are co-crystallized. There are hydrophilic substrate channels with narrow entrances, which resemble that of stearoyl-ACP Δ^9D.[118] The benzoyl moiety is positioned near the active site with one side of the benzene ring facing the diiron cluster. A dioxygen molecule can be modeled as a μ-1,2-peroxo ligand of the diiron cluster and pointing toward the C2 and C3 atoms of the benzoyl moiety. The crystal structure data thus provides the rationale for the exclusive observation of 2,3-epoxide product of BoxB (Scheme 1.2).[47] Likewise, 1,2-epoxide is the sole product of the reaction of PaaA (Scheme 1.2), which is likely a result of precise positioning of carrier-tethered substrate. Such strict regioselectivity is observed for desaturases that act on carrier protein-bound fatty acids[118, 119] but not for BMMs.

1.3. New reactivity of the canonical motif: alkane synthesis by aldehyde decarbonylase

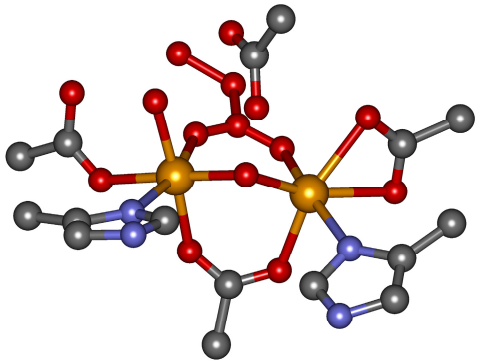

Figure 1.3. Crystal structure of fatty acid decarbonylase from from *P. marinus* MIT9313 (2OC5). Fe-μO = 1.940, 2.007 Å, $\angle$Fe-O-Fe = 109.9^o, Fe---Fe = 3.232 Å. Sequence motif: $E^{45}X_{28}E^{73}X_2H^{75}$ and $E^{128}X_{29}E^{157}X_2H^{160}$

Scheme 1.3. Synthesis pathway of alkane or alkene from fatty acids with possible C1 co-products.[19-22] N/F/FR = NADPH, ferredoxin, and ferredoxin reductase system. N/P = NADH and 5-methylphenazinium methylsulfate system.

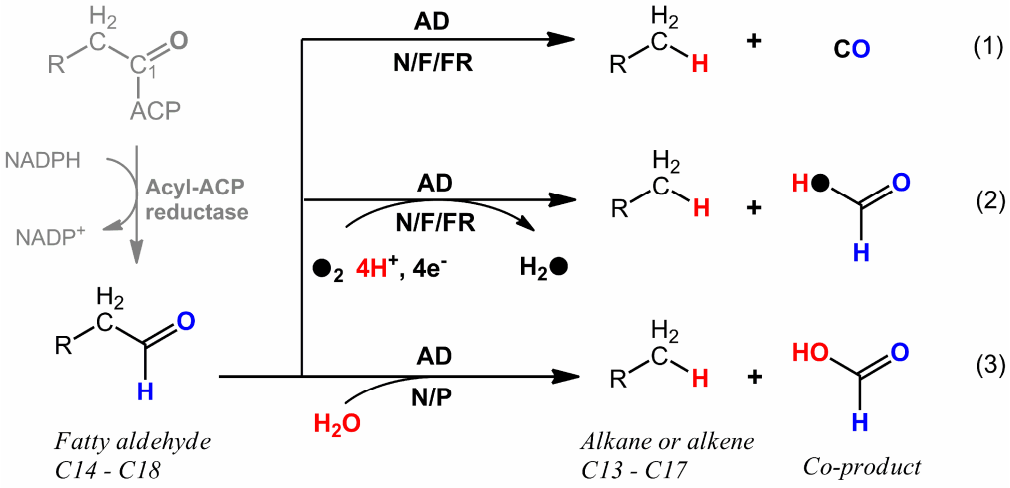

The biosythensis of alkanes is one of the newest approaches toward renewable fuel. A two-step pathway in cyanobacteria was discovered recently in which ACP-bound fatty acids are reduced to corresponding aldhydes that in turn undergo C1-C2 bond scission to produce alkane (Scheme 1.3).[19] The removal of the carbonyl group is carried out by the enzyme aldehyde decarbonylase (AD) as first reported by Schirmer *et al* in 2010. A 1.68 Å crystal structure of AD from *Prochlorococcus marinus* MIT9313 (*Pm*AD) was deposited in 2006 by the Joint Center for Structural Genomics before its function was found (pdb code 2OC5). The overall protein fold of *Pm*AD and its apparent diiron active site, which is yet to be confirmed, closely resemble that of class Ia R2, except that there is an unidentified μ-1,3 ligand, possibly a fatty acid molecule, displacing a Glu ligand (Fig. 1.3). A detailed review by Krebs, Bollinger, and Booker on ADs has been recently published (ref. 120). Summarized here are the most important details on AD reaction, some of which are not included in ref. 120.

The original study by Shirmer *et al.* focused on elucidating the role of AD in the synthesis of alkane and alkene; they only tentatively assigned the C1 co-product as CO, which makes it a self-redox reaction (Reaction 1, Scheme 1.3). The *in vitro* assay of ADs from various sources required a reducing system such as NADPH, ferredoxin, and ferredoxin reductase (N/F/FR).[19] The requirement for reducing reagents by ADs, and the fact that ADs bear the structure motif of O_2-activating dinuclear metal enzymes, prompted Krebs, Bollinger, Booker and co-workers to further investigate the identity of the C1 co-product. They obtained three important results for the reaction of AD from *Nostoc punctiforme* (*Np*AD): 1) the C1 co-product is formate, not CO; 2) the aldehyde H atom remains on the formate co-product; and 3) O_2 is required for the reaction and one oxygen atom from O_2 is incorporated into the formate co-product. Based on this observation, Krebs, Bollinger, Booker and co-workers proposed a "cryptic" reaction for *Np*AD (Reaction 2, Scheme 1.3).[21, 23] Several O_2-activation mechanisms of AD using different types of dinuclear active sites were also hypothesized although supporting experimental data have yet to be obtained.[23, 120]

Shortly after the work by Krebs, Bollinger, Bookers and co-workers, Das *et al.* reported their study on *Pm*AD, in which for the first time AD is shown unequivocally to be an iron-dependent enzyme.[20] *In vitro* reconstitution of apo AD with Mn(II), Fe(II), Co(II), Ni(II), Cu(II) and Zn(II) revealed that only Fe(II) supports alkane formation. More importantly, in the presence of the NADH:PMS reducing system (N/P), *Pm*AD is only active under strict anaerobic conditions, but inactive under aerobic conditions. Formate was also found as the C1 co-product in the anaerobic reaction of *Pm*AD. Labeling experiments using D_2O or deuterated substrate unequivocally indicated that

aldehyde H atom remained on the formate co-product, which is also observed for the reaction of *Np*AD under aerobic condition, while a hydrogen atom from water is incorporated to the alkane product (Reaction 3, Scheme 1.3). In the absence of a reducing system and under anaerobic conditions, Das *et al.* observed the formation of a high spin iron(III) species at $g = 4.3$ when adding heptadecanal to *Pm*AD. Using the spin trapping reagent phenyl-N-tert-butylnitrone (PBN), they was also able to probe another radical species that formed together with the high spin iron(III) species. These observations led to a proposed mechanism involving electron transfer from iron to aldehyde to initiate C1-C2 bond cleavage with the reducing system serves as an "electron buffer".

Notably, *Pm*AD turns over about 0.4 times per minute under anaerobic conditions with N/P, which is about 100 to 1000-fold more active than *Np*AD under aerobic conditions with N/F/FR (~ 3 turnovers in 20 hours).[21, 23] It is unclear why *Pm*AD is more reactive than *Np*AD, although there are differences in the sequences of *Pm*AD and *Np*AD (60% sequence identity) and the reaction conditions are likely among the causes. More importantly, why one AD requires O_2 to function while the other is only active in the absence of O_2 is intriguing and should draw immediate attention.

1.4. An additional His ligand and a new reactive species: Substrate oxidizing peroxo intermediates in AurF and CmlI

A considerable number of natural products exhibiting remarkable biological activities contain nitroaryl groups, which are often synthesized via the oxygenation of the corresponding aminoaryl groups.[121, 122] AurF from *Streptomyces thioluteus* was the first

binuclear metalloenzyme reported to catalyze *N*-oxygenation of *p*-aminobenzoic acid (PABA) to *p*-nitrobenzoic acid (PNBA), a step involved in the biosynthesis of the polyketide antibiotic aureothin (Scheme 1.4).[12, 123] Homologs of AurF are found in a number of non-ribosomal peptide synthetase (NRPS) or polyketide synthase (PKS) pathways,[124, 125] including CmlI from *Streptomyces venezuelae* that is involved in the biosynthesis of chloramphenicol.[104]

Scheme 1.4. Oxygenation of *p*-aminobenzoic acid (PABA) by AurF as a step in the aureothin PKS synthesis pathway (left) and its proposed mechanisms.

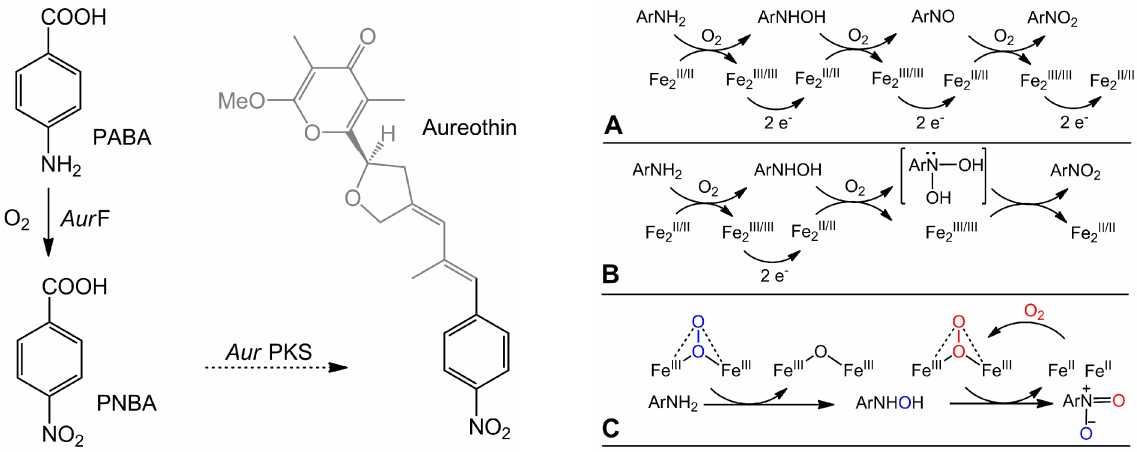

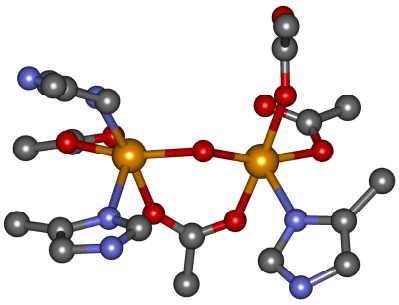

Figure 1.4. Active site structure of AurF from *Streptomyces thioluteus* (3CHU). Sequence motif: $E^{101}X_{34}E^{136}$ X_2H^{139}, $E^{196}X_{26}H^{223}X_3E^{227}$ X_2H^{230}

The sequence of AurF contains the conserved diiron binding motif $\mathbf{E}^{101}X_{34}\mathbf{E}^{136}$ $X_2\mathbf{H}^{139}$, $\mathbf{E}^{196}X_{30}\mathbf{E}^{227}$ $X_2\mathbf{H}^{230}$ with an additional His at position 223. The crystal structure of AurF shows that a binuclear active site is indeed supported by a 4-helix bundle protein fold.[15] Furthermore, there is an electron transfer pathway similar to that found in class Ia R2.[126] The active site of AurF was at times proposed to be a diiron,[12] dimanganese,[14] and iron/manganese[127] cluster based on crystallographic and spectroscopic studies. Choi *et al.* later showed in reconstitution experiments of apo AurF with mixtures of Fe and Mn that the *N*-oxygenase activity of AurF is optimal with Fe:Mn ratio of 1:0 and decreases as the Fe:Mn ratio decreases.[15] The pure manganese form showed only nominal activity compared to the iron form. The ligand arrangement in the oxidized AurF crystal structure is similar to that found in R2 and MMOH, except that H233 replaces a labile coordinating water molecule (Fig. 1.4).[15] In pH 7.5 solution, the diiron(III) cluster of AurF exists mainly in a μ-oxo bridged form (~ 78 % by Mössbauer spectroscopy), but a μ-OH bridged form is also observed (~ 22 %), indicating that the μ-oxo ligand of AurF is reversibly protonatable under physiological conditions.[103] Sequence comparison and Mössbauer studies[104] together with EXAFS analysis (Chapter 5) of CmlI showed that this enzyme also contains a diiron cluster with 3 His ligands that exists in a mixture of μ-oxo-bridged and μ-hydroxo-bridged forms. Having an additional His ligand and a reversibly protonatable μ-oxo ligand, AurF and CmlI are clearly different from the canonical diiron enzymes.

In the reaction of reduced AurF with O_2, a broad chromophore at 500 nm (ε = 500 $M^{-1}cm^{-1}$) is observed, which differs from both the reduced form and the oxidized form of AurF.[103] This chromophore is associated with two sets of Mössbauer parameters, δ_1 =

0.54 mm/s, $\Delta E_{Q,1}$ = 0.66 mm/s and δ_2 = 0.61 mm/s, $\Delta E_{Q,2}$ = 0.35 mm/s at a ratio of ~ 1.5:1. These parameters are typical of high-spin iron(III) species[128] but different from the parameters of oxidized AurF. This species is thus assigned as a peroxo intermediate (AurFperoxo) that is perhaps present as an equilibrium mixture of two or more isomers. A peroxo intermediate with similar spectroscopic parameters has also been observed for CmlI (CmlIperoxo).[104] Unlike in AurFperoxo, the Mössbauer spectrum of CmlIperoxo exhibits two doublets with equivalent intensities, which more likely arise from one diiron(III) species.[104] The UV/Vis and Mössbauer parameters of AurFperoxo and CmlI are different from those of μ-1,2-peroxo intermediates of the canonical diiron enzymes, [82, 83, 106, 109, 129-131] but their Mössbauer parameters resemble those of the optically inactive ToMOperoxo.[90]

AurFperoxo, which forms with $t_{1/2}$ ~ 5 ms, and is relatively stable ($t_{1/2}$ ~ 7 min at pH 7.5 and 20 ^{o}C) but decays rapidly upon the addition of 1 equivalent of PABA ($t_{1/2}$ = 5 ms). No intermediate is observed in the reaction of AurFperoxo with PABA, suggesting that this intermediate is the substrate-oxygenating species. It is proposed that the peroxo moiety is nucleophilically attacked by the electron rich arylamine and subsequently undergoes O-O bond cleavage, which may also be the case for the reaction of ToMOperoxo with its nonnative substrate phenol.[90] More interestingly, Li *et al.* found that AurFperoxo is capable of 4-electron oxidation of the *p*-hydroxyaminobenzoic acid (PHABA) intermediate *in vitro* to form PNBA and the active diferrous AurF (Scheme 1.4C).[132] An alternative stepwise reaction is proposed for AurF (Scheme 1.4B), in which the enzyme uses only two equivalents of O_2 and two equivalents of reducing reagent. This mechanism is much more chemically economical than the generally accepted

mechanism involving 3 equivalents of O_2 and 6 equivalents of reducing reagent (Scheme 1.4A). While it is unclear whether 4-electron oxidation of PHABA truly occurs *in vivo*, there is also a discrepancy with the study reported by Li *et al*. The incubation of 450 μM PHABA with reduced AurF and 900 μM O_2 generates 50 – 70 μM PABA based on the reported HPLC traces in ref.[132] This formation of PABA cannot be assigned to the auto-decomposition of PHABA as the incubation of PHABA with O_2 in the absence of reduced AurF did not produce PABA. The production of PABA from PHABA in the presence of reduced AurF clearly complicates the kinetics of the reaction. Nevertheless, the *in vitro* 4-electron oxidation is an unique reactivity of a (peroxo)diiron(III) species.

CmlIperoxo decays much more slowly than AurFperoxo ($t_{1/2}$ = 0.5 and 3 hours at 25 and 4 ^{o}C, respectively),[104] which allowed us to characterize this species in solution with resonance Raman spectroscopy (Chapter 5). Surprisingly, our resonance Raman study revealed an unusually low ν(O-O) frequency (791 cm^{-1}) for CmlIperoxo, which was attributed to a (μ-η^1:η^2-peroxo)diiron(III) cluster instead of the more common (μ-1,2-peroxo)diiron(III) species (Table 1.2). The additional His ligand in CmlI perhaps contributes to the shift in peroxo binding geometry of CmlIperoxo. Although this peroxo binding geometry has been found in heterobinuclear Fe-heme copper peroxo intermediates,[133] it has not been previously observed for any (peroxo)diiron(III) species. A similar peroxo binding geometry is also expected for AurFperoxo given the spectroscopic similarity of AurFperoxo and CmlIperoxo. It could be possible that the μ-η^1:η^2-peroxo is a common geometry in the peroxo intermediates of the diiron N-oxygenase family of enzymes, which significantly expands our current knowledge of oxygen activation by nonheme diiron enzymes.

1.5. A new reactive species: Substrate oxidizing superoxo intermediate in MIOX

Scheme 1.5. Reaction of MIOX and formation of the proposed C-H bond cleaving superoxo intermediate G.

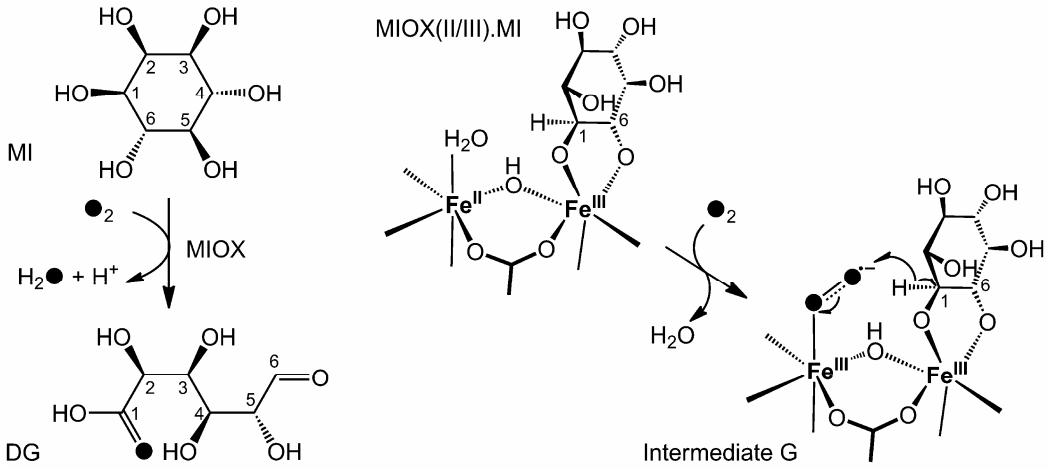

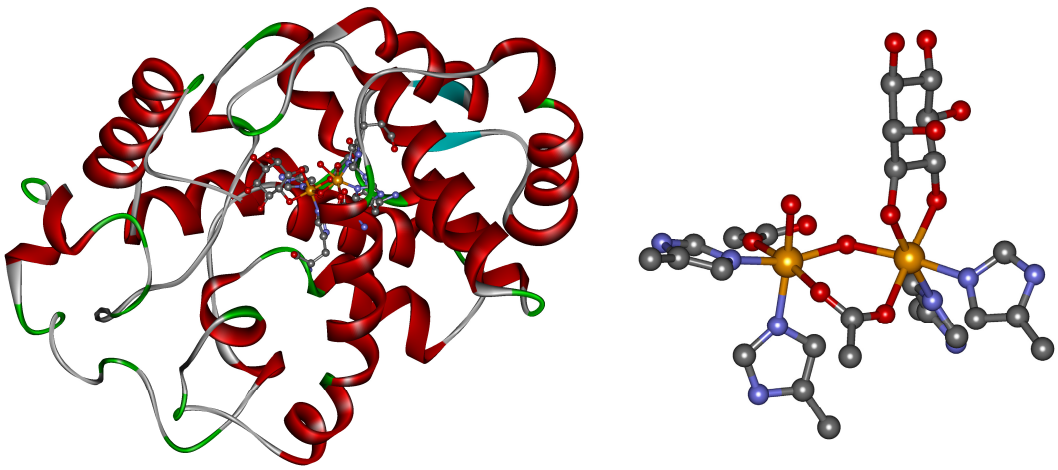

Figure 1.5. Crystal structure of mouse MIOX with bound substrate (2HUO).

myo-Inositol (MI) and its various biochemical derivatives play various cellular roles including membrane structure, signal transduction, and osmoregulation.[48, 49] MI is converted by *myo*-inositol oxygenase (MIOX) to D-glucuronate (DG) (Scheme 1.5), which is subsequently transformed to xylitol. Aberrant homeostasis of MI, i.e. depletion of MI and overproduction of xylitol, are sometime linked to diabetes, suggesting MIOX as a target for treatment of this disease.[48, 49]

Despite being found in 1950's, MIOX has only been well studied recently. The sequence of MIOX is conserved among many species.[51] The crystal structures of substrate-bound MIOX from mouse and humans are almost identical.[11, 55] Although it is a diiron enzyme that oxidizes an organic subtrate, MIOX is different from the canonical enzymes in several ways. First, MIOX carries out the 4-electron oxidation of its substrate using one equivalent of O_2, as opposed to 2-electron oxidation by the canonical enzymes. Thus, MIOX does not formally require a reducing system as found for the canonical enzymes. Second, MIOX does not bear the 4-helix bundle motif (Fig. 1.5). Third, the ligand set of MIOX contains 4 His and 2 Asp residues supported by 5 helices (Fig. 1.5). Fourth, MIOX is active in a mixed valent diiron(II/III) form in contrast to the diiron(II) state in the canonical enzymes. Finally, and most interestingly, the substrate-oxidizing intermediate in MIOX is found to be a terminal superoxo-diiron(III) species, not a high-valent species. The crystal structures of MIOX from mouse and humans both reveal that MI binds to the iron(III) center in a bidentate mode using the hydroxy groups at positions 1 and 6, the oxidation target. A labile terminal water molecule is found on the iron(II) center that is *syn* to the MI molecule (Fig. 1.5). This structure suggests that O_2 could replace this water ligand and get activated to the form of a superoxide that points toward

the C1-H bond of MI (Scheme 1.5). As the reaction goes on, the oxidation state of the substrate-binding iron center remains unchanged. Based on the structure and proposed mechanism of MIOX, the O_2-binding iron center of MIOX can be considered as a monoiron enzyme with 2-His-1-carboxylate facial triad. The function of the iron(III) center, which occupies to coordination sites of the facial triad through the μ-hydroxo and μ-1,3-carboxylato ligands, is to arrange the substrate to an optimal position for C1-H bond activation. Additional details can be found in a recent excellent review of MIOX structure and chemistry (ref. 54).

1.6. A new structural motif for hydroxylase: DOHH, the first human diiron hydroxylase

Scheme 1.6. Post-translational (+)-hypusine biosynthesis. DHS = deoxyhypusine synthase.

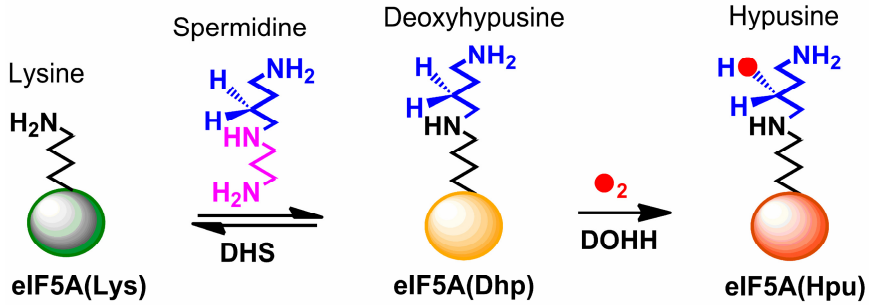

(+)-Hypusine, (+)-N-4-amino-(2-hydroxybutyl)lysine, is an unusual amino acid found only in the sequence of the eukaryotic initiation factor 5A (eIF5A),[56, 57] which is synthesized posttranslationally in a two-step pathway involving deoxyhypusine synthase (DHS) and deoxyhypusine hydroxylase (DOHH). eIF5A is highly conserved among

eukaryotes and is required for cell proliferation. Based on the crystallographic study of EF-P, a homolog of eIF5A in *Thermus thermophilus*, it is proposed that eIF5A(Hpu) binds to the complexes of ribosome and fMet-tRNA$_i^{fMet}$ and properly positions them for the formation of the first peptide bond.[134] eIF5A(Hpu), but not the other forms of eIF5A, has been shown to promote translation elongation.[135] Inhibition of DHS and/or DOHH leads to a decreased amount of cellular eIF5A(Hpu), resulting in the inhibition of cell growth. Thus, DOHH is an attractive target for interfering with cell proliferation in antitumor, antimalaria, and anti-HIV-1 therapy.[29, 30, 56, 57] Indeed, two potential drugs have been reported to inhibit HIV-1 gene expression in cells at clinically relevant concentrations by preventing the maturation of eIF5A.[29]

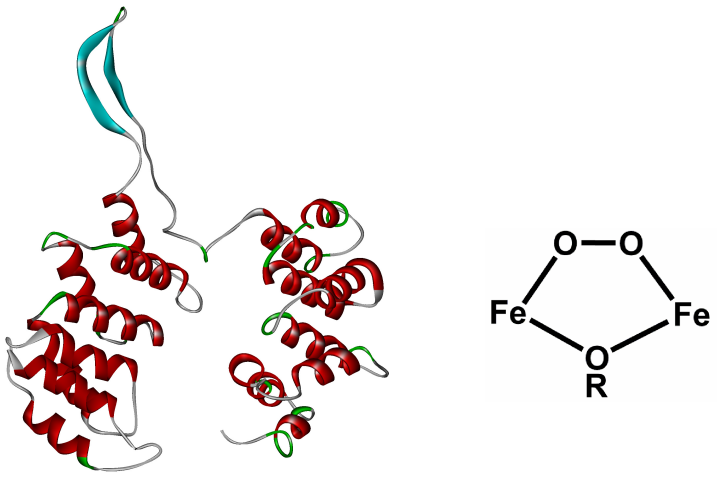

Figure 1.6. Hypothetical structure of hDOHH and a proposed structure of its (μ-1,2-peroxo)diiron(III) intermediate.

Although DOHH was found twenty years ago, its structure and mechanism have not been well understood. DOHH has been shown to be an oxygen- and iron-dependent

enzyme.[58, 136, 137] Although it carries out C-H bond hydroxylation, DOHH has an amino acid sequence that does not resemble those of BMMs or monoiron hydroxylases. Instead DOHH has a superhelical structure consisting of 8 HEAT motifs, with four strictly conserved pairs of adjacent His-Glu residues.[58] Based on mutagenesis experiments and metal analysis of holoprotein, DOHH is proposed to have a 4-His, 2-Glu ligand combination to bind two iron atoms.[136] Later spectroscopic analysis showed that DOHH indeed contains a diiron active site, making it the first diiron enzyme found to stereospecifically hydroxylates protein-bound substrate.[16]

Interestingly, human DOHH (hDOHH) expressed in *E. coli* has a blue color (λ_{max} ~ 630 nm),[136] which has been shown by our recent spectroscopic study (reported in Chapter 2) to arise from a (μ-1,2-peroxo)diiron(III) species (hDOHHperoxo) by various spectroscopic techniques.[16] A ~ 3.4 Å Fe---Fe distance was unequivocally derived by EXAFS analysis for hDOHHperoxo. The spectroscopic properties of this species suggest that it is similar to (peroxo)diiron(III) model compounds with an additional single-atom bridge, but differs substantially from those in the canonical enzymes and their relevant model compound (Table 1.2). Notably, although hDOHH is stable ($t_{1/2}$ = weeks at 4 ^{o}C at pH 8.2), it is on the eIF5A(Dhp) hydroxylation pathway[16] and one of its peroxo oxygen atom is incorporated in the product (our unpublished result). hDOHHperoxo is thus the only extensively characterized functional peroxo intermediate of diiron enzymes thus far. The activation of hDOHHperoxo may involve protein conformational change upon protein substrate binding, as well as the removal of this single-atom bridge that allows the peroxo moiety to isomerize to a more activated geometry. A regulatory analogous to those of BMMs may also be required for peroxo activation. Further studies on activation

of hDOHHperoxo would bring significant insight into the oxygen activation mechanism by diiron enzymes.

1.7. A new structural motif for hydroxylase: CmlA, a hydroxylase with a β-lactamase fold

Many natural products, including pharmaceutically important antibiotic and chemotherapeutic drugs, are synthesized in nonribosomal peptide synthetase (NRPS)-based pathways and contain *β*-hydroxy amino acid moieties. [138-140] The hydroxyl group is the target of many tailoring reactions required for pharmacological activity, including glycosylation, oxidation, and macrocycle formation.[141] The *β*-hydroxy group is typically introduced stereospecifically by cytochrome P450s and alpha-ketoglutarate-dependent nonheme iron-containing enzymes.

Scheme 1.7. The biosynthetic pathway of chloramphenicol

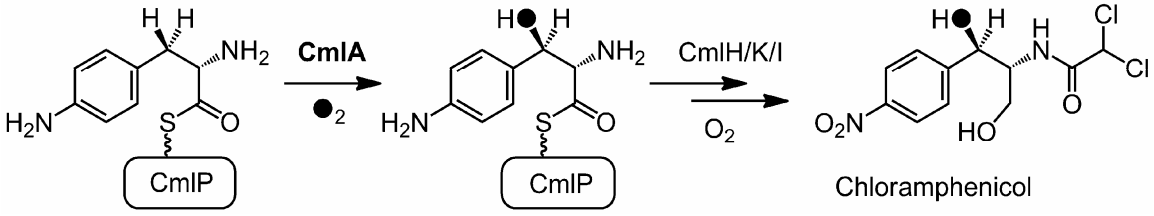

Recently, a large new family of tailoring enzymes that contain a nonheme oxo-bridged diiron active site has been identified.[18] These enzymes catalyze β-hydroxylation in the biosynthesis of a wide range of antibiotic and cytostatic agents, including

bleomycin and the planin family of antibiotics. The first isolated member of this family is CmlA that catalyzes β-hydroxylation of *p*-aminophenylalanine (L-PAPA) linked by a thioester bond to the thiolation domain of the NRPS CmlP (Scheme 1.7). CmlA is the second example of a diiron monooxygenase that hydroxylates protein-bound substrate.

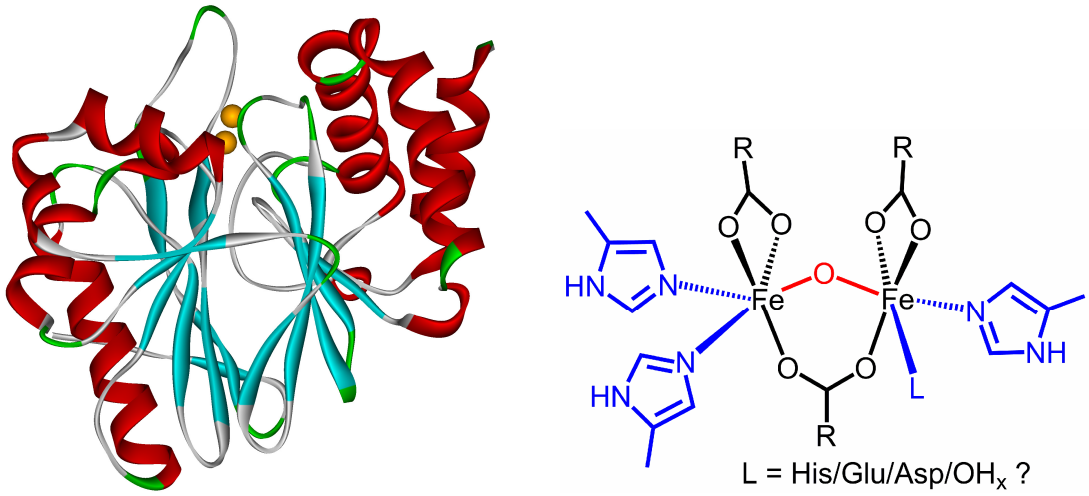

Figure 1.7. A dinuclear metalloprotein with αββα (β-lactamase fold) and a proposed core structure of CmlA

Interestingly, CmlA and its family have sequences that are distinct from those of the BMMs. They infact belong to a superfamily of metalloenzymes bearing the αββα fold (β-lactamase). β-lactamase enzymes are often known to carry out hydrolysis chemistry, but iron-dependent β-lactamase enzymes, FprA and ROO, function as NO and O_2 reductase. CmlA is the first example of a β-lactamase fold enzyme shown to catalyze C-H bond hydroxylation. While the X-ray crystal structure of an enzyme from CmlA and its family has not been reported, XAS and other spectroscopic analysis of CmlA suggested that it contain a (μ-oxo)(μ-1,3-carboxylato)diiron cluster with 3 or 4 His ligands, a

structure similar to that found in AurF or FprA and ROO (Chapter 6). The CmlA structure indicates that the conserved active-site structure motif of BMMs may only valid for that family, and different active site structure could also catalyze oxygen atom transfer to hydrocarbon.

1.8. Summary

New reactivities have been found for enzymes with canonical 4-helix bundle and 2-His-4-carboxylate motifs, including fatty aldehyde decarbonylation to form alkanes with one less carbon atom (aldehyde decarbonylase) and aromatic ring epoxidation (PaaA and BoxB). AurF and CmlI with the 4-helix bundle protein fold and a 3-His-4-carboxylate ligand set oxidize arylamines to nitro compounds with a new type of peroxo intermediate. Surprisingly, a μ-η^1:η^2-peroxo geometry, instead of the more common μ-1,2-peroxo configuration, has been found for CmlIperoxo. Equally exciting are the discoveries of enzymes with different protein folds and ligand sets, even one with structural motif typical of hydrolases, that could catalyze oxygenase chemistry (*myo*-inositol oxygenase (MIOX), deoxyhypusine hydroxylase (DOHH), and CmlA). A substrate-oxidizing superoxo intermediate has been characterized for MIOX. A stable peroxo intermediate of DOHH has been isolated and thoroughly studied. The new structural motifs and reactive intermediates have brought significant insight into the oxygen activation mechanisms by diiron enzymes.

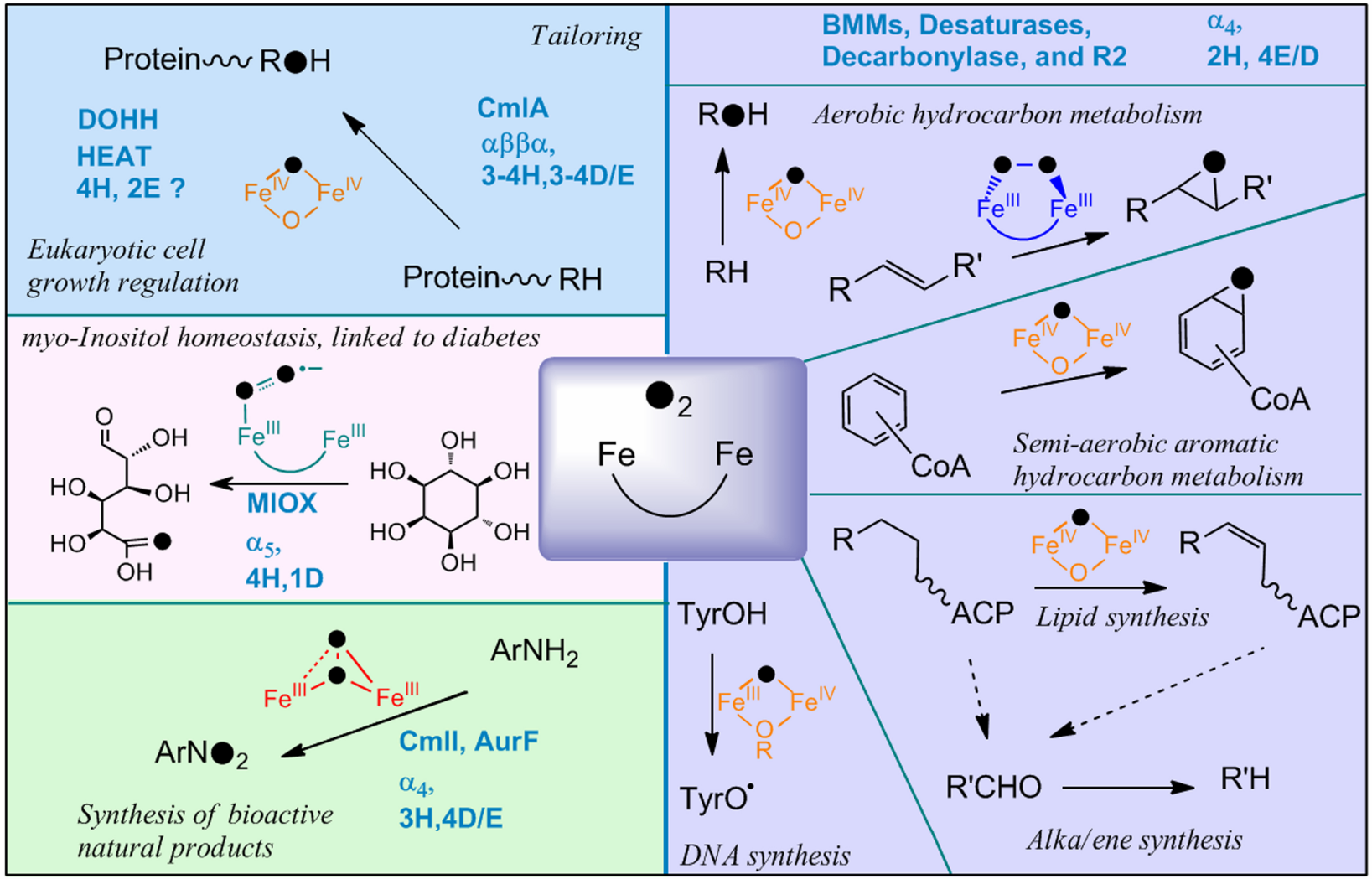

Figure 1.8. The diverse functions, structural motifs, reactivities, and mechanisms of diiron enzymes

1.9. Scope and aims of thesis

The ultimate goal of this thesis work is to elucidate how substrate-oxidizing and oxygen-activating diiron enzymes work at the molecular level. Thus, both structural and mechanistic aspects of diiron enzymes and their key intermediates will be targeted. As the canonical enzymes have been well studied, the mechanistic picture of oxygen activation by diiron enzymes remains incomplete; especially the structure of the peroxodiiron(III) intermediate and how this intermediate is activated to form substrate-oxidizing high-valent species are not well understood. Hence, novel enzymes with different structural motifs and new intermediates will provide important pieces of information to the oxygen activation picture. As the three-dimensional structures of the enzymes studied in this work, hDOHH, CmlA, and CmlI, are not available, spectroscopic methods play instrumental roles to gain insight into their active sites at different states along their reaction cycles. The spectroscopic interpretations for these enzymes are aided with parallel studies of relevant model complexes and related enzymes. In addition to structural and mechanistic aspects, the biochemistry of DOHH at a more physiologically relevant level are also investigated as it is of therapeutic and pharmaceutical interests.

Chapter 2

Human deoxyhypusine hydroxylase, an enzyme involved in regulating cell growth, is an oxygen-activating nonheme diiron enzyme

This work has been published in its entirety as:

Vu, V. V.; Emerson, J. P.; Martinho, M.; Kim, Y. S.; Munck, E.; Park, M. H.; Que, L., Jr., Human deoxyhypusine hydroxylase, an enzyme involved in regulating cell growth, activates O2 with a nonheme diiron center. *Proc. Nat. Acad. Sci. U. S. A.* **2009**, *106*, 14814-14819.

2.1. Introduction

Hypusine is an unusual, but highly conserved, amino acid that is found only in the eukaryotic translational initiation factor 5A (eIF5A), a protein that regulates cell proliferation.[56, 57] The biosynthesis of eIF5A involves a post-translational modification of the eIF5A precursor, where a lysine residue is first modified to deoxyhypusine (Dhp) by deoxyhypusine synthase (DHS) and then the nascent Dhp is hydroxylated by deoxyhypusine hydroxylase (DOHH) to form hypusine (Hpu) (Scheme 2.1).[56, 57] The importance of hypusine and these two enzymes has been shown by several studies where depletion of spermidine[142] or inhibition of either DHS or DOHH[143, 144] leads to a decrease of hypusine-containing eIF5A (eIF5A(Hpu)) and inhibition of eukaryotic cell growth. Consequently, these results suggest that eIF5A and DOHH could be promising targets for antitumor[145] and anti-HIV-1 therapies.[146]

Scheme 2.1. Biosynthesis of hypusine on eIF5A

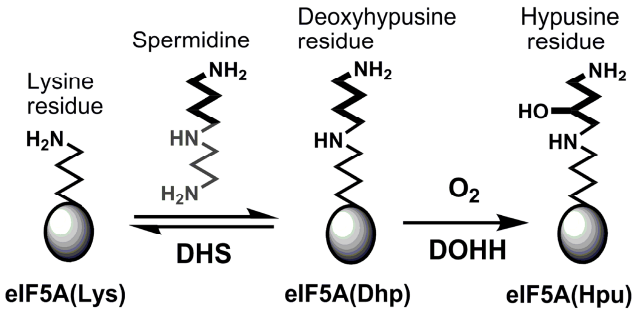

The hydroxylase activity of recombinant human DOHH (hDOHH) has been shown to depend on Fe(II), and not on any other physiologically relevant divalent metal ion. An estimated iron-to-holoprotein stoichiometry of 2 is observed.[136] Sequence

examination, homology modeling and mutagenesis experiments suggest two possible iron binding sites consisting of histidine and carboxylate ligands.[58, 136] Thus at first glance, hDOHH appears to resemble members of the superfamily of bacterial diiron multicomponent monooxygenases, like methane or toluene monooxygenase, that utilize nonheme diiron centers to activate dioxygen for the hydroxylation of hydrocarbons.[2, 4, 5] However there is little sequence similarity between the latter enzymes and DOHH.

hDOHH can be overexpressed in *E. coli*, and the enzyme isolated from such cells is blue in color. This chromophore gives rise to two absorption features at 320 nm and 630 nm with molar extinction coefficients indicative of ligand-to-metal charge transfer transitions.[136] These features resemble those associated with diiron(III)-peroxo intermediates of the hydroxylase component of methane monooxygenase (MMOH),[2] stearoyl-acyl carrier protein Δ^9 desaturase (Δ^9D),[76, 78] the R2 proteins of class I ribonucleotide reductases (R2),[74, 77, 79, 84, 87] and the ferroxidase site of frog M ferritin.[71, 73] Some of these intermediates have been characterized by resonance Raman spectroscopy and found to exhibit vibrational features typical of a (μ-1,2-peroxo)diiron(III) unit.[77, 78, 81]

Here we report direct spectroscopic evidence for a diiron cluster in hDOHH. Interestingly, as-isolated hDOHH is blue in color, and the blue chromophore derives from a peroxo-bridged diiron(III) center that is generated by reaction of the reduced enzyme with oxygen. Comparisons with related diiron(III)-peroxo enzyme intermediates and synthetic complexes shed light on the nature of this active site and augment our understanding of the mechanism of oxygen activation by diiron enzymes.

2.2. Experimental

2.2.1. Protein expression and purification

hDOHH plasmid was generously provided by Dr. Myung Hee Park at National Intitutes of Health (NIH). Dr. Park and her coworker, Dr. Yeon Sook Kim provided hDOHH for initial studies. Protein expression and purification was carried out as described previously by Park *et al*.[58, 136] To prepare ^{57}Fe-hDOHH, ~10 mg of ^{57}Fe (Cambridge Isotope Laboratories INC) metal was dissolved in ~ 3 mL concentrated HCl and added to the culture (5 L) at induction. Typical enzyme sample purified by one-step GSH affinity chromatography is a mixture of ~ 30 – 50 % holoenzyme and 50-70% apoenzyme, designated as as-isolated sample. Unless otherwise noted, the final enzyme solutions were in thrombin cleavage buffer (20 mM Tris-HCl, 150 mM NaCl, 2.5 mM $CaCl_2$, pH 8.4).

2.2.2. Reduction and Re-oxidation of hDOHH

Sodium dithionite (Sigma-Aldrich) was dissolved in anaerobic buffer, and the concentration was determined using ε_{316} = 8000 $M^{-1}cm^{-1}$.[147] Protein solutions were made anaerobic in conical vials or in cuvettes sealed with septa by equilibrating under argon atmosphere for 2 hours in an ice bath. For tandem reduction-oxidation study, approximate 2.2 equiv. (with respect to diiron cluster) of dithionite was added to the protein solution in a sealed cuvette and the cuvette was opened to introduce oxygen after A_{630} reached a minimum value. For resonance Raman studies, 10 equiv. of dithionite was used, and after complete reduction (judged by UV/Vis spectroscopy) protein samples were equilibrated with anaerobic buffer using 10K cut-off spin-filters (Pall Corp.) in an anaerobic glove

box until no dithionite was detected in the flow through solution prior to exposure to dioxygen sources.

2.2.3. Activity assay

~800 μL solution of ~50 μM hDOHHperoxo and ~50 μM deoxyhypusine-containing eIF5A in Tris.HCl buffer pH 7.5 was incubated at room temperature for 24 hours. At each incubation time a UV/Vis spectrum was collected and 100 μL reaction solution was mixed with 100 μL 20% trichloroacetic acid solution. Self-decay of hDOHHperoxo was monitored under the same conditions but without protein substrate. Hypusine and deoxyhypusine quantification was then carried out by Dr. Myung Hee Park as described else where.[137]

2.2.4. Spectroscopic Studies

Electron paramagnetic resonance spectroscopy (EPR) spectra were recorded in both perpendicular and parallel modes at X-band and Bruker E500 spectrometer equipped with an Oxford ESR-910 cryostat. Mössbauer analysis was carried out by Dr. Marlene Martinho and Prof. Eckard Münck at Carnegie Mellon University. Mössbauer spectra were collected with constant acceleration spectrometers, using two cryostats that allowed studies at 4.2 K in applied fields up to 8.0 T. Isomer shifts are reported with respect to iron metal at 298 K. The WMOSS software package (WEB Research, Edina, MN) was used to analyze the data. Resonance Raman experiments were performed on an Acton AM-506 spectrophotometer (1,200-groove grating) with a Princeton Instruments LN_CCD-1100-PB_UVAR detector cooled to -120^{o}C with liquid nitrogen. The 647.1 nm excitation line at 100-mW power was provided by a Spectra-Physics BeamLok 2060-KR-

RS krypton ion laser, which is filtered out by a Kaiser Optical holographic super notch filter. Samples were contained in flat-bottomed NMR quartz tubes and maintained at a temperature range of -10°C to 10°C, and spectra were collected in 90° scattering geometry at resolution of 4 cm^{-1}, and referenced to indene. Typically, 256 accumulations of 30 second exposures were collected for each sample. UV/Vis spectra of sample show no change after laser exposure. GRAMS/AI (Thermo Galactic, Salem, NH) was utilized for baseline correction and curve fitting.

Analysis of the exchange coupling in as-isolated hDOHH. Analysis of the exchange coupling of diferric complexes has been described by Kauffmann and Münck[148] and by Krebs and coworkers.[93] The variable temperature spectra were analyzed with a spin Hamiltonian appropriate for an exchange coupled dinuclear complex comprising two high-spin ($S_1 = S_2 = 5/2$) Fe^{III} ions,

$$\hat{H} = \mathrm{J}\hat{\mathbf{S}}_1 \cdot \hat{\mathbf{S}}_2 + \sum_{i=1,2} \left\{ 2\beta \hat{\mathbf{S}}_i \cdot \hat{\mathbf{B}} + A_o \hat{\mathbf{S}}_i \cdot \hat{\mathbf{I}}_i - g_n \beta_n \hat{\mathbf{B}} \cdot \hat{\mathbf{I}}_i \right\} \qquad (1)$$

where i = 1,2 sums over the two iron sites. The zero-field splittings of the high-spin ferric sites with octahedral N/O coordination of the type encountered in non-heme proteins are generally small, $|D_i| < 2$ cm^{-1}, and can be neglected. Under conditions where the electronic spin fluctuates fast among the thermally populated spin levels (in the present case, essentially the S= 0 ground state and the S = 1 excited state of the spin-coupled system) the ^{57}Fe nuclei experience an internal field B_{int}, which opposes the applied field B.

$$B_{int} = -\langle S_i \rangle_{th} A_o / g_n \beta_n \qquad (2)$$

In eq 2, $\langle S \rangle_{th}$ is the thermally averaged electronic spin

$$\langle S \rangle_{th} = v/ \Sigma_n \exp(-E_n/kT) \qquad (3)$$

where $E_n = E(S, M) = JS(S+1)/2 + 2\beta BM$ labels the energy levels of the coupled system. For the Fe^{III} sites under consideration, $A_o/g_n\beta_n \approx -21$ T.

According to eq. 1 the system is magnetically isotropic, so the effect of J on the spectra is felt by a reduction of the splitting at higher temperature (as if the applied field had been reduced) relative to the splitting at 4.2 K. We have evaluated the data by using eq. 1 and the 2Spin option of WMOSS. We should mention that Mössbauer spectroscopy is very suitable for the determination of J in hDOHH, mainly because the technique "recognizes" impurities such as the 18% Fe^{III} contaminant which would difficult to deal with in magnetic susceptibility studies.

X-ray absorption spectroscopy (XAS). XAS data were collected in fluorescence mode on beamline 9-3 at Stanford Synchrotron Radiation Lightsource (SSRL) of the SLAC National Accelerator Laboratory and on beamline X3B at the National Synchrotron Light Source of Brookhaven National Laboratory. At SSRL, the synchrotron ring SPEAR was operated at 3.0 GeV and 80-100 mA. Energy resolution of the focused incoming X-rays was achieved using a Si(220) double crystal monochromator. At NSLS, the synchrotron ring was operated at 2.8 GeV and 100-300 mA and a Si(111) double crystal monochromator. Fluorescence data were collected over the energy range of 6.8 - 8.0 keV using a 30-element Ge detector (SSRL) for as-isolated hDOHH and 13-element Ge detector (NSLS) for chemically reduced hDOHH. The sample temperature was

maintained at ~ 10 – 15 K (SSRL) or 20 – 25 K (NSLS). All protein samples contained 25% glycerol and were frozen using liquid isopentane at 113K. 130 μL of ^{56}Fe-hDOHH solution containing 4mM Fe was frozen in an EXAFS solution cell for data collection at SSRL, while 250 μL chemically reduced hDOHH sample (1mM in Fe) frozen in a tandem Mössbauer/XAS cup was used for XANES scans at NSLS. The beam spot size was 13 mm (horizontal) x 1 mm (vertical) for the SSRL samples and 4 mm (horizontal) x 1 mm (vertical) for the NSLS sample. All spectra were referenced again Fe foil, and energy was calibrated to 7112 eV.

At SSRL, the edge energy gradually decreased upon continuous scans at the same spot. Thus, first scans on five different spots of two samples were collected and assigned to as-isolated sample. At one spot, the sample was exposed to the X-ray beam at 8000 eV for 20 min, and then 16 scans were collected, for which no further edge energy shift was observed.

Standard procedures were used to reduce, average and process the raw data using EXAFSPAK,[149] which was also used for EXAFS analysis. Theoretical EXAFS amplitude and phase functions were calculated using FEFF 8.40.[150] The model for FEFF calculation that is shown in Fig. 2.1 unbiasedly leads to reasonably good fits with only single scattering paths. The parameters r and σ^2 were floated, while N was kept fixed for each fit and systematically varied between fits. The scale factor was fixed at 0.9 and threshold energy (E_0) was varied but maintained at a common value for all shells. The goodness of fit was reported as $F = \sqrt{\sum k^6(\chi_{exp} - \chi_{cal})^2 / \sum k^6 \chi_{exp}{}^2}$.[149] Pre-edge quantification was carried out with SSExafs using a standard procedure.[151]

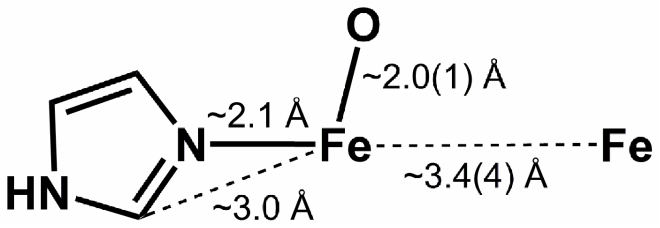

Figure 2.1. Models for FEFF calculation, generated by ChemBioDraw Ultra 11.0, which differs in the Fe-O and Fe···Fe distances. The Fe-O distance and Fe···Fe distance vary 0.1 Å steps from 1.9 to 2.1 Å and from 3.0 to 3.8 Å, respectively.

Estimation of the photoreduction yield (PY). PY, or the percentage of the photoreduced form present in a sample spot of an XAS sample, can be considered roughly proportional to the amount of time it is exposed to the beam. Fig. 2.2 shows the exposure time profile for the first and second scan on the same sample spot. XANES comparison provides a mean to estimated the PY at the edge jump of the second scan Linear combination fitting of the XANES spectrum of the second scan using those of the first and fully photoreduced scans as standards results in the percentage of the photoreduced form present in the sample spot at the edge jump of the second scan. From this value, PY at different exposure time, k-range, and energy can be calculated (Table 2.1). Fig. 2.4 shows that 100% photoreduction results in a significant change in the inner shell peak but no evident change in the outer shell peak. There is no clear effect of photoreduction on the first scan data at 10, 11, and 12 $Å^{-1}$.

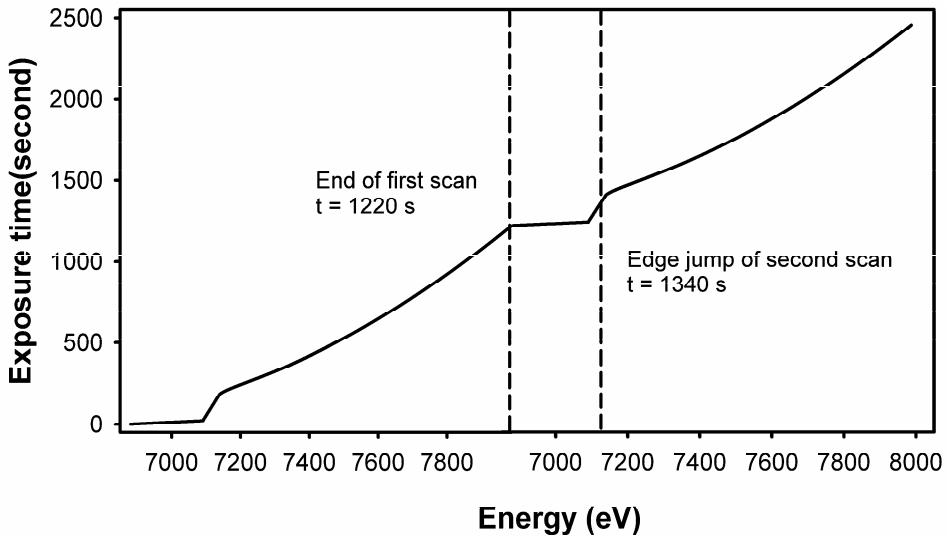

Figure 2.2. Energy-dependence of exposure time. Exposure time after 1st scan (15 $Å^{-1}$) is 1200 s, at 0 $Å^{-1}$ (edge) is 140 s. Total exposure time at the edge of 2nd scan is 1340 s.

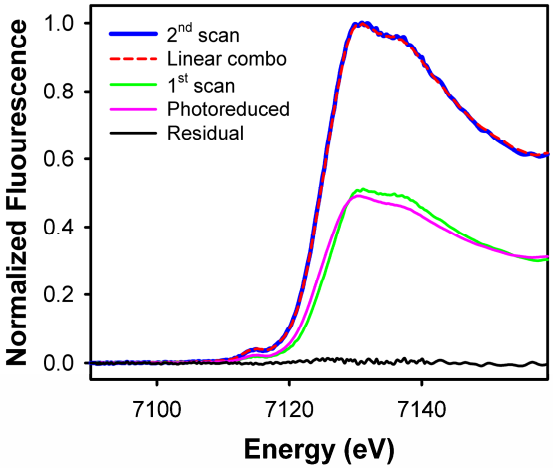

Figure 2.3. XANES linear combination fitting using Athena program.[152] A linear combination fit (linear combo) to a second scan was obtained using a 1st scan and fully photoreduced data as standards. E_0 values, determined as the first inflection points of the edges using derivative plots, are ~ 7126.3, 7125.5, and 7124.5 eV for 1st scan, 2nd scan and photoreduced data, respectively. Fit range = E_0-20 – E_0+30 eV. The weight of photoreduced data in the linear combination is ~ 49 %, which is assigned as photoreduction yield at 1340 seconds exposure.

Table 2.1. Photoreduction yields (PY) at different *k* values of first scan data, assuming photoreduction rate is proportional to exposure time (t).[153] PY = 49×t/1340 (%).

k_{max} (Å^{-1})	Energy (eV)	Exposure time (s)	PY (%)
13.0	7768	880	32
12.5	7720	815	30
12.0	7673	750	27
11.5	7627	690	25
11.0	7586	630	23
10.5	7545	578	21
10.0	7506	535	20
9.5	7469	493	18
9.0	7433	455	17

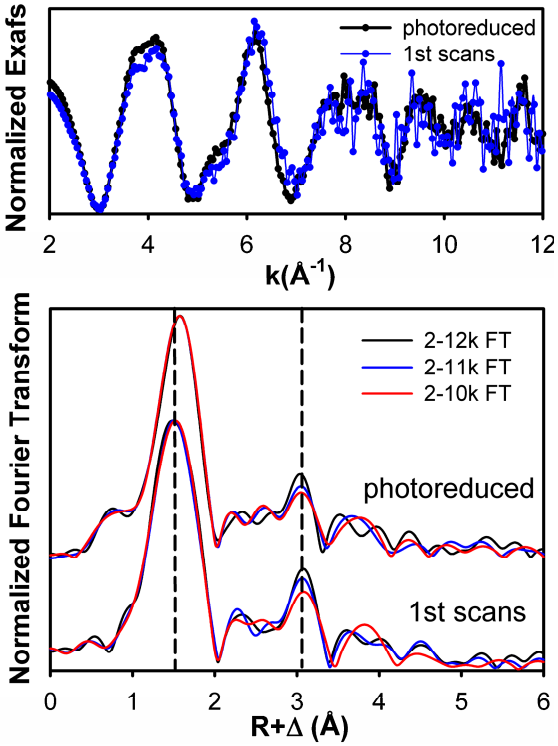

Figure 2.4. EXAFS data ($k^3\chi(k)$) photoreduced sample ($hDOHH_{phr}$) and the average data of first scans on 5 different fresh sample spots are shown in the top panel, while Fourier transforms at different k ranges are presented in the bottom panel. The k range of first scans data reflects the exposure time, which in turn reflects the photoreduction yield (see Table 2.1). Upon photoreduction, the inner shell *r'* ~ 1.5 – 1.6 Å clearly shifts to a longer distance, but there is no apparent change in the position of the *r'* = 3 Å peak. The first scans data in the k range = 2 – 12 Å^{-1} is then assigned to hDOHHperoxo.

2.3. Results

2.3.1. Evidence for an O_2-activating diiron cluster in hDOHH

As-isolated hDOHH is blue in color, with characteristic UV-Vis absorption features at 320 nm and 630 nm (Fig. 2.5). The features are apparently due to enzyme-bound iron, as they are absent in the iron-free apoenzyme.[136] Upon addition of dithionite, these absorption features decrease slowly over approximately 3 hours, but rapidly reappear upon exposure of the colorless solution to air, regaining *ca.* 80% of their initial intensities (Fig. 2.5 inset). The blue chromophore of hDOHH thus appears to undergo reduction by dithionite and regeneration by exposure to O_2. Reduced hDOHH therefore resembles many oxygen activating nonheme diiron enzymes like RNR R2, MMO, and Δ^9D^2 in its ability to react readily with O_2.

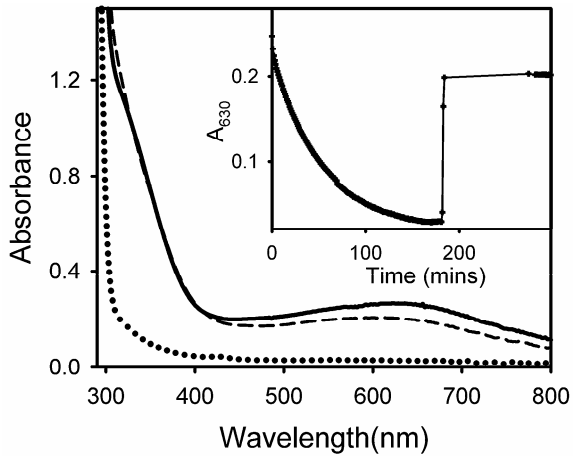

Figure 2.5. The UV-Visible spectra of hDOHH at room temparature. Conversion of as-isolated hDOHH (—) by 2.2 equiv. dithionite to reduced hDOHH (···) and its regeneration upon exposure to air after 180 minutes of anaerobic incubation (---). Inset: Change of A_{630} with time.

As-isolated hDOHH is EPR silent. Its 4.2 K zero-field Mössbauer spectrum, shown in Fig. 2.6A, consists of a broadened doublet (representing 82% of total Fe) that can be simulated as a superposition of two doublets with sharp absorption lines of width 0.27 mm/s (FWHM). The four lines can either be assigned to a nested pair, with $\Delta E_Q(1)$ = 1.16(2) mm/s, $\delta(1)$ = 0.55(1) mm/s and $\Delta E_Q(2)$ = 0.88(2) mm/s, $\delta(2)$ = 0.58(1) mm/s, or to a non-nested pair with $\Delta E_Q(1)$ = 1.05(2) mm/s, $\delta(1)$ = 0.49(1) mm/s and $\Delta E_Q(2)$ = 0.99(2) mm/s, $\delta(2)$ = 0.63(1) mm/s. Spectra recorded at 4.2, 20, 50 and 80 K in an 8.0 T applied field show that these doublets belong to an antiferromagnetically coupled pair of high-spin Fe(III) ions , with 50 cm^{-1} < J < 70 cm^{-1} (with the convention $\mathcal{H} = J \cdot S_1 \cdot S_2$, $S_1 = S_2 = 5/2$). The solid lines in Fig. 2.6 are spectral simulations obtained with WMOSS option 2Spin. The 8.0 T spectra can be simulated equally well for the nested or the non-nested pair. The sample also contained a high-spin Fe^{3+} contaminant representing ~18% of the Fe in the sample; a spectrum of this contaminant and comments on the fits of Figs. 2.6C and D are presented in the Mössbauer spectroscopy section in Supporting Information.

Protein and Fe concentrations of the sample of Figure 2.6A were 0.85 mM and 0.56 mM, respectively. Given that ~18% of the Fe belongs to the Fe(III) contaminant, these concentrations suggest that only 27% of the active sites are occupied by a diiron(III) cluster. Assuming that all absorption at 630 nm can be attributed to the diiron(III) cluster then yields for this sample ε(630 nm) = 2800 $M^{-1}cm^{-1}$.

Upon treatment with dithionite, the diiron(III) cluster is reduced into the diiron(II) state, $hDOHH_{red}$. This state exhibits two doublets characteristic of high-spin Fe(II), with

$\Delta E_Q(1) = 3.26$ mm/s, $\delta(1) = 1.29$ mm/s and $\Delta E_Q(2) = 2.90$ mm/s, $\delta(2) = 1.29$ mm/s (Fig. 2.6B). The sample also contained ~ 5 % of the original diiron(III) cluster and a high-spin Fe(II) species with $\Delta E_Q = 2.4$ mm/s (~ 20 %). The percentage of the latter suggests that it represents the reduced form of the Fe(III) contaminant present in the as-isolated sample. We have subtracted the remaining diiron(III) and the Fe(II) contaminant from the raw data to obtain the spectrum of Fig. 2.6B.

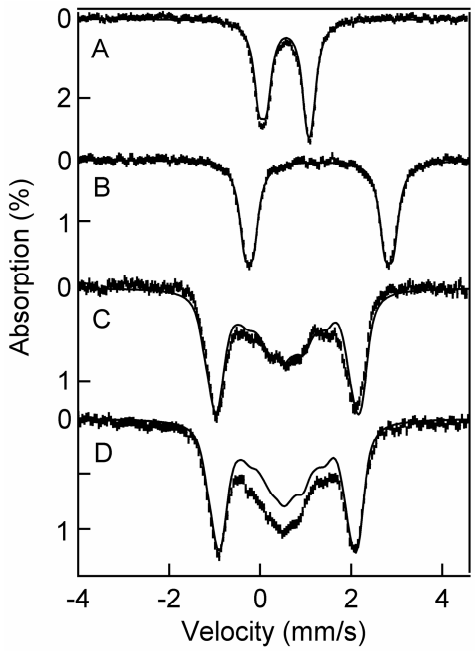

Figure 2.6. Mössbauer studies of hDOHH. 4.2 K zero field Mössbauer spectra of as-isolated hDOHH (A) and reduced with dithionite (B). The solid line in (A) is a simulation assuming two nested doublets as described in the text. (B) The solid line is a simulation of $hDOHH_{red}$ assuming two equally intense doublets representing ~ 75% of Fe. Details of data reduction and analyses are given in Supporting Information. 8.0 T Mössbauer spectra of as-isolated hDOHH recorded at 4.2 K (C) and 50 K (D). The solid lines are spectral simulations for an antiferromagnetically coupled diiron(III) center containing two high-spin ($S = 5/2$) Fe(III) sites. For the simulation of the 50 K spectrum we used $J = 70$ cm^{-1}. At 50 K the central features of the 8.0 T spectrum contain contributions from the mononuclear Fe(III) contaminant (see Mössbauer spectroscopy section in Supporting Information).

2.3.2. Evidence for a (μ-peroxo)diiron(III) unit in hDOHH

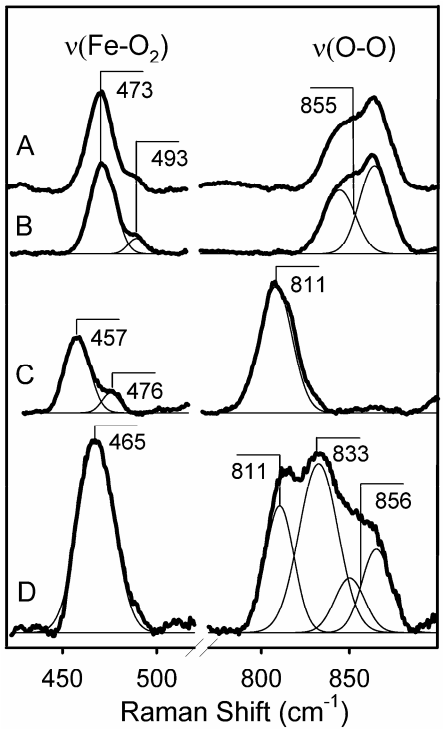

Figure 2.7. Resonance Raman spectra of hDOHH samples. A: as-isolated hDOHH. B-D: reduced hDOHH exposed to $^{16}O_2$, $^{18}O_2$, and mixed-labeled O_2 ($^{16}O_2$, $^{18}O_2$ and $^{16}O^{18}O$). Background features due to the protein itself have been subtracted using the spectrum of fully-reduced hDOHH collected under the same conditions. Experimental data are presented with thick lines and fits are presented with thin lines.

Figure 2.7 shows resonance Raman spectra of different hDOHH samples obtained with 647.1 nm excitation. The spectra of as-isolated and $^{16}O_2$-reoxidized hDOHH ($hDOHH_{16}$) overlay perfectly, indicating that the reoxidized blue species is identical to the as-isolated form (Figs. 2.7A and B). Three features are observed in these spectra at 855 (observed as a Fermi doublet), 493 and 473 cm^{-1}. The combination of these features suggests an iron(III)-peroxo chromophore, with observed features corresponding to ν(O–O) and ν(Fe–O_2) modes.[77, 78, 81] In confirmation, $^{18}O_2$-labeled hDOHH ($hDOHH_{18}$),

obtained by exposing $hDOHH_{red}$ to $^{18}O_2$, exhibits features downshifted to 811, 476, and 457 cm^{-1} (Fig. 2.7C), with $\Delta\nu$ values of 44, 17, and 16 cm^{-1}, respectively, that are consistent with those expected for the mass change in the diatomic O–O and Fe–O oscillators (~50 cm^{-1} and ~20 cm^{-1}, respectively). From this point on, we designate the blue form of hDOHH as hDOHHperoxo.

Table 2.2. Properties of diiron(III)-peroxo units in enzymes and related model complexes

Species	λ (nm)	δ (mm/s)	ΔE_Q (mm/s)	J (cm^{-1})	ν(O-O) (cm^{-1})	r(Fe···Fe) (Å)	Ref.
hDOHHperoxo	**630**	**0.55,0.58** ***(0.49,0.63)****	**1.16,0.88** ***(1.05,0.99)****	**50-70**	**855**	**3.44**	**This work**
MMOH	725	0.66	1.51				154
D84E R2	700	0.63	1.58	50	868	2.50	77, 79, 84, 87, 93
Δ^9D	700	0.68,0.64	1.90,1.06		898		76, 78, 93
Frog M Ferritin	650	0.62	1.08	70	851	2.53	85, 93, 155
ToMOH	†	0.54	0.66				75
OxyHr	500	0.51,0.54	1.09,1.92	154	844		101, 102
1	694	0.66	1.40	66	885	4.01	106, 107
2	600	0.51	0.80	85	900	3.46	109, 130
3	644	0.50	1.31		908	3.40	131
4	700(br)	0.58,0.65	0.74,1.70			3.33	82

* Mössbauer data can be assigned either to a nested pair of doublets with parameters shown in plain text or to an overlapping pair of doublets with parameters shown in italics.
† No chromophore observed.
1 = $[Fe_2(HB(3,5\text{-}iPr_2pz)_3)_2(\mu\text{-}O_2)(\mu\text{-}O_2CCH_2C_6H_5)_2]$ (pz = pyrazole).
2 = $[Fe_2(N\text{-}Et\text{-}HPTB)(\mu\text{-}O_2)(OPPh_3)_2]^{3+}$ (N-Et-HPTB = anion of *N*,*N*,*N*′,*N*′-tetrakis(1′-ethylbenzimidazolyl-2′-methyl)-2-hydroxy-1,3-diaminopropane).
3 = $[Fe_2(6\text{-}Me_2\text{-}BPP)_2(\mu\text{-}O_2)\ (\mu\text{-}OH)]^+$ (6-Me_2-BPP = *N*,*N*-bis(6-methyl-2-pyridylmethyl)-3-aminopropionate).
4 = $[Fe_2(Ph\text{-}bimp)(\mu\text{-}O_2)(\mu\text{-}O_2CC_6H_5)]^{2+}$ (Ph-bimp = 2.6-bis[bis{2-(1-methyl-4,5-diphenylimidazolyl)methyl}-aminomethyl]-4-methylphenolate).

For the sample prepared by exposing reduced hDOHH to a mixture of 25% $^{16}O_2$, 50% $^{16}O^{18}O$ and 25% $^{18}O_2$ ($hDOHH_M$), a band appears at 833 cm^{-1}, halfway between the

ν(O–O) bands in the $hDOHH_{16}$ and $hDOHH_{18}$ spectra, and is assigned to the $^{16}O^{18}O$ isotopomer (Fig. 2.7D). The three components of the ν(O–O) band at 856, 833, and 811 cm^{-1} exhibit an intensity ratio consistent with the isotopomer ratio of the mixed-labeled O_2 used. Due to the relative large (~20-25 cm^{-1}) width of the individual features, the central component does not show evidence for the presence of distinct $^{16}O^{18}O$ and $^{18}O^{16}O$ isotopomers, as found for oxyhemerythrin[100] but resembles that observed for the mixed-labeled Δ^9D peroxo intermediate,[78] which has been assigned as having a symmetric 1,2-O–O bridge. The observations that hDOHHperoxo has a peroxo-to-iron(III) charge transfer band with λ_{max} of 630 nm and exhibits Raman spectra resembling those of other (μ-1,2-peroxo)diiron(III) centers in proteins and model complexes (Table 2.2) lead us to propose that the O–O moiety in hDOHHperoxo also bridges the two iron atoms in a μ-1,2 mode.

Figure 2.8A shows X-ray absorption near edge spectra (XANES) of hDOHH. For the as-isolated enzyme, the K-edge energy was observed to downshift by ~ 2 eV in the first scan with increasing exposure to the synchrotron beam, suggesting photoreduction of the sample. This downshift of the photoreduced sample ($hDOHH_{phr}$) can be compared to the further downshift of 2.0 eV observed in a sample of the dithionite-reduced enzyme. This progression suggests that roughly half of the Fe(III) sites in the frozen as-isolated sample in the layer exposed to X-ray beam were reduced to Fe(II), resulting in an edge energy that is the average of the diiron(III) and diiron(II) species. The same stepwise progression has been observed for MMOH as the diiron(III) form was reduced to the diiron(II) form one electron at a time.[156]

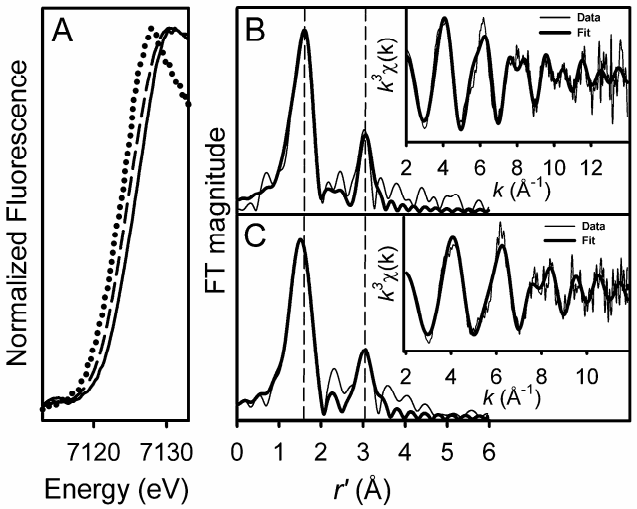

Figure 2.8. X-ray absorption spectroscopic analysis of hDOHH. A: XANES spectra of hDOHHperoxo first scans (—), $hDOHH_{phr}$ (---), and $hDOHH_{red}$ (···). B and C: Fe K-edge EXAFS data $k^3\chi(k)$ of $hDOHH_{phr}$ and hDOHHperoxo and their Fourier transforms (thin lines) in k range = 2 – 14 $Å^{-1}$ and 2 – 11.8 $Å^{-1}$, respectively. Best fits are represented by the thick lines. Details of the fitting protocols are provided in Table 2.3.

Information about the iron coordination number can be deduced from the intensity of the pre-edge feature that is attributed to 1s → 3d transitions.[157] The pre-edge areas of 12.0 units for hDOHHperoxo and 13.8 units for $hDOHH_{phr}$ are similar to those of the diiron(III) forms of Δ^9D (~ 11 – 11.5 units),[158] $metHrN_3$ (~10.4 units), and RNR $R2_{met}$ (10.1 units) but larger than those for the diiron(II,III) form of uteroferrin (4.8 units).[159] The larger pre-edge areas associated with hDOHH suggest that its iron centers deviate significantly from centrosymmetry with likely coordination numbers of 5.

Because of its superior signal-to-noise ratio we have focused on the analysis of the extended X-ray absorption fine structure (EXAFS) data of $hDOHH_{phr}$ with maximum usable data extending to 14 $Å^{-1}$ (Fig. 2.8B). The Fourier transform of the k^3-weighted EXAFS data exhibits prominent peaks at 1.6 and 3 Å. The r' = 1.6 Å feature of the

$hDOHH_{phr}$ data is best fit with 5 O/N scatterers at 2.08 Å, consistent with the pre-edge analysis. The average iron-ligand bond distance of 2.08 Å is close to those associated with the principal shell of scatterers in the iron(II)iron(III) forms of MMOH (2.06 – 2.09) (2 histidine/4 carboxylate ligand set)[156] but shorter than the 2.13 Å average distance found in $semimetHrN_3$ (5 histidine/2 carboxylate ligand set),[150] suggesting a ligand set with more carboxylate ligands than histidines. The *r'* = 3 Å feature corresponds to an Fe scatterer at 3.44 Å, the addition of which significantly improves the fit quality (compare Fits in bold text in Table 2.3). This 3.44-Å distance is close to the Fe···Fe distances found in the iron(II)iron(III) sites of photoreduced MMOH,[156] uteroferrin,[159] and $semimetHrN_3$.[96] EXAFS analysis thus further corroborates the diiron nature of the active site of $hDOHH_{phr}$.

We have collected first scans on five different fresh spots of an as-isolated hDOHH sample, during which photoreduction yield is estimated to be at most ~ 25% at k = 12 $Å^{-1}$ based on the edge position of the second scans. The summation of these first scans enables us to carry out a preliminary structural analysis of hDOHHperoxo. The best fit to the k^3-weighted EXAFS data of hDOHHperoxo (Table 2.3) also gives an Fe···Fe distance of 3.44 Å, suggesting that the iron atoms do not move from their original positions upon photoreduction at ~ 20 K. Interestingly, the average Fe-O/N distance in the first shell is 2.05 Å, which is 0.03 Å shorter than that for $DOHH_{phr}$, consistent with the change in the diiron oxidation state. The lengthening of the average first-shell distance upon photoreduction without changing the Fe···Fe distance has also been observed in a similar study of MMOH.[146]

Table 2.3. Parameters for fits to unfiltered k^3-weighted EXAFS data of photoreduced $hDOHH_{phr}$ and hDOHHperoxo.

	Fe-O/N			Fe-N/O			Fe-Fe			Fe-C			
Fit#	**N***	**R†**	**σ^{2}‡**	**N**	**R**	**σ^2**	**N**	**R**	**σ^2**	**N**	**R**	**σ^2**	***F*(%)§**
$hDOHH_{phr}$													
O3	3	2.06	8.0										53.53
O4	**4**	**2.06**	**10.8**										**49.87**
O5	5	2.05	13.8										50.85
O6	6	2.05	17.1										53.81
N3				3	2.08	6.5							55.15
N4				4	2.08	8.7							50.36
N5				**5**	**2.08**	**10.9**							**49.16**
N6				6	2.08	13.3							50.56
O3N1	3	2.03	7.8	1	2.18	3.5							49.48
O2N2	2	2.01	5.3	2	2.16	4.8							49.30
O1N3	1	1.98	3.0	3	2.13	4.9							49.23
O4N1	4	2.06	10.8	1	2.34	30.3							49.70
O3N2	3	2.05	9.5	2	2.13	22.6							49.85
O2N3	2	2.03	9.5	3	2.11	13.6							49.50
O1N4	1	1.99	6.6	4	2.12	10.5							49.13
O4-F1	**4**	**2.05**	**10.8**				**1**	**3.44**	**4.6**				**43.82**
N5-F1				***5***	***2.08***	***11.0***	***1***	***3.44***	***4.6***				***42.96***
O4-C4	4	2.05	10.9							4	3.46	2.5	49.37
N5-C4				5	2.08	10.9				4	3.46	2.3	47.80
hDOHHperoxo													
O3	3	2.02	7.13										56.74
O4	4	2.03	9.59										51.60
O5	**5**	**2.02**	**11.93**										**49.42**
O6	**6**	**2.02**	**14.31**										**49.55**
N3				3	2.05	5.8							60.27
N4				4	2.05	7.8							53.97
N5				5	2.05	9.7							50.11
N6				**6**	**2.05**	**11.6**							**48.43**
O4N1	4	2.00	8.2	1	2.17	0.9							48.33
O3N2	3	1.98	5.6	2	2.15	2.8							48.11
O2N3	2	1.96	3.4	3	2.13	4.0							47.96
O1N4	1	1.93	0.5	4	2.07	5.7							48.00
O5N1	5	2.00	11.4	1	2.17	3.7							48.94
O4N2	4	1.98	9.3	2	2.15	5.3							48.51
O3N3	3	1.97	7.1	3	2.13	6.1							48.06
O2N4	2	1.95	5.1	4	2.11	7.1							47.67
O1N5	1	1.93	2.6	5	2.07	8.4							47.42
O5-F1	**5**	**2.02**	**12.1**				**1**	**3.44**	**3.6**				**41.47**
N6-F1				***6***	***2.05***	***11.7***	***1***	***3.44***	***3.5***				***40.39***
O5-C4	5	2.02	12.0							4	3.47	0.9	46.04
N6-C4				6	2.05	11.7				4	3.47	0.9	44.26

k range = 2-14 $Å^{-1}$ for $hDOHH_{phr}$ and 2-11.8 $Å^{-1}$ for hDOHHperoxo. Resolution ~0.13 Å for $hDOHH_{phr}$ and 0.17 Å for hDOHHperoxo. * Coordination number. † Distance in Å. ‡ σ^2 in units of 10^{-3} $Å^2$. §

$$F = \sqrt{\sum k^6(\chi_{exp} - \chi_{cal})^2 / \sum k^6 \chi_{exp}{}^2}$$

2.3.3. Long-lived hDOHHperoxo can hydroxylate the deoxyhypusine residue in eIF5A

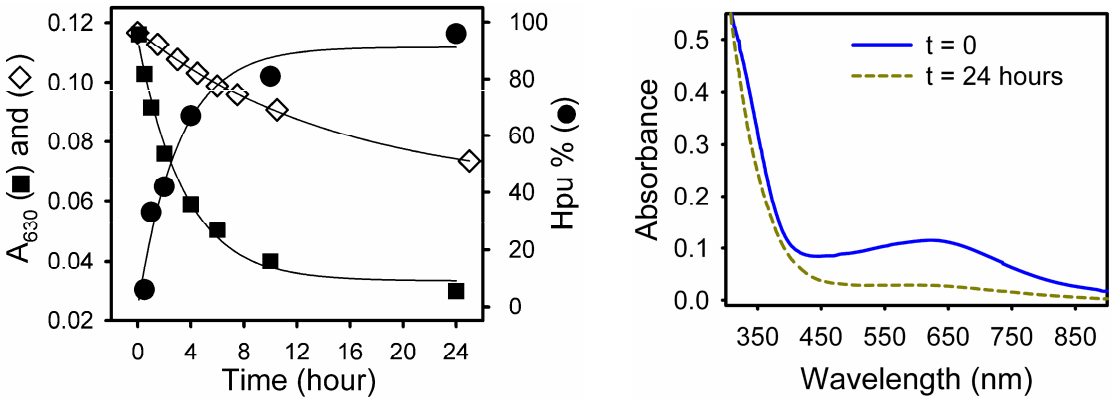

Figure 2.9. Reaction of hDOHHperoxo with ~ 1 equiv. of substrate, deoxyhypusine-containing eIF5A. Left: The decay of hDOHHperoxo was monitored by following the change in A_{630} at different incubation times in the absence of eIF5A(Dhp) (◇) and in the presence of eIF5A(Dhp) (■).Yields of hypusine (●) are calculated based on the observed amounts of hypusine (Hpu) and deoxyhypusine (Dhp); % Hpu = (Hpu×100)/(Hpu+Dhp). Right: UV/Vis spectra of hDOHHperoxo (blue) incubated with substrate for 24 hours at room temperature (yellow). After 24 hour incubation, the reaction mixture was cloudy and the precipitate was removed using centrifugation before the yellow spectrum was recorded.

Fig. 2.9 shows the fate of hDOHHperoxo upon treatment of one equiv. of its protein substrate, deoxyhypusine-containing eIF5A (eIF5A(Dhp)). At room temperature, the absorption at 630 nm of hDOHHperoxo, shown above to result from peroxo-to-iron charge transfer transition, slowly decreases with time. Upon addition of eIF5A(Dhp), the decay rate of A_{630} increases and is comparable to the rate of hypusine formation. After 24 hours incubation, deoxyhypusine is almost completely converted to hypusine (~ 96 %) and hDOHHperoxo turns yellow (Fig. 2.9). This result indicates that long-lived hDOHHperoxo is activated by substrate binding and carries out the hydroxylation of deoxyhypusine in eIF5A.

2.4. Discussion

Our spectroscopic studies have shown that recombinant human DOHH has a nonheme diiron active site, the reduced form of which can react readily with oxygen. This finding extends the family of oxygen activating nonheme diiron enzymes[2-5] to include for the first time a hydroxylase that is not of bacterial origin and of vital importance for human metabolism. These nonheme diiron enzymes are capable of carrying out a variety of dioxygen-dependent chemical transformations under mild physiological conditions, including methane hydroxylation by MMO, desaturation of fatty acids by Δ^9D and related desaturases, and the generation of a catalytically essential tyrosyl radical by R2 in DNA biosynthesis.[2]

Despite their functional diversity, the diiron enzymes characterized thus far share a common structural motif. They all have a pair of conserved (D/E)$X_{29-37}EX_2H$ ligand sequence motifs that provide the ligands to a common diiron active site formed within a four-α-helix bundle.[3] hDOHH appears not to follow this pattern. Instead, hDOHH has a pair of conserved $HEX_{31}HE$ sequences that are symmetrically located near the C- and N-termini, which possibly provide the metal binding ligands.[58] On the basis of homology modeling and circular dichroism experiments, the overall structure of hDOHH has been proposed to contain a dyad of four consecutive α-hairpins (called a HEAT repeat motif) surrounding the active site.[58] Mutagenesis experiments show that both iron binding and activity are lost upon single mutations of the H_n, H_{n+33} and E_{n+34} residues of each $HEX_{31}HE$ sequence to A, but mutation of the E_{n+1} residues to A results in loss of activity but with no loss in iron content.[136] These results suggest a 4-His-2-carboxylate ligand set for hDOHH, which is different from the 2-His-4-carboxylate ligand set found in many

oxygen-activating diiron enzymes.[3] However, EXAFS analysis of hDOHH shows that the average Fe-O/N bond length from the principal shell of ligands to the iron is in fact comparable to those found for diiron enzymes with 2-His-4-carboxylate ligand sets, but shorter than that of the histidine-rich diiron site in hemerythrin (Table 2.4). Additional experiments are needed to determine which ligands are bound to the diiron site of hDOHH.

Table 2.4. Representative best fits to k^3-weighted EXAFS data of hDOHH and related diiron enzymes

		Fe-O/N			Fe-Fe			
Species	**Protein Ligands**	**N***	**R†**	**σ^{2}‡**	**N**	**R**	**σ^2**	**Ref.**
$hDOHH_{phr}$		5	2.08	11.0	1	3.44	4.6	This
hDOHHperoxo		6	2.05	11.7	1	3.44	3.5	work
Fe(II)Fe(III)								
MMOH§	2H-4(E/D)		2.07		1	3.42		156
Uteroferrin	3H-3(E/D)-1Y		2.08		1	3.52		159
SemimetHr¶	5H-2(E/D)		2.13		1	3.46		96
Peroxo								
R2¶	2H-4(E/D)		2.06		0.7	2.50		84
Ferritin	1H-4(E/D)		2.00		0.6	2.53		85
OxyHr¶	5H-2(E/D)		2.17		1	3.24		95

* Coordination number.
† Distance in Å.
‡ σ^2 in units of 10^{-3} Å^2.
§ Average values for several samples.
¶Average Fe-O/N distance not including Fe-μ-O bond.

In contrast, the accumulated spectroscopic information on hDOHH does shed some light on the nature of its non-protein-derived ligands. Clearly established is a dioxygen-derived ligand that is identified by resonance Raman experiments to be a peroxide (Fig. 2.8); this result shows that dioxygen binding to $hDOHH_{red}$ results in the 2e-reduction of O_2. Concomitant oxidation of the diiron(II) center to the diiron(III)

oxidation state is demonstrated by Mössbauer spectroscopy. The peroxide ligand most likely binds to the diiron(III) center in a 1,2-bridging mode and acts as the principal conduit for the antiferromagnetic interaction (J = 50 – 70 cm^{-1}) deduced from the analysis of Mössbauer spectra recorded in strong applied magnetic fields. This J value is too small for an oxo bridge (150 < J < 300 cm^{-1}) but too large for a hydroxo bridge (10 < J < 35 cm^{-1}) (Table II of ref. 160). It is in fact comparable to J values found for the (μ-1,2-peroxo)diiron(III) intermediates of RNR W48F/D84E R2 and frog M ferritin[93] and related model (μ-1,2-peroxo)diiron(III) complexes (Table 2.4).

The Fourier-transformed EXAFS data for hDOHHperoxo and $hDOHH_{phr}$ (Fig. 2.8) show a strong feature at r' ~ 3 Å that corresponds to an Fe scatterer at ~ 3.44 Å. The intensity of this peak and the small Debye-Waller factor associated with the Fe scatterer implicate a relatively rigid diiron core structure, which could probably not derive from the presence of the peroxide bridge alone and requires an additional single atom bridge. A perusal of the few synthetic (*cis*-μ-1,2-peroxo)diiron(III) complexes that have been characterized by X-ray crystallography shows that an Fe-Fe distance of 3.4 ± 0.1 Å is associated with those peroxo complexes with an additional hydroxo or alkoxo bridge[82, 130, 131] (but not an oxo bridge, because it gives rise to shorter Fe-Fe distances of 3.1 ± 0.1 Å[86, 161]). Based on these results, we propose the dibridged diiron(III) core structure of hDOHHperoxo shown in Fig. 2.10.

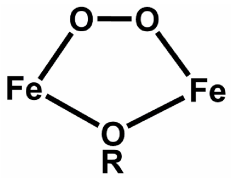

Figure 2.10. Proposed core structure of hDOHHperoxo

The 3.44-Å Fe···Fe distance found in hDOHHperoxo stands in distinct contrast to the much shorter 2.5-Å Fe-Fe distances determined by EXAFS for the peroxo intermediates of W48A/D84E R2[123] and the ferroxidase site of frog M ferritin.[85] Such very short metal-metal separations are found only for synthetic complexes that have 2 or 3 single-atom bridges.[86, 161] Despite this apparent difference, these three diiron(III)-peroxo intermediates exhibit ν(O-O) Raman features of comparable frequency, at 855, 868 (observed for the peroxo intermediate of W48F/D84E R2 and assumed to resemble that of W48A/D84E R2 in structure), and 851 cm^{-1}, respectively.[85, 87] The similarity of the ν(O-O) values suggests that the diiron-peroxo core structures may not be as different as suggested by the EXAFS results. This notion derives from a model developed by Brunold and Solomon to rationalize the vibrations of (μ-1,2-peroxo)diiron(III) complexes.[162] In this model, the observed ν(O-O) frequency is modulated by mechanical coupling of the O-O and the Fe-O stretching modes, the extent of which is governed by the Fe-O-O angle. As the Fe-O-O angle is related to the Fe···Fe distance, the ν(O-O) can reflect the Fe···Fe distance. This mechanical coupling model is supported by a recent study of a series of synthetic (*cis*-μ-1,2-peroxo)diiron(III) complexes.[109] Indeed, a detailed spectroscopic and DFT analysis of the W48F/D84E R2 peroxo intermediate also

questions the 2.5-Å Fe···Fe distance deduced by EXAFS and favors an Fe···Fe distance of 3.68 Å[87] that is closer to the 3.44 Å distance we have determined for hDOHHperoxo by EXAFS analysis. Based on the calculations, it is proposed that the R2 peroxo intermediate has a (*cis*-μ-1,2-peroxo)diiron(III) center supported by two bidentate carboxylate bridges. The absence of a single-atom bridge may rationalize why the predicted Fe scatterer is not observed at 3.7 Å in the EXAFS analysis. There thus appears to be a discrepancy between the Raman and EXAFS results for the peroxo intermediates of D84E R2 and frog M ferritin, which will need to be resolved. For hDOHHperoxo, however, the Raman and EXAFS results are in good agreement with respect to the Fe···Fe distance.

Lastly, it is interesting that it is the hDOHHperoxo form that is isolated directly from the expression strain. Its blue chromophore persists for at least several days at room temperature, so its stability surpasses even that of peroxo Δ^9D, the peroxo intermediate obtained from chemically reduced Δ^9D, which has a half-life of ~30 minutes at room temperature.[76] Thus the lifetimes of diiron-peroxo intermediates of these enzymes vary significantly and can range from milliseconds to days.[74, 76, 77, 79, 81, 84, 87, 154] Interestingly, the decay of hDOHHperoxo is accelerated by the addition of its substrate, the deoxyhypusine containing eIF5A. But more remarkable is the observation that the deoxyhypusine residue is in fact hydroxylated to hypusine (Fig. 2.9). This result implicates hDOHHperoxo as an intermediate on the catalytic pathway of hDOHH.

The extended stability of active hDOHHperoxo raises the questions of what makes it stable and how it is activated. From their studies of W48F/D84E R2, Skulan *et al*. conclude that a *cis*-μ-1,2-peroxo form is the most stable structure for the diiron(III)-

peroxo intermediate and must undergo a structural change prior to O-O bond cleavage to generate the high valent iron species required for substrate oxidation.[87] The additional single-atom bridge deduced to be present in the diiron(III)-peroxo unit in hDOHHperoxo (Fig. 2.10) is likely to further stabilize the *cis*-μ-1,2-peroxo structure, raising the barrier for O-O bond cleavage to form the high-valent iron oxidant. Indeed a number of metastable synthetic complexes are characterized to have core structures like that shown in Fig. 2.10; some in fact are stable enough to have been crystallized.[82, 109, 130, 131] As the target hydroxylation site of hDOHH resides on a protein substrate, it seems plausible that substrate binding triggers a conformation change that activates the (μ-1,2-peroxo)diiron(III) intermediate to carry out eIF5A(Dhp) hydroxylation (Scheme 2.1). The important role of such protein-protein interactions in modulating enzyme activity has been demonstrated for several diiron enzymes.[6, 39, 163] As the *in vitro* reaction of hDOHHperoxo with its protein substrate is very slow, additional protein factors yet to be identified may be required to further accelerate this reaction in the cell.

2.5. Supporting information

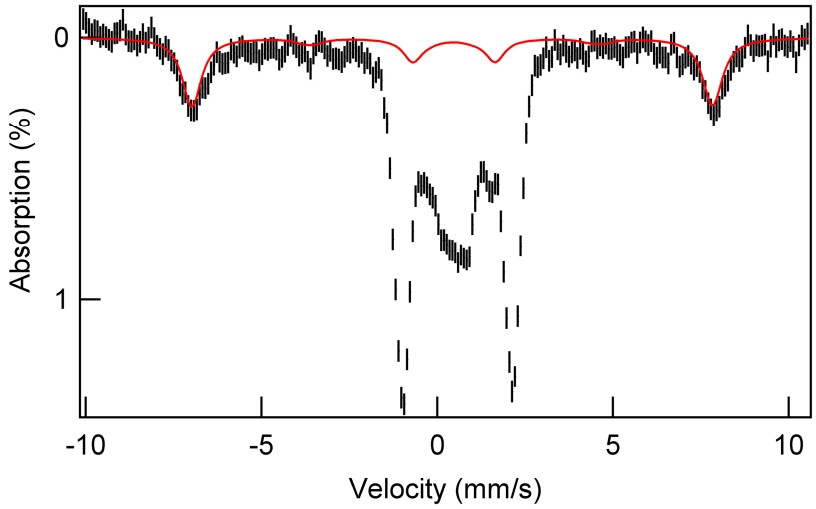

Figure S.2.1. 4.2 K spectrum of hDOHH as isolated recorded in an external field of 8.0 T applied parallel to the observed γ-radiation; same conditions as in Fig. 2.6C but wider velocity scan. The red line is a spectral simulation, using A_o = -21.7 T for the magnetic hyperfine constant, of the mononuclear high-spin ferric contaminant.

Fig. S.2.1 shows a 4.2 K spectrum of as-isolated hDOHH, recorded in a parallel field of 8.0 T. The spectrum shown contains the contribution of a mononuclear high-spin ferric contaminant. Matching the simulated spectrum (red line) to the data suggests that this contaminant represents about 18% of the iron in the sample. The two (weak) innermost lines of the contaminant superimpose with the features of the dinuclear center of hDOHH which dominates the central part of the spectrum. At 4.2 K, the presence of the contaminant interferes only minimally with the data analysis. At 50 K, however, the electronic spin system of the contaminant was found to be in the intermediate relaxation regime, yielding featureless absorption underneath the DOHH spectrum. Fortunately, the

positions of the main hDOHH bands at – 1 mm/s and + 2.1 mm/s are little affected by the presence of the contaminant; the position of these two bands convey the main information about the exchange coupling constant *J*. For the manipulation of the data yielding Fig. 2.6B, see caption of Fig. S.2.2.

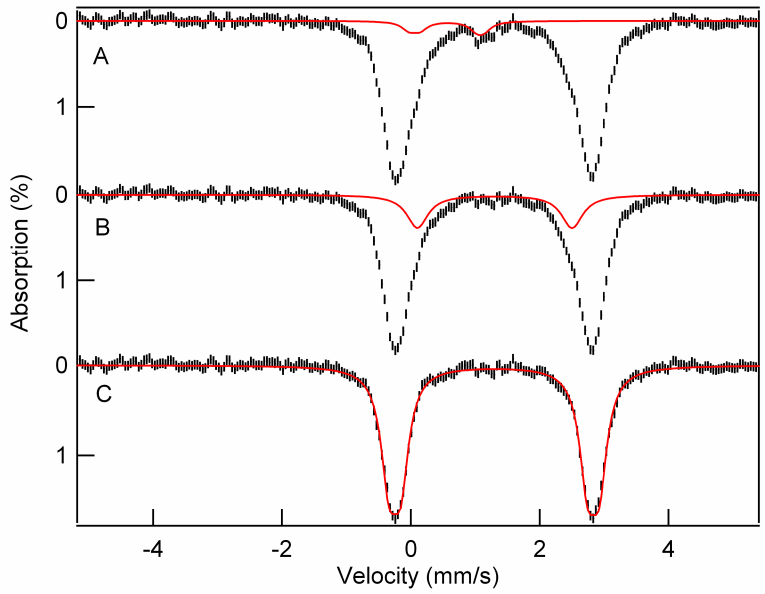

Figure S.2.2. (A) 4.2 K zero field spectrum of $DOHH_{red}$ (raw data). The red curve outlines the remnant (5% of Fe) oxidized hDOHH. Subtraction of the oxidized fraction from (A) yields the "data" in (B). The red line in (B) indicates a high-spin ferrous species; as this species accounts for ~20% of the Fe, it is reasonable to assume that it represents the ferrous form of the mononuclear ferric contaminant (18%) of Fig. S.2.1. Subtraction of this contaminant yields (C) which is the spectrum shown in Fig. 2.6B.

Chapter 3

The bridging structure of hDOHHperoxo

3.1. Introduction

The core structures of diiron(III) peroxo intermediates can play an important role in how these intermediates are activated. Spectroscopic and computational studies have proposed that the cis-μ-1,2 geometry is the most stable conformation of a diiron(III)-peroxo species.[87, 162] Isomerization to a more activated geometry is thus necessary for O-O bond cleavage. Indeed, the cis-μ-1,2 geometry is the sole conformation of diiron(III) peroxo intermediates characterized spectroscopically and/or crystallographically thus far.[82, 83, 106, 109, 129-131] In well studied model complexes, additional ligands are shown to support this geometry. In most cases, a single atom bridge ligand (μ-oxo, μ-hydroxo, or μ-alkoxo) is present (see complexes **1 – 7** in Fig. 3.1 for examples),[82, 83, 109, 129-131] but two complexes containing two μ-1,3-carboxylato ligands and no single atom bridge have also been reported (complexes **8** and **9**, Fig. 3.1).[106, 107]

We previously tentatively proposed that hDOHHperoxo contains at least a single atom bridging ligand in addition to the μ-1,2 peroxo ligand on the basis of its spectroscopic analysis. The Mössbauer isomer shifts of hDOHHperoxo (δ = 0.55 and 0.58 mm/s) are somewhat smaller than those of MMOHperoxo, D84E-R2peroxo, Ferittinperoxo, Δ^9Dperoxo and model complex **9** ($\delta \geq 0.63$ mm/s). The crystal structure of **9** shows that it does not contain any single atom bridge, which is also proposed for the peroxo intermediates of diiron enzymes. Instead, the δ values of hDOHHperoxo are rather similar to those of (μ-O(R))(μ-1,2-peroxo)diiron(III) clusters ($\delta \leq 0.58$ mm/s), suggesting that hDOHHperoxo contains a μ-O(R) ligand. However, this argument is undermined by the observation of large isomer shifts (δ = 0.58 and 0.65 mm/s) in

$[Fe_2(Ph\text{-}bimp)(O_2CPh)(O_2)]^{2+}$ (**11**) in which the diiron cluster is triply bridged by μ-OR, μ-1,2-O_2 and μ-1,3-O_2CPh ligands with Ph-bimp = 2.6-bis[bis{2-(1-methyl-4,5-diphenylimidazolyl) methyl}aminomethyl]-4-methylphenolate).[82]

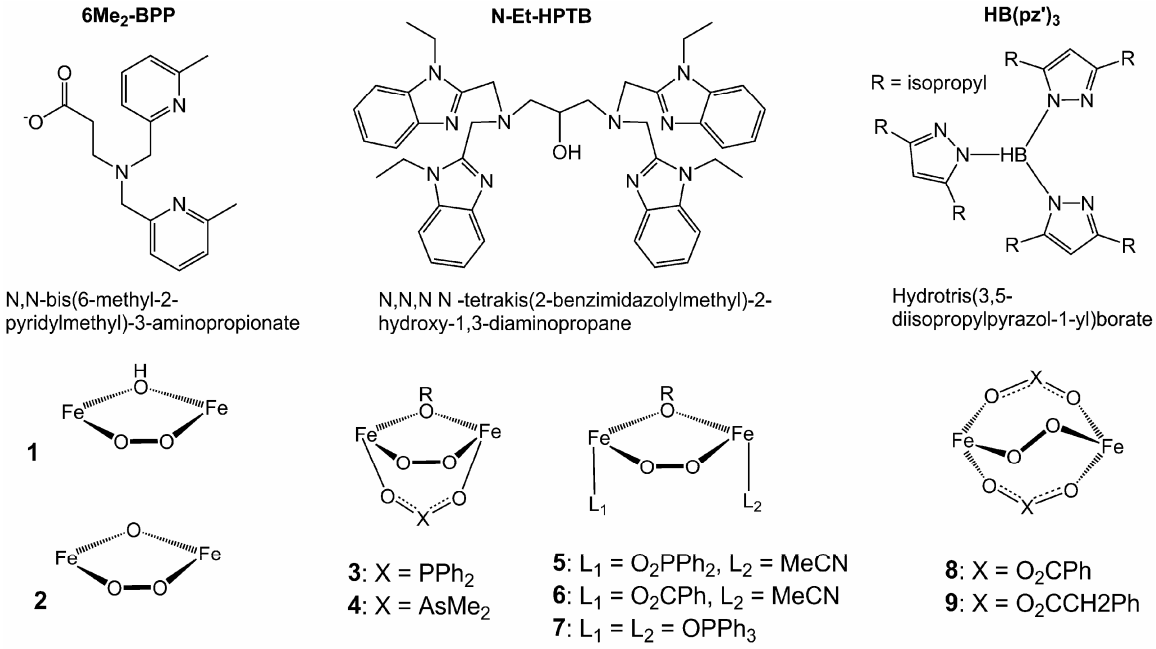

Figure 3.1. (μ-1,2-Peroxo)diiron(III) complexes for XAS study or discussed in this chapter.

The unequivocal observation of the ~3.4 Å Fe---Fe distance in the photoreduced form of hDOHHperoxo by EXAFS provides another hint for the μ-O(R) ligand in hDOHHperoxo. Preliminary EXAFS analysis of hDOHHperoxo reported earlier suggest that the Fe---Fe distance did not change upon photoreduction and data collection at temperature < 20 K.[16] The single atom bridging ligand could make the diiron cluster of hDOHHperoxo more rigid such that both the thermal and statistic disorders of the ~3.4 Å Fe---Fe path are small enough to enable its observation by EXAFS. Here we report a

systematic XAS study of hDOHHperoxo and model complexes that provides more compelling evidence for the (μ-O(R))(μ-1,2-peroxo)diiron(III) core in hDOHHperoxo. In addition, an EPR study of cryo-reduced hDOHHperoxo shows that the single atom bridging ligand of hDOHHperoxo is a μ-OH ligand.

3.2. Experimental

3.2.1. Sample preparation

hDOHHperoxo was prepared using GSH-Sepharose affinity resin as previously described[58] except that O_2-saturated buffer was used. hDOHH is purified as a mixture of apo and holo peroxo form. Using O_2-saturated buffer significantly improves the yield of the peroxo form. The protein was then further purified with size exclusion chromatography (SEC) using a S200 HR 26×60 column (GE Healthcare) and mobile phase (25 mM Tris buffer containing 125 mM NaCl at pH 8.25) flow rate at 0.5 or 1.0 ml/min. 2 ml fractions were collected. Fractions that contain holo hDOHHperoxo (A280/A630 ~ 15) were pooled and concentrated. All steps were performed at 0 – 4 ^{o}C.

To prepare $^{17}O_2$-hDOHHperoxo, ~ 3 ml of hDOHH mixture (A630 ~ 0.5) (obtained from the first affinity purification step) was reduced with slightly excess dithionite. The reduced hDOHH solution was exposed to 70 % enriched $^{17}O_2$ gas (Cambridge Isotopes), which was kindly provided by Michael Mbughuni and Professor John D. Lipscomb. The re-oxidized hDOHH mixture was purified with SEC as described above. The incorporation of 70 % $^{17}O_2$ in to hDOHHperoxo was verified by resonance Raman spectroscopy (see Supporting Information) using our reported procedure.[16]

Oxyhemerythrin (oxyHr) was generously provided by Dr. Thomas M. Makris in Professor Lipscomb's group. $^{17}O_2$-oxyHr was prepared by reducing oxyHr with a stoichimetry amount of dithionite and exposing the reduced sample to 60 % enriched $^{17}O_2$ (Cambridge Isotopes). The resulting $^{17}O_2$-oxyHr was then transferred to standard X-band EPR and Raman sample tubes in a glove box maintained at 0 ppm O_2 for further studies. Resonance Raman spectroscopy confirmed the incorporation of ~ 60% $^{17}O_2$ into oxyHr (see Supporting Information).

3.2.2. X-ray absorption spectroscopy

Two concentrated samples of hDOHH (~ 3 mM in [Fe]T) were prepared in pH 6.5 (200 mM MES) or pH 9.5 (200 mM CHES). 20% glycerol was added to prevent the formation of ice crystals in the samples. The samples were frozen in tandem Mössbauer/XAS cups with large sample windows allowing data to be collected on 11 sample spots on each sample. One scan was collected on each sample spot. 9 scans were collected for each sample. Sample preparation and data collection of a chemically reduced hDOHH sample and a photoreduced hDOHHperoxo sample at pH 8.2 are described in ref. 16 and Chapter 2.

We noted from previous experiments (Chapter 2) that hDOHHperoxo is photoreduced rapidly upon exposure to the X-ray beam. To minimize photoreduction during the sample aligment process, the beam flux was reduced by placing aluminum foils between the samples and the incident beam and the monochromator was set at 7130 eV instead of ~ 8000 eV as usually carried out for stable samples. As a result, the XANES spectra of hDOHHperoxo at pH 9.5 and 6.5 are almost identical with the edges at slightly higher energy than that of hDOHHperoxo at pH 8.2 collected earlier (Fig. 3.3).

A photoreduction yield of ~ 20 – 25 % is estimated when the first scans of the pH 8.2 samples were collected to energy of the edge jump.

The model complexes **1**, **2**, **6**, **7**, **8**, and **10** ([Fe_2(N-Et-HPTB)(μ-OH)$(NO_3)_2$]$(NO_3)_2$) were prepared according to previously published methods. Complexes **3**, **4**, and **5** were originally synthesized by Dr. Jonathan R. Frisch and reported in ref. 83. All samples were prepared in tandem Mössbauer/XAS cups or solution cells with sample spot sizes typical of 1 mm × 5 mm.

Table 3.1. Model complexes used in this study

Complex	Concentration (mM)	Prepared by	Ref.	Scans	Beamline
1	5	Dr. Xiaopeng Shan	131	16	SSRL 7-3
2	6	Dr. Xiaopeng Shan	131	15	SSRL 7-3
3	5	Dr. Jonathan R. Frisch	83	12	SSRL 9-3
4	5	Dr. Jonathan R. Frisch	83	12	NSLS X3B
5	5	Dr. Jonathan R. Frisch	83	8	SSRL 9-3
6	5	Dr. Jonathan R. Frisch	129	16	SSRL 7-3
7	3.6	Dr. Jonathan R. Frisch	130	16	SSRL 9-3
8	3	Dr. Anusree Mukherjee	106	16	SSRL 7-3
10	Solid sample*	Dr. Feifei Li	164	4	NSLS X3B

*Sample was mixed with dry BN at ~1:20 sample:BN ratio.

XAS data were collected on beamlines 7-3 and 9-3 at Stanford Synchrotron Radiation Lightsource (SSRL) of the SLAC National Accelerator Laboratory and on beamline X3B at the National Synchrotron Lightsource of Brookhaven National Laboratory (NSLS). At SSRL, the synchrotron ring SPEAR was operated at 3.0eV and 50-100 mA beam current. Energy resolution of the focused incoming X-rays was achieved using a Si(220) double crystal monochromator. At NSLS, the synchrotron ring was operated at 2.8 GeV and 100-300 mA beam current and a Si(111) double crystal monochromator was used. Fluorescence data were collected over the energy range of 6.8

- 8.0 keV using a 30-element Ge detector at 25 minutes/scan (SSRL) or 13-element Ge detector at 55 minutes/scan (NSLS). XAS spectra of an iron foil were collected concomitantly with that of the samples, the first inflection points of which were set at 7112 eV, to calibrate the energy of the sample spectra.

Standard procedures were used to reduce, average and process the raw data using the EXAFSPAK package,[149] which was also used for pre-edge quantification following a standard method[165] and EXAFS fitting. The XAS data was normalized using the MBACK method.[166] Theoretical EXAFS amplitude and phase functions were calculated using the FEFF package (version 8.4). The input models for FEFF calculations are built based on the crystal structures of **1**, **7**, and **9**. The parameters *r* and σ^2 were floated, while N was kept fixed for each fit and systematically varied in integer steps between fits. The scale factor was fixed at 0.9 and threshold energy (E_0) was varied but maintained at a common value for all paths. All fits with E_0 outside of the ± 10 eV range were not considered. The goodness of fit was calculated as $F = \sqrt{\sum k^6(\chi_{exp} - \chi_{cal})^2}$. To judge the effect of the addition of a shell to the fit, a normalized goodness of fit, F', was used. $F' = F^2/n\nu$, where $\nu = n_{idp} - n_{var}$, n is the number of data point, nidp is the number of independent points, and nvar is the number of variables used in each optimization step.

3.2.3. Cryo-reduction of hDOHHperoxo using X-ray beam or ^{60}Co γ rays

hDOHHperoxo and oxyHr (~ 0.5 mM peroxo, 50% glycerol) were frozen in X-band quartz EPR tubes. These samples were irradiated with ~ 5 Mrad of ^{60}Co γ rays at 77 K and a dose rate 0.95 Mrad/hour. Cryo-reduction with ^{60}Co γ rays was carried out at the

Nuclear Radiation Laboraotry at University of Illinois-Urbana Champaign with a great help from Dr. Stoyan A Toshkov, as well as Dr. Ilia Denisov in Prof. Steve Sligar's group at UIUC and Dr. Thomas M. Makris. EPR spectra of the samples were collected before annealing, after annealing at 77K with 120 W white light, and after annealing at 150 – 170 K for 5, 10, and 15 minutes. An hDOHHperoxo sample was prepared in a tube made from kapton tape and exposed to the X-ray beam on beamline X-3B at NSLS for about one hour at ~ 20 K. The kapton tube was then put in to a regular X-band EPR tube and maintained at 77 K for later EPR measurement.

3.3. Results

3.3.1. XANES analysis

It has been established that the nature of the coordination sphere of a diiron cluster can be deduced from the pre-edge features in their Fe-K edge XAS spectra.[157, 165] Fig. 3.2 shows the pre-edge features of hDOHHperoxo at pH 6.5 and model complexes. The XAS spectra of hDOHHperoxo at pH 6.5, and 9.5 are almost identical (Fig 3.3). The features can be fitted with two Gaussian peaks (Table 3.2), which is typical for octahedral high-spin iron(III) species. These two peaks are assigned to $1s \rightarrow 3d(t_{2g})$ and $1s \rightarrow 3d(eg)$ transitions, the ratio between which reflects the magnitude of 3d-4p mixing and thus the order of distortion of the electronic geometry around the iron center.[165]

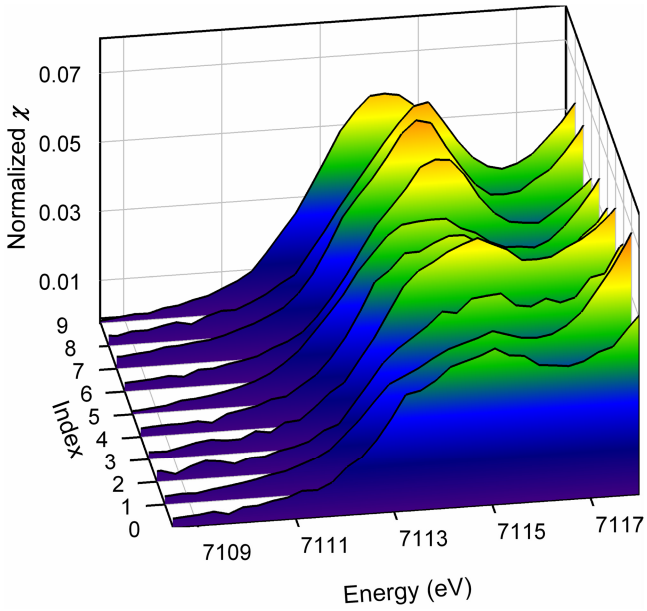

Figure 3.2. Fe K-edge XAS pre-edge features of hDOHHperoxo at pH 6.5 and model complexes. Index: 0: hDOHHperoxo; 1: **8**; 2: **1**; 3: **2**;4: **3**; 5: **4**; 6: **5**; 7: **6**; 8: **7**; 9: **10**.

The pre-edge feature of hDOHHperoxo changes significantly upon photoreduction (Fig. 3.3). The photoreduction of hDOHH peroxo yields a mixtures of iron(III) and iron(II) oxidation states as evidenced by the position of the Fe-K edge of the photoreduced sample compared to that of the non-photoreduced and fully reduced samples. The pre-edge intensity between 7113-7115 eV of reduced hDOHH (2.8 units) is significantly smaller than that of the hDOHHperoxo (~ 7 units), suggesting that the photoreduction would yield a much less intense pre-edge feature. Unexpectedly, the pre-edge feature of the photoreduced sample increases to 8.7(2) units. More importantly, the pre-edge peak ratio increases from 1:1 to 1:1.5 (Fig. 3.4), indicating that there is a considerable distortion of the electronic geometry around the iron center upon photoreduction.

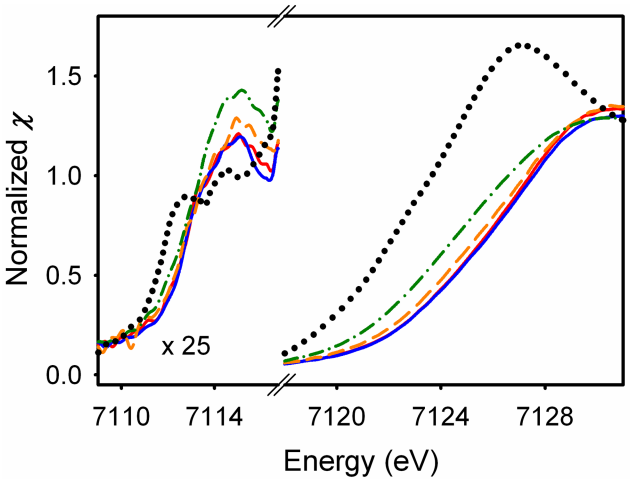

Figure 3.3. XANES spectra of hDOHHperoxo at pH 6.5 (——), 9.5 (——), 8.2 (– –) (partially photoreduced, photoreduced hDOHHperoxo at pH 8.2 (— • —), and chemically reduced hDOHH at pH 8.2 (••••).

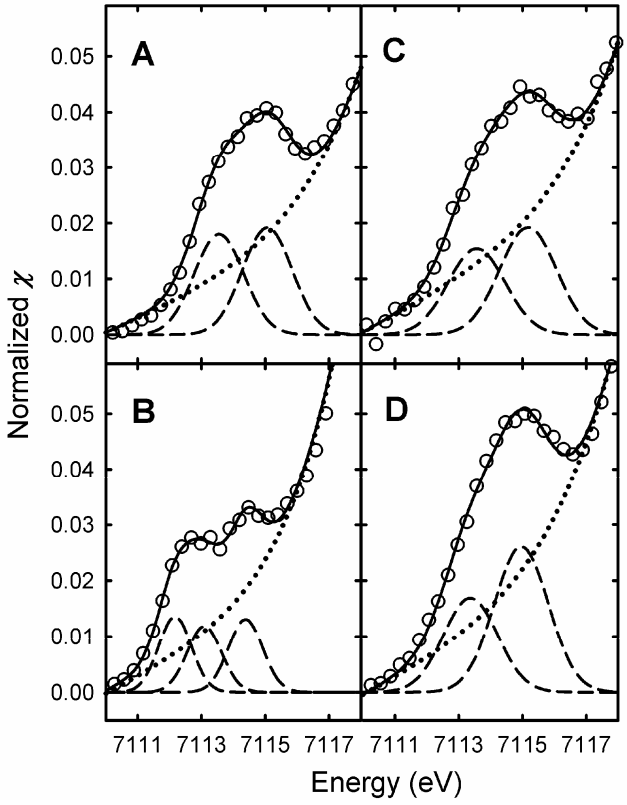

Figure 3.4. Fitting of the pre-edge feature of hDOHH. A: hDOHHperoxo at pH 9.5; B: reduced hDOHH at pH 8.2; C: hDOHHperoxo at pH 8.2, partially photoreduced (see Fig. 3.3); D: photoreduced hDOHHperoxo at pH 8.2. Legend: data (ooo), fit (——), background (••••), pre-edge peaks (— — —).

Table 3.2. XANES parameters for various hDOHH forms and model complexes

Complex	μ-O(R)	Peak 1 (eV)	Int. 1	Peak 2 (eV)	Int. 2	Total Int.	Int. ratio	FWHM
hDOHH								
pH 6.5[$]		7113.5(0)	3.3(2)	7115.1(1)	3.5(2)	6.8(4)	1:1.1	1.84(10)
pH 9.5[$]		7113.5(0)	3.2(1)	7115.0(0)	3.6(1)	6.8(2)	1:1.1	1.76(6)
pH 8.2[$]		7113.5(0)	3.1(1)	7115.1(0)	3.9(1)	7.0(3)	1:1.3	1.98(10)
Photored.[&]		7113.5(1)	3.5(3)	7114.9(0)	5.1(1)	8.7(2)	1:1.5	2.14(16)
Reduced[#]		7112.2(0)	1.7(2)	7114.4(1)	1.4(2)	4.5(6)		1.24(2)
				7113.2(3)	1.4(1)			
Model complexes								
1	OH	7113.8(0)	3.4(2)	7115.3(0)	3.1(3)	6.5(5)	1:0.9	1.84(8)
2	O/OH ?	7113.7(0)	5.1(2)	7115.2(1)	5.8(1)	10.9(3)	1:1.1	2.14(2)
3	OR	7113.5(0)	4.1(1)	7115.0(0)	4.3(1)	8.4(2)	1:1.0	1.80(2)
4	OR	7113.3(1)	4.1(3)	7114.8(1)	4.4(3)	8.5(6)	1:1.1	1.96(8)
5	OR	7113.6(1)	3.4(1)	7115.0(0)	6.0(3)	9.4(4)	1:1.8	1.82(4)
6	OR	7113.3(0)	3.4(0)	7114.7(0)	6.2(1)	9.6(1)	1:1.8	1.68(2)
7	OR	7113.4(1)	3.1(1)	7114.9(0)	6.3(4)	9.4(5)	1:2.0	1.64(4)
8	None	7113.3(0)	3.1(1)	7115.0(0)	3.5(1)	6.6(2)	1:1.1	1.96(6)
10[*]	OR/OH			7114.1(0)		14(1)		2.96(12)

FWHM = Full width at half maximum. [*]Symmetric pre-edge feature that can best fitted with one Gaussian peak. [$]hDOHHperoxo. [&] Photoreduced hDOHHperoxo at pH 8.2. [#] Chemically reduced hDOHH at pH 8.2

The total pre-edge area of **1, 3** – **8** are all smaller than 10 units, which are consistent with 6-coordinate diiron clusters without a μ-oxo ligand. The pre-edge areas of **3** – **7** are on the higher end of the range found for non-oxo bridged 6-coordinate diiron(III) species, while those of **1**, **8**, and hDOHHperoxo are on the lower end.[157, 165] Complex **10** with the same ligand framework as that of **3** – **7** exhibits an unusually intense pre-edge feature (14 units) for a non-oxo-bridged 6-coordinate diiron(III) compound. Thus, the higher intensities of the pre-edge features in **3** – **7** can be attributed to the alkoxo ligand, which is very unlikely to be present in hDOHHperoxo. The peak ratios (Table 3.2) of **5** – **7** (~ 1:2) indicate that these compounds have distorted geometries, while hDOHHperoxo, **1, 3, 4,** and **8** with peak ratios of ~ 1:1 have more

symmetric geometries. The total pre-edge area of **2** is ~ 11 units, which is relatively small for a μ-oxo bridged 6-coordinate diiron(III) cluster.[157, 165] The peak ratio of **2** is close to 1:1, which is not expected for a (μ-oxo)diiron(III) cluster. A duplicate sample of **2** gave the same data. EXAFS analysis (*vide infra*) of these data indicates that the sample is an ~ 1:1 mixture of **1** and **2**, consistent with the report that **2** gradually converts to **1** even in crystal form.[131]

3.3.3. EXAFS analysis

Fig. 3.5 shows the EXAFS spectra of hDOHHperoxo at pH 6.5 and 9.5. These two spectra are almost identical and similar to that of the sample at pH 8.2 reported earlier (Chapter 2). The FT spectra exhibit an intense inner shell features between r' = 1 – 2 Å, a second shell feature between r' = 2 – 2.8 Å, and a third shell peak at r' ~ 3.0 Å. These features are typical of diiron clusters with the inner-shell feature arise from the first coordination sphere, the second shell from C/N atoms of the ligands, and the symmetric third shell peak from an iron scatterer. The outer shell peaks of the hDOHHperoxo data are symmetric and intense as observed in the model complexes (*vide infra*) but not in diiron enzyme peroxo intermediates.

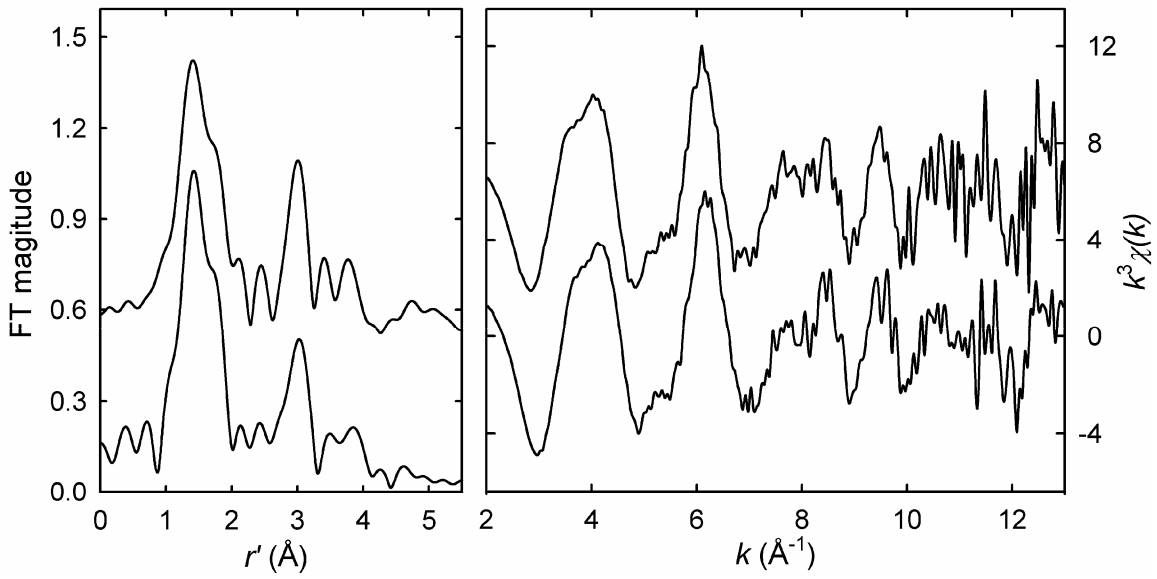

Figure 3.5. Fourier transforms (left) and unfiltered Fe K-edge k^3-weighted EXAFS data (right) of hDOHHperoxo at pH 6.5 (top traces) and pH 9.5 (bottom traces).

Table 3.3. EXAFS fitting results for hDOHHperoxo

Fit	Fe-O/N			Fe-N.O			Fe---C			Fe---Fe/C				
#	N	R	σ^2	N	R	σ^2	N	R	σ^2	N	R	σ^2	*F*	*F'*
hDOHHperoxo at pH 9.5														
1	6	2.01	14.6										114	0.0655
2	5	2.01	12.5										115	0.0658
3	3	1.95	5.3	3	2.12	3.0							86	0.0572
4	2	1.93	3.0	4	2.11	4.4							85	0.0561
5	1	1.91	0.5	5	2.08	6.7							85	0.0565
6	2	1.94	3.4	4	2.11	4.6	3	3.13	2.3				70	0.0550
7	**2**	**1.93**	**3.0**	**4**	**2.11**	**4.4**	**3**	**3.10**	**7.9**	**1Fe**	**3.43**	**3.1**	**25**	**0.0239**
8	2	1.93	2.9	4	2.11	4.2	3	3.11	3.6	4C	3.47	0.7	33	0.0320
hDOHHperoxo at pH 6.5														
1	6	2.03	14.4										131	0.0769
2	5	2.03	12.4										133	0.0781
3	1	1.91	0.2	5	2.09	6.0							94	0.0636
4	2	1.94	2.7	4	2.12	3.7							92	0.0622
5	3	1.96	5.1	3	2.13	2.3							93	0.0629
6	2	1.95	3.2	4	2.12	3.9	3	3.15	0.9				73	0.0586
7	**2**	**1.93**	**2.7**	**4**	**2.11**	**3.6**	**2**	**3.12**	**4.4**	**1Fe**	**3.43**	**2.5**	**17**	**0.0173**
8	2	1.94	2.7	4	2.12	3.5	2	3.13	1.1	4C	3.47	0.1	25	0.0248

N = coordination number. R = distance (Å). σ^2 = respective Debye-Waller factor ($10^{-3}\times$Å^2). Scale factor S_0^2 = 0.9. For both hDOHHperoxo data: *k* range = 2 – 13.5 Å^{-1}, resolution ~ 0.14 Å, back transform range 0.85-3.3 Å, n = 116, n_{idp} = 18.

The fitting results to Fourier-filtered data of hDOHHperoxo at pH 6.5 and pH 9.5 are identical and shown in Table 3.3 and Fig. 3.6. The inner shell features data are fitted with two subshells of Fe-O/N paths at 1.93 Å and 2.11 Å. The weak second shells are fitted with several Fe---C paths at ~ 3.1 Å. The intense outer shell peak is well simulated with an Fe---Fe path at 3.43 Å. Replacing this path with several Fe---C paths at the same distance does not reproduce the outer shell feature (compare Fits 7 and 8). Thus, EXAFS analysis clearly shows that the Fe---Fe distance is 3.43 Å for hDOHHperoxo at both pH's 6.5 and 9.5. This distance is also derived from preliminary EXAFS analysis for of hDOHHperoxo at pH 8.2.[16]

Fig. 3.6 shows Fourier-filtered EXAFS spectra and best fit results of model complexes **1-8** in comparison with the hDOHHperoxo spectra**.** The spectra of **2** are significantly different from those of **1**, indicating that there is significant structural change upon deprotonation of **1**. The fitting results of **1** and **2** are provided in Table 3.4. The progressive fit of **1** is essentially similar to that of hDOHHperoxo. The best fit parameters of **1** (Fit 7, Table 3.4) is consistent with its crystal structure, with an Fe---Fe distance of 3.42 Å.[131] As suggested by pre-edge quantification, the sample of **2** is indeed a mixture of **1** and **2**. An Fe-O distance at 1.84 Å is derived from the fit, which is slightly longer than the 1.80 Å distances normally observed for the Fe-μO bond by both XRD and EXAFS. More importantly, the outer shell feature can be well simulated with ~ 0.6 Fe---Fe path at 3.17 Å and ~ 0.4 Fe---Fe path at ~ 3.46 Å, but not with only one Fe---Fe path at either distance (compare fit 11 to fits 7-9, Table 3.4). These distances are similar to those observed in the crystal structure of **1** and **2**, respectively.[131] Unlike the spectra of hDOHHperoxo and other model complexes, the Fourier transform of **8** does not exhibit

any peak at ~ 3.0 Å (Fig. 3.5). Instead, its outer shell feature is near 3.3 Å. The best fit of **8** required two subshells of Fe-O/N paths at 1.98 Å and 2.14 Å, several Fe---C paths at 3.13 Å, and one Fe---Fe path at 3.61 Å. Replacing the Fe---Fe path with several Fe---C path at ~ 3.6 Å significantly decreases the fit quality (compare Fit 7 and 8, Table 3.4). In addition, the presence of light atoms at ~ 3.6 Å with disorder small enough to contribute to the EXAFS signal of **8** is difficult to justify. Thus, it is clear that the outer shell feature of **8** arises from an Fe---Fe path at 3.61 Å. Furthermore, introducing an Fe---Fe path at shorter distances (Fits 9 and 10, Table 3.4) only results in very large σ^2 value for this path and significantly lower fit quality. EXAFS analysis of **8** thus clearly shows that its Fe---Fe distances is 3.61 Å.

Table 3.4. EXAFS fitting result for **1**, **2**, and **8**

Fit	Fe-O/N			Fe-N.O			Fe---C			Fe---Fe/C				
#	N	R	σ^2	N	R	σ^2	N	R	σ^2	N	R	σ^2	*F*	*F'*
Complex 1														
1	6	1.97	24.6										319	0.1608
2	5	1.95	19.4										**314**	0.1583
3	2	1.95	2.1	4	2.19	6.9							189	0.1087
4	3	1.96	5.0	3	2.19	3.2							186	0.1067
5	4	1.96	8.8	2	2.20	0.6							193	0.1110
6	3	1.95	4.9	3	2.19	3.3	4	2.99	2.8				113	0.0754
7	**3**	**1.95**	**4.9**	**3**	**2.19**	**3.4**	**4**	**3.00**	**2.0**	**1Fe**	**3.42**	**1.6**	**18**	**0.0140**
8	3	1.95	4.8	3	2.19	3.2	4	3.00	2.7	4C	3.45	-0.7	31	0.0243
Complex 2														
1				6	2.21	48.5							318	0.1378
2	1	1.85	1.3	5	2.16	19.5							215	0.1053
3	1	1.95	0.7	2	2.06	8.0							202	0.1134
				3	2.25	4.5								
4	1	1.84	0.6	2	2.02	8.5	5	2.95	1.0				108	0.0711
				3	2.22	4.6								
5	1	1.84	1.1	2	2.02	9.6	5	2.97	1.2	1Fe	3.16	2.4	44	0.0353
				3	2.22	4.9								
6	1	1.84	0.4	2	2.02	7.8	5	2.94	1.1	1Fe	3.46	3.1	76	0.0607
				3	2.22	4.4								
7	1	1.84	1.0	2	2.02	9.4	5	2.97	1.6	1Fe	3.17	2.5	30	0.0302
				3	2.22	4.8				4C	3.48	3.7		
8	1	1.84	0.8	2	2.02	8.9	5	2.96	1.6	4C	3.20	1.1	29	0.0291
				3	2.22	4.8				1Fe	3.45	6.3		
9	1	1.84	0.8	2	2.02	8.9	5	2.96	2.0	4C	3.19	0.3	47	0.0470
				3	2.22	4.8				4C	3.51	5.1		
10	**1**	**1.84**	**0.9**	**2**	**2.02**	**9.0**	**5**	**2.97**	**2.3**	**0.6Fe**	**3.17**	**0.8**	**28**	**0.0284**
				3	**2.22**	**4.7**				**0.4Fe**	**3.46**	**1.6**		
Complex 8														
1	6	2.06	15.7										104	0.0607
2	5	2.07	12.7										95	0.0555
3	3	2.01	9.6	2	2.15	1.8							67	0.0445
4	2	1.98	6.5	3	2.14	2.9							65	0.0434
5	1	1.94	3.2	4	2.13	4.6							67	0.0445
6	2	1.98	6.7	3	2.14	3.0	4C	3.14	7.8					
7	**2**	**1.98**	**6.4**	**3**	**2.14**	**2.8**	**4C**	**3.13**	**7.3**	**1Fe**	**3.61**	**5.4**	**19**	**0.0177**
8	2	1.98	6.5	3	2.12	2.9	4C	3.14	7.7	4C	3.64	3.1	32	0.0302
9	2	1.97	6.3	3	2.14	2.8	1Fe	3.10	11.7	4Fe	3.64	3.4	50	0.0464
10	2	1.98	7.2	3	2.14	3.3	1Fe	2.58	21.2	4C	3.64	3.2	28	0.0331
							4C	3.12	9.5					

N = coordination number. R = distance (Å). σ^2 = respective Debye-Waller factor ($10^{-3}\times$Å^2). Scale factor S_0^2 = 0.9.

1: *k* range = 2 – 15 Å^{-1}, resolution ~ 0.12 Å, back transform range ~ 0.85 – 3.4, n = 131, n_{idp} = 20.6.

2: *k* range = 2 – 14 Å^{-1}, resolution ~ 0.13 Å, back transform range = 0.85 – 3.4 Å, n = 121, n_{idp} = 19.4

8: *k* range = 2 – 12.6 Å^{-1}, resolution ~ 0.16 Å, back transform range = 0.85 – 3.7 Å, n = 107, n_{idp} = 19.

The five N-Et-HPTB complexes can be divided into two subgroups, one includes **3** and **4** and the other includes **5**, **6**, and **7**, based on the similarities in their FT spectra, as well as in their EXAFS spectra in the region beyond 8 $Å^{-1}$ (Fig. 3.6). Table 3.5 shows the progressive fits the N-Et-HPTB complexes. The fitting results for **3** – **5** have been published[83] and only the best fit parameters are listed here for discussion. The inner shell features of the N-Et-HPTB complexes can best be fitted with a total coordination number of six with 4 to 5 ligands near 2.0 to 2.2 Å and one ligand near 2.3 Å, corresponding to the Fe-N_{amine} bond as observed in the crystal structures of **7**[130] and the diferrous precursors of **3** and **4**.[83] In **5**, **6**, and **7**, a short Fe-O distance of 1.88 – 1.89 Å can be resolved from other Fe-O/N distances and is assigned to the peroxo ligand.[107, 109, 130, 131] The second shell peaks of these complexes correspond to 3 to 5 Fe···C paths near 2.95 Å, which arise from carbon atoms adjacent to the ligating nitrogen atoms of the benzimidazole rings of the N-Et-HPTB ligand.

Similar to the analysis of hDOHHperoxo and **1**, the 3.1 Å feature of **5** – **7** is best fitted with an Fe···Fe path at 3.46 – 3.47 Å. Replacing this Fe···Fe path by either one Fe···P path or five Fe···C paths results in significantly lower fit quality. Thus, the $r' = 3.1$ Å feature is attributed to an Fe···Fe path at 3.46 – 3.47 Å. This distance is consistent with that in the crystal structure of **7**,[130] which is significantly longer than the 3.21 – 3.26 Å Fe···Fe distance found in **3** and **4**. An Fe···P path is not required for the best fits to the data of **5** and **7**, suggesting that in the terminal binding mode of O_2PPh_2 and $OPPh_3$ ligands, the outer atoms are too disordered relative to the iron centers.

Table 3.5. EXAFS fitting result for N-Et-HPTB model complexes

Fit	Fe-O/N			Fe-N.O			Fe---C			Fe---Fe/C				
#	N	R	σ^2	N	R	σ^2	N	R	σ^2	N	R	σ^2	*F*	*F'*
Complex 3														
1	6	1.97	24.6										319	0.1608
2	5	1.95	19.4										**314**	0.1583
Complex 4														
1	**3**	**1.97**	**3.5**	**2**	**2.14**	**3.9**	**3**	**2.96**	**2.8**	**1Fe**	**3.27**	**1.3**	**13**	**0.0135**
				1	**2.31**	**6.3**								
2	**3**	**1.96**	**3.8**	**2**	**2.13**	**4.3**	**3**	**2.94**	**5.5**	**1As**	**3.21**	**2.2**	**12**	**0.0130**
				1	**2.30**	**5.9**								
Complex 5														
1	**1**	**1.89**	**0.2**	**3**	**2.04**	**3.1**	**4**	**2.97**	**2.7**	**1Fe**	**3.47**	**4.5**	**14**	**0.0141**
				1	**2.36**	**3.2**	**2**	**3.23**	**7.0**					
Complex 6														
1	6	1.98	13.1										228	0.1253
2	5	1.99	10.3										205	0.1128
3	1	1.84	1.11	4	2.01	4.4							165	0.1039
4	1	1.88	1.1	3	2.03	2.3							135	0.0992
				1	2.40	3.5								
5	1	1.88	0.3	3	2.03	1.7	4	2.96	1.1				62	0.0696
				1	2.43	8.4	4	3.17	2.9					
6	**1**	**1.88**	**0.4**	**3**	**2.03**	**2.0**	**4**	**2.95**	**2.4**	**1Fe**	**3.47**	**3.0**	**19**	0.0280
				1	**2.42**	**6.5**	**2**	**3.18**	**4.0**					
7	1	1.88	0.5	3	2.03	2.0	4	2.95	2.1	4C	3.51	0.34	28	0.0426
				1	2.41	6.0	2	3.17	1.1					
Complex 7														
1	6	1.97	13.2										268	0.1130
2	5	1.98	10.8										248	0.1046
3	1	1.86	1.4	4	2.01	5.2							222	0.1053
4	1	1.89	0.8	3	2.03	2.8							179	0.0969
				1	2.40	1.6								
5	1	1.90	1.4	3	2.04	3.3	4	2.98	1.1				191	0.1444
				1	2.40	1.2	4	3.19	1.6					
6	**1**	**1.89**	**0.7**	**3**	**2.03**	**2.8**	**4**	**2.96**	**2.2**	**1Fe**	**3.46**	**1.7**	**18**	**0.0170**
				1	**2.41**	**1.6**	**2**	**3.18**	**5.1**					
7	1	1.89	1.0	3	2.03	3.0	4	2.97	1.9	4C	3.49	-0.2	34	0.0320
				1	2.41	1.5	2	3.17	0.2					

N = coordination number. R = distance (Å). σ^2 = respective Debye-Waller factor ($10^{-3}\times$Å^2). Scale factor S_0^2 = 0.9.

3: *k* range = 2 – 15 Å^{-1}, resolution ~ 0.12 Å, back transform range = 0.85 – 3.1 Å, *n* = 131, n_{idp} = 18.3
4: *k* range = 2 – 13 Å^{-1}, resolution ~ 0.14 Å, back transform range = 0.85 – 3.4 Å, *n* = 117, n_{idp} = 18.3
5: *k* range = 2 – 15 Å^{-1}, resolution ~ 0.12 Å, back transform range = 0.85 – 3.4 Å, *n* = 129, n_{idp} = 20.7
6: *k* range = 2 – 13.5 Å^{-1}, resolution ~ 0.14 Å, back transform range = 0.85 – 3.1 Å, *n* = 116, n_{idp} = 18.7
7: *k* range = 2 – 15 Å^{-1}, resolution ~ 0.12 Å, back transform range = 0.85 – 3.4 Å, *n* = 131, n_{idp} = 21.1

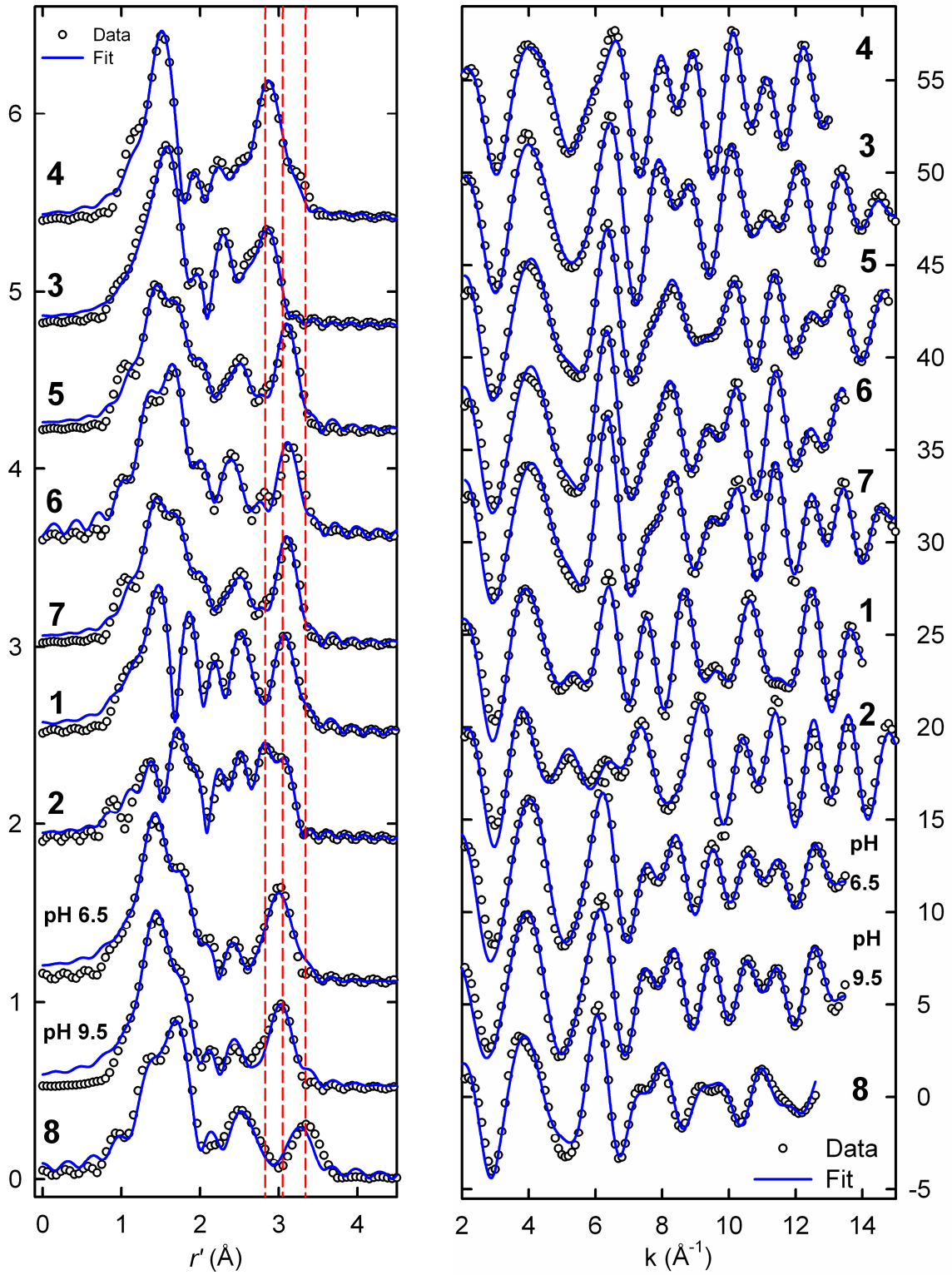

Figure 3.6. Fourier transforms (left) of the Fourier-filtered Fe K-edge k^3-weighted EXAFS data (right) of hDOHHperoxo and model complexes. Data and fit parameters are shown bold in Tables 3.3 – 3.5. The red lines indicate the peaks corresponding to Fe---Fe paths in the Fourier transform spectra.

3.3.4. EPR analysis of cryo-reduced hDOHHperoxo (pH 8.2) and oxyhemerythrin

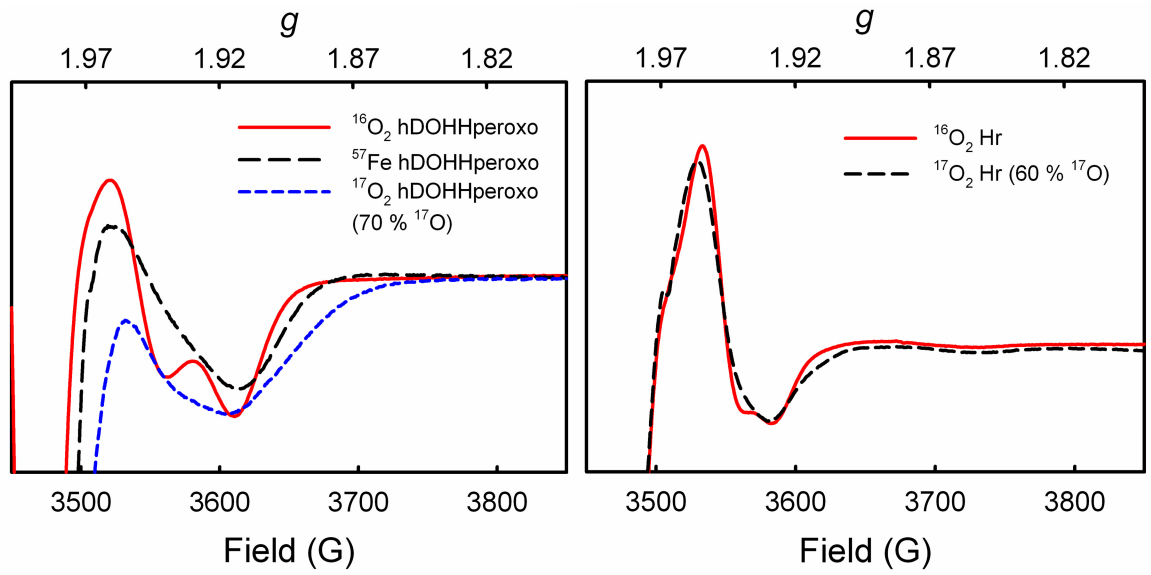

Figure 3.7. EPR spectra of hDOHHperoxo (left) and oxyHr (right) after cryo-radiolysis with ^{60}Co γ source. The spectra were collected in perpendicular mode, at ~ 12 K, and 10 mW power, 5G modulation amplitude. The cryo-reduced hDOHHperoxo samples were annealed at ~ 150 – 170 K for 10 mins. The cryo-reduced oxyHr samples were photoannealed at 77 K. The estimated g values for the cryo-reduced $^{16}O_2$-hDOHHperoxo sample are 1.909 and 1.947. The estimated g values for the $^{16}O_2$-oxyHr are 1.924 and 1.943

Fig. 3.7 shows the EPR spectra of hDOHHperoxo and oxyHr after cryo-radiolysis with ^{60}Co γ rays. The as-isolated hDOHHperoxo and oxyHr samples are EPR silent in perpendicular mode. The annealing profiles of the samples are provided in Supporting Information. Prior to annealing, the EPR spectrum of this sample exhibits a strong $g = 2$ signal that arises from solvated electrons and free radicals generated during radiolysis. Upon photoannealing at 77 K for ~ 2 hours (for oxyHr samples) or thermal annealing at ~ 150 – 170 K for ~ 10 minutes (for hDOHHperoxo samples), these signals decayed

significantly, allowing the observation of $g < 2.0$ axial signals. The $^{16}O_2$-hDOHHperoxo sample cryo-reduced with an X-ray beam exhibits weak free radical signal at $g = 2$, allowing the observation of the $g < 2$ signal without annealing (see Supporting Information). The similarity of the $g < 2$ signals of hDOHHperoxo before and after annealing indicates that thermal annealing at 150 – 170 K does not affect the species giving rise to this signal.

In the spectrum of cryo-reduced ^{57}Fe-hDOHHperoxo, the $g < 2$ signal is significantly broadened. This line broadening is attributed to the hyperfine coupling of the electron to the ^{57}Fe nuclei ($I = 1/2$) (^{56}Fe has nuclear spin $I = 0$ and does not exhibit hyperfine coupling), indicating that this signal is associated with the iron center(s) of hDOHH. More importantly, this signal is also broadened in the spectrum of cryo-reduced $^{17}O_2$-hDOHHperoxo. Since the nuclear spins of ^{16}O and ^{17}O are 0 and 5/2, respectively, this broadening is attributed to the (super)hyperfine coupling of the electron to ^{17}O nuclei. This result clearly shows that at least one of the oxygen atoms of the peroxo moiety remains bound to the diiron cluster upon cryo-reduction. Similar ^{17}O line broadening is also observed in the spectra of cryo-reduced oxyHr (Fig. 3.7).

3.4. Discussion

EXAFS analysis unequivocally derives an Fe---Fe distance of 3.43 Å for hDOHHperoxo. Such a clear observation of the Fe---Fe distance has not been obtained for any other peroxo intermediates of diiron enzymes. This distance provides valuable

information about the bridging structure of the diiron cluster in hDOHHperoxo when compared to model complexes with well characterized core structures (Table 3.6).

8 contains two μ-1,3 carboxylate ligands in addition to the μ-1,2-peroxo moiety and has an Fe---Fe distance of 3.61 Å. This result is consistent with previous spectroscopic and computational studies that predicted a bis(μ-1,3-carboxylato)(μ-1,2-peroxo)diiron(III) structure for **8** and W48F/D84E-R2perox with the Fe---Fe distances at ~ 3.6 – 3.7 Å.[87, 162] This distance is shorter than that observed in the crystal structure of **9** (4.00 Å). **8** only differs from **9** in that **8** has two O_2CPh ligands instead of O_2CCH_2Ph ligand. This difference in the Fe---Fe distances suggests that the bis(μ-1,3-carboxylato)(μ-1,2-peroxo)diiron(III) core arranges in solution differently from that in the crystal. For example, the gauche cis-1,2-peroxo geometry observed in the crystal structure of **9** could change to a planar cis-1,2-peroxo geometry in solution for **8**, which would significantly reduce the Fe---Fe distance. Regardless this difference, it is clear that without any single atom bridging ligand, the Fe---Fe distance of **8** and **9** is longer than the distance of 3.43 Å found for hDOHHperoxo.

Table 3.6. Correlation of the bridging structure of (μ-1,2-peroxo)diiron(III) with its Fe---Fe distance

Complex	**hDOHH**	**8** and **9**	**2**	**1**	**5 – 7**	**3**, **4**, and **11**
Additional Bridge(s)	μ-OH ?	bis(μ-1,3-O_2CR) R = Ph or CH_2Ph	μ-O	μ-OH	μ-OR	μ-OR and μ-1,3-$O_2XR'_2$, X = C, P, As; R' = Ph or Me
r(Fe---Fe) (Å) by EXAFS	3.43	3.61	3.17	3.42	3.46 – 3.47	3.26 – 3.27
r(Fe---Fe) (Å) by XRD		4.000(4)[a]	3.171(1)[b]	3.396(1)[b]	3.462(3)[c]	3.327(2)[d]

[a] Complex **9**, ref. 107; [b] Complexes **1** and **2**, ref. 131; [c] Complex **7**, ref. 130; [d] Complex **11**, ref. 82.

In contrast to **8** and **9**, **2** with only a μ-oxo ligand in addition to the μ-1,2-peroxo moiety has an Fe---Fe distance of 3.17 Å, which is significantly shorter than that in hDOHHperoxo. Protonation of the μ-oxo ligand of **2** lengthens the Fe---Fe distance to ~ 3.4 Å, a value similar to that of hDOHHperoxo. Likewise, complexes **5** – **7** with an μ-alkoxo ligand in the place of the μ-hydroxo ligand have similar Fe---Fe distances at 3.46 – 3.47 Å. Introduction of an additional μ-1,3 ligand to the five membered-ring (μ-OR)(μ-1,2-peroxo)diiron(III) core in **3**, **4**, and **11** shortens its diiron distance to ~ 3.3 Å. This comparison demonstrates that hDOHHperoxo contains one and only a μ-OR ligand in addition to its μ-1,2-peroxo ligand.

The presence of a single atom bridging ligand in hDOHHperoxo is further supported by the EPR and XAS data of the 1-electron reduced hDOHHperoxo in frozen state. The EPR signal observed of cryo-reduced hDOHHperoxo at $g < 2.0$ is typical of a (μ-O(H))diiron(III/II) clusters in both model and enzymatic systems, prepared by chemical reduction or cryo-radiolysis.[105, 167-169] From extensive studies of many model complexes, a general trend has been observed that (μ-hydroxo)diiron(II/III) clusters exhibit rhombic EPR signals at g_{ave} = 1.43–1.87 with relatively large rhrombicity (Δg ~ 0.14 – 0.55), while (μ-oxo)diiron(II/III) clusters exhibit axial EPR signals at g_{ave} = 1.90–1.98 with smaller rhrombicity ($\Delta g < 0.07$). The small rhrombicity of the (μ-oxo)diiron(II/III) cluster very likely arise from the ability of the μ-oxo ligand to strongly mediate the exchange coupling between the two iron centers.[167, 168]

The g_{ave} = 1.94 and Δg = 0.05 values for cryo-reduced hDOHHperoxo are more consistent with the presence of a (μ-oxo)diiron(II/III) cluster rather than a (μ-

hydroxo)diiron(II/III) cluster. While hDOHHperoxo does not contain a μ-oxo ligand as clearly demonstrated by Mössbauer and XAS study, the presence of the μ-oxo ligand in cryo-reduced hDOHHperoxo can be explained by the proposed mechanism in Scheme 3.1. The EPR signal of cryo-reduced hDOHHperoxo is distinct from the isotropic $g = 2$ signal of intermediate X in RNR R2 and its model complexes.[63, 67, 170, 171] In addition, during XAS measurement, the Fe K-edge of hDOHHperoxo gradually red shifted, indicating that the overall oxidation state of the diiron cluster decreased upon cryo-reduction. Thus, we propose that the 1-electron reduction of hDOHHperoxo likely leads to the dissociation of the peroxo ligand from one iron center as opposed to O-O bond cleavage observed for RNR R2. The resulting terminal anionic peroxo ligand then deprotonates the hydroxo ligand to form a Fe^{II}-O-Fe^{III}-OOH species. As a precedent for the proton transfer to a terminal peroxo anion at 20 K and 77 K in this proposed mechanism, the same process was observed for heme oxygenase even at 4 K.[168] This mechanism is supported by the pre-edge quantification results. Upon photoreduction of hDOHHperoxo, the pre-edge intensity increases from ~ 6.8 units to 8.7 units and pre-edge peak ratio increases from 1:1 to 1:5, consistent with a geometrical change from a more symmetric octahedral field to a distorted field.[165] In the mechanism in Scheme 3.1, one 6-coordinate iron center converts to a 5-coordinate center while a μ-oxo ligand is formed, which both contribute to the increases in pre-edge intensity and peak ratio.

The presence of a hydroperoxo ligand bound to a (μ-oxo)diiron(II/III) cluster is precedented by the study on oxyhemerythrin and its model complexes.[105] [Fe_2(μ-OH)(μ-Ph_4DBA)(TMEDA)$_2$(OTf)] (**12**) and [Fe_2(μ-OH)(μ-Ph_4DBA)(DPE)$_2$(OTf)] (**13**), where Ph_4DBA2^- is the dinucleating bis(carboxylate) ligand dibenzofuran-4,6-

bis(diphenylacetate), are two model complexes that closely resemble the active site of deoxyhemerithrin with an asymmetric Fe^{II}-OH-Fe^{II} core. The reaction of deoxyhemerythrin, as well as of **12** and **13**, with O_2 results in the formation of a Fe^{III}-O-Fe^{III}-OOH species, in which the proton is transferred from the μ-OH ligand to the terminal peroxo ligand. The EPR spectra of cryoreduced oxyHr and **13-O_2** exhibit axial signals typical of (μ-oxo)diiron(II/III) species. Importantly, ^{1}H-ENDOR spectra of cryoreduced oxyHr and **13-O_2** show weak doublets with $A \sim 11.5$ MHz and $A \sim 9.5$ MHz, respectively, which arise from the proton of a hydroperoxo terminally bound to a mixed valent (μ-oxo)diiron(II/III) cluster.[105] Given the ligand sets of oxyhemerythrin and **13-O_2**, their cryo-reduction likely results in a Fe^{II}-O-Fe^{III}-OOH species similar to what we propose for cryoreduced hDOHHperoxo in Scheme 3.1. Our EPR study of cryo-reduced $^{17}O_2$-oxyHr provides further evidence that upon cryo-reduction, the peroxo moiety remains bound to the diiron cluster in Hr.

Scheme 3.1. Proposed cryo-reduction of hDOHHperoxo.

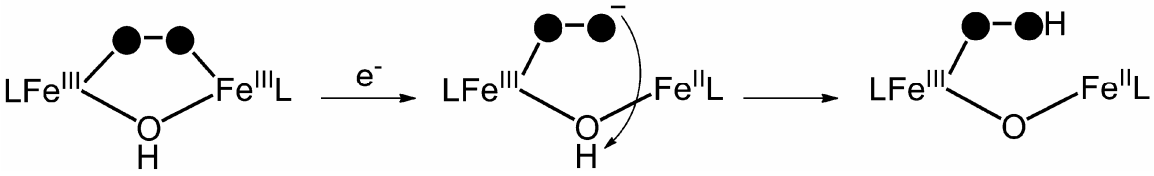

Together, our XAS and EPR study provide compelling evidence for the (μ-hydroxo)(μ-peroxo)diiron(III) structure of hDOHHperoxo. A μ-hydroxo has thus far not been observed in any other peroxo intermediates of diiron enzymes. This additional bridging ligand may lead to the difference in the Mössbauer parameters of

hDOHHperoxo compared to those of other diiron enzyme peroxo intermediates. More importantly, this μ-hydroxo ligand may contribute significantly to the stability of hDOHHperoxo and affect its reactivity. XAS data of hDOHHperoxo at pH 6.5 and 9.5 are almost identical, indicating that this ligand, as well as the core of hDOHHperoxo active site is not affected by pH in this range. Great attention should be paid to this ligand in further structural and mechanistic studies of hDOHH.

3.5. Supporting Information

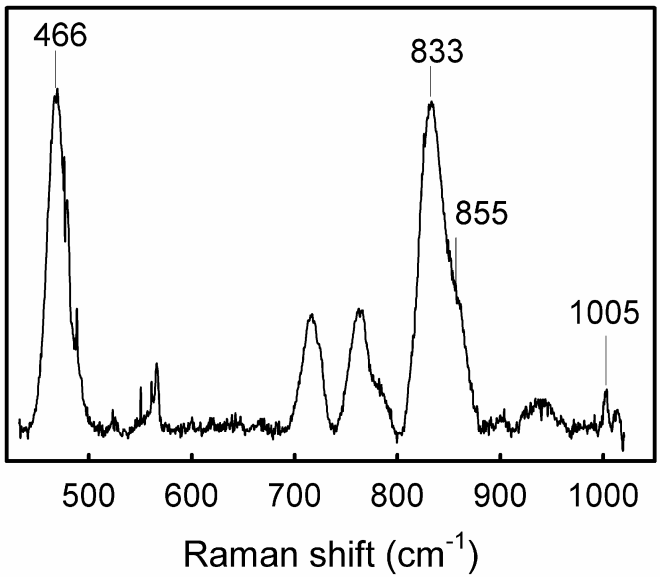

Figure S.3.1. Resonance Raman spectrum of holo hDOHHperoxo prepared with 70 % enriched $^{17}O_2$ (647.1 nm excitation, 200 mW, 0 ^{o}C)

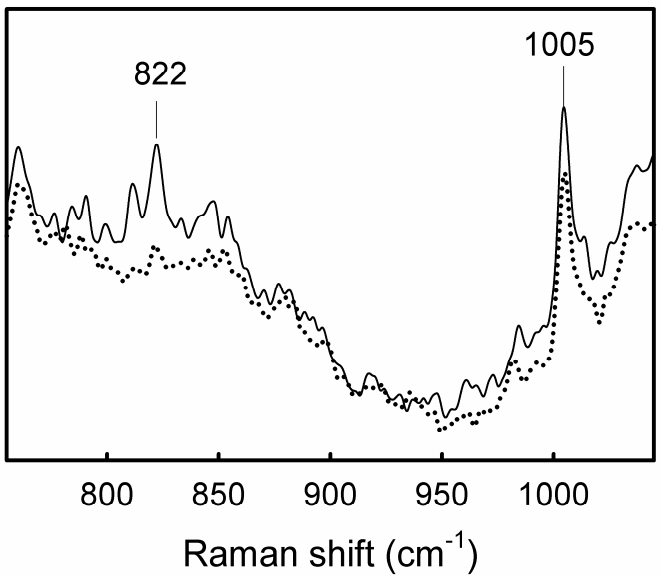

Figure S.3.2. Resonance Raman spectra of oxyHr prepared with 60 % enriched $^{17}O_2$ (—) and decayed Hr after exposed to 488 nm excitation laser (300 mW at ~ 0 ^{o}C).

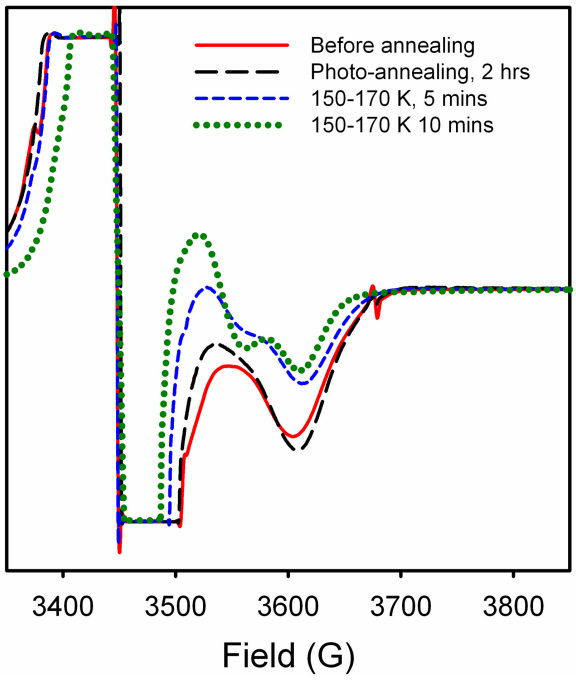

Figure S.3.3. Annealing profile for cryo-reduced $^{16}O_2$-hDOHHperoxo

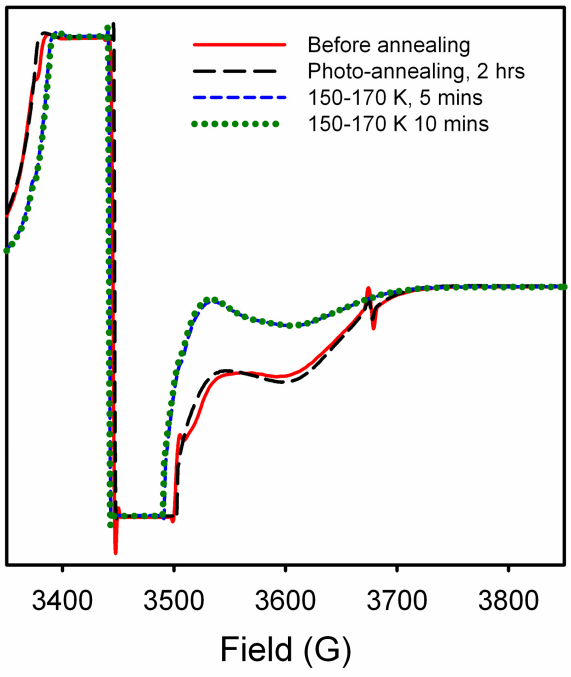

Figure S.3.4. Annealing profile for cryo-reduced $^{17}O_2$-hDOHHperoxo

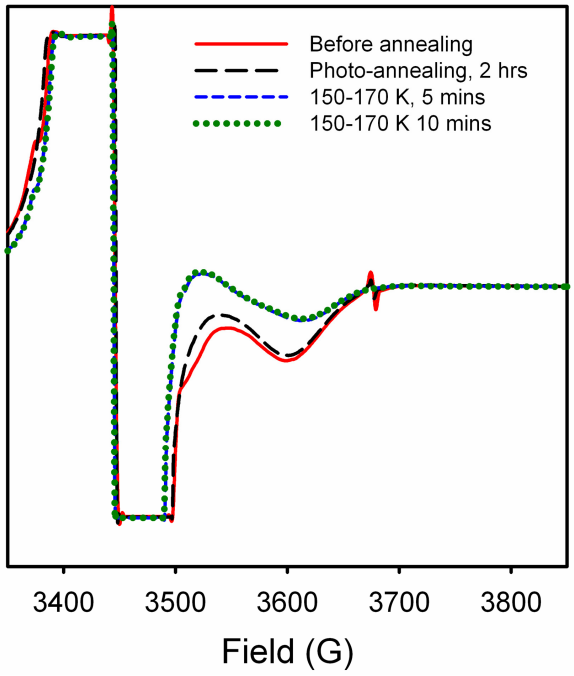

Figure S.3.5. Annealing profile for cryo-reduced ^{57}Fe-hDOHHperoxo

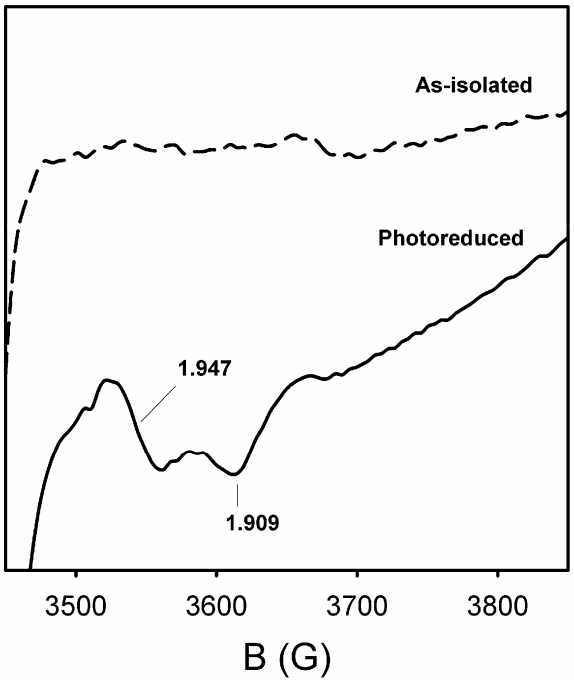

Figure S.3.6. EPR spectra of hDOHHperoxo before and after cryo-reduction with X-ray beam at the XAS beamline X3B of the National Synchrotron Light Source. The cryo-reduced sample was not annealed.

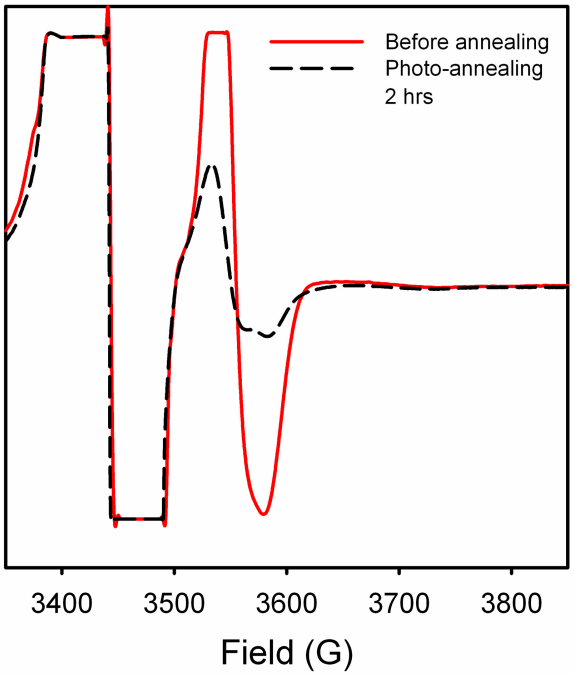

Figure S.3.7. Annealing profile for cryo-reduced $^{16}O_2$-oxyHr

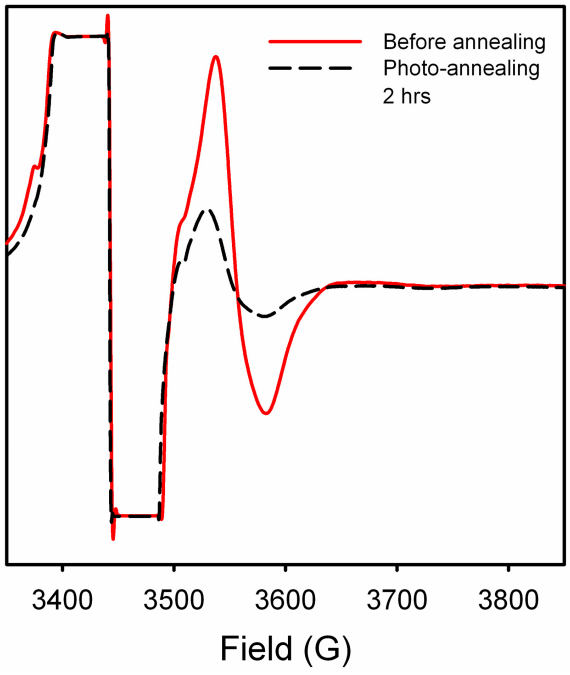

Figure S.3.8. Annealing profile for cryo-reduced $^{17}O_2$-oxyHr

Chapter 4

Formation and reaction of hDOHHperoxo

4.1. Introduction

The binding of O_2 to the reduced diiron cluster and how the resulting peroxo intermediate undergoes O-O bond cleavage are the most important aspects in oxygen activation by diiron enzymes. Extensive studies on MMO reveals that each of these two steps requires the transfer of one proton.[88, 89] The oxygen binding and activation steps of MMO and RNR R2 happen on the millisecond time scale.[2, 88, 89] For MMO and R2 reaction cycle, the rate determining step happens after O-O bond cleavage steps.[2]

We have shown in previous chapters that the hDOHHperoxo contains a (μ-1,2-peroxo)diiron(III) cluster with a possible additional μ-hydroxo ligand (Scheme 4.1). This μ-hydroxo ligand is a unique feature of hDOHHperoxo, which possibly contributes to its unusual stability. Because hDOHH is different from the canonical diiron enzymes in overall protein fold and structure of the peroxo intermediate, it is intriguing to compare the formation and activation of hDOHHperoxo to those of the well characterized enzymes. These insights are required to augment our understanding of oxygen activation by diiron enzymes. Moreover, such insights are important to understand how mature eIF5A, a growth regulation factor, is synthesized.

In this work, various kinetic, spectroscopic, and biochemical techniques are utilized to study the formation and reaction of hDOHHperoxo. The results obtained herein indicate that hDOHHperoxo activation also requires a proton transfer step as found for MMOHperoxo. However, the formation and reaction of hDOHHperoxo differs from those of MMOHperoxo in many aspects, presumably due to the additional μ-hydroxo ligand and a flexible overall structure of hDOHH.

Scheme 4.1. Reaction of deoxyhypusine synthase (DHS) (left) and deoxyhypusine hydroxylase (DOHH) (right).

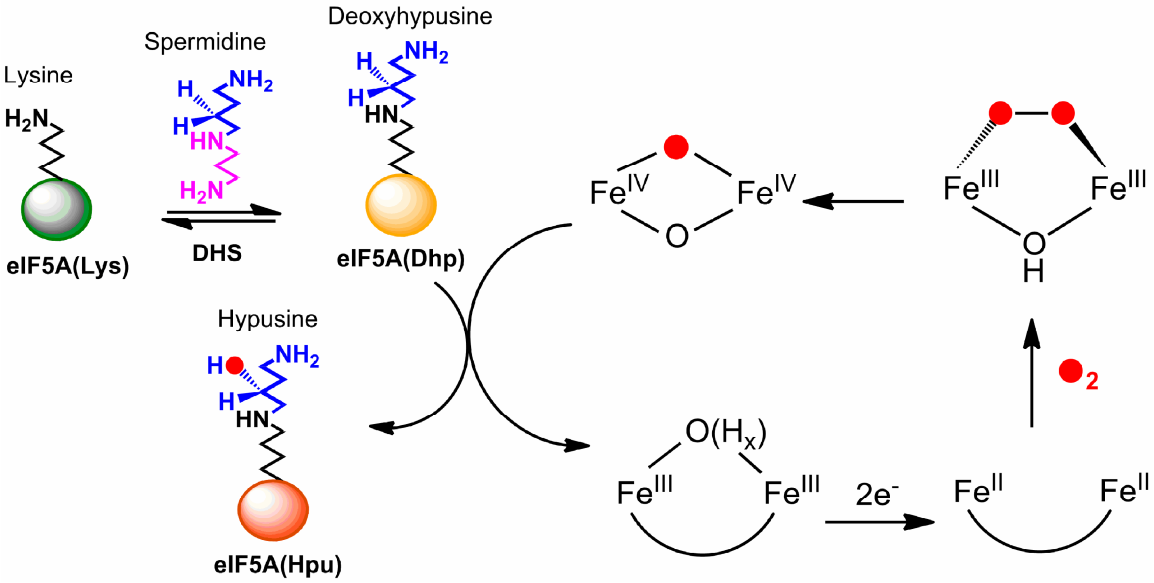

4.2. Experimental

4.2.1. hDOHH purification

A published protocol was used to purify hDOHH with slight modifications. Cell paste (~15 g) was mixed with ~ 80 mL anaerobic buffer A (50 mM Tris, 100 mM NaCl, pH 7.7) and stirred on an ice bath for ~ 15 min or until an even suspension was obtained. The suspension was then lyzed with sonication, which was subsequently centrifuged for ~ 30 minutes at ~ 30000xg. The clear supernatant (~ 80 mL) was divided into two 50-mL centrifuge tubes. 6 mL bed volume of GSH-sepharose (GE Healthcare) was added to each tube, which was then capped and rotated at 4 ^{o}C overnight. The content in each centrifuge tube was then split evenly into two empty PD-10 columns (4 columns in total). Columns 1 and 2 were washed thoroughly with air-saturated buffer. Columns 3 and 4

were first washed with anaerobic buffer (~ 100 mL), which was followed with air-saturated buffer. hDOHH was then cleaved from the GSH-Sepharose resin using thrombin as previously described.[58] Separation of holo hDOHHperoxo with preparative size-exclusion chromatography (SEC) was carried out as described in Chapter 3.

4.2.2. Stopped-flow experiments

2.5 mL of anaerobic 0.2 mM holo hDOHHperoxo (A630 ~ 0.5) in SEC buffer (pH 8.2, 25 mM Tris, 125 mM NaCl) containing 0.1 equivalent of methylviologen was prepared by equilibrating with Ar for ~ 2 hours while being stirred in an ice-bath. To this solution ~ 10 equivalents of sodium dithionite were added to obtain a solution with the characteristic bright blue color of reduced methylviologen. The reaction mixture was applied to a PD-10 desalting column (G-25, GE Healthcare) in a glove box maintained at 0 ppm oxygen. Reduced hDOHH was eluted with 3.5 mL anaerobic 50 mM MOPS pH 7.5 buffer while excess dithionite, methylviologen, and other salt remained bound to the column. The colorless reduced hDOHH sample was then mixed rapidly with O_2-saturated 50 mM MOPS pH 7.5 buffer solution using an Applied Photophysics SX.18MV model stopped-flow device at 4 ^{o}C. The concentration of hDOHH and O_2 after mixing were 0.1 and 1.0 mM, respectively. The formation of hDOHHperoxo was monitored at 620 nm.

4.2.3. pH-dependent reaction of hDOHHperoxo

MES, BisTRRIS, MOPS, TRIS, and CHES were used to prepare 50 mM buffer solutions at desired pH. The pH's of the solutions were measured at both room temperature and 37 ^{o}C. 10 μL of holo hDOHHperoxo was mixed with ~ 200 μL buffer to obtain a final concentration of ~ 35 - 40 μM (A_{630} ~ 0.1). The reaction was monitored at

37 ^{o}C using a diode-array UV/Vis spectrometer. The self decay rate of hDOHHperoxo was estimated by following A_{630}.

4.2.4. Analytical size exclusion chromatography

Analytical SEC analysis was performed using a GF-250 column (4.6 mm ID, 250 mm length) on an HP Agilent 1100 HPLC system equipped with an autosampler. The mobile phase contains 50 mM Tris and 125 mM NaCl pH 7.5. Column temperature was maintained at 25 ^{o}C. GST-Apo protein was provided by Dr. Park Myung Hee. The GST tag was removed using thrombin as described elsewhere.[58] Reduced hDOHH was obtained by treating holo hDOHHperoxo with excess dithionite. For SEC analysis of the reduced sample, the mobile phase was degassed thoroughly with Ar and the system was purged and equilibrated with degassed buffer for prior to sample injection. holo hDOHHperoxo in with 200 mM buffer at pH 6.5 (MES) or 9.5 (CHES) was kept at room temperature (22 ^{o}C) and automatically injected. The time interval between runs of each sample was 15 minutes. 4 mM phthalic acid was added to each sample and used as an internal standard. The injection volume of each sample was 10 μL.

4.2.5. Reaction of hDOHHperoxo with eIF5A(Dhp) substrate and its analogues

eIF5A(Dhp) was synthesized *in vivo* using a polycistronic plasmid coding for both eIF5A(Lys) and DHS.[187] eIF5A(Dhp) and eIF5A(Lys) were expressed and purified using ion-exchange chromatography as reported recently.[172] eIF5A(Dhp) can also be synthesized *in vitro* analogues were prepared *in vitro* using DHS reaction (Scheme 4.1) following a protocol described elsewhere.[173] By substituting spermidine (Spd) with its derivatives, several eIF5A(Dhp) analogues can also be synthesized. Spermidine

derivatives were provided by Dr. Myung Hee Park and Dr. Jack E. Folk at NIH. Typically, 1 mg eIF5A(Lys) was mixed with 1 mM NAD, 1 mM DTT, 100 ug His-hDHS, and 0.5 mM Spd or Spd analogues in 0.2 M Gly buffer NaOH (pH 9.5). The reaction mixtures were incubated at 37 ^{o}C for 3 h. The solutions were then buffer-exchanged to 50 mM MOPS buffer at pH 7.5. His_6-DHS was purified using Ni-NTA superflow resin (Qiagen) following a standard procedure provided with the product by Qiagen.

eIF5A(Dhp) and its analogues (1 equivalent) were reacted with ~ 40-50 μM hDOHHperoxo in 50 mM MOPS solution at pH 7.5 and 22 ^{o}C. eIF5A(Dhp) was also reacted with hDOHHperoxo at pH 6.0 (50 mM MES). The UV/Vis spectrum of the reaction solution was monitored using an diode-array spectrometer. The decay rate of hDOHHperoxo was reported based on A_{630}.

eIF5A(Dhp), its analogues, and their DOHH-oxidized products were precipitated with 10% trichloroacetic acid and hydrolyzed with 6 N HCl at 110 ^{o}C overnight. The hydrolysates were dried using a SpeedVac system. The remaining dried solids were redisolved in HPLC water for further analysis. Ion-exchange chromatography using *o*-phthaldialdehyde derivatization was carried out by Dr. Myung Hee Park as described elsewhere.[137] Hydrophilic interaction liquid chromatography (HILIC) coupled with ESI mass spectrometric detection was carried out using a Bruker microOTOF-Q by Dr. Joseph Dalluge in the Mass Spectrometry Laboratory, Department of Chemistry, University of Minnesota.

Intact protein solutions were also analyzed with reverse phase HPLC by Dr. Dalluge using a Water Acquity UPLC/TQD system equipped with triple quadrupole mass

spectrometric detection. A standard C18 columns was used with acetonitrile mobile phase containing 0.1% HCOOH. 5 μL aliquots of ~ 1 mg/mL protein solutions were injected.

4.2.6. Mössbauer spectroscopy

Holo ^{57}Fe-hDOHHperoxo was prepared as previously described,[16] and exchanged into buffer solutions at pH 6.5, 7.5, and 9.5. The samples at pH 6.5 and 9.5, ~ 0.1 mM each, were incubated at 37 ^{o}C until A_{630} reached a minimum values. The sample at pH 7.5 was reacted with ~ 1 equivalent of eIF5A(Dhp) (~ 0.1 mM final concentration) at 37 ^{o}C until A_{630} reached a minimum value. All samples were then concentrated to ~ 0.5 mM protein (~ 1.0 mM in [Fe]), and frozen in Mössbauer cups. Mössbauer spectroscopy was performed by Dr. Mrinmoy Chakrabarti in the laboratory of Professor Eckard Münck at Carnegie Mellon University, following a procedure described in Chapter 2.

4.3. Results

4.3.1. Formation of hDOHHperoxo

Fig. 4.1 illustrates the purification of hDOHH using GSH-Sepharose affinity resin. The colorless resin bound GST-tagged hDOHH (or GST-hDOHH) and turned blue upon washing with air-saturated buffer (columns 1 and 2). When the protein bound columns were washed with anaerobic buffer, they remained colorless and only turned blue when washed with aerobic buffer (columns 3 and 4). These results demonstrate that hDOHH was expressed in a reduced form in the expression cells and reacted with O_2 to form hDOHHperoxo during purification. Tag-free hDOHH was then cleaved off the

columns using thrombin. hDOHH isolated from affinity columns contains a mixture of hDOHHperoxo and other forms of hDOHH as shown by size-exclusion chromatography and designated as as-isolated hDOHH. The pure hDOHHperoxo form can be isolated from this mixture using either native gel electrophoresis[136] or preparative size exclusion chromatography as described in previous chapter, which is designated as holo hDOHHperoxo.

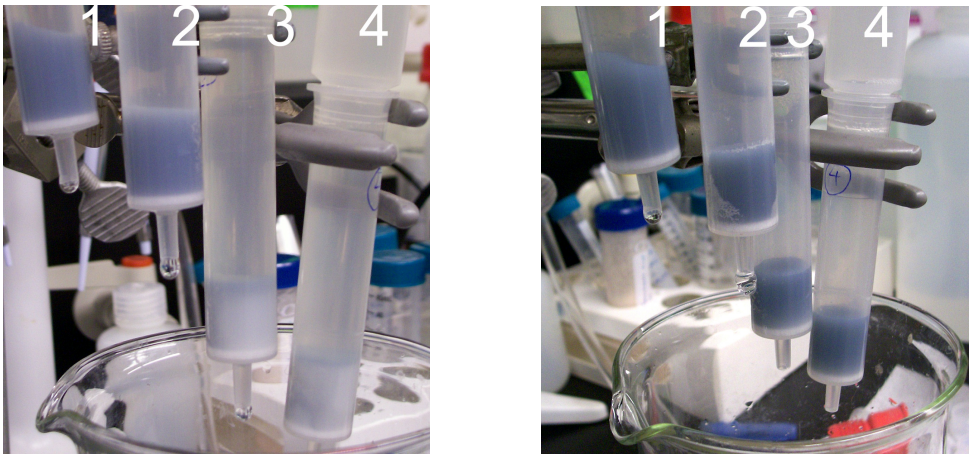

Figure 4.1. Purification of hDOHH with GSH-Sepharose affinity resin. Columns 1 and 2 were washed with air-saturated buffer, while column 3 and 4 were first washed with anaerobic buffer (left panel) followed by air-saturated buffer (right panel).

Fig. 4.2 shows the spectra of hDOHH in various forms. Treatment of holo hDOHHperoxo (blue trace, left panel) with ~ 2 equivalents of dithionite resulted in a colorless solution (black trace). Exposing this solution to the air without any sample workup steps regenerated hDOHHperoxo at 80% yeild (long dashed green trace). The addition of excess ascorbate to the solution increases the absorption at 630 nm to the value found for the initial holo hDOHHperoxo sample, but at the same time decreases the aborption at ~ 320 nm (short dashed red trace). The same ~ 20 % increase in the

absorption at 630 nm was also observed upon the addition of ascorbate to an as-isolated hDOHH sample (left panel). The reaction of a solution containing iron(II) and excess ascorbate with O_2 results in a purple solution with λ_{max} ~ 520 nm and ε ~ 0.6 mM (Fig. 4.2, left panel). The addition of excess ascorbate to an iron(III) solution leads to a similar result, which is significantly different from the more intense absorption at 630 nm (ε = 2.8 mM) of hDOHHperoxo. The absorption at 520 nm did not increase when ascorbate was added to re-oxidized hDOHH and as-isolated hDOHH solutions. Thus, the increase in absorption at 630 nm to the expected value for stoichimetric reaction of reduced hDOHH with O_2 (Fig. 4.2, left panel inset) upon the addition of ascorbate to oxidized hDOHH can be attributed to hDOHHperoxo.

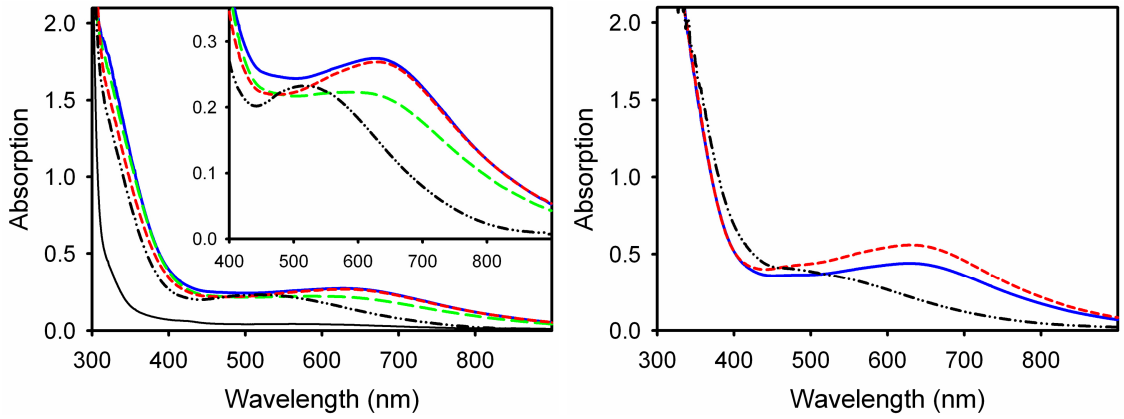

Figure 4.2. UV/vis spectra of hDOHHperoxo in various forms at pH 8.2. **Left panel**: ~ 0.1 mM holo hDOHHperoxo (——) was reduced with 2 equivalents of dithionite (——), which was then completely reacted with O_2 (— —) before 5 mM ascorbate was added (----). A solution containing ~0.36 mM $Fe(NH_4)_2(SO_4)_2$ and 5 mM ascorbate was exposed to the air ~ 1 minute (—••—). **Right panel**: ~ as-isolated hDOHH solution containing ~ 0.2 mM hDOHHperoxo (——) was mixed with 5 mM ascorbate (----). An $FeCl_3$ solution was mixed with 5 mM ascorbate 1 minute (—••—).

.

The above results indicate that the reaction of reduced hDOHH with O_2 always leads to ~ 20 % side product in addition to the main product hDOHHperoxo. The side product is presumably monomeric high spin iron(III) as observed by EPR and Mössbauer spectroscopies at similar yields in multiple samples. This side product appears to be scavenged by ascorbate to form hDOHHperoxo. Further experiments are required to confirm this interpretation as well as to understand why A_{320} decreases upon the addition of ascorbate to re-oxidized hDOHH sample.

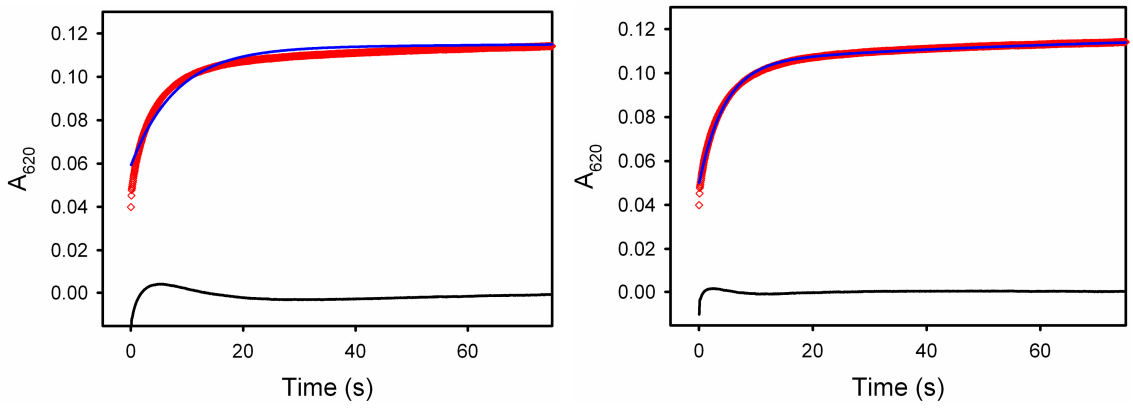

Figure 4.3. Formation kinetics of hDOHHperoxo from the reaction of reduced hDOHH with O_2-saturated buffer solution (1:1 mixing) at 4 ^{o}C, pH 7.5. Data is displayed with red diamonds, fit with blue line, and residual with black line. Fits to the data with two and three exponential growth step are shown on the left and right, respectively.

As the formation of hDOHHperoxo from the reaction of reduced hDOHH with O_2 occurs within minutes, UV/Vis-detected stopped-flow techniques were utilized to study this reaction. Preliminary stopped-flow result is shown in Fig. 4.3. The absorption at 620 nm increases faster within the first 20 seconds and more slowly after 20 seconds and does not reach the maximum even after 10 minutes. The kinetic curves can be fitted with a

triple exponential growth function, with rate constant of ~ 0.226 s^{-1}, 0.0217 s^{-1}, and 0.0147 s^{-1}. The use of a double exponential growth function fails to simulate the data. The formation of hDOHHperoxo is about 100 – 1000 times slower than that found for MMOHperoxo and other peroxo intermediates.[2] Furthermore, the yield of hDOHHperoxo in stopped-flow experiment is only ~ 50% of the expected value. This result, consistent with the above observation that only 80% of hDOHHperoxo was regained in re-oxidation experiments, suggests that hDOHH does not tightly bind Fe(II) and a fraction of Fe(II) was lost during sample work up for the stopped-flow experiments.

4.3.2. pH-Dependent reaction of hDOHHperoxo

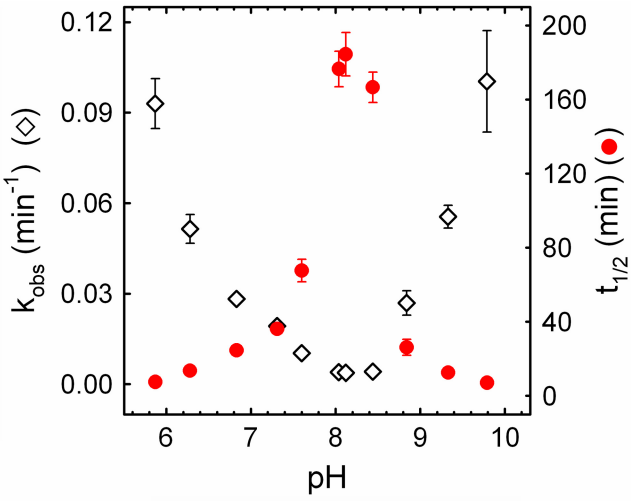

Figure 4.4. pH dependent self-decay of hDOHHperoxo at 37 °C. pH was measured at 37 °C. k_{obs} is displayed with open diamonds (◇) and $t_{1/2}$ with filled red circles (●).

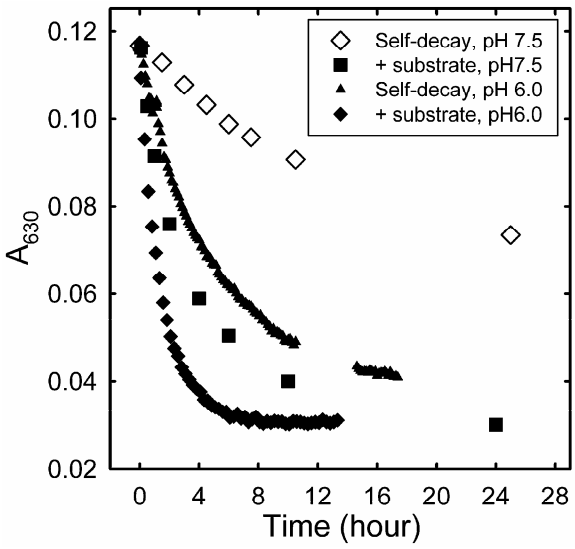

Figure 4.5. Self-decay and reaction of hDOHHperoxo with 1 equivalent of eIF5A(Dhp) at 22 ^{o}C and pH's 6.0 and 7.5.

Fig. 4.4 shows the pH dependence of self decay of hDOHHperoxo at 37 ^{o}C monitored by its characteristic absorption at 630 nm. In the pH range of 5.8 – 8.2, the self-decay rate of hDOHHperoxo decreases as the pH increases. In contrast, when pH > 8.2, increasing the pH lowers the self-decay rate of hDOHHperoxo. This result suggests that there are probably two different decay mechanisms for hDOHHperoxo. In addition, hDOHHperoxo is most stable at pH ~ 8.2.

A preliminary study in D_2O solution at pD 6.7 (pH 6.3) provides a kinetic solvent isotope effect (KSIE) of ~ 1.6. The inverse effect of pH on the decay rate of hDOHHperoxo and KSIE indicate that hDOHHperoxo self-decay is proton dependent at pH < 8.2. Because the amount of eIF5A(Dhp) substrate was limited, reaction of hDOHHperoxo with 1 equivalent of substrate was carried out at pH's 7.5 and 6.0 (Fig. 4.5) instead of in the whole possible pH range. The addition of eIF5A(Dph) significantly enhances the decay rate of hDOHHperoxo at both pH's 6.0 and 7.5. eIF5A(Hpu) product

was previously observed to form to ~ 100% yield at a rate similar to the decay rate of hDOHHperoxo at pH 7.5.[16] These results clearly demonstrate that the enhancement of decay rate by the substrate is associated with substrate oxidation, which is very likely to involve O-O bond cleavage to generate a substrate-hydroxylating species. The effect of substrate on the decay rate of hDOHHperoxo at pH 6.0 is also expected to happen in the same manner as that at pH 7.5. Although more studies are needed, it is clear that the activation of hDOHHperoxo requires a proton transfer step as observed previously for MMOHperoxo.[88, 89]

Mössbauer analysis has been carried out (by Dr. Mrinmoy Chakrabarti in the laboratory of Professor Eckard Münck at Carnegie Mellon University) for the decayed hDOHH obtained from the reaction of hDOHHperoxo with ~ 1 equivalent of eIF5A(Dhp) (Fig. 4.6)). The spectrum in Fig. 4.3 is simulated with 55% of a diamagnetic species (δ = 0.48 mm/s and ΔE_Q = 0.70 mm/s) and ~ 20 % of unreacted hDOHHperoxo. The rest of a sample is ~ 15% monomeric high-spin iron(III) as typically found in all hDOHH preparations. The Mössbauer parameters of the main species in the decayed hDOHHperoxo samples are consistent with high spin iron(III) centers that are antiferromagnetically coupled to give a diamagnetic ground state. Preliminary variable field variable temperature analysis reveals an exchange coupling constant J ~ 15 cm^{-1} for this species. Mössbauer results indicate that hDOHHperoxo reacts with substrate to yield a (μ-hydroxo)diiron(III) species as observed for MMO. This species is designated as hDOHHmet.

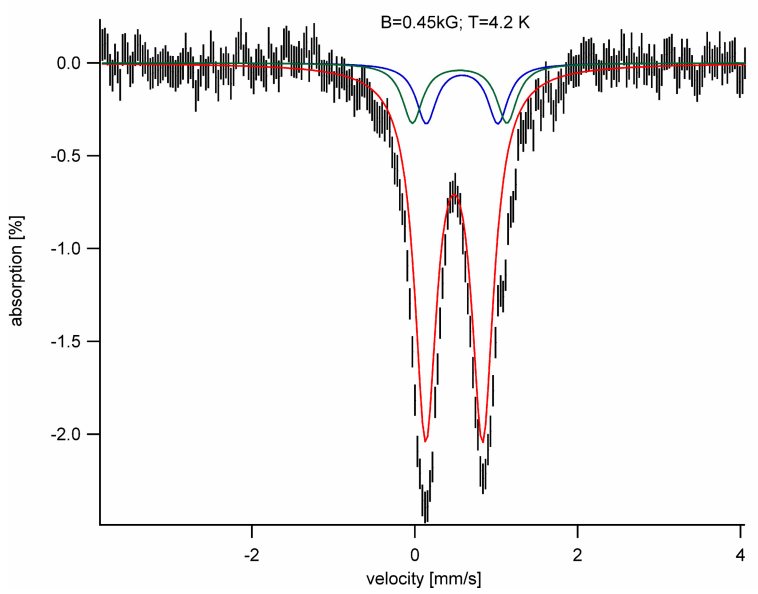

Figure 4.6. Mössbauer spectrum of hDOHHperoxo reacted with ~ 1 equivalent of eIF5A(Dhp).

Mössbauer analysis also shows that the self-decay of hDOHHperoxo at pH 6.5 resulted in a sample containing ~ 50 % of a species similar to hDOHHmet and ~ 50% monomeric high-spin iron(III). In contrast, decayed hDOHH sample at pH 9.5 contains ~ 100 % monomeric high-spin iron(III). Consistent with the pH-dependent study, this result leads us to propose that there are two different decay pathways for hDOHHperoxo. One of the pathways involves O-O bond cleavage and results in the formation of a (μ-hydroxo)diiron(III) species. This pathway is preferred in the presence of substrate and/or at pH lower than 8.2. The other pathway occurs at pH higher than 8.2 and leads to uncoupled high spin iron(III) centers, which probably involves peroxo substitution rather than O-O bond cleavage.

4.3.3. Analytical size-exclusion chromatography

It has been shown previously by native gel electrophoresis[136] and small angle X-ray scattering (SAXS)[174] that that apo hDOHH is significantly larger and more flexible than holo hDOHHperoxo. The formation of monomeric iron(III) species in the self-decay of hDOHHperoxo, as well as the unusually slow rate of hDOHHperoxo formation led us to postulate that similar structural change may also occur upon reduction or decay of hDOHHperoxo. We thus utilized size-exclusion chromatography (SEC) to study the reaction of hDOHHperoxo (Fig. 4.7). The holo hDOHHperoxo chromatogram exhibits a sharp peak at t_R = 5.11 minutes (FWHM = 0.17 minutes), while the apo hDOHH chromatogram show a broader peak at t_R = 4.92 minutes (FWHM = 0.36 minutes), consistent with previous native gel electrophoresis and SAXS studies.[136, 174]

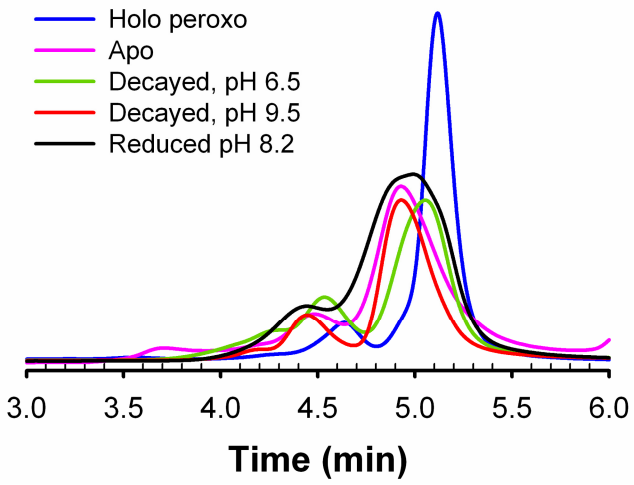

Figure 4.7. Size-exclusion chromatographic analysis of hDOHH in various forms. All traces are aligned to the peak of the internal standard phthalic acid at t_R = 6.56 minutes (see Fig. 4.8).

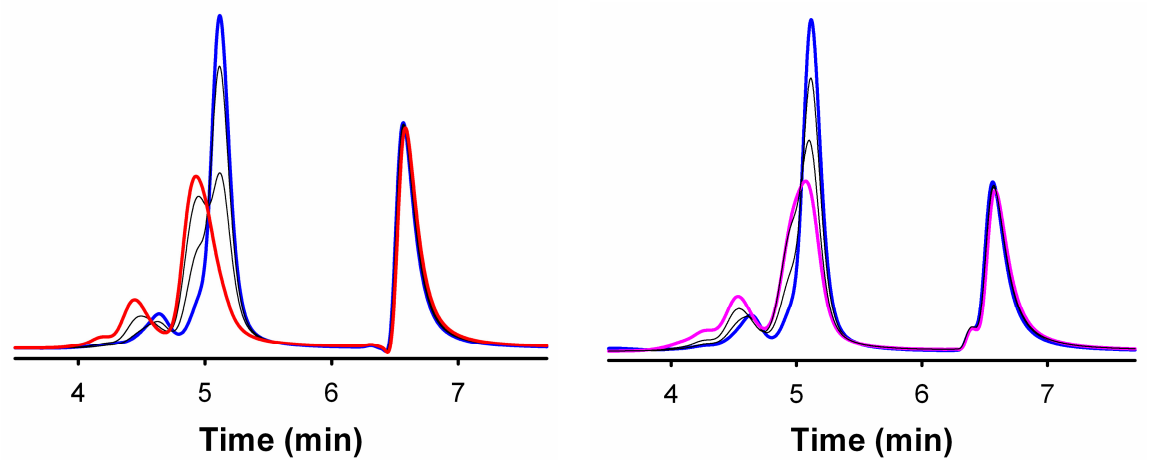

Figure 4.8. Size-exclusion chromatographic analysis of the self-decay of hDOHHperoxo at pH 9.5 (left) and pH 6.5 (right). The peak at t_R = 6.56 minutes correspond to the phthalate standard.

At pH 9.5, the sharp peak corresponding to holo hDOHHperoxo decays to a much broader peak that is similar to that of apo hDOHH at t_R = 4.92 minutes (FWHM = 0.27 minutes) (Figs. 4.7 and 4.8). This result shows that at pH > 8.2, there is a significant conformational change upon hDOHHperoxo decay that separates the iron centers apart to form 100 % monomeric high spin (III). At pH 6.5, decayed hDOHHperoxo also exhibits a broader peak but at t_R = 5.05 minutes (FWHM = 0.28 minutes). It is likely that at pH < 8.2 a portion of hDOHH undergoes the same conformational changes to result in monomeric high spin iron(III) species, while the rest remains intact to form the putative (μ-hydroxo)diiron(III) species.

The chromatogram of reduced hDOHH exhibits a very broad peak centered near t_R = 4.98 minutes (FWHM = 0.51 minutes). This retention time and large peak width indicates that there are even more conformations adopted by reduced hDOHH than by apo hDOHH. One rationale for this observation is that upon reduction of hDOHHperoxo,

iron(II) partially dissociate from the protein. The portion of hDOHH that loses iron(II) become apo hDOHH, while the rest that binds iron adopts a conformation with smaller size. This model is consistent with the studies on the formation of hDOHHperoxo (*vide supra*). Iron dissociation from active site upon reduction may result in lower hDOHHperoxo yield upon reoxidation of reduced hDOHH (80%) expected). Sample work up resulted in an even greater loss of iron as only ~ 50% of hDOHHperoxo was regained. The reaction of O_2 with reduced hDOHH solution may involve an equilibrium between apo and iron(II)-bound hDOHH, as well as a conformational change, which slows down the formation of hDOHHperoxo.

4.3.4. Reaction of hDOHHperoxo with substrate analogues

Fig. 4.8 shows the substrate analogues that have been successfully synthesized and their reaction with ~ 1 equivalent of hDOHHperoxo. The substrate analogues and their hDOHH-oxidized products were quantified using ion-exchange HPLC by Dr. Myung Hee Park (Table 4.1) and verified with HILIC LC/MS after hydrolysis with 6 N HCl. The acronyms for the substrates are provided in the footnote of Table 4.1. The relative yields of DOHH products in Table 4.1 are consistent with the kinetics traces in Fig. 4.8. eIF5A(d^8-Dhp) and eIF5A(trans=Dhp) reacts with hDOHHperoxo at rates comparable to that found for the native eIF5A(Dhp) substrate. eIF5A(Lys) and other substrate analogues have negligible effects on the decay rate of hDOHHperoxo.

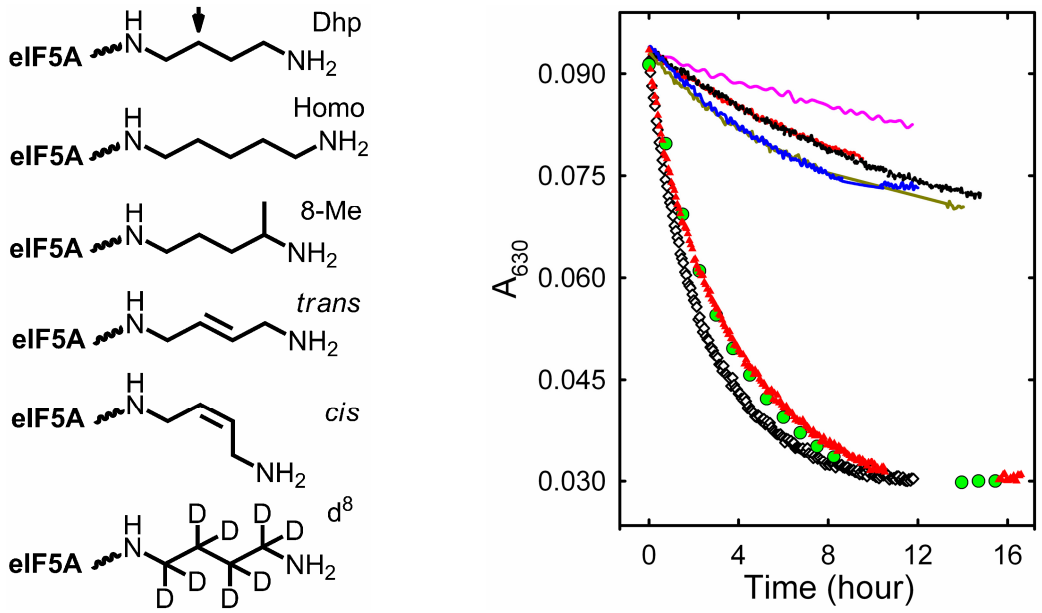

Figure 4.9. Reaction of hDOHHperoxo with ~ 1 equivalent of eI5A(Lys), eIF5A(Dhp), and eIF5A(Dhp) analogues (shown on the right). Legends: self-decay (—), reaction with eIF5A(Lys) (—), eIF5A(HomoDhp) (----), eIF5A(8Me-Dhp) (—), eIF5A(cis=Dhp) (—), eIF5A(trans=Dhp) (●), eIF5A(d8-Dhp) (▲), and eIF5A(Dhp) (◇).

Hypusine, Hpu, was detected at m/z = 234.2 (M+H) unit as predicted based on its molecular formula. This mass shifted to 236.2 when hDOHHperoxo was labeled with $^{18}O_2$, but remained the same when the DOHH reaction was carried out in $H_2{}^{18}O$. Deuterated d^7-Hpu was detected at m/z 241.2. Consistent with ion exchange HPLC and kinetic results, the DOHH product with 8Me-Dhp, HomoDhp, and cis=Dhp were not detected with HILIC LC/MS. The oxidation product of trans=Dhp analogues was observed at 250.2 m/z, which is consistent with the addition of two OH groups (diol) but not an oxide group (epoxide). However, this result does not necessarily reflect the nature of the DOHH-oxidized product of eIF5A(trans=Dhp). Because the sample hydrolysis was carried out in 6 N HCl solution at 110 ^{o}C, if an epoxide product was formed, it would have be hydrolyzed to form the corresponding diol product.

Table 4.1. Ion exchange HPLC and HILIC LC/MS analysis of DHS and DOHH products digested with 6 N HCl at 110 ^{o}C

Spd analogues	DHS products	Relative yield	M+H (m/z)	DOHH products	Relative yield	M+H (m/z)
Spd (3,4)	Dhp	++++	218.2	Hpu	++++	234.2
				$^{18}O_2$		236.2 (85%) 234.2 (15%)
				$H_2{}^{18}O$		234.2 (100%)
d8-Spd (3,4)	d^8-Dhp		226.2	d^7-Hpu		241.2
Cis=Spd (3,4)	cis=Dhp	++	216.2	Cis=Dhp[O]	+-	216.2$^{\$}$
Trans=Spd (3,4)	trans=Dhp	+++	216.2	trans=Dhp[O]	+++	250.2
Caldene (3,3)	norDhp	++	*	norDhp[O]	-	*
8Me-Spd (3,Me4)	8Me-Dhp	++	232.2	8Me-Dhp[O]	+-	232.2$^{\$}$
ApCad (3,5)	homoDhp	+++	232.2	homoDhp[O]	+-	232.2$^{\$}$

*Neither reacted with hDOHH nor analyzed with LC/MS. $^{\$}$Unreacted.
Spd: spermidine, $NH_2(CH_2)_3NH(CH_2)_4NH_2$. **$d^8$-Spd**: $NH_2(CH_2)_3NH(CD_2)_4NH_2$.
Cis=spd and **trans=Spd**: *cis/trans*-$NH_2(CH_2)_3NH$-CH_2CH=$CHCH_2NH_2$. **Caldene**: $NH_2(CH_2)_3NH(CH_2)_3NH_2$.
8Me-Spd: $NH_2(CH_2)_3NH(CH_2)_3CH(CH_3)NH_2$. **ApCad(3,5):** $NH_2(CH_2)_3NH(CH_2)_5NH_2$.
Dhp: deoxyhypusine, $HC(CO_2H)(NH_2)(CH_2)_4NH(CH_2)_4NH_2$.
Cis/trans=Dhp: *cis/trans*= $HC(CO_2H)(NH_2)(CH_2)_4NH$ CH_2CH=$CHCH_2NH_2$.
NorDhp: $HC(CO_2H)(NH_2)(CH_2)_4NH(CH_2)_3NH_2$. **8Me-Dhp**: $HC(CO_2H)(NH_2)(CH_2)_4NH(CH_2)_3CH(CH_3)NH_2$.
HomoDhp: $HC(CO_2H)(NH_2)(CH_2)_4NH(CH_2)_5NH_2$.
Hpu: hypusine, $HC(CO_2H)(NH_2)(CH_2)_4NHCH_2CH(OH)CH_2)_2NH_2$.
d^7-Hpu: $HC(CO_2H)(NH_2)(CH_2)_4NHCD_2CD(OH)CD_2)_2NH_2$
trans=Dhp[O]: $HC(CO_2H)(NH_2)(CH_2)_4NH$ CH_2-(C_2H_2O)-CH_2NH_2 or $HC(CO_2H)(NH_2)(CH_2)_4NHCH_2(CHOH)_2$ CH_2NH_2. Other DOHH-oxidized products were not detected.

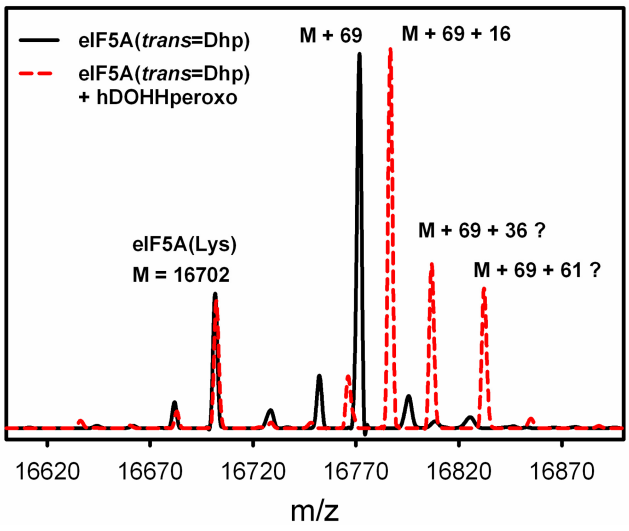

Figure 4.10. ESI-MS spectra of eIF5A(trans=Dhp) synthesized from the DHS reaction and its DOHH-oxidized product.

To examine the nature of DOHH-oxidized product of eIF5A(trans=Dhp), we analyzed the intact protein with reverse phase LC/MS. Fig. 4.9 shows the mass spectra of eIF5A(trans=Dhp) synthesized using the DHS reaction and its DOHH-oxidized product. Both spectra exhibit a peak at 16702 m/z that corresponds to unmodified eIF5A(Lys). The major peak in the spectrum of eIF5A(trans=Dhp) is at 69 mass units higher than that of eIF5A(Lys), confirming the formation this analogue (Fig. 4.8). After the reaction with hDOHHperoxo, this M+69 m/z peak disappeared, and a new peak appeared at M + 85 m/z, which is consistent with the introduction of one oxygen atom to the eIF5A(trans=Dhp) substrate. This peak is attributed to an epoxide product, which is designated as eIF5A(DhpO). Because eIF5A(trans=Dhp) and eIF5A(DhpO) have the same charge, and their mass and overall structures are almost identical are, they are expected to fly similarly well in the MS detector. Because the peak intensity ratio of M+69:M is similar to that of M+85:M, the conversion of eIF5A(trans=Dhp) to its epoxide product is estimated to be quantitative. There are two additional significant peaks at M+105 m/z and M+130 m/z in the spectrum of the DOHH reaction sample. The M+105 m/z peak is close to the expected mass for a diol product (M+103 m/z) (resolution ~ 2 m/z). Because the DOHH reaction was carried out in slightly basic solution (pH 7.5) and the LC/MS method was run with ~ 0.1% HCOOH solution, a part of the epoxide product could potentially be hydrolyzed to form a the diol product. More studies are required to identify this M+105 m/z peak, as well as the M+130 m/z.

4.4. Discussion

Scheme 4.2. Proposed working model for hDOHH.

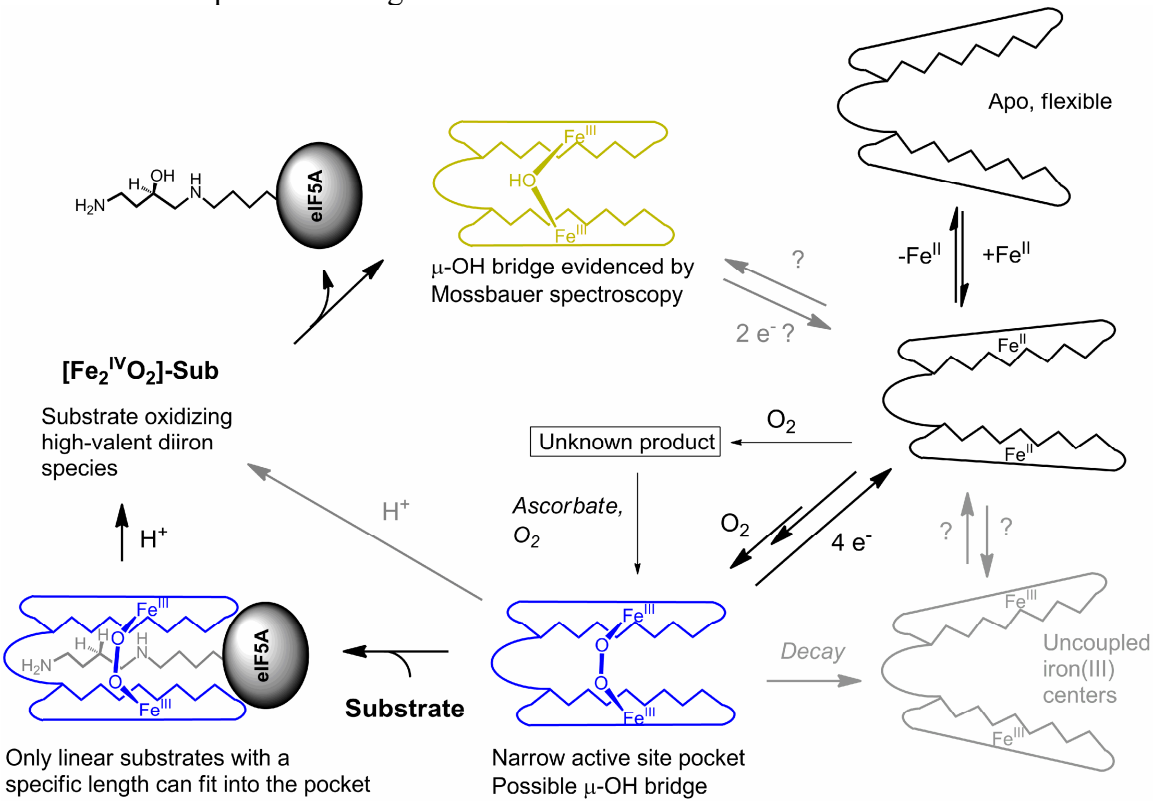

The results obtained from this study have allowed us to propose a mechanism of hDOHH for the first time, which is shown in Scheme 4.2. Unlike other diiron enzymes, the best characterized form of hDOHH is hDOHHperoxo, which serves as a focal point in Scheme 4.2. The reaction of reduced hDOHH with O_2 to form hDOHHperoxo occurs in multiple steps, which is overall about 100-1000 time slower than that in other diiron enzymes. This slow formation of hDOHHperoxo can be attributed to the low iron(II) affinity of apo hDOHH as well as a requirement for significant entropy-disfavored

conformational changes to assemble hDOHHperoxo. The low iron affinity results in ~ 20% of side product in the reaction of reduced hDOHH with O_2. This side product can be scavenged to the peroxo form by ascorbate, a physiologically relevant reductant.

The reaction of hDOHHperoxo depends on pH. At pH > 8.2, hDOHH decays, presumably via peroxo displacement, to form monomeric iron(III) species. Proton transfer occurs at pH < 8.2 to assist O-O bond cleavage, generating substrate-oxidizing species. At pH < 8.2, hDOHHperoxo decays or reacts with its substrate to form a (μ-hydroxo)diiron(III) species as observed for MMO and other diiron enzymes. A negligible substrate H/D kinetic isotope effect is observed, indicating that C-H bond cleavage is not the rate determining step. It has been shown previously that holo hDOHH binds eIF5A(Dhp) tightly so that their complex can be pulled out of the solution using an affinity resin.[175] Thus, given the unusual stability of hDOHHperoxo, O-O bond cleavage is probably the rate determining step.

Several substrate analogues with very slightly different sizes and shapes were reacted with hDOHHperoxo. eIF5A(HomoDhp) contains one more CH_2 group on the side chain, while eIF5A(8Me-Dhp) is branched at the terminal position (Fig. 4.8). Both of these two analogues fail to enhance the decay rate of hDOHHperoxo. Surprising is the inability to promote hDOHHperoxo decay by eIF5A(cis=Dhp), which has the same length as that of the native substrate but with a double bond at the oxidation site (Fig. 4.8), while its *trans* counterpart reacts at the same rate as the native substrate does. This result suggests that the active site of hDOHHperoxo, once assembled, is very well constructed in a way that only linear substrates with a specific length can fit in (Scheme 4.2), which contributes to the strict stereospecificity of hDOHH.

LC/MS on intact protein shows that hDOHHperoxo is involved in the epoxidation C=C double bond, which has also been observed for MMOHperoxo and model complexes. More importantly, as hDOHH stereospecifically hydroxylates eIF5A(Dhp) (Scheme 4.1 and Scheme 4.3), it is also expected to produce only one isomer of eIF5A(DhpO) (Scheme 4.3). The hydroxyl group on the Dhp moiety of eIF5A(Dhp) has been proposed to properly position tRNA and ribosome in their complex via a hydrogen bonding network, which is required for the formation of first peptide bond,[134] as well as for translation elongation.[135] Similar studies on the epoxide analogue of eIF5A(Dhp) could provide valuable information on the role of hypusination of eIF5A on translation.

Scheme 4.3. Proposed mechanism that leads to the stereospecificity of hDOHH.

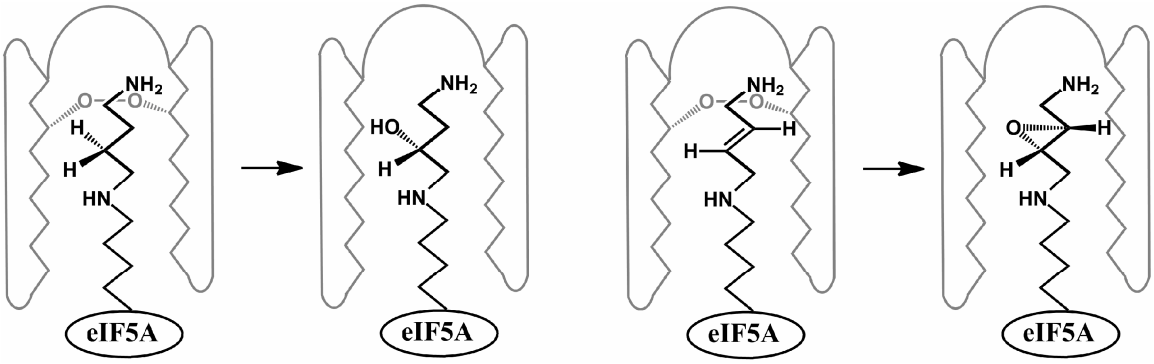

Dedication note: I would like to dedicate this work to Dr. Jack E. Folk (NIH), who passed away in December 2010. I deeply thank him for generously providing us with the spermidine derivatives, which were crucial for this study.

Chapter 5

Characterization of a novel peroxodiiron(III) intermediate of an amine N-oxygenase in the biosynthesis pathway of chloramphenicol

5.1. Introduction

The core geometry of the peroxo intermediate very likely governs its activation, i.e. O-O bond cleavage, as well as its reactivity. Most of the peroxo intermediates of diiron enzymes and model complexes exhibit cis-μ-1,2-peroxo geometry.[16, 77, 78, 81, 83, 108, 109] This geometry is proposed to be the most stable form of a peroxo-bridged diiron(III) cluster, and isomerization to a more activated geometry is necessary for O-O bond cleavage.[87, 162] Studies of hDOHHperoxo and model complexes proposed that introducing a single atom bridging ligand would further stabilize the cis-μ-1,2-peroxo core.[16]

While the terminal η^2-peroxo binding mode has been observed for monoiron species,[108, 176-179] the μ-η^1:η^2 and μ-η^2:η^2 geometries have not been observed for any (μ-peroxo)diiron(III) intermediate. In contrast, the μ-η^2:η^2 geometry, which was once overlooked, is not uncommon in both dicopper enzymes and model complexes.[180, 181] In iron-heme copper model complexes, several iron(III)-peroxo-copper(II) intermediates have been characterized spectroscopically, and even crystallographically.[133] In these intermediates, the peroxo binds η^2 to the iron(III) center and either η^1 or η^2 to the copper(II) center. This suggest that a (μ-η^1:η^2-peroxo)diiron(III) cluster or (μ-η^2:η^2-peroxo)diiron(III) cluster may be feasible.

In both diiron enzymes and model systems, the cis-μ-1,2-peroxo intermediates contain high-spin iron(III) centers and exhibit a broad UV/Vis absorption feature with λ_{max} > 600 nm and ε > 1,000 $M^{-1}cm^{-1}$.[16, 77, 78, 81, 83, 108, 109] This feature is attributed to the peroxo-to-iron(III) charge transfer transition as evidenced by extensive resonance Raman studies. Recently, two new peroxodiiron(III) species have been observed, which are

spectroscopically different from the usual (μ-1,2-peroxo)diiron(III) species.[90, 103] The first species is the colorless ToMOperoxo with a Mössbauer isomer shift δ of 0.55 mm/s and a quadupole splitting ΔE_Q = 0.67 mm/s ,[90] which are smaller than the corresponding values (δ > 0.63 mm/s and ΔE_Q > 1.00 mm/s) of the colored (μ-1,2-peroxo)diiron(III) intermediates of other diiron enzymes.[16, 77, 78, 81, 83, 108, 109] The other species is AurFperoxo that also has small an isomer shifts and quadrupole splittings but exhibits a weak broad UV/Vis feature at 500 nm (ε = 500 $M^{-1}cm^{-1}$).[98] The spectroscopic properties of ToMOperoxo and AurF peroxo suggest that these two species may differ structurally from the more common (μ-1,2-peroxo)diiron(III) intermediate. However, as vibrational data for the Fe_2O_2 cores in these two intermediates have not been obtained, the definitive proof for the nature and the geometry of these putative peroxo species is still missing.

Scheme 5.1. The biosynthesis pathway of chloramphenicol

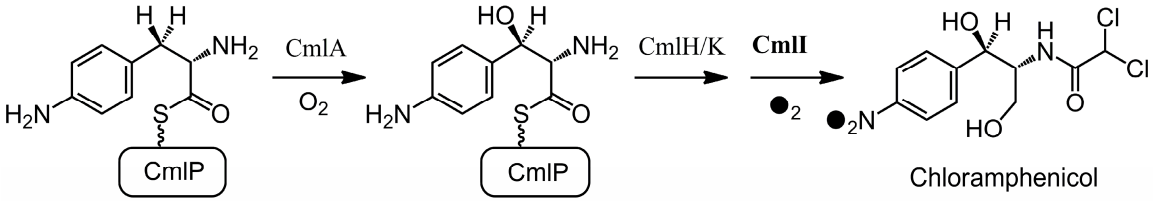

Here, in collaboration with Dr. Thomas M. Makris and Professor John D. Lipscomb at the University of Minnesota, we report the resonance Raman study of a putative peroxo intermediate of CmlI, a homolog of AurF that is involved in the biosynthesis of chloramphenicol (Scheme 5.1).[104] CmlIperoxo forms in the reaction of reduced CmlI with O_2 and exhibits a similar UV/Vis feature as that of AurFperoxo.

Compared to AurFperoxo, CmlIperoxo is relatively stable at room temperature ($t_{1/2}$ ~30 mins) and decays to the diferric resting state with different UV/Vis features.[104] The stability of the CmlIperoxo chromophore enabled us to obtain its resonance Raman spectrum in solution, which clearly shows a peroxo binding geometry significantly different from the cis-1,2-peroxo geometry commonly found for the peroxo intermediates of canonical diiron enzymes with 2-His-4-carboxylate ligand sets. The difference may arise from an additional His ligand in CmlI, deduced from EXAFS and sequence homology analyses,[104] which may cause the shift in peroxo binding geometry of CmlIperoxo.

5.2. Experimental

5.2.1. X-ray absorption spectroscopy of oxidized CmlI at pH 7.0

CmlI was originally cloned and purified by Dr. Thomas M. Makris in the laboratory of Prof. John D. Lipscomb at the University of Minnesota. 2 mM CmlI (4 mM in [Fe]) in 200 mM HEPES pH 7.0 solution containing 10% glycerol was frozen in tandem Mossbauer/XAS cups. XAS data (8 scans, one on each sample spot) were collected on beamline 9-3 at Stanford Synchrotron Radiation Lightsource (SSRL) of the SLAC National Accelerator Laboratory. Further details on data collection and analysis are provided in Supporting Information.

5.2.2. Resonance Raman spectroscopy

CmlIperoxo was prepared by Dr. Thomas M. Makris.[104] In resonance Raman experiments, as isolated CmlI (2 mM (4 mM in [Fe]) in 50 mM Bicine at pH 9.0) was

reduced under anaerobic conditions with an excess amount of dithionite in the presence of 0.1 equivalent of methylviologen. Excess reductant and methylviologen were removed using a PD-10 desalting column (G-25, GE Healthcare) in an anaerobic chamber. (*Note: It is important to remove methylviologen because it can be photoreduced by the excitation laser as previously reported,[182] which inturn reduces CmlIperoxo*). Aliquots of reduced CmlI from the same batch were exposed to either $^{16}O_2$, $^{18}O_2$, or a mixture containing 25 % $^{16}O_2$, 50 % $^{16}O^{18}O$, and 25 % $^{18}O_2$ at ~ 4 ^{o}C for several minutes. The samples were then snap-frozen with liquid nitrogen and kept at 77 K for future experiments. $^{16}O_2$ and $^{18}O_2$ samples were repeated three times while the mixed lable sample was repeated twice. Multiple measurements were carried out for each sample. For each measurement, a ~ 70 μL aliquot of samples was thawed and transferred to flat-bottomed NMR quartz tubes and maintained at a temperature range of -10^{o}C to 10^{o}C. The isotopically labeled samples were transferred into septum-sealed tubes that were evacuated and equilibrated with argon.

Resonance Raman experiments were performed on an Acton AM-506 spectrophotometer (1,200-groove grating) with a Princeton Instruments LN_CCD-1100-PB_UVAR detector cooled to -120^{o}C with liquid nitrogen. The 488 nm excitation line at 100 – 600 mW power was provided by a Spectra-Physics BeamLok 2060-KR-RS Argon ion laser, which is filtered out by a Kaiser Optical holographic super notch filter. Spectra were collected in 90^{o} scattering geometry at resolution of 4 cm^{-1}, and referenced to indene. Spectra were continuously collected with each spectrum obtained from 80 or 40 accumulations of 15-second exposures (20 or 10 minutes/spectrum). Spectra within desired time range were added to improve the signal-to-noise ratio. Multiple

measurements were performed for each CmlIperoxo sample. GRAMS/AI (Thermo Galactic, Salem, NH) was utilized data processing.

5.3. Results and Discussion

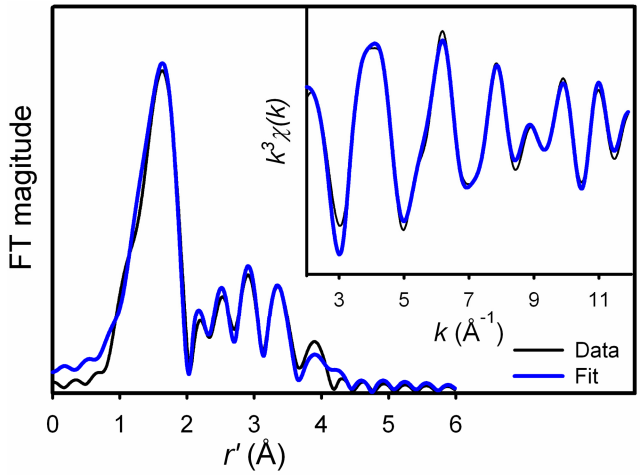

Figure 5.1. Fourier filtered k^3-weighted EXAFS spectrum of CmlI at pH 7.0 and its Fourier transform. k range = 2 – 12 Å^{-1}, back transform range = 0.85 – 4.00 Å, resolution = 0.16 Å. Best fit parameters :1 Fe-O at 1.89 Å, 4 Fe-N/O at 2.06 Å, 2 Fe---C at 3.01 Å, 0.5 Fe at 3.34 Å, 0.5 Fe at 3.59 Å, and 3.5 Fe---His multiple scattering paths at ~ 4.3 Å. See Table S.5.2 for more details.

The pre-edge feature of an oxidized CmlI at pH 7.0 is a doublet with a peak ratio of 1:1.2 and a total intensity of 8.6(4) units (Table S.5.1 and Fig. S.5.1). The observed intensity and peak ratio are consistent with a high-spin iron(III) center with slightly distorted octahedral geometry.[174] Details on EXAFS fitting procedures are provided in Supporting Information. The Fourier-filtered data and best fit results are shown in Table 5.3. The outer shell features at ~ 3.0 and 3.5 Å are simulated with 0.5 Fe---Fe path at 3.34 Å and 0.5 Fe---Fe path at 3.59 Å. The XANES and EXAFS analysis results are consistent

with UV/Vis and Mössbauer analysis that suggests that CmlI exists in a mixture of (μ-oxo)diiron(III) and (μ-hydroxo)diiron(III) forms,[104] which was previously found for Δ^9D.[158] Furthermore, multiple scattering analysis reveals that the diiron cluster of CmlI contains about 3 His ligands, consistent with sequence analysis and models to the crystallographically solved AurF homolog.[104]

Fig. 5.2 shows the resonance Raman spectra of CmlIperoxo prepared with different dioxygen isotopes and the spectrum of decayed CmlIperoxo. The $^{16}O_2$ spectrum exhibits a peak at 791 cm^{-1} that slowly decays over time in ~ 6 – 7 hours at ~ 0 ^oC. The spectra of samples incubated overnight at 4 ^oC are similar to that of the decay trace in Fig. 5.2. In the $^{18}O_2$ spectrum, the 791 cm^{-1} peak has a much weaker intensity and a new peak appears at 747 cm^{-1}. The 791 cm^{-1} and 748 cm^{-1} peaks in the $^{18}O_2$ sample also decay over time and give rise to the spectrum of the decay trace in Fig. 5.2. The 43 cm^{-1} downshift of the 791 cm^{-1} peak is consistent with the value calculated by Hooke's law for an O-O oscillator, indicating that this peak arises from a peroxo moiety. Notably, this is the lowest ν(O-O) frequency observed to date for a peroxodiiron(III) intermediate. In the spectra of samples prepared with this gas mixture (Figs. 5.2 and A.5.5), a new peak appears at 768 cm^{-1}, halfway between the ν(^{16}O-^{16}O) and ν(^{18}O-^{18}O) peaks, which is assigned to the $^{16}O^{18}O$ isotopomer. This ν(^{16}O-^{18}O) peak (FWHM = ~ 14 cm^{-1}) is somewhat broader than the ν(^{16}O-^{16}O) and ν(^{18}O-^{18}O) peaks (FWHM ~ 10 – 11 cm^{-1}) (Table 5.1), suggesting that the two oxygen atoms of the O-O moiety are bound unsymmetrically and are thus inequivalent. There is no other oxygen isotope-sensitive peak observed in the spectral window of 230 – 1360 cm^{-1} (see Supporting Information).

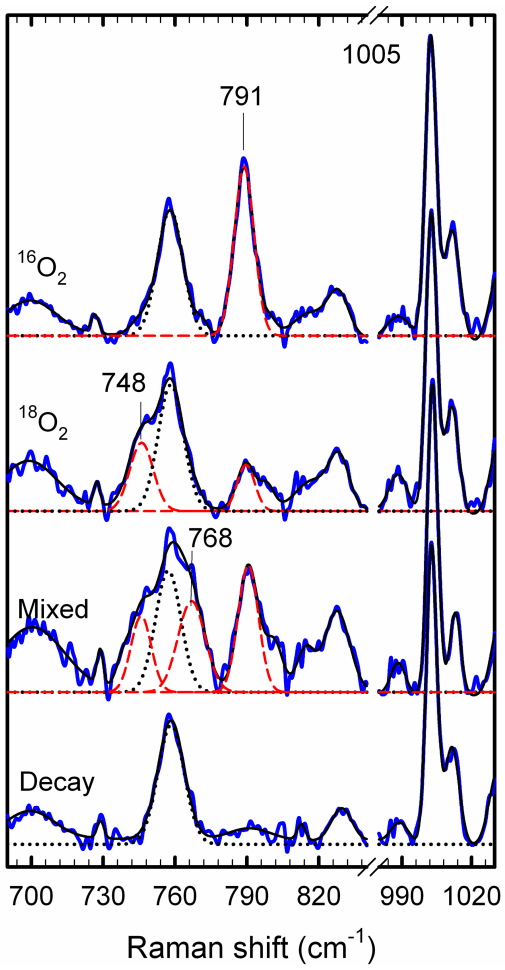

Figure 5.2. Resonance Raman spectra of CmlIperoxo samples prepared with $^{16}O_2$, $^{18}O_2$, 1:2:1 mixture of $^{16}O_2$, $^{16}O^{18}O$, and $^{18}O_2$, respectively, as well as a peroxo decay sample. Spectra were obtained with ~ 200 – 300 mW laser power and subjected to two-point baseline subtraction. No smoothing or zapping was required. Spectra were aligned and normalized based on the sharp peak at 1005 cm^{-1} that arises from phenylalanine residues of the protein. Peak fitting results are provided in Table 5.1.

Table 5.1. Gaussian peak fitting results for CmlIperoxo

Sample	Peak 1 (cm^{-1}) (FWHM (cm^{-1}))	Peak 2 (cm^{-1}) (FWHM (cm^{-1}))	Peak 3 (cm^{-1}) (FWHM (cm^{-1}))	Peak ratio
$^{16}O_2$	791 (9.8)			1:0:0
Mixed label 1*	791 (10.5)	769 (13.6)	747 (10.6)	1.6.:1.5:1
Mixed label 2*	791 (10.1)	768 (14.6)	747 (10.4)	1:1:1.1
$^{18}O_2$	791 (8.7)		748 (11.6)	1:0: 2
Decay	-	-	-	-

* 1:2:1 mixture of $^{16}O_2$, ^{16}O-^{18}O, and $^{18}O_2$. FWHM = Full width at half maximum. Spectra were aligned and normalized to the phenylalanine signal at 1005 cm^{-1}, which are shown in Fig. 5.2 and Fig S.5.5 (mixed label 2). The parameters of the background peak at 758 cm^{-1} were kept the same for all samples (FWHM = 12.5 cm^{-1}, intensity ratio of 1005 cm^{-1} peak: 758 cm^{-1} peak ~ 1.05 – 1.10).

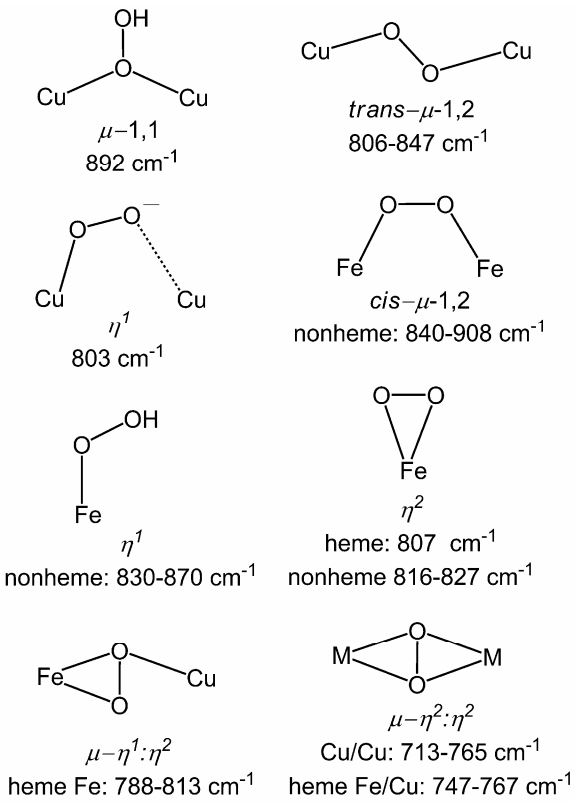

Figure 5.3. ν(O-O) values reported for various mononuclear iron, binuclear copper or iron, and heterobinuclear copper(II)/iron(III) peroxo complexes.[16, 77, 78, 81, 83, 108, 109 133, 177, 179, 181, 184, 185]

Information about the binding geometry of the O-O ligand of CmlIperoxo can be deduced by comparing its vibrational properties and other spectroscopic parameters to those of well characterized systems. Fig. 5.3 shows the ν(O-O) frequencies reported for various binding geometries in iron(III) and copper(II) peroxo clusters. As CmlIperoxo contains high spin iron(III) centers,[104] complexes with low spin iron(III) centers are not considered here. The μ-1,1-OOH geometry can be ruled out for CmlIperoxo because: 1) the ν(O-O), as found for one dicopper complex at 892 cm^{-1}, is much higher than the 791 cm^{-1} ν(O-O) of CmlIperoxo; and 2) this geometry is computationally predicted to be very

reactive.[87, 162] The terminal η^1-O-O$^-$, a possible example of which is tentatively proposed for a dicopper complex in aprotic solvent,[183] is also not feasible for CmlIperoxo in aqueous solution.

The η^1 or μ-η^1:η^1 geometries have the highest ν(O-O) values (830 – 910 cm^{-1}) for peroxo iron complexes. This frequency decreases to 807 – 827 cm^{-1} in (η^2-peroxo)iron(III) complexes. When the η^2 peroxo ligand binds to another metal center, its ν(O-O) further decreases to 788 – 813 cm^{-1} and 713 – 767 cm^{-1} in μ-η^1:η^2 and μ-η^2: η^2 geometries, respectively. The fact that the 791 cm^{-1} ν(O-O) observed for CmlIperoxo is remarkably smaller than those found for η^1 or μ-η^1:η^1 indicates clearly that CmlIperoxo does not possess either of these two geometries for peroxo iron(III) species.

Instead, the ν(O-O) of CmlIperoxo falls in the range found for the μ-η^1:η^2 binding mode. Because the frequency ranges of terminal η^2 and μ-η^1:η^2 peroxo complexes overlap and neither μ-η^1:η^2 nor μ-η^2:η^2 peroxo diiron(III) species have been characterized (Fig. 5.3), we are not able to unequivocally rule out the terminal η^2 and μ-η^2:η^2 modes on the basis of ν(O-O) comparisons. While the ν(Fe-O_2) mode has been observed by resonance Raman spectroscopy for all (η^2-peroxo)iron(III) complexes studied thus far, with intensity equivalent to or much higher than that of the corresponding ν(O-O),[108, 177, 179] ν(Fe-O_2) and ν(Cu-O_2) features are usually not observed for μ-η^1:η^2 and μ-η^2:η^2 peroxo dicopper and copper/iron complexes.[133, 180, 181, 186] It is likely that in these binding modes the excitation into the LMCT band only enhances the O-O bond vibration by removing the electron density from the π^* orbital of the peroxo moiety, while the M-O_2 bonds are not sizably affected.[186] This results in the observation

of the ν(O-O) but not the ν(M-O_2) by resonance Raman spectroscopy. The η^2-peroxo assignment is less preferred for CmlIperoxo because of the absence of a peak corresponding to ν(Fe-O_2) in the resonance Raman spectrum of CmlIperoxo and the fact that the ν(O-O) of CmlIperoxo is more than 20 cm^{-1} lower than the range found for nonheme (η^2-peroxo)iron(III) species (Fig. 5.3).

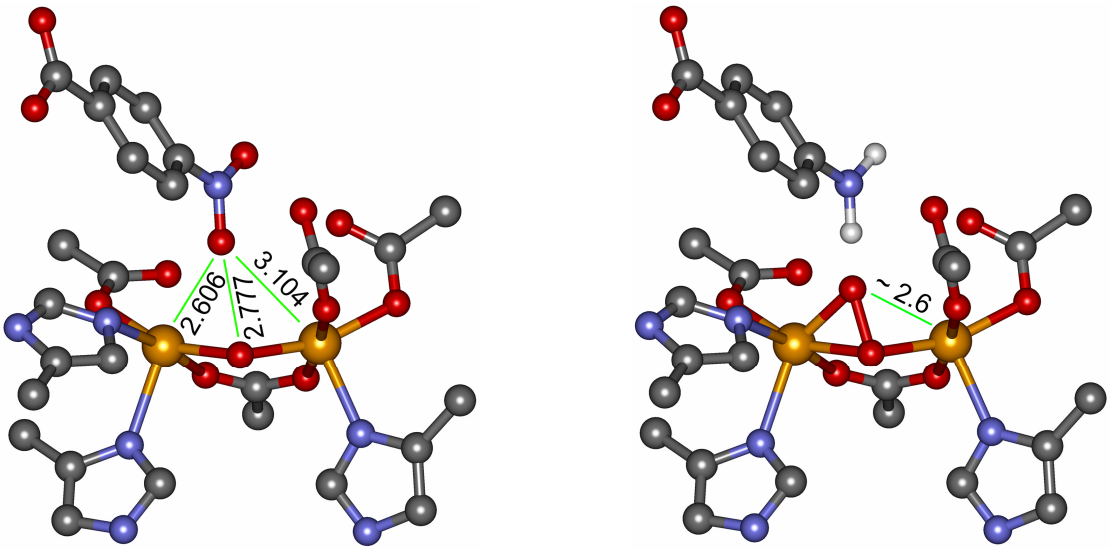

Figure 5.4. Proposed structure of CmlIperoxo (right) built based on the crystal structure of oxidized AurF–4-nitrobenzoate complex (3CHT) (left). Fe, O, C, N, and H atoms are shown in orange, red, dark grey, blue, and light grey, respectively. The green lines and numbers indicate the distances (in Å). Based on these distances, as well as to balance the charges on each iron center, the peroxo moiety is expected to bind η^2 to the Fe center on the left. In this proposed structure, the peroxo moiety is *cis* to both His ligands, a feature previously found in the crystal structure of the ternary enzyme–substrate–O_2 complex of naphthalene dioxygenase.[196]

As the ν(O-O) frequency of CmlIperoxo is over 20 cm^{-1} higher than the range currently available for the μ-η^2:η^2 mode (Fig. 5.3), we favor a μ-η^1:η^2 structure for CmlIperoxo as shown in Fig. 5.4. This structure was modeled based on the crystal structure of AurF-product complex (3CHT). While *cis*-μ-1,2-peroxo geometry is the sole binding mode observed for the canonical diiron enzymes with 2-His-4-carboxylate ligand set, it is possible that the extra His ligand, which is deduced by EXAFS and sequence analysis for CmlI, could contribute to the shift in peroxo binding geometry of CmlIperoxo. The terminal η^2 mode has been observed crystallographically for the ternary enzyme–substrate–O_2 complex of naphthalene dioxygenase[176] that contains the 2-His-1-carboxylate facial triad motif. In this structure, the η^2-peroxo moiety is *cis* to both His ligands. This proposed structure is further supported by observation that the two oxygen atoms of the O-O moiety of CmlIperoxo are inequivalent as suggested by the moderate broadening of the ν(^{16}O-^{18}O) peak (Table 5.1, and Figs. 5.2 and S.5.5).

Such ν(^{16}O-^{18}O) peak broadening or splitting has not been observed for any μ-η^1:η^2-peroxo model complexes. There are two heme(Fe^{III})–peroxo–Cu^{II} model complexes with ν(O-O) = 808 cm^{-1} and 803 cm^{-1} (both with a FWHM ~ 10 cm^{-1}) that were initially thought to contain a μ-η^2:η^2-peroxo moiety because of the lack of the splitting or broadening of the ν(^{16}O-^{18}O) peak.[187, 188] However, later crystallographic characterization of a closely related system with ν(O-O) = 790 cm^{-1} clearly revealed a μ-η^1:η^2-peroxo geometry.[189] In this structure the distance from the copper(II) center to the non-bridging oxygen atom of the peroxo moiety is 2.65 Å, which is similar to that in the structure we proposed for CmlIperoxo (Fig. 5.4). It is possible that in the μ-η^1:η^2 mode, the difference

between the two oxygen atoms of the O-O moiety may be difficult to probe by resonance Raman spectroscopy. Therefore the moderate $\nu(^{16}O\text{-}^{18}O)$ peak broadening observed for CmlIperoxo is indeed relatively significant for a $\mu\text{-}\eta^1\text{:}\eta^2$-peroxo species.

Scheme 5.2. Two possible mechanisms involving the putative ($\mu\text{-}\eta^1\text{:}\eta^2$-peroxo)diiron(III) intermediate of CmlI.

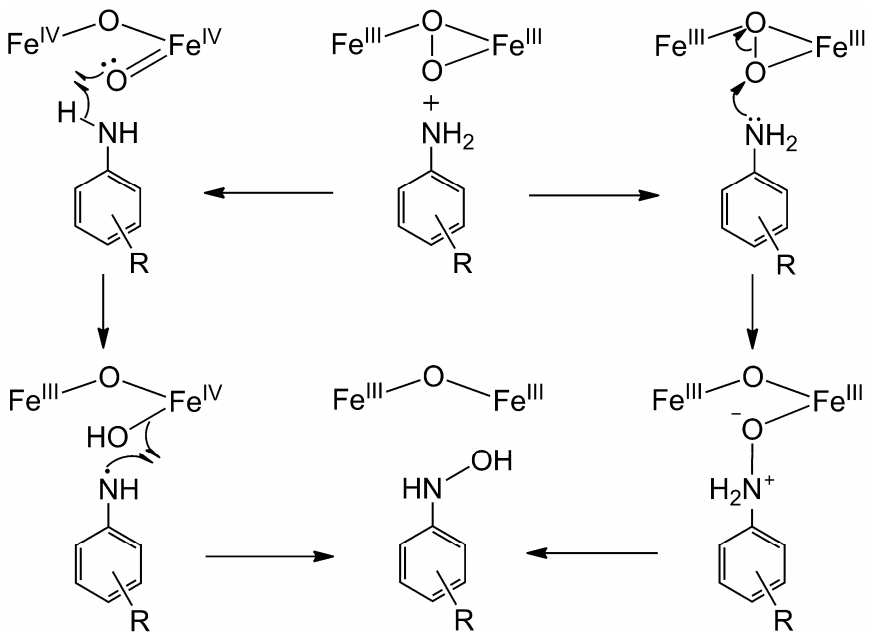

If CmlIperoxo exhibits either $\mu\text{-}\eta^1\text{:}\eta^2$ or $\mu\text{-}\eta^2\text{:}\eta^2$ peroxo geometry, then oxygen activation by CmlI can be related to that of dicopper systems, in which ($\mu\text{-}\eta^2\text{:}\eta^2$-peroxo)dicopper(II) species can reversibly convert to substrate-oxidizing bis(μ-oxo)dicopper(III) species.[190] Substrate binding could facilitate the O-O bond cleavage in CmlIperoxo to form a putative (μ-oxo)diiron(IV) or bis(μ-oxo)diiron(IV) species (Scheme 5.2, left pathway) capable of cleaving N-H bonds (BDE ~ 95 kcal/mol).

Alternatively, a nucleophilic attack mechanism (Scheme 5.2, right pathway), which was previously proposed for AurF,[103] is also possible given the electron-rich nature of the aromatic amine substrates.

We note that there is a significant residual $^{16}O_2$ signal in the resonance Raman spectra of all samples CmlIperoxo prepared with $^{18}O_2$. Moreover, the spectra of mixed labeled samples do not exhibit the expected 1:2:1 $\nu(^{16}O\text{-}^{16}O)$: $\nu(^{16}O\text{-}^{18}O)$:$\nu(^{18}O\text{-}^{18}O)$ peak intensity ratio (Figs 5.2 and A.5.5, and Table 5.1). Using the same sample preparation technique and labeled oxygen sources for hDOHHperoxo, we did not observe sizable $^{16}O_2$ signals in the spectra of $^{18}O_2$-hDOHHperoxo, while the $\nu(^{16}O\text{-}^{16}O)$: $\nu(^{16}O\text{-}^{18}O)$:$\nu(^{18}O\text{-}^{18}O)$ peak intensity ratio in the spectrum of mixed labeled hDOHHperoxo was close to 1:2:1 (Chapter 2). Thus, the adventitious introduction of atmospheric oxygen during sample preparation step can be ruled out. Scheme 5.3 describes two possible mechanisms leading to the exchange of the peroxo moiety of CmlIperoxo. The top pathway involves the reversible binding of oxygen to reduced CmlI, in which the peroxo moiety is replaced by contaminant atmospheric oxygen introduced during the resonance Raman experiment. An alternative pathway (bottom) involves reversible O-O bond cleavage and the exchange of oxygen atoms of the peroxo moiety by solvent.

Further experiments are required to understand the spectroscopic properties, reactivity, and mechanism of CmlIperoxo reaction. Activity assay and resonance Raman studies in $H_2{}^{18}O$ water, as well as a Hammett analysis will help to discriminate the proposed mechanisms in Schemes 5.2 and 5.3. This work also poses a difficult but attractive challenge for biomimetic chemists to obtain relevant nonheme diiron model

complexes that may provide a better understanding of the structure and reactivity of CmlIperoxo.

Scheme 5.3. Two possible peroxo-exchange mechanisms for CmlIperoxo

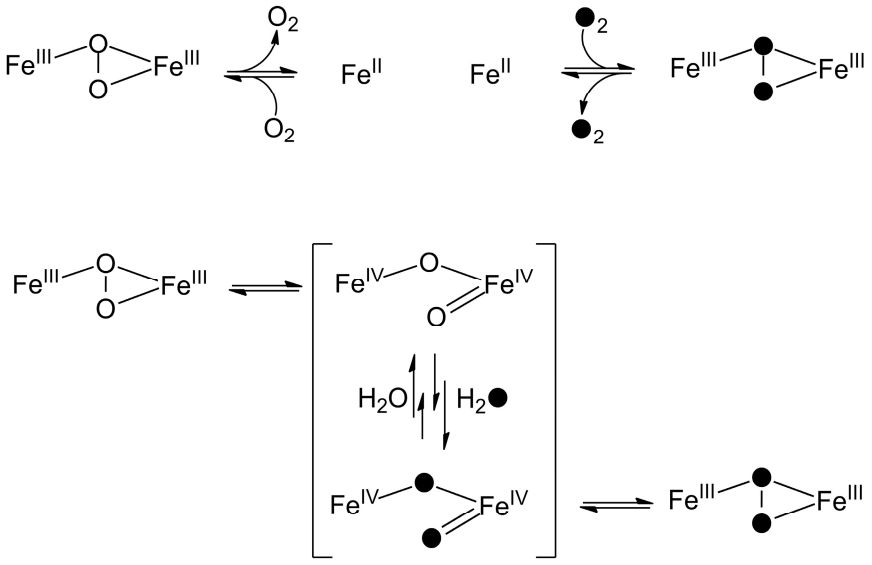

5.5. Supporting Information

X-ray absorption spectroscopy. The synchrotron ring SPEAR was operated at 3.0eV and 50-100 mA beam current. Energy resolution of the focused incoming X-rays was achieved using a Si(220) double crystal monochromator. All spectra were referenced against an iron foil, the first inflection point in the spectrum of which was set at 7112 eV.

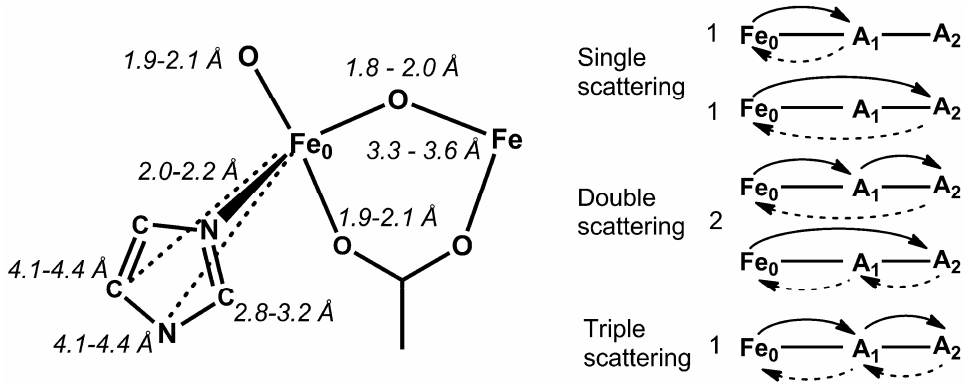

Figure S.5.1. FEFF model and important scattering paths that were considered in the fitting procedure. The single scattering path from A_2 is associated with double and triple scattering paths involving A_1. Two double scattering paths are indistinguishable. A_1 = N at ~ 2.0 – 2.2 Å , A_2 = C or N at ~ 4.1 – 4.4 Å for imidazole moiety.

Standard procedures were used to reduce, average and process the raw data using the EXAFSPAK package,[149] which was also used for pre-edge quantification following a standard method[165] and EXAFS fitting. The XAS data was normalized using the MBACK method[166] prior to pre-edge quantification. Theoretical EXAFS amplitude and phase functions were calculated using the FEFF package (version 8.4). The FEFF input model is shown in Fig. S.5.1. The parameters r and σ^2 were floated, while N was kept fixed for each fit and systematically varied in integer steps between fits. Scale factor was fixed at 0.9 and threshold energy (E_0) was varied but maintained at a common value for

all paths. All fits with E_0 outside of the $\pm$ 10 eV range are not considered. The goodness of fit is calculated as $F = \sqrt{\sum k^6(\chi_{exp} - \chi_{cal})^2}$. To judge the effect of the addition of a shell to the fit, a normalized goodness of fit, F', is used. $F' = F^2/n.\nu$, where $\nu = n_{idp} - n_{var}$, n is the number of data point, n_{idp} is the number of independent points, and n_{var} is the number of variables used in each optimization step.

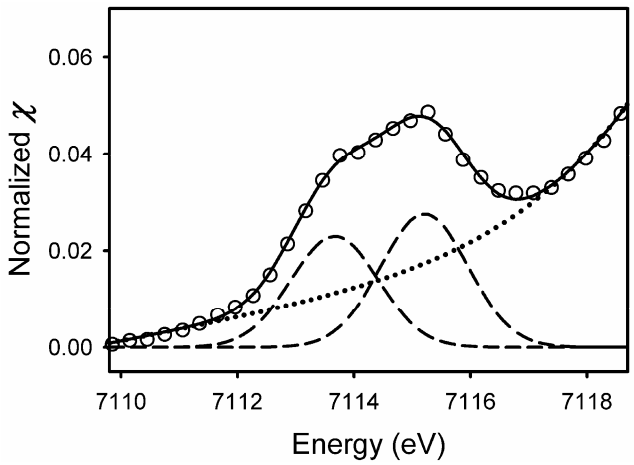

Figure S.5.2. Pre-edge feature of CmlI at pH 7.0. Peak parameters are provided in Table S.5.1.

Table S.5.1. Pre-edge parameters for CmlI at pH 7.0

Peak 1 (eV)	Int. 1	Peak 2 (eV)	Int. 2	Total Int.	Int. ratio	FWHM
7113.7(0)	3.9(1)	7115.2(0)	4.6(2)	8.6(4)	1:1.2	1.69(4)

Int. = intensity. FWHM = Full width at half maximum.

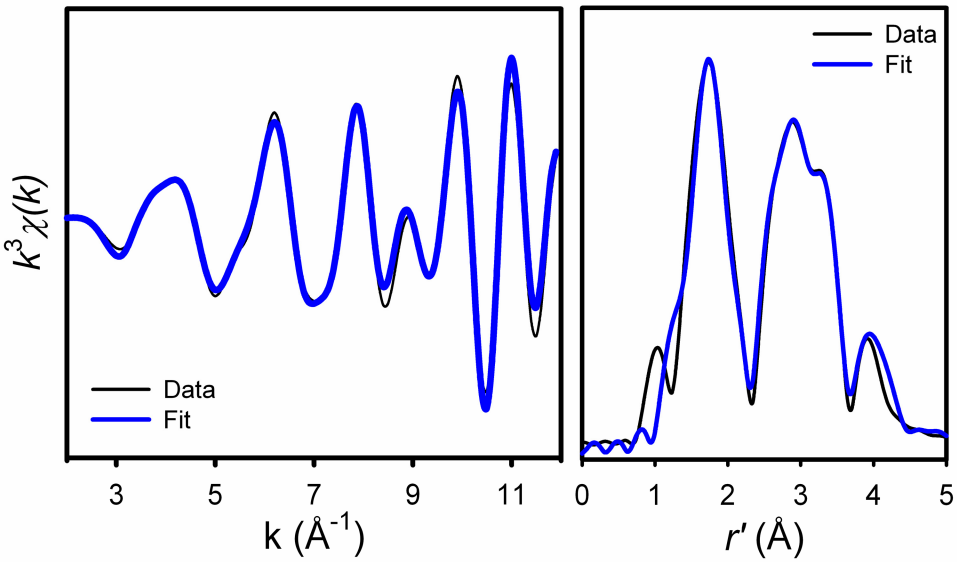

Figure S.5.3. Fourier filtered k^5-weighted EXAFS spectrum of CmlI at pH 7.0 and its Fourier transform. See Table S.5.2 footnote for other data parameters. Best fit parameter are provided in Table S.5.2 (Fit 14).

Fig. 5.1 shows Fourier filtered k^3-weighted EXAFS spectrum of CmlI at pH 7.0 and its Fourier transform. The inner shell feature at r' ~ 1.7 Å can be fitted with one shell of Fe-O/N paths, but could be split into two subshells with more reasonable σ^2 values (Fit 3, Table S.5.2). The outer shell features between 2 – 4 Å may arise from C/N/O scatterers on the ligands or a near by iron scatterer. As the photoelectrons at higher energy interact better with heavy atoms than with light atoms, the amplitude of the Fe---Fe path in comparison with Fe-C/N/O paths would be much more enhanced in k^5-weighted data than in k^3-weighted data. In the k^5-weighted data of CmlI (Fig. S.5.3), the outer shell feature at r' ~ 3.0 – 3.5 Å are remarkably enhanced compared to other features, indicating that this feature arises from a heavy scatterer, which is most likely to be an iron atom. Indeed, the

r' ~ 3.0 – 3.5 Å feature cannot be simulated with only Fe---C/N/O paths (Fits 4 – 8). However, adding an Fe---Fe path does not improve the fit either (Fits 9 and 10). This *r'* ~ 3.0 – 3.5 Å feature could only be well modeled with two Fe---Fe paths at ~ 3.3 and 3.6 Å, both with a coordination number of 0.5 (Fit 11). This result clearly shows that at pH 7.0 CmlI exists in two populations, which is consistent with the pre-edge analysis, as well as with UV/Vis and Mössbauer data.[104] The 3.3 Å Fe---Fe distance likely arises from the (μ-oxo)diiron(III) form and the 3.6 Å Fe---Fe distance from the (μ-hydroxo)diiron(III) form as observed for Δ^9-desaturase;[78] however, further evidence is required.

The outermost feature at *r'* ~ 4.0 Å (Figs. S.5.3 and 5.4) can be well simulated with single scattering paths and important multiple scattering paths involving the coordinating N atom and the outer C/N atoms of an imidazole moiety (Fig. S.5.1). When the coordination numbers of these paths are varied, the optimized values required 3 – 4 set of these paths per iron center (Fits 12 and 13). As each imidazole moiety contains two set of such scattering paths, the best fits require about 1.5 – 2 imidazole per iron center. This result indicates that the diiron active site of CmlI may contain at least 3 His ligand, consistent with its sequence analysis.[104]

Table S.5.2. EXAFS fitting results for CmlI at pH 7.0

Fit	Fe-O/N			Fe-N.O			Fe---C			Fe---Fe/C				
#	N	R	σ^2	N	R	σ^2	N	R	σ^2	N	R	σ^2	*F*	*F'*
1	6	2.05	16.0										70	0.0400
2	5	2.05	13.1										61	0.0352
3	1	1.90	5.6										57	0.0367
	4	2.07	7.9											
4	1	1.89	8.5	2	3.01	3.1							48	0.0360
	4	2.06	8.5											
5	1	1.89	7.8	2	3.01	-0.3	4C	3.66	1.8				38	0.0334
	4	2.06	8.5											
6	1	1.89	7.9	2	3.03	1.0	4C	3.33	3.7				45	0.0397
	4	2.06	8.3											
7	1	1.89	7.8	2	3.04	0.4	1	3.29	6.4				32	0.0279
	4	2.06	8.3											
8	1	1.89	7.1	2	3.01	0.2	1	3.63	4.3				29	0.0254
	4	2.06	8.2											
9	1	1.88	6.5	2	3.02	2.8	1Fe	3.33	6.4				26	0.0277
	4	2.06	8.0				4C	3.62	2.8					
10	1	1.89	6.3	2	3.01	1.6	4C	3.38	6.7				32	0.0339
	4	2.06	7.9				1Fe	3.61	4.1					
11	1	1.89	5.8	2	3.00	4.4	#0.5	3.34	2.5				19	0.0225
	4	2.06	7.7				#0.5	3.59	1.5					
12	**1**	**1.89**	**5.7**	**2**	**3.01**	**4.4**	**#0.5**	**3.34**	**2.6**	***3.5**	**4.31**	**2.0**	**11**	**0.0204**
	4	**2.06**	**7.7**				**#0.5**	**3.59**	**2.0**	**|7.0**	**|4.35**	**|4.0**		
										|3.5	**|4.39**	**|2.0**		
13[$]	**1**	**1.89**	**5.9**	**2**	**3.00**	**2.6**	**#0.5**	**3.35**	**5.1**	***3.3**	**4.30**	**2.04**		
	4	**2.06**	**8.0**				**#0.5**	**3.61**	**0.3**	**|6.6**	**|4.34**	**|4.08**		
										|3.3	**|4.38**	**|2.04**		

k range = 2 – 12 $Å^{-1}$. Back transform range = 0.85 – 4.00 Å. Resolution = 0.16 Å. n = 100; n_{idp} = 20.4. N = coordination number. R = distance. σ^2 = respective Debye-Waller factor in unit of 10^{-3} $Å^2$. [$] Fit to k^5-weighted EXAFS data.[&] Multiple scattering paths from an imidazole moiety (Fig. S.5.1). *N floated during the fit. | Parameters linked with the corresponding floated parametters. [#]Two N's varied in the fit but their sum maintained at 1.0.

Resonance Raman spectroscopy

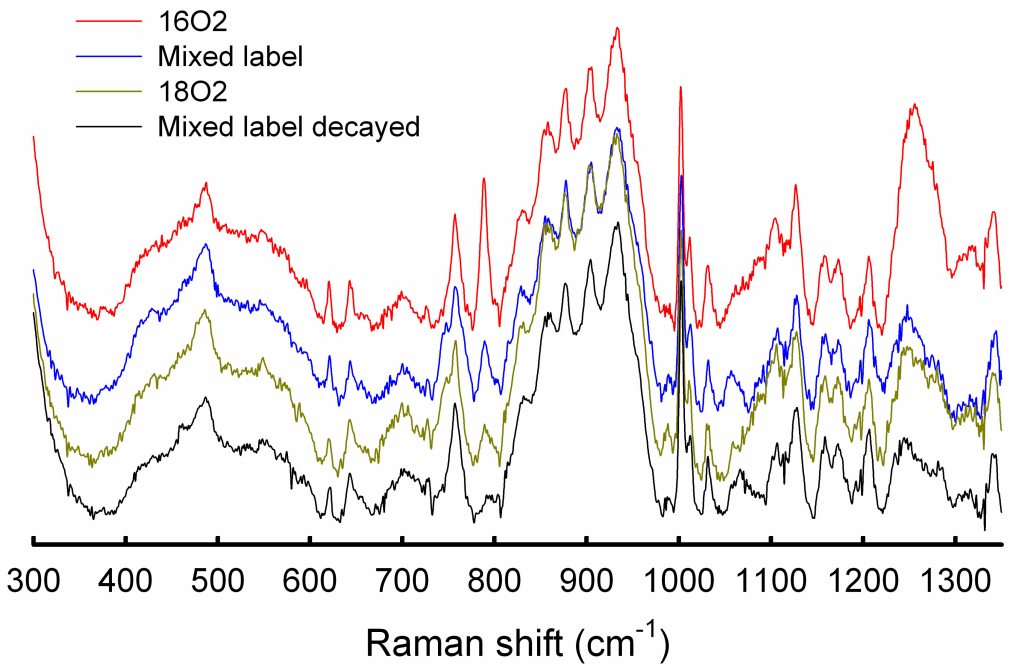

Figure S.5.4. Resonance Raman spectra of CmlIperoxo. From top to bottom: $^{16}O_2$, 1:2:1 $^{16}O_2$, $^{16}O^{18}O$ (mixed label), $^{18}O_2$; $^{18}O_2$, and mixed label decay. Two-point baseline subtraction was applied. No smoothing or zapping was required.

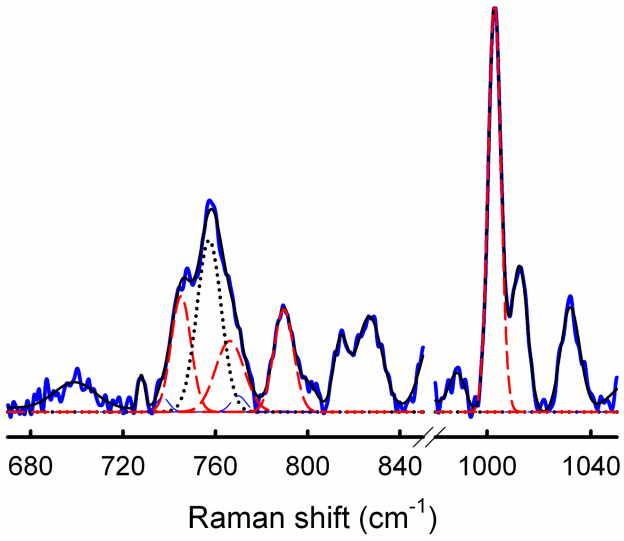

Figure S.5.5. Gaussian peak fitting result to the mixed label 2 sample (Table 5.1).

Chapter 6

Active site structure of a β-hydroxylase in antibiotic biosynthesis

6.1. Introduction

Amino acid β-hydroxylation occurs during the biosynthesis of many natural products in nonribosomal peptide synthetase (NRPS)-based pathways.[141] The products include many pharmaceutically important antibiotic and chemotherapeutic drugs.[138-140] The newly introduced hydroxyl groups serve as sites for further modifications including glycosylation, oxidation, and macrocycle formation.[141] These tailoring reactions are usually required for pharmacological activity.

Scheme 6.1. The biosynthetic pathway of chloramphenicol

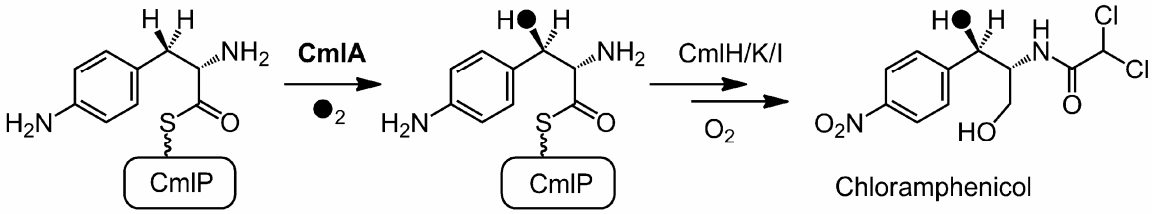

While β-hydroxylation in NRPS biosynthetic pathways is typically catalyzed by cytochrome P450s[191] and alpha-ketoglutarate-dependent nonheme iron-containing enzymes,[192, 193] a large new family of tailoring enzymes that contain a nonheme oxo-bridged diiron active site has been recently characterized.[18] The first member of this family to be isolated was CmlA from the chloramphenicol biosynthetic pathway. CmlA catalyzes β-hydroxylation of *p*-amino phenylalanine linked by a thioester bond to the thiolation domain of the NRPS CmlP (Scheme 6.1).[18] Other enzymes from this family catalyze β-hydroxylation in the biosynthesis of a wide range of antibiotic and cytostatic

agents, including bleomycin and the planin family of antibiotics. Unlike bacterial multicomponent monooxygenases (BMMs), which utilize a canonical four helix bundle (α4) protein fold to provide the carboxylate and imidazole ligands to the diiron center,[2, 3, 9] members of the CmlA family of monooxygenases employ a metallo β-lactamase ($\alpha\beta\beta\alpha$) fold to bind the cluster. While a few other diiron enzymes have been shown to utilize a lactamase fold,[10] CmlA is the first example shown to catalyze substrate hydroxylation.[18] As such, a detailed description of the CmlA active-site is warranted in order to understand how this unique enzyme class catalyzes hydroxylation at the dinuclear center. To date, no X-ray crystal structure of an enzyme from this family has been reported. In this communication, we utilize resonance Raman and X-ray absorption spectroscopies to structurally characterize the CmlA active site, including the bridging structure of the diiron center and elucidation of the ligand environment.

6.2. Experimental

6.2.1. Resonance Raman spectroscopy

CmlA was prepared as described previously.[18] To prepare the ^{18}O-labeled CmlA, 500 μL of 50 mM MOPS buffer at pH 7.75 was first dried using a SpeedVac system. To the dried solid, 500 μL $H_2{}^{18}O$ (98%) was added to obtain the $H_2{}^{18}O$ buffer solution. A similar buffer solution was prepared with $H_2{}^{16}O$ and a pH measurement confirmed that the pH remained at 7.75. Typically, 150 μL CmlA was mixed with 150 μL of $H_2{}^{18}O$ buffer and concentrated to less than 100 μL. To this concentrated sample, 200 μL $H_2{}^{18}O$ buffer was added to give a final solution containing >85 % $H_2{}^{18}O$ and ~ 0.4 mM protein.

Three samples were prepared and incubated at 4 °C for two days before their spectra were collected. Samples in $H_2{}^{16}O$ and D_2O buffer were prepared in the same manner.

Resonance Raman experiments were performed on an Acton AM-506 spectrophotometer (1,200-groove grating) with a Princeton Instruments LN_CCD-1100-PB_UVAR detector cooled to -120 °C with liquid nitrogen. The 413.1 nm excitation line was provided by a Spectra-Physics BeamLok 2060-KR-RS krypton ion laser, which was filtered out by a Kaiser Optical holographic super notch filter. Samples were contained in flat-bottomed NMR quartz tubes (A407 ~ 0.5, 4 mm path length) and maintained at a temperature range of -5 – 5 °C. Spectra were collected in a 90° scattering geometry at a resolution of 4 cm-1 and referenced to indene. 20 spectra of 20 15 s accumulations were collected for each sample at different sample positions at 50 – 100 mW of laser power. The spectra were then summed. Alternatively, one spectrum of ~250 15 s accumulations at 50 – 100 mW gave similar data quality. GRAMS/AI software (Thermo Galactic, Salem, NH) was utilized for baseline correction and smoothing. All spectra were subjected to polynomial baseline correction in the spectral region of interest (300 – 1200 cm-1) and 2-point binomial smoothing. The sharp signal at 1005 cm-1 from the protein phenylalanine was used to align the spectra collected on different days.

6.2.2. X-ray absorption spectroscopy

XAS experiments were performed at beamline 7-3 of the Stanford Synchrotron Radiation Lightsource with the storage ring operating at 3 GeV and 80-100 mA. Fe-K edge XAS spectra were collected in fluorescence mode over an energy range of 6900 – 7820 eV using a Si(220) monochromator and a solid state 30-element Ge detector (Canberra). Samples were oriented at 45° relative to the incident beam and maintained at

10 – 15 K using an Oxford Instruments CF1208 continuous-flow liquid helium cryostat. For internal energy calibration, an iron foil spectrum was collected concomitantly and its first inflection point was set to 7112.0 eV.

The CmlA solution (4 mM $[Fe]_T$, 20% glycerol, 50 mM HEPES, pH 7.5) was frozen in 6 XAS solution cells. Each cell has two or three sample spots of ~ 0.8 mm x 8 mm. Two scans were collected on each spot to obtain a total of 14 first scans and 14 second scans. To obtain data on a photoreduced sample, 13 scans were collected on one sample spot. A similar sample was then prepared in a tandem Mössbauer/XAS cup with a larger sample window that allowed irradiation 12 spots of ~ 8 mm × 0.8 mm. 12 first scans were collected. The first scans on every spot superimposed well and were averaged and designated as the non-photoreduced data (CmlA). The second scans on several spots also overlaid well on each other and were averaged and designated $CmlA_{2nd}$ data. The edge shift was observed from scan to scan in the photoreduced data scans, so only the last scan was assigned as the $CmlA_{phr}$ data. A photoreduction yield of 11% was estimated when the first scans were collected to 13 $Å^{-1}$ based on the comparision of the XANES spectra of CmlA, $CmlA_{2nd}$, and $CmlA_{phr}$ (Fig. 6.1) using a previously reported method.[16]

Data reduction and processing were performed using EXAFSPAK.[149] XAS data were normalized using the Athena program[152] or to tabulated mass absorption coefficients using the MBACK program.[166] The Athena program was also used to perform XANES linear combination for determination of the photoreduction yield. Pre-edge quantification was carried out using Edg_Fit of EXAFSPAK following a standard procedure.[165] EXAFS analysis was carried out using the Opt program of EXAFSPAK.

Theoretical scattering paths were calculated using FEFF8.4[150] using the model shown in Fig. 6.2.

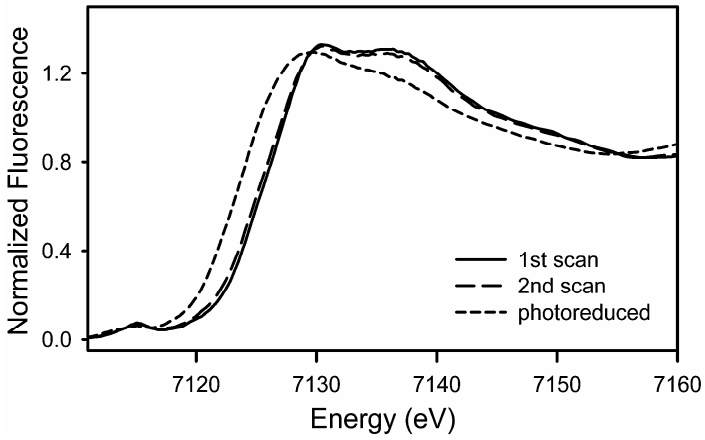

Figure 6.1. Comparison of the edges of normalized first scan, second scan, and photoreduced data.

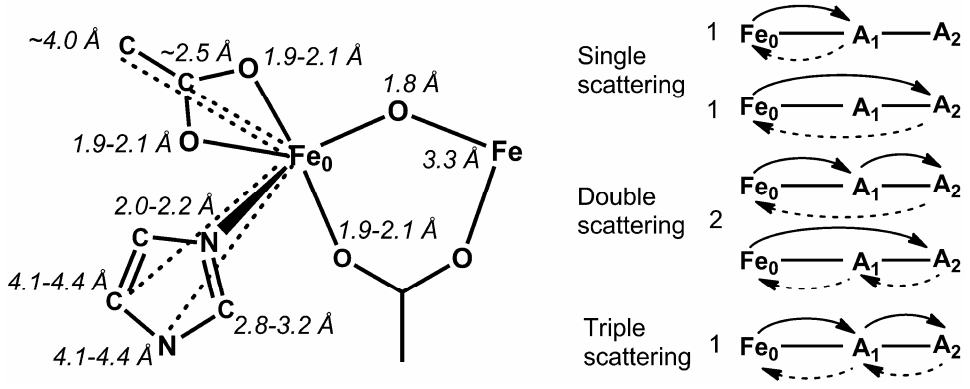

Figure 6.2. FEFF model and important scattering paths that were considered in the fitting procedure. The single scattering path from A_2 is associated with double and triple scattering paths involving A_1. Two double scattering paths are indistinguishable. A_1 = C at ~ 2.5 Å , A_2 = C at ~ 4.0 Å for bidentate carboxylate moiety. A_1 = N at ~ 2.0 – 2.2 Å , A_2 = C or N at ~ 4.1 – 4.4 Å for imidazole moiety.

6.3. Results

6.3.1. Resonance Raman spectroscopy

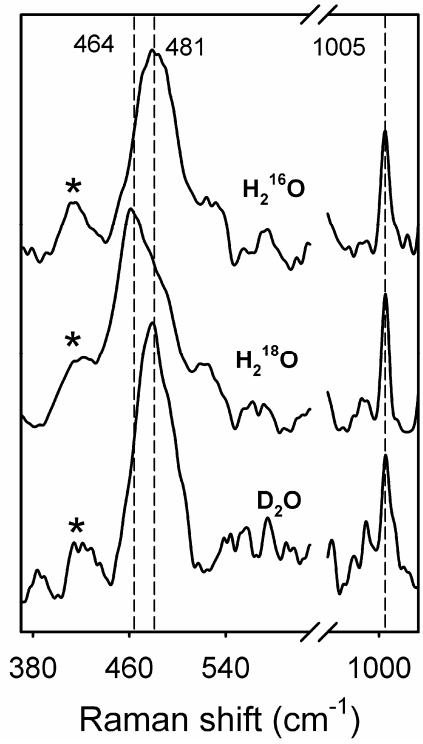

Figure 6.3. Resonance Raman spectra of CmlA in $H_2{}^{16}O$, > 85 % $H_2{}^{18}O$, and > 85 % D_2O buffer solutions. All spectra were subjected to polynomial baseline correction and 2 points binomial smoothing. The sharp phenylalanine signal at 1005 cm^{-1} was used to align the data. Asterisks indicate the laser plasma lines.

Oxidized CmlA has a chromophore at ~340 nm, which typically originates from an oxo-to-iron(III) charge transfer band associated with the bridging oxygen of the diiron cluster.[18] Resonance Raman (rR) spectroscopy provides a direct probe for the nature of this chromophore, including the precise bridging structure of the CmlA diiron center. Fig. 6.3 shows the rR spectrum of as isolated, diferric CmlA in $H_2{}^{16}O$, $H_2{}^{18}O$, and D_2O. The spectrum of the sample in $H_2{}^{16}O$ has a peak at 481 cm^{-1} (top trace), which downshifts

to 464 cm^{-1} in $H_2{}^{18}O$ buffer (middle trace) but is unaffected in D_2O buffer (bottom trace). The oxygen-isotopic sensitivity of this band clearly indicates that the 481 cm^{-1} peak arises from an oxygen-linked vibration. Indeed, the 481 cm^{-1} peak and its 17 cm^{-1} isotopic downshift values are consistent with a (μ-oxo)diiron cluster, as found in other diiron enzymes and model systems,[194, 195] but not with a μ-hydroxo or bis(μ-oxo) cluster. Previous results have demonstrated a strong correlation between the observed ν(Fe-O-Fe) and ∠Fe-O-Fe values;[194, 195] from this correlation, an Fe-μ-O-Fe angle of ~130° can be deduced for CmlA.

6.3.2. XANES analysis

The XAS spectrum of CmlA exhibits a relatively intense pre-edge feature which can be fit with a single peak (Fit 1, Table 6.1) or two peaks (Fit 2, Table 6.1) (Fig. 6.4). Fit with two peaks has better goodness of fit. The total pre-edge areas obtained in these fits are ~ 13 – 14 units, which is significantly larger than those found for octahedral diiron(III) cluster without a μ-oxo ligand. The pre-edge area of CmlA is much smaller than those found for (μ-oxo)diiron(III) clusters with 5- or 4-coordinate iron centers but falls in the range found for those with 6-coordinate iron centers.[62, 157, 159, 165] Furthermore, the peak pattern and their ratio in Fit 2 is consistent with a high-spin d^5 metal center in compressed octahedral ligand field.[165]

Table 6.1. Pre-edge parameters for CmlA obtained with EDG_FIT

Fit	Position (eV)	Area	Position (eV)	Area	Width (eV)	Total area	Peak ratio	GOF
1			7114.9(0)	13.4(4)	2.70(2)	13.4(4)		3.54×10^{-6}
2	7113.5(1)	3.2(1)	7115.2(0)	10.5(5)	2.08(3)	13.7(6)	1: 3.2	1.90×10^{-6}

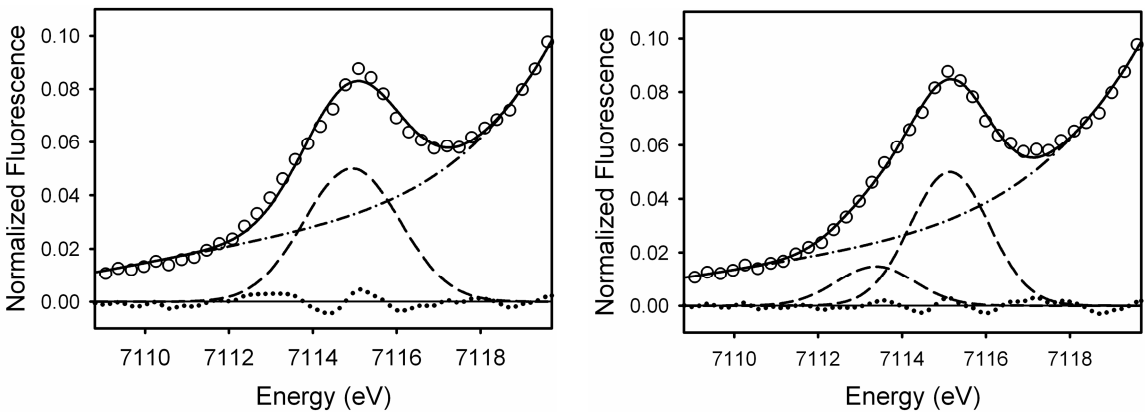

Figure 6.4. Pre-edge quantification for first scan data with one peak (left) and two peaks (right). Parameters are provided in Table 5.1. Legend: Data (o), fit (—), background (–·–·), peaks (— —), and residual (·····).

6.3.3. EXAFS analysis

Fig. 6.5 shows unfiltered EXAFS data for CmlA and its Fourier transform. The observed signal-to-noise ratio allowed a useable k range up to 13.0 $Å^{-1}$, and a negligible photoreduction yield of ~ 11 % was estimated using a method described elsewhere.[16] The Fourier transform (FT) consists of a prominent first-shell feature in the range of r' = 1 – 2.5 Å, a second shell around 3.0 Å, and a third shell from ~3.2 – 4.0 Å. This third shell is associated with the double-humped feature at 4 $Å^{-1}$ in the EXAFS data. Removal of the third shell by Fourier back transformation only to *r'* = 3.2 Å results in the loss of the double-humped feature in the EXAFS data (Fig. 6.5, green EXAFS trace). EXAFS analysis of FT-back-transformed data was carried out for the first shell and then the second shell, consecutively. Because the third shell possibly arises from multiple scattering paths, and no clear FT peaks were observed beyond 4.5 Å, EXAFS analysis of the third shell was carried out with the unfiltered data. The FEFF model and important

scattering paths are shown in Fig. 6.2. The fitting procedure was similar to that reported elsewhere.[16, 196]

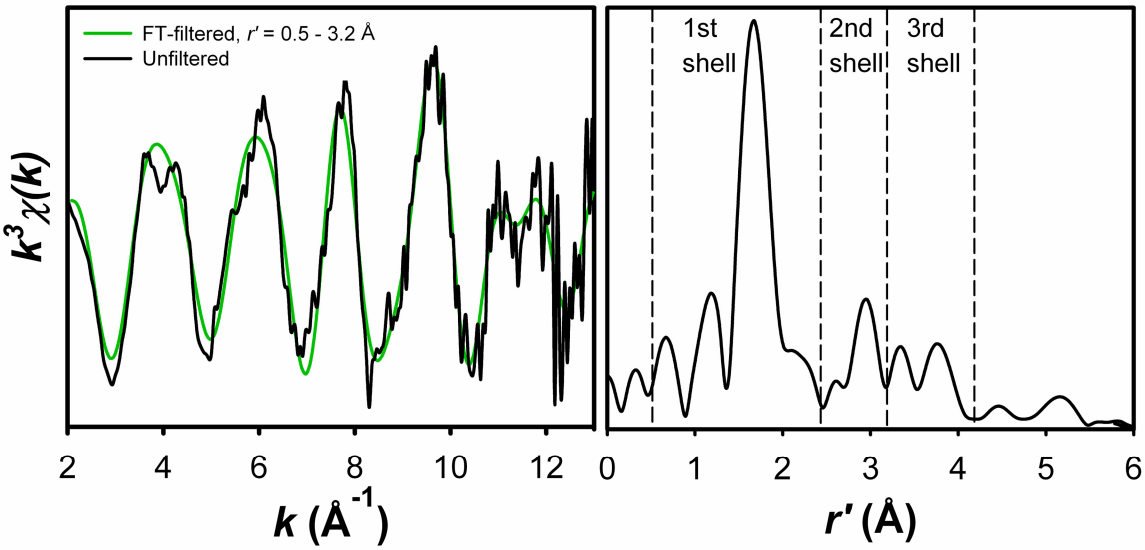

Figure 6.5. Left: Unfiltered (black) and filtered (green) EXAFS data for CmlA. Right: Fourier transform of unfiltered data with *k* range = 2 – 13 Å^{-1}.

6.3.3.1. Single scattering analysis of the first and second shells

Table 6.2 shows EXAFS fits for the first shell features. The first shell feature cannot be simulated well with a single shell of O/N atoms (Fits 1-6). Splitting this shell into two subshells results in a significant improvement in fit quality, with fit 11 representing the best two-shell fit consisting of one short 1.8 Å Fe-O path and five ~ 2.1 Å Fe-O/N paths. The short Fe-O distance is indicative of a μ-oxo bridge as observed for many oxo-bridged diiron complexes and enzymes. Decreasing the coordination number to lower than 6 gives a poorer fit (Fit 12), indicating that the Fe centers are 6-coordinate.

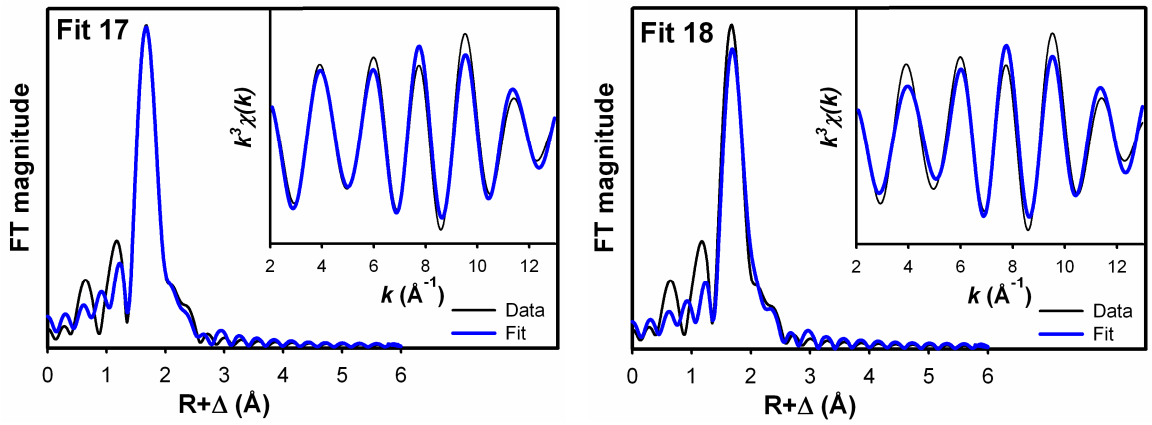

Figure 6.6. Fits to the first shell filtered data. Fit parameters are provided in Table 6.2.

Table 6.2. Results of EXAFS fitting to the first shell for CmlA

Fit	Fe-O			Fe-O/N			Fe-N/O			Fe···C/N/O				
#	N	R	σ^2	N	R	σ^2	N	R	σ^2	N	R	σ^2	*F*	*F'*
1				6	2.09	9.85							182	0.1504
2				5	2.09	7.24							126	0.1041
3				4	2.09	5.04							81	0.0669
4							6	2.11	7.15				130	0.1074
5							5	2.11	5.38				89	0.0736
6							4	2.11	3.72				63	0.0521
7				5	2.05	30.4	1	2.10	-2.20				108	0.1093
8				4	1.96	52.2	2	2.10	0.15				72	0.0728
9	3	1.86	45.7				3	2.10	1.85				54	0.0547
10	2	1.81	20.1				4	2.10	3.08				47	0.0476
11	**1**	**1.79**	**4.23**				**5**	**2.10**	**5.20**				**32**	**0.0324**
12	1	1.80	6.56				4	2.10	3.48				38	0.0384
13	1	1.77	2.24	1	1.97	0.25	4	2.12	2.12				35	0.0457
14	1	1.78	1.71	2	1.99	3.07	3	2.13	1.26				30	0.0392
15	1	1.76	2.55	3	2.03	6.88	2	2.13	1.35				40	0.0522
16	1	1.77	1.15	4	2.03	6.73	1	2.15	-1.80				34	0.0443
17	**1**	**1.80**	**4.33**				**5**	**2.10**	**5.15**	**1**	**2.53**	**1.73**	**21**	**0.0275**
18	1	1.80	6.57				4	2.10	3.23	1	2.52	1.15	31	0.0405

k range = 2 – 13 Å^{-1}, resolution ~ 0.14 Å, back transform range 0.5-2.5 Å. N = coordination number. R = distance. σ^2 = respective Debye-Waller factor in unit of 10^{-3} Å^2. Scale factor $S_0^2 = 0.9$. GOF = goodness of fit calculated as $F = \sqrt{\sum k^6(\chi_{exp} - \chi_{cal})^2}$. $F' = F^2/n.\nu$, where $\nu = n_{idp} - n_{var}$, $n = 111$ is the number of data point, $n_{idp} = 13.9$ is the number of independent points, and n_{var} is the number of variables used in each optimization step. F' is used to indicate the improvement of fit upon the addition of a shell.

Any combination of 1 short Fe-O path and two shells of O/N atoms near 2.0 Å (Fits 13-16) gives a poorer fit compared to Fit 11. Addition of a low-Z atom at 2.5 Å significantly enhances the fit quality (Fit 17). However, this scatterer cannot arise from a loosely bound ligand with a long Fe-ligand distance, as a poorer fit is obtained compared to both fit 11 and fit 17 when the number of scatterers in the 2.10-Å shell is decreased by 1 (Fit 18) (Fig. 6.6). We assign the 2.5-Å scatterer to the carbon atom of a symmetric bidentate carboxylate ligand, as observed by EXAFS for iron enzymes and complexes.[106, 196]

Table 6.3. Results of EXAFS fitting to first and second shells for CmlA

Fit	Fe-O			Fe-O/N			Fe-N/O			Fe···C/N/O				
#	N	R	σ^2	N	R	σ^2	N	R	σ^2	N	R	σ^2	*F*	*F'*
19	1	1.79	3.95	1	2.52	0.00	2	3.37	-0.09				31	0.0288
	5	2.10	5.32											
20	1	1.79	4.00	1	2.52	0.10	3	3.37	1.02				36	0.0335
	5	2.10	4.29											
21	1	1.79	4.07	1	2.53	0.20	4	3.37	2.77				43	0.0399
	5	2.10	5.24											
22	**1**	**1.80**	**4.07**	**1**	**2.53**	**0.38**				**1**	**3.35**	**5.16**	**26**	**0.0241**
	5	**2.10**	**5.21**											
23	**1**	**1.80**	**4.13**	**1**	**2.53**	**0.55**	**2**	**3.09**	**5.32**	**1**	**3.34**	**5.71**	**23**	**0.0269**
	5	**2.10**	**5.19**											

Back transform range 0.5-3.2 Å. n_{idp} = 18.7. See footnote of Table 6.2 for information on other parameters.

Table 6.3 shows the fitting results to the filtered data up to the second shell. The second shell feature is well simulated with an Fe···Fe scattering path at ~ 3.3 Å (Fit 22 and Fig. 6.7). This value falls in the range of Fe···Fe distances found for other diiron enzymes and their model complexes.[62, 95-97, 105, 109, 159, 164, 197-200] Replacing the Fe···Fe path by several Fe···C paths gives poorer fits (Fits 19-21). Thus, EXAFS fitting clearly shows

that CmlA has a diiron cluster with an Fe-Fe distance of ~3.3 Å bridged by a μ-oxo ligand. The addition of several Fe···C paths at ~ 3.1 Å slightly improves the fit (Fit 23 and Fig. 6.7). However, as the *F'* factor of Fit 23 is higher than that of Fit 22 the inclusion of the ~ 3.1 Å Fe···C paths may not be required at this point.

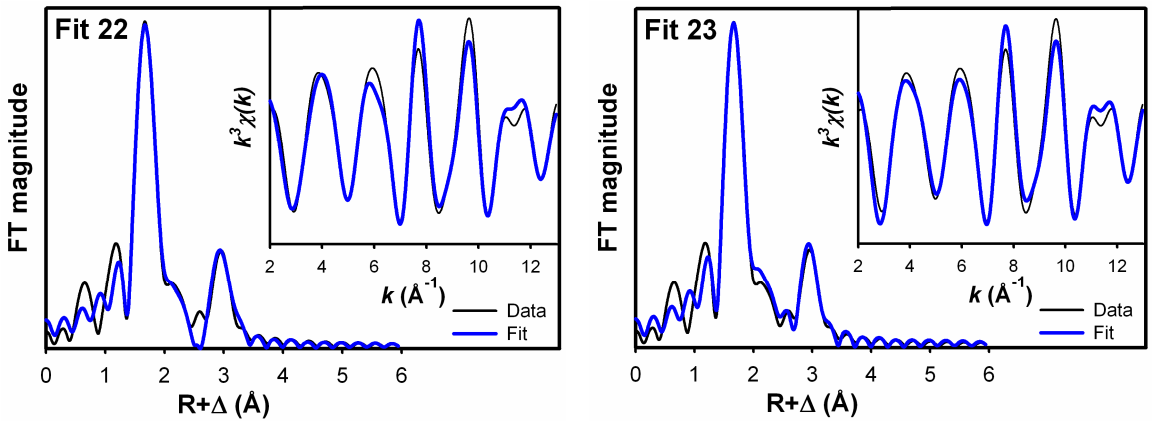

Figure 6.7. Fits to the first and second shell filtered data. Fit parameters are provided in Table 6.3.

6.3.3.2. Multiple scattering analysis of the unfiltered data

Multiple scattering contributions are important to consider for the fitting of the CmlA EXAFS data. Significant multiple scattering paths from His and bidentate carboxylate ligands are shown in Fig. 6.2. The double-humped feature can not be simulated with the parameters of the best fit to the second shell filtered data (Fits 24 and 25, Table 6.4). Addition of single-scattering paths in the range of 4.0 – 4.5 Å or single- and multiple scattering paths from the symmetric bidentate carboxylato moiety also fails to simulate this feature (Fits 26 and 27). However, when the single-scattering paths and

the important multiple-scattering paths from the imidazole ring are included, the third shell feature is well simulated (Fit 28) (Fig. 6.8). Including important paths from both imidazole and symmetric bidentate carboxylato moieties noticeably enhances the fit quality (Fig. 6.9). The numbers of paths from the imidazole moiety were varied during the fit. The optimized values of ~4 C single, ~8 double, and ~4 triple scattering paths require the presence of ~2 imidazole moieties per iron center.

Table 6.4. EXAFS fitting results to unfiltered data for CmlA

Fit	Fe-O/N			Fe···C			Fe···C/N			Fe···Fe			
#	N	R	σ^2	N	R	σ^2	N	R	σ^2	N	R	σ^2	*F'*
24	1	1.80	4.28	1	2.53	0.66				1	3.34	4.20	0.4163
	5	2.10	5.00										
25	1	1.80	4.39	1	2.53	1.11	2	3.09	1.55	1	3.32	5.04	0.4041
	5	2.10	4.98										
26	1	1.80	4.45	1	2.53	1.22	2	3.09	1.17	1	3.32	4.86	0.3812
	5	2.10	4.91				3	4.47	1.45				
27	1	1.80	4.44	1	2.53	1.32	2	3.09	0.98	1	3.32	5.43	0.3970
	5	2.10	4.98	1	3.93	3.63							
				2	|3.98	|7.26							
				1	|3.94	|3.63							
28	**1**	**1.80**	**4.31**	**1**	**2.53**	**1.14**	**2**	**3.09**	**1.75**	**1**	**3.31**	**4.97**	**0.3643**
	5	**2.10**	**4.92**				***3.6**	**4.35**	**3.12**				
							|7.2	**|4.35**	**|6.31**				
							|3.6	**|4.35**	**|3.12**				
29	**1**	**1.80**	**4.41**	**1**	**2.53**	**1.09**	**2**	**3.09**	**1.19**	**1**	**3.32**	**5.36**	**0.3496**
	5	**2.10**	**4.97**	**1**	**3.94**	**5.13**	***3.9**	**4.36**	**3.80**				
				2	**|3.94**	**|10.3**	**|7.8**	**|4.36**	**|7.78**				
				1	**|3.94**	**|5.13**	**|3.9**	**|4.36**	**|3.80**				

F-factor calculated as $F' = \sqrt{\sum k^6(\chi_{exp} - \chi_{cal})^2 / \sum k^6 \chi_{exp}{}^2}$. See footnote of Table 6.2 for information about other parameters. Gray- and black-shaded cells indicate single scattering paths (top) associated with double (middle) and triple (bottom) scattering paths from the symmetric bidendate carboxylato and imidazole moieties, respectively (Fig. 6.2). | = parameters of multiple scattering paths linked with that of the corresponding single scattering paths. * = varied coordination numbers.

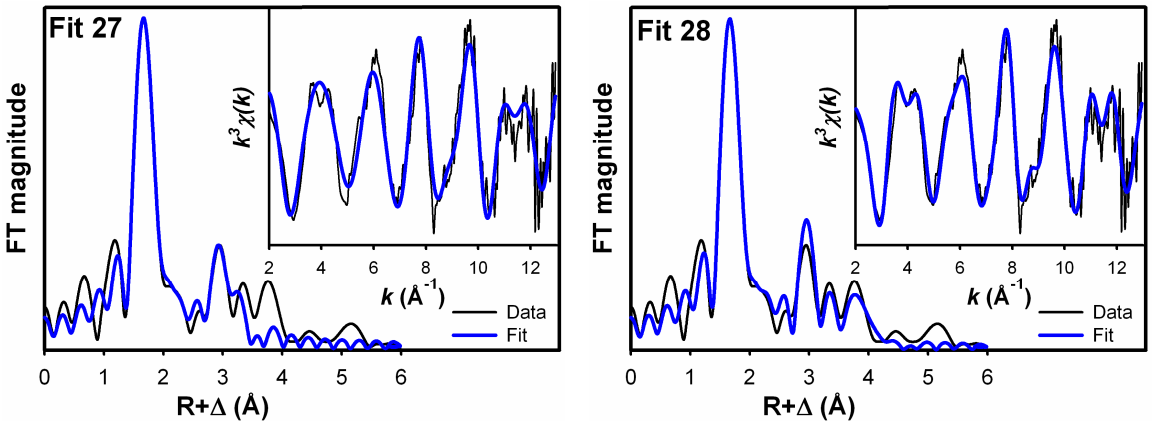

Figure 6.8. Fits to the unfiltered EXAFS data for CmlA. Both Fits 27 and 28 are lower in quality compared to Fit 29.

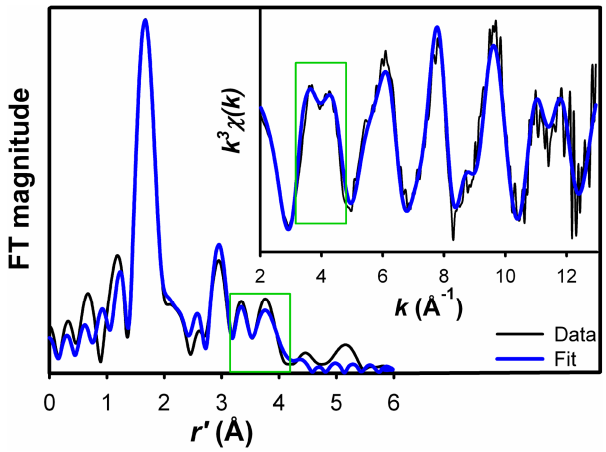

Figure 6.9. Best fit to unfiltered EXAFS data for CmlA (Fit 29). Fit parameters are provided in Table 6.4.

6.4. Discussion

The structure of the diferric CmlA active site was probed by resonance Raman spectroscopy and X-ray absorption spectroscopy (XAS). The XAS data analysis shows that CmlA contains a (μ-oxo)diiron(III) cluster with Fe-μ-O and Fe···Fe distances of ca. 1.80 and 3.32 Å, respectively, the latter clearly associated with the peak at r' = 3 Å (Fig.

6.9). The Fe-μ-O and Fe···Fe distances together require an ∠Fe-O-Fe angle of ca. 134°, which agrees with the Raman results in Fig. 6.3. Based on comparisons with synthetic diiron(III) complexes,[194, 195] the spectroscopic data for CmlA indicate the presence of a (μ-oxo)(μ-1,3-carboxylato)diiron core, as also found in the β subunit of Class Ia ribonucleotide reductases (R2).[201, 202]

EXAFS analysis provides further insight into the nature of the iron ligands of CmlA. The average Fe-O/N bond distance (excluding the oxo bridge) for CmlA is 2.10 Å, which reflects the relative number of histidines and oxyanion ligands. This distance is shorter than those for various forms of metHr (2.13-2.17 Å),[95, 96] which has a total of five histidines and two carboxylate ligands for the diiron cluster,[1] but longer than those for other diiron enzymes with four carboxylates and one or two His ligands (1.99-2.06).[62, 96, 156, 197-199, 201] The average Fe-O/N distance found for CmlA suggests that its diiron active site should have more than 2 but less than 5 His ligands.

Support for this notion comes from an analysis of the outer shell features found in the 3.2 – 4.0 Å region of the FT data of CmlA (see green box in Fig. 6.9). These features can be attributed to the more distant atoms of imidazole-like ligands, the intensities of which are enhanced by multiple scattering pathways,[203] and correspond to the double-humped feature at 4 $Å^{-1}$ in the unfiltered k-space data (Fig. 6.9 inset). Similarly well defined double-humped features near 4.0 $Å^{-1}$ can be found in unfiltered EXAFS data of metHr and model complexes that have 4–6 imidazole-like ligands per cluster.[95, 96, 164] In contrast, such features are less well defined in the spectra of other diiron enzymes with only 1 – 2 His ligands per cluster.[62, 96, 156, 197-199, 201] Diiron complexes without imidazole-like ligands do not exhibit this feature.[105, 109] Thus, the clearly defined double-humped

feature in the EXAFS spectrum of CmlA suggests that there are more than 2 His ligands bound to its diiron active site.

To obtain a more quantitative analysis of the data, we have applied a multiple scattering approach to simulate the double-humped feature (Table 6.4 and Figs. 6.8 and 6.9). The best fit is shown in Fig. 6.9 and Table 6.4. The optimized numbers of scattering paths associated with the imidazole moiety require the presence of ~2 His ligands per iron, or ~4(±1) His ligands per cluster, given the ~25% uncertainty in the number of scatterers for a given shell determined from EXAFS analysis.[204] However, the presence of 5 His ligands is highly unlikely on the basis of the average Fe-O/N distance of 2.10 Å found for CmlA, as discussed above.

The best fit of the EXAFS data also requires the inclusion of one low-Z scatterer per iron at 2.53 Å (Table 6.2). The small σ^2 value associated with the scatterer excludes the possibility that it arises from the ligating atom of a weakly bound ligand and leads us to assign it to the carboxylate C atom (C_{car}) of a symmetrically bidentate carboxylate ligand. Scatterers at similar distance have also been found in the EXAFS spectra of the terephthalate complex of protocatechuate 3,4-dioxygenase[205] and the ternary complex of tyrosine hydroxylase with substrate and cofactor[196] and are associated with the carbon atom of a bidentate carboxylate. The tyrosine hydroxylase result is corroborated by the crystal structure of the corresponding complex of the homologous phenylalanine hydroxylase.[206] For CmlA, the C_α atom of the bidentate carboxylate can also be included in the best fit because of the collinearity of the Fe center and the carboxylate C_{car} and C_α atoms; including the multiple scattering paths involving these atoms noticeably enhances the fit (Table 6.4). Taken together, the rR and XAS analyses described above show that

CmlA contains a (μ-oxo)(μ-1,3-carboxylato)diiron(III) cluster with 6-coordinate iron centers, 2 symmetrically bidentate carboxylate ligands, and 3 – 4 His ligands (Fig. 6.10A).

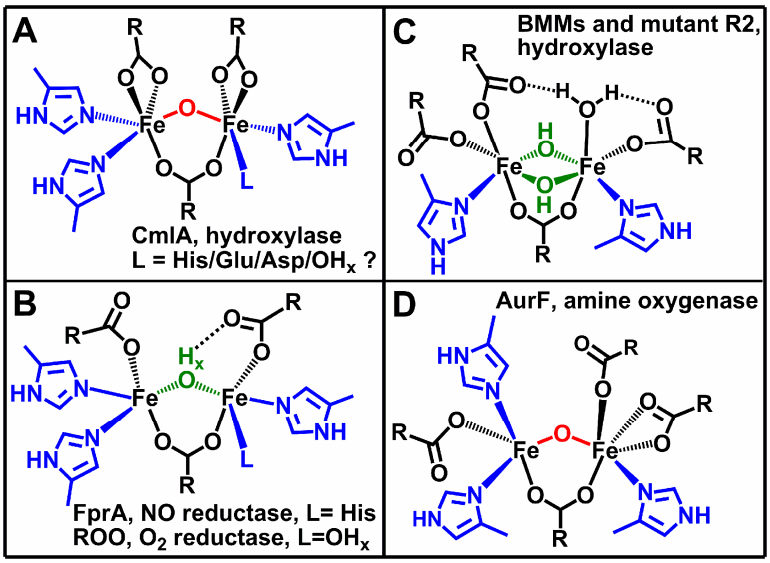

Figure 6.10. Comparison of the diiron(III) clusters of CmlA and related diiron proteins.

This structure is similar to that proposed in our previous study[18] which was based on alignment of the sequences of CmlA and its homologs with the consensus sequence for metallo-β-lactamases. Sequence alignment predicted only 3 His ligands for CmlA,[18] but the presence of an additional His ligand is also possible. Both the CmlA and metallo-β-lactamase sequences share the signature HxHxDH motif that provides one carboxylate and 3 His ligands for the metal cluster. Downstream of this sequence in CmlA, one Asp and two Glu residues are conserved and found at approximately the same positions as the other amino acid ligands of the dizinc cluster of the metallo-β-lactamases (2 His and 1

Cys/Ser). There is only one conserved His residue downstream of the signature sequence for CmlA (His378), and this could be the fourth His predicted in the current study. However, this His is adjacent to one of the postulated Glu ligands, and based on metallo-β-lactamases structures, replacement of this Glu by His would place three His ligands on one iron and one on the other. This would be expected to yield two quite different iron environments, which is not apparent in the Mössbauer spectrum of CmlA.[18] It is possible that CmlA adopts a slightly different fold than a metallo-β-lactamase, changing the iron to which the additional His coordinates.

Several new insights derive from the proposed structure of the diiron cluster of CmlA. First, it is clear from the current studies that the diiron cluster of CmlA differs from those of the flavo-diiron protein (FDP) family[10] in which it was first shown that a diiron cluster can be supported in the metallo-β-lactamase αββα fold. FDPs are widespread among bacteria and archaea and function as reductases for O_2 and NO rather than oxygenases. All crystal structures of FDPs reported thus far show that their diiron clusters are bridged by a water-derived ligand with an Fe-O distance of ~2.0 Å (Fig. 6.10B).[10] This distance and the other spectroscopic features of the cluster indicate that this bridge is not a μ-oxo ligand as found here for CmlA, but rather a protonated form such as a hydroxo or an aqua ligand. Furthermore, the bridging atom appears to be hydrogen bonded to one of the terminal monodentate carboxylates. These structural differences between CmlA and FDPs may account for the contrasting reactivities, but additional structural and kinetic studies of both the FDPs and CmlA will be required to identify the molecular origin of these differences.

Second, despite having monooxygenase reactivity, the diiron core structure of CmlA differs from those of the clusters of all canonical oxygen-activating nonheme diiron enzymes characterized thus far.[2, 3, 9] BMMs, desaturases, and R2 have a conserved 2-His-4-carboyxlate ligand set with 1 His per iron center (Fig. 6.10C). This ligand set promotes a generally accepted oxygen activation mechanism involving a (μ-1,2-peroxo)diiron(III) intermediate that converts to high-spin higher-valent diiron species responsible for substrate oxidation.[2, 3, 9]

Distinct oxygen activation mechanisms are postulated for some enzymes that have more than two His ligands bound to the diiron active site, including myo-inositol oxygenase (MIOX) with a total of 4 His ligands[11] and AurF with a total of 3 His ligands[15] (Fig. 6.10D). MIOX is unique in that it activates O_2 with a mixed-valent diiron(II/III) cluster to form a C-H bond-cleaving (superoxo)diiron(III) intermediate that initiates the 4e-oxidation of substrate.[13] AurF effects the conversion of aromatic amines to nitro groups via a diiron(III)-peroxo intermediate that differs from the canonical (μ-1,2-peroxo)diiron(III) intermediate discussed above.[103]

Like MIOX and AurF, CmlA has an additional His ligand on at least one and possibly both irons of its diiron cluster, but its molecular mechanism is unlikely to be similar to those of MIOX or AurF. In contrast to MIOX, we have shown that it is the diiron(II) state of CmlA that reacts with O_2 to initiate catalysis.[18] With respect to AurF, a similar peroxo intermediate may also be formed by CmlA, but this species is unlikely to be sufficiently reactive to attack the C-H bond on the substrate (BDE ~ 85 kcal/mol, Scheme 6.1). Accordingly, the peroxo intermediate of AurF has not been observed to attack C-H bonds of any substrate.

This analysis suggests that CmlA may generate some type of high valent diiron oxygen species in which the O-O bond of O_2 has been broken as found for the canonical diiron monooxygenases such as methane monooxygenase (MMO). However, the additional His ligand(s) may alter the nature of this reactive species. There are many options for the species that could be formed as alternatives to the $Fe^{IV}_2O_2$ diamond core of MMO intermediate Q.[61, 207, 208] For example, our recent work has identified synthetic diiron(IV) complexes with nitrogen-rich ligand environments that are quite reactive towards C-H bonds.[233, 249] Although experimental evidence is needed to support the hypothesis for an alternative reactive species in CmlA, it is clear that variations to the canonical MMO reactive intermediate are emerging and may be relevant to catalysis by CmlA.[200, 209]

References

1. Stenkamp, R. E., Dioxygen and hemerythrin. *Chem. Rev.* **1994,** *94*, 715-726.
2. Wallar, B. J.; Lipscomb, J. D., Dioxygen activation by enzymes containing binuclear non-heme iron clusters. *Chem. Rev.* **1996,** *96*, 2625-2657.
3. Kurtz, D. M., Jr., Structural similarity and functional diversity in diiron-oxo proteins. *J. Biol. Inorg. Chem.* **1997,** *2*, 159-167.
4. Leahy, J. G.; Batchelor, P. J.; Morcomb, S. M., Evolution of the soluble diiron monooxygenases. *FEMS Microbiol. Rev.* **2003,** *27*, 449-479.
5. Notomista, E.; Lahm, A.; Di Donato, A.; Tramontano, A., Evolution of bacterial and archaeal multicomponent monooxygenases. *J. Mol. Evol.* **2003,** *56*, 435-445.
6. Fox, B. G.; Lyle, K. S.; Rogge, C. E., Reactions of the diiron enzyme stearoyl-acyl carrier protein desaturase. *Acc. Chem. Res.* **2004,** *37*, 421-429.
7. Kurtz, D. M., Jr, Avoiding high-valent iron intermediates: Superoxide reductase and rubrerythrin. *J. Inorg. Biochem.* **2006,** *100*, 679-693.
8. Nordlund, P. a.; Reichard, P., Ribonucleotide reductases. *Annu. Rev. Biochem.* **2006,** *75*, 681–706.
9. Sazinsky, M. H.; Lippard, S. J., Correlating structure with function in bacterial multicomponent monooxygenases and related diiron proteins. *Acc. Chem. Res.* **2006,** *39*, 558-566.
10. Kurtz, D. M., Jr., Flavo-diiron enzymes: Nitric oxide or dioxygen reductases? *Dalton Trans.* **2007**, 4115-4121.
11. Brown, P. M.; Caradoc-Davies, T. T.; Dickson, J. M. J.; Cooper, G. J. S.; Loomes, K. M.; Baker, E. N., Crystal structure of a substrate complex of myo-inositol oxygenase, a di-iron oxygenase with a key role in inositol metabolism. *Proc. Nat. Acad. Sci. U. S. A.* **2006,** *103*, 15032-15037.
12. Simurdiak, M.; Lee, J.; Zhao, H., A new class of arylamine oxygenases: Evidence that *p*-aminobenzoate *n*-oxygenase (aurf) is a di-iron enzyme and further mechanistic studies. *ChemBioChem* **2006,** *7*, 1169-1172.
13. Xing, G.; Diao, Y.; Hoffart, L. M.; Barr, E. W.; Prabhu, K. S.; Arner, R. J.; Reddy, C. C.; Krebs, C.; Bollinger, J. M., Jr., Evidence for c–h cleavage by an iron–superoxide complex in the glycol cleavage reaction catalyzed by myo-inositol oxygenase. *Proc. Nat. Acad. Sci. U. S. A.* **2006,** *103*, 6130-6135.
14. Zocher, G.; Winkler, R.; Hertweck, C.; Schulz, G. E., Structure and action of the n-oxygenase aurf from streptomyces thioluteus. *J. Mol. Biol.* **2007,** *373*, 65-74.
15. Choi, Y. S.; Zhang, H.; Brunzelle, J. S.; Nair, S. K.; Zhao, H., In vitro reconstitution and crystal structure of p-aminobenzoate n-oxygenase (aurf) involved in aureothin biosynthesis. *Proc. Nat. Acad. Sci. U. S. A.* **2008,** *105*, 6858-6863.
16. Vu, V. V.; Emerson, J. P.; Martinho, M.; Kim, Y. S.; Munck, E.; Park, M. H.; Que, L., Jr., Human deoxyhypusine hydroxylase, an enzyme involved in regulating cell growth, activates o2 with a nonheme diiron center. *Proc. Nat. Acad. Sci. U. S. A.* **2009,** *106*, 14814-14819.
17. Behan, R. K.; Lippard, S. J., The aging-associated enzyme clk-1 is a member of the carboxylate-bridged diiron family of proteins. *Biochemistry* **2010,** *49*, 9679-9681.

18. Makris, T. M.; Chakrabarti, M.; Münck, E.; Lipscomb, J. D., A family of diiron monooxygenases catalyzing amino acid beta-hydroxylation in antibiotic biosynthesis. *Proc. Nat. Acad. Sci. U. S. A.* **2010,** *107*, 15391-15396.
19. Schirmer, A.; Rude, M. A.; Li, X.; Popova, E.; del Cardayre, S. B., Microbial biosynthesis of alkanes. *Science* **2010,** *329*, 559-562.
20. Das, D.; Eser, B. E.; Han, J.; Sciore, A.; Marsh, E. N. G., Oxygen-independent decarbonylation of aldehydes by cyanobacterial aldehyde decarbonylase: A new reaction of diiron enzymes. *Angew. Chem. Int. Ed.* **2011,** *50*, 7148-7152.
21. Li, N.; Nørgaard, H.; Warui, D. M.; Booker, S. J.; Krebs, C.; Bollinger, J. M., Conversion of fatty aldehydes to alka(e)nes and formate by a cyanobacterial aldehyde decarbonylase: Cryptic redox by an unusual dimetal oxygenase. *J. Am. Chem. Soc.* **2011,** *133*, 6158-6161.
22. Vu, V. V.; Makris, T. M.; Lipscomb, J. D.; Que, L., Active-site structure of a β-hydroxylase in antibiotic biosynthesis. *J. Am. Chem. Soc.* **2011,** *133*, 6938-6941.
23. Warui, D. M.; Li, N.; Nørgaard, H.; Krebs, C.; Bollinger, J. M.; Booker, S. J., Detection of formate, rather than carbon monoxide, as the stoichiometric coproduct in conversion of fatty aldehydes to alkanes by a cyanobacterial aldehyde decarbonylase. *J. Am. Chem. Soc.* **2011,** *133*, 3316-3319.
24. Xiong, J.; Kurtz, D. M., Jr.; Ai, J.; Sanders-Loehr, J., A hemerythrin-like domain in a bacterial chemotaxis protein. *Biochemistry* **2000,** *39*, 5117-5125.
25. Isaza, C. E.; Silaghi-Dumitrescu, R.; Iyer, R. B.; Kurtz, D. M., Jr.; Chan, M. K., Structural basis for o_2 sensing by the hemerythrin-like domain of a bacterial chemotaxis protein: Substrate tunnel and fluxional n terminus. *Biochemistry* **2006,** *45*, 9023-9031.
26. Onoda, A.; Okamoto, Y.; Sugimoto, H.; Shiro, Y.; Hayashi, T., Crystal structure and spectroscopic studies of a stable mixed-valent state of the hemerythrin-like domain of a bacterial chemotaxis protein. *Inorg. Chem.* **2011,** *50*, 4892-4899.
27. Cooley, R. B.; Arp, D. J.; Karplus, P. A., Symerythrin structures at atomic resolution and the origins of rubrerythrins and the ferritin-like superfamily. *J. Mol. Biol.* **2011,** *In press*.
28. Harrison, P. M.; Arosio, P., The ferritins: Molecular properties, iron storage function and cellular regulation. *BBA-Bioenergetics* **1996,** *1275*, 161-203.
29. Hoque, M.; Hanauske-Abel, H.; Palumbo, P.; Saxena, D.; D'Alliessi Gandolfi, D.; Park, M.; Pe'ery, T.; Mathews, M., Inhibition of hiv-1 gene expression by ciclopirox and deferiprone, drugs that prevent hypusination of eukaryotic initiation factor 5a. *Retrovirology* **2009,** *6*, 90.
30. Kerscher, B.; Nzukou, E.; Kaiser, A., Assessment of deoxyhypusine hydroxylase as a putative, novel drug target. *Amino Acids* **2010,** *38*, 471-477.
31. Park, M. H.; Nishimura, K.; Zanelli, C. F.; Valentini, S. R., Functional significance of eif5a and its hypusine modification in eukaryotes. *Amino Acids* **2010,** *38*, 491-500.
32. Tinberg, C. E.; Lippard, S. J., Dioxygen activation in soluble methane monooxygenase. *Acc. Chem. Res.* **2011,** *44*, 280-288.
33. Rosenzweig, A. C.; Frederick, C. A.; Lippard, S. J.; Nordlund, P., Crystal structure of a bacterial non-haem iron hydroxylase that catalyses the biological oxidation of methane. *Nature* **1993,** *366*, 537-543.

34. Rosenzweig, A. C.; Nordlund, P. r.; Takahara, P. M.; Frederick, C. A.; Lippard, S. J., Geometry of the soluble methane monooxygenase catalytic diiron center in two oxidation states. *Chem. Biol.* **1995,** *2*, 409-418.
35. Elango, N. A.; Radhakrishnan, R.; Froland, W. A.; Wallar, B. J.; Earhart, C. A.; Lipscomb, J. D.; Ohlendorf, D. H., Crystal structure of the hydroxylase component of methane monooxygenase from *methylosinus trichosporium* ob3b. *Prot. Sci.* **1997,** *6*, 556-568.
36. Rosenzweig, A. C.; Brandstetter, H.; Whittington, D. A.; Nordlund, P.; Lippard, S. J.; Frederick, C. A., Crystal structures of the methane monooxygenase hydroxylase from methylococcus capsulatus (bath): Implications for substrate gating and component interactions. *Proteins: Struct., Funct., Bioinf.* **1997,** *29*, 141-152.
37. Sazinsky, M. H.; Bard, J.; Di Donato, A.; Lippard, S. J., Crystal structure of the toluene/o-xylene monooxygenase hydroxylase from pseudomonas stutzeri ox1 - insight into the substrate specificity, substrate channeling, and active site tuning of multicomponent monooxygenases. *J. Biol. Chem.* **2004,** *279*, 30600-30610.
38. McCormick, M. S.; Sazinsky, M. H.; Condon, K. L.; Lippard, S. J., X-ray crystal structures of manganese(ii)-reconstituted and native toluene/o-xylene monooxygenase hydroxylase reveal rotamer shifts in conserved residues and an enhanced view of the protein interior. *J. Am. Chem. Soc.* **2006,** *128*, 15108-15110.
39. Bailey, L. J.; McCoy, J. G.; Phillips, G. N.; Fox, B. G., Structural consequences of effector protein complex formation in a diiron hydroxylase. *Proc. Nat. Acad. Sci. U. S. A.* **2008,** *105*, 19194-19198.
40. Carter, E. L.; Tronrud, D. E.; Taber, S. R.; Karplus, P. A.; Hausinger, R. P., Iron-containing urease in a pathogenic bacterium. *Proc. Nat. Acad. Sci. U. S. A.* **2011,** *In press*.
41. Klabunde, T.; Krebse, B., The dimetal center in purple acid phosphatases. In *Metal sites in proteins and models*, **1997**; pp 177-198.
42. Guddat, L. W.; McAlpine, A. S.; Hume, D.; Hamilton, S.; de Jersey, J.; Martin, J. L., Crystal structure of mammalian purple acid phosphatase. *Structure* **1999,** *7*, 757-767.
43. Sträter, N.; Jasper, B.; Scholte, M.; Krebs, B.; Duff, A. P.; Langley, D. B.; Han, R.; Averill, B. A.; Freeman, H. C.; Guss, J. M., Crystal structures of recombinant human purple acid phosphatase with and without an inhibitory conformation of the repression loop. *J. Mol. Biol.* **2005,** *351*, 233-246.
44. Rather, L. J.; Weinert, T.; Demmer, U.; Bill, E.; Ismail, W.; Fuchs, G.; Ermler, U., Structure and mechanism of the diiron benzoyl-coenzyme a epoxidase boxb. *J. Biol. Chem.* **2011,** *286*, 29241-29248.
45. Grishin, A. M.; Ajamian, E.; Tao, L.; Zhang, L.; Menard, R.; Cygler, M., Structural and functional studies of the escherichia coli phenylacetyl-coa monooxygenase complex. *J. Biol. Chem.* **2011,** *286*, 10735-10743.
46. Teufel, R.; Mascaraque, V.; Ismail, W.; Voss, M.; Perera, J.; Eisenreich, W.; Haehnel, W.; Fuchs, G., Bacterial phenylalanine and phenylacetate catabolic pathway revealed. *Proc. Nat. Acad. Sci. U. S. A.* **2010,** *107*, 14390-14395.
47. Rather, L. J.; Knapp, B.; Haehnel, W.; Fuchs, G., Coenzyme a-dependent aerobic metabolism of benzoate via epoxide formation. *J. Biol. Chem.* **2010,** *285*, 20615-20624.

48. Holub, B. J., Metabolism and function of myo-inositol and inositol phospholipids. *Annu. Rev. Biochem.* **1986,** *6*, 563-597.
49. Majerus, P. W., Inositol phosphate biochemistry. *Annu. Rev. Biochem.* **1992,** *61*, 225-250.
50. Arner, R. J.; Prabhu, K. S.; Reddy, C. C., Molecular cloning, expression, and characterization of myo-inositol oxygenase from mouse, rat, and human kidney. *Biochem. Biophys. Res. Comm.* **2004,** *324*, 1386-1392.
51. Arner, R. J.; Prabhu, K. S.; Thompson, J. T.; Hildenbrandt, G. R.; Liken, A. D.; Reddy, C. C., Myo-inositol oxygenase: Molecular cloning and expression of a unique enzyme that oxidizes myo-inositol and d-chiro-inositol. *Biochem. J.* **2001,** *360*, 313-320.
52. Xing, G.; Barr, E. W.; Diao, Y.; Hoffart, L. M.; Prabhu, K. S.; Arner, R. J.; Reddy, C. C.; Krebs, C.; Bollinger, J. M., Jr., Oxygen activation by a mixed-valent, diiron(ii/iii) cluster in the glycol cleavage reaction catalyzed by myo-inositol oxygenase. *Biochemistry* **2006,** *45*, 5402-5412.
53. Xing, G.; Hoffart, L. M.; Diao, Y.; Prabhu, K. S.; Arner, R. J.; Reddy, C. C.; Krebs, C.; Bollinger, J. M., Jr., A coupled dinuclear iron cluster that is perturbed by substrate binding in myo-inositol oxygenase. *Biochemistry* **2006,** *45*, 5393-5401.
54. Bollinger, J. M., Jr.; Diao, Y.; Matthews, M. L.; Xing, G.; Krebs, C., *Myo*-inositol oxygenase: A radical new pathway for o2 and c-h activation at a nonheme diiron cluster. *Dalton Trans.* **2009**, 905-914.
55. Thorsell, A.-G.; Persson, C.; Voevodskaya, N.; Busam, R. D.; Hammarström, M.; Gräslund, S.; Gräslund, A.; Hallberg, B. M., Structural and biophysical characterization of human myo-inositol oxygenase. *J. Biol. Chem.* **2008,** *283*, 15209-15216.
56. Wolff, E. C.; Kang, K. R.; Kim, Y. S.; Park, M. H., Posttranslational synthesis of hypusine: Evolutionary progression and specificity of the hypusine modification. *Amino Acids* **2007,** *33*, 341–350.
57. Park, M. H., The post-translational synthesis of a polyamine-derived amino acid, hypusine, in the eukaryotic translation initiation factor 5a (eif5a). *J. Biochem.* **2006,** *139*, 161-169.
58. Park, J.-H.; Aravind, L.; Wolff, E. C.; Kaevel, J.; Kim, Y. S.; Park, M. H., Molecular cloning, expression, and structural prediction of deoxyhypusine hydroxylase: A heat-repeat-containing metalloenzyme. *Proc. Nat. Acad. Sci. U. S. A.* **2006,** *103*, 51-56.
59. Voegtli, W. C.; Khidekel, N.; Baldwin, J.; Ley, B. A.; Bollinger, J. M., Jr.; Rosenzweig, A. C., Crystal structure of the ribonucleotide reductase r2 mutant that accumulates a μ-1,2-peroxodiiron(iii) intermediate during oxygen activation. *J. Am. Chem. Soc.* **2000,** *122*, 3255-3261.
60. Baldwin, J.; Voegtli, W. C.; Khidekel, N.; Moenne-Loccoz, P.; Krebs, C.; Pereira, A. S.; Ley, B. A.; Huynh, B. H.; Loehr, T. M.; Riggs-Gelasco, P. J.; Rosenzweig, A. C.; Bollinger, J. M., Jr., Rational reprogramming of the r2 subunit of escherichia coli ribonucleotide reductase into a self-hydroxylating monooxygenase. *J. Am. Chem. Soc.* **2001,** *123*, 7017-7030.
61. Shu, L.; Nesheim, J. C.; Kauffmann, K.; Münck, E.; Lipscomb, J. D.; Que, L., Jr., An $fe_2^{iv}o_2$ diamond core structure for the key intermediate q of methane monooxygenase. *Science* **1997,** *275*, 515-518.

62. Riggs-Gelasco, P. J.; Shu, L.; Chen, S.; Burdi, D.; Huynh, B. H.; Que, L.; Stubbe, J., Exafs characterization of the intermediate x generated during the assembly of the escherichia coli ribonucleotide reductase r2 diferric tyrosyl radical cofactor. *J. Am. Chem. Soc.* **1998,** *120*, 849-860.
63. Dong, Y.; Zang, Y.; Shu, L.; Wilkinson, E.; Que, L., Jr.; Kauffmann, K.; Munck, E., Models for nonheme diiron enzymes. Assembly of a high-valent $fe_2(\mu\text{-}o)_2$ diamond core from its peroxo precursor. *J. Am. Chem. Soc.* **1997,** *119*, 12683-12684.
64. Xue, G.; Wang, D.; De Hont, R.; Fiedler, A. T.; Shan, X.; Münck, E.; Que, L., Jr., A synthetic precedent for the $[fe^{iv2}(\mu\text{-}o)_2]$ diamond core proposed for methane monooxygenase intermediate q. *Proc. Nat. Acad. Sci. U. S. A.* **2007,** *104*, 20713-20718.
65. Nesheim, J. C.; Lipscomb, J. D., Large kinetic isotope effects in methane oxidation catalyzed by methane monooxygenase: Evidence for c-h bond cleavage in a reaction cycle intermediate. *Biochemistry* **1996,** *35*, 10240-10247.
66. Brazeau, B. J.; Lipscomb, J. D., Kinetics and activation thermodynamics of methane monooxygenase compound q formation and reaction with substrates. *Biochemistry* **2000,** *39*, 13503-13515.
67. Bollinger, J. M., Jr.; Edmondson, D. E.; Huynh, B. H.; Filley, J.; Norton, J. R.; Stubbe, J., Mechanism of assembly of the tyrosyl radical-dinuclear iron cluster cofactor of ribonucleotide reductase. *Science* **1991,** *253*, 292-298.
68. Bollinger, J. M., Jr.; Stubbe, J.; Huynh, B. H.; Edmondson, D. E., Novel diferric radical intermediate responsible for tyrosyl radical formation in assembly of the cofactor of ribonucleotide reductase. *J. Am. Chem. Soc.* **1991,** *113*, 6289-6291.
69. Ravi, N.; Bollinger, J. M.; Huynh, B. H.; Stubbe, J.; Edmondson, D. E., Mechanism of assembly of the tyrosyl radical-diiron(iii) cofactor of e. Coli ribonucleotide reductase: 1. Moessbauer characterization of the diferric radical precursor. *J. Am. Chem. Soc.* **1994,** *116*, 8007-8014.
70. Jiang, W.; Bollinger, J. M., Jr.; Krebs, C., The active form of chlamydia trachomatis ribonucleotide reductase r2 protein contains a heterodinuclear mn(iv)/fe(iii) cluster with s=1 ground state. *J. Am. Chem. Soc.* **2007,** *129*, 7504-+.
71. Jiang, W.; Hoffart, L. M.; Krebs, C.; Bollinger, J. M., Jr., A manganese(iv)/iron(iv) intermediate in assembly of the manganese(iv)/iron(iii) cofactor of chlamydia trachomatis ribonucleotide reductase. *Biochemistry* **2007,** *46*, 8709-8716.
72. Jiang, W.; Yun, D.; Saleh, L.; Barr, E. W.; Xing, G.; Hoffart, L. M.; Maslak, M. A.; Krebs, C.; Bollinger, J. M., Jr., A manganese(iv)/iron(iii) cofactor in chlamydia trachomatis ribonucleotide reductase. *Science* **2007,** *316*, 1188-1191.
73. Song, W. J.; Behan, R. K.; Naik, S. G.; Huynh, B. H.; Lippard, S. J., Characterization of a peroxodiiron(iii) intermediate in the t201s variant of toluene/o-xylene monooxygenase hydroxylase from pseudomonas sp. Ox1. *J. Am. Chem. Soc.* **2009,** *131*, 6074-6075.
74. Yun, D.; García-Serres, R.; Chicalese, B. M.; An, Y. H.; Huynh, B. H.; Bollinger, J. M., Jr., (μ-1,2-peroxo)diiron(iii/iii) complex as a precursor to the diiron(iii/iv) intermediate x in the assembly of the iron-radical cofactor of ribonucleotide reductase from mouse. *Biochemistry* **2007,** *46*, 1925-1932.
75. Murray, L. J.; Garcia-Serres, R.; Naik, S.; Huynh, B. H.; Lippard, S. J., Dioxygen activation at non-heme diiron centers: Characterization of intermediates in a mutant form

of toluene/*o*-xylene monooxygenase hydroxylase. *J. Am. Chem. Soc.* **2006,** *128*, 7458-7459.
76. Broadwater, J. A.; Achim, C.; Münck, E.; Fox, B. G., Mössbauer studies of the formation and reactivity of a quasi-stable peroxo intermediate of stearoyl-acyl carrier protein δ^9-desaturase. *Biochemistry* **1999,** *38*, 12197-12204.
77. Moënne-Loccoz, P.; Baldwin, J.; Ley, B. A.; Loehr, T. M.; Bollinger, J. M., Jr., O_2 activation by non-heme diiron proteins: Identification of a symmetric μ-1,2-peroxide in a mutant of ribonucleotide reductase. *Biochemistry* **1998,** *37*, 14659-14663.
78. Broadwater, J. A.; Ai, J.; Loehr, T. M.; Sanders-Loehr, J. S.; Fox, B. G., Peroxodiferric intermediate of stearoyl-acyl carrier protein δ^9 desaturase: Oxidase reactivity during single turnover and implications for the mechanism of desaturation. *Biochemistry* **1998,** *37*, 14664-14671.
79. Bollinger, J. M., Jr.; Krebs, C.; Vicol, A.; Chen, S.; Ley, B. A.; Edmondson, D. E.; Huynh, B. H., Engineering the diiron site of *escherichia coli* ribonucleotide reductase protein r2 to accumulate an intermediate similar to h_{peroxo}, the putative peroxodiiron(iii) complex from the methane monooxygenase catalytic cycle. *J. Am. Chem. Soc.* **1998,** *120*, 1094-1095.
80. Liu, K. E.; Wang, D.; Huynh, B. H.; Edmondson, D. E.; Salifoglou, A.; Lippard, S. J., Spectroscopic detection of intermediates in the reaction of dioxygen with the reduced methane monooxygenase/hydroxylase from *methylococcus capsulatus* (bath). *J. Am. Chem. Soc.* **1994,** *116*, 7465-7466.
81. Moënne-Loccoz, P.; Krebs, C.; Herlihy, K.; Edmondson, D. E.; Theil, E. C.; Huynh, B. H.; Loehr, T. M., The ferroxidase reaction of ferritin reveals a diferric μ-1,2 bridging peroxide intermediate in common with other o_2-activating non-heme diiron proteins. *Biochemistry* **1999,** *38*, 5290-5295.
82. Ookubo, T.; Sugimoto, H.; Nagayama, T.; Masuda, H.; Sato, T.; Tanaka, K.; Maeda, Y.; Okawa, H.; Hayashi, Y.; Uehara, A.; Suzuki, M., Cis-μ-1,2-peroxo diiron complex: Structure and reversible oxygenation. *J. Am. Chem. Soc.* **1996,** *118*, 701-702.
83. Frisch, J. R.; Vu, V. V.; Martinho, M.; Münck, E.; Que, L., Jr., Characterization of two distinct adducts in the reaction of a nonheme diiron(ii) complex with o_2. *Inorg. Chem.* **2009,** *48*, 8325-8336.
84. Baldwin, J.; Krebs, C.; Saleh, L.; Stelling, M.; Huynh, B. H.; Bollinger, J. M., Jr.; Riggs-Gelasco, P., Structural characterization of the peroxodiiron(iii) intermediate generated during oxygen activation by the w48a/d84e variant of ribonucleotide reductase protein r2 from *escherichia coli*. *Biochemistry* **2003,** *42*, 13269-13279.
85. Hwang, J.; Krebs, C.; Huynh, B. H.; Edmondson, D. E.; Theil, E. C.; Penner-Hahn, J. E., A short fe-fe distance in peroxodiferric ferritin: Control of fe substrate versus cofactor decay? *Science* **2000,** *287*, 122-125.
86. Bossek, U.; Weyhermueller, T.; Wieghardt, K.; Nuber, B.; Weiss, J., $[l_2mn_2(\mu\text{-}o)_2(\mu\text{-}o_2)](clo_4)_2$. The first binuclear ($\mu$-peroxo)dimanganese(iv) complex (l = 1,4,7-trimethyl-1,4,7-triazacyclononane). A model for the $s_4 \rightarrow s_0$ transformation in the oxygen-evolving complex in photosynthesis. *J. Am. Chem. Soc.* **1990,** *112*, 6387-6388.
87. Skulan, A. J.; Brunold, T. C.; Baldwin, J.; Saleh, L.; Bollinger, J. M., Jr.; Solomon, E. I., Nature of the peroxo intermediate of the w48f/d84e ribonucleotide

reductase variant: Implications for o_2 activation by binuclear non-heme iron enzymes. *J. Am. Chem. Soc.* **2004,** *126*, 8842-8855.
88. Lee, S.-K.; Lipscomb, J. D., Oxygen activation catalyzed by methane monooxygenase hydroxylase component: Proton delivery during the o-o bond cleavage steps. *Biochemistry* **1999,** *38*, 4423-4432.
89. Tinberg, C. E.; Lippard, S. J., Revisiting the mechanism of dioxygen activation in soluble methane monooxygenase from m. Capsulatus (bath): Evidence for a multi-step, proton-dependent reaction pathway. *Biochemistry* **2009,** *48*, 12145-12158.
90. Murray, L. J.; Naik, S. G.; Ortillo, D. O.; Garcia-Serres, R.; Lee, J. K.; Huynh, B. H.; Lippard, S. J., Characterization of the arene-oxidizing intermediate in tomoh as a diiron(iii) species. *J. Am. Chem. Soc.* **2007,** *129*, 14500-14510.
91. Song, W. J.; McCormick, M. S.; Behan, R. K.; Sazinsky, M. H.; Jiang, W.; Lin, J.; Krebs, C.; Lippard, S. J., Active site threonine facilitates proton transfer during dioxygen activation at the diiron center of toluene/o-xylene monooxygenase hydroxylase. *J. Am. Chem. Soc.* **2010,** *132*, 13582-13585.
92. Song, W. J.; Lippard, S. J., Mechanistic studies of reactions of peroxodiiron(iii) intermediates in t201 variants of toluene/o-xylene monooxygenase hydroxylase. *Biochemistry* **2011,** *50*, 5391-5399.
93. Krebs, C.; Bollinger, J. M., Jr; Theil, E. C.; Huynh, B. H., Exchange coupling constant j of peroxodiferric reaction intermediates determined by mössbauer spectroscopy. *J. Biol. Inorg. Chem.* **2002,** *7*, 863-869.
94. Jameson, G. N. L.; Jin, W.; Krebs, C.; Perreira, A. S.; Tavares, P.; Liu, X.; Theil, E. C.; Huynh, B. H., Stoichiometric production of hydrogen peroxide and parallel formation of ferric multimers through decay of the diferricâ’peroxo complex, the first detectable intermediate in ferritin mineralizationâ€ *Biochemistry* **2002,** *41*, 13435-13443.
95. Zhang, K.; Stern, E. A.; Ellis, F.; Sanders-Loehr, J.; Shiemke, A. K., The active site of hemerythrin as determined by x-ray absorption fine structure. *Biochemistry* **1988,** *27*, 7470-7479.
96. Scarrow, R. C.; Maroney, M. J.; Palmer, S. M.; Que, L., Jr.; Roe, A. L.; Salowe, S. P.; Stubbe, J., Exafs studies of binuclear iron proteins: Hemerythrin and ribonucleotide reductase. *J. Am. Chem. Soc.* **1987,** *109*, 7857-7864.
97. Hedman, B.; Co, M. S.; Armstrong, W. H.; Hodgson, K. O.; Lippard, S. J., Exafs studies of binuclear iron complexes as models for hemerythrin and related proteins. *Inorg. Chem.* **1986,** *25*, 3708-3711.
98. Armstrong, W. H.; Lippard, S. J., Reversible protonation of the oxo bridge in a hemerythrin model compound. Synthesis, structure, and properties of (.Mu.-hydroxo)bis(.Mu.-acetato)bis[hydrotris(1-pyrazolyl)borato]diiron(iii) [(hb(pz)3)fe(oh)(o2cch3)2fe(hb(pz)3)2]+. *J. Am. Chem. Soc.* **1984,** *106*, 4632-4633.
99. Kurtz, D. M.; Shriver, D. F.; Klotz, I. M., Structure and chemistry of hemerythrin. *Coord. Chem. Rev.* **1977,** *24*, 145-178.
100. Kurtz, D. M., Jr; Shriver, D. F.; Klotz, I. M., Resonance raman spectroscopy with unsymmetrically isotopica ligands. Differentiation of possible structures of hemerythrin complexes. *J. Am. Chem. Soc.* **1976,** *98*, 5033-5035.

101. Dawson, J. W.; Gray, H. B.; Hoenig, H. E.; Rossman, G. R.; Schredder, J. M.; Wang, R.-H., A magnetic susceptibility study of hemerythrin using an ultrasensitive magnetometer. *Biochemistry* **1972,** *11*, 461-465.
102. Okamura, M. Y.; Klotz, I. M.; Johnson, C. E.; Winter, M. R. C.; Williams, R. J. P., The state of iron in hemerythrin. A mössbauer study. *Biochemistry* **1969,** *8*, 1951-1958.
103. Korboukh, V. K.; Li, N.; Barr, E. W.; Bollinger, J. M., Jr.; Krebs, C., A long-lived, substrate-hydroxylating peroxodiiron(iii/iii) intermediate in the amine oxygenase, aurf, from streptomyces thioluteus. *J. Am. Chem. Soc.* **2009,** *131*, 13608–13609.
104. Makris, T. M., *et al.*, *Unpublished data*.
105. Mizoguchi, T. J.; Kuzelka, J.; Spingler, B.; DuBois, J. L.; Davydov, R. M.; Hedman, B.; Hodgson, K. O.; Lippard, S. J., Synthesis and spectroscopic studies of non-heme diiron(iii) species with a terminal hydroperoxide ligand: Models for hemerythrin. *Inorg. Chem.* **2001,** *40*, 4662-4673.
106. Kitajima, N.; Tamura, N.; Amagai, H.; Fukui, H.; Moro-oka, Y.; Mizutani, Y.; Kitagawa, T.; Mathur, R.; Heerwegh, K.; Reed, C. A.; Randall, C. R.; Que, L., Jr.; Tatsumi, K., Monomeric carboxylate ferrous complexes as models for the dioxygen binding sites in non-heme iron proteins. The reversible formation and characterization of μ-peroxo diferric complexes. *J. Am. Chem. Soc.* **1994,** *116*, 9071-9085.
107. Kim, K.; Lippard, S. J., Structure and mössbauer spectrum of a (μ-1,2-peroxo)bis(μ-carboxylato)diiron(iii) model for the peroxo intermediate in the methane monooxygenase hydroxylase reaction cycle. *J. Am. Chem. Soc.* **1996,** *118*, 4914-4915.
108. Girerd, J.-J.; Banse, F.; Simaan, A. J., Characterization and properties of non-heme iron peroxo complexes. In *Metal-oxo and metal-peroxo species in catalytic oxidations*, Meunier, B., Ed. Springer-Verlag Berlin Heidelberg New York: 2000; Vol. 97, pp 145-177.
109. Fiedler, A. T.; Shan, X.; Mehn, M. P.; Kaizer, J.; Torelli, S.; Frisch, J. R.; Kodera, M.; Que, L., Jr, Spectroscopic and computational studies of (μ-oxo)(μ-1,2-peroxo)diiron(iii) complexes of relevance to nonheme diiron oxygenase intermediates. *J. Phys. Chem. A* **2008,** *112*, 13037-13044.
110. Cao, B.; Nagarajan, K.; Loh, K.-C., Biodegradation of aromatic compounds: Current status and opportunities for biomolecular approaches. *Appl. Microbiol. Biotechnol.* **2009,** *85*, 207-228.
111. Gibson, D. T.; Parales, R. E., Aromatic hydrocarbon dioxygenases in environmental biotechnology. *Curr. Opin. Biotechnol.* **2000,** *11*, 236-243.
112. Wang, Y. Z.; Lipscomb, J. D., Cloning, overexpression, and mutagenesis of the gene for homoprotocatechuate 2,3-dioxygenase frombrevibacterium fuscum. *Protein Expression Purif.* **1997,** *10*, 1-9.
113. Boll, M.; Fuchs, G., Benzoyl-coenzyme a reductase (dearomatizing), a key enzyme of anaerobic aromatic metabolism. Atp dependence of the reaction, purification and some properties of the enzyme from thauera aromatica strain k172. *Eur. J. Biochem.* **1995,** *234*, 921–933.
114. Kurtz, D. M., Jr, Oxo- and hydroxo-bridged diiron complexes: A chemical perspective on a biological unit. *Chem Rev* **1990,** *90*, 585-606.

115. K.S, M., Binuclear oxo-bridged iron(iii) complexes. *Coord. Chem. Rev.* **1974,** *12*, 1-35.
116. Hotzelmann, R.; Wieghardt, K.; Ensling, J.; Romstedt, H.; Guetlich, P.; Bill, E.; Floerke, U.; Haupt, H. J., Synthesis, crystal structures, moessbauer, susceptibility, and epr studies of a series of spin exchange coupled complexes containing the (.Mu.-oxo)bis(.Mu.-acetato)rutheniummetal core and its hydroxo-bridged analog (metal = vanadium, chromium, manganese, iron, cobalt). *J .Am. Chem. Soc.* **1992,** *114*, 9470-9483.
117. Sazinsky, M. H.; Dunten, P. W.; McCormick, M. S.; DiDonato, A.; Lippard, S. J., X-ray structure of a hydroxylase-regulatory protein complex from a hydrocarbon-oxidizing multicomponent monooxygenase, *pseudomonas sp.* Ox1 phenol hydroxylase. *Biochemistry* **2006,** *45*, 15392-15404.
118. Guy, J. E.; Whittle, E.; Moche, M.; Lengqvist, J.; Lindqvist, Y.; Shanklin, J., Remote control of regioselectivity in acyl-acyl carrier protein-desaturases. *Proc. Nat. Acad. Sci. U. S. A.* **2011,** *In press*.
119. Shanklin, J.; Guy, J. E.; Mishra, G.; Lindqvist, Y., Desaturases: Emerging models for understanding functional diversification of diiron-containing enzymes. *J. Biol. Chem.* **2009,** *284*, 18559-18563.
120. Krebs, C.; Bollinger, J. M., Jr.; Booker, S. J., Cyanobacterial alkane biosynthesis further expands the catalytic repertoire of the ferritin-like 'di-iron-carboxylate' proteins. *Curr. Opin. Chem. Biol.* **2011,** *15*, 291-303.
121. Busch, B.; Hertweck, C., Evolution of metabolic diversity in polyketide-derived pyrones: Using the non-colinear aureothin assembly line as a model system. *Phytochemistry* **2009,** *70*, 1833-1840.
122. Winkler, R.; Hertweck, C., Biosynthesis of nitro compounds. *ChemBioChem* **2007,** *8*, 973-977.
123. He, J.; Hertweck, C., Biosynthetic origin of the rare nitroaryl moiety of the polyketide antibiotic aureothin: Involvement of an unprecedented n-oxygenase. *J. Am. Chem. Soc.* **2004,** *126*, 3694-3695.
124. Platter, E.; Lawson, M.; Marsh, C.; Sazinsky, M. H., Characterization of a non-ribosomal peptide synthetase-associated diiron arylamine n-oxygenase from pseudomonas syringae pv. Phaseolicola. *Arch. Biochem. Biophys.* **2011,** *508*, 39-45.
125. Pacholec, M.; Sello, J. K.; Walsh, C. T.; Thomas, M. G., Formation of an aminoacyl-s-enzyme intermediate is a key step in the biosynthesis of chloramphenicol. *Org. Biomol. Chem.* **2007,** *5*, 1692-1694.
126. Fries, A.; Bretschneider, T.; Winkler, R.; Hertweck, C., A ribonucleotide reductase-like electron transfer system in the nitroaryl-forming n-oxygenase aurf. *ChemBioChem* **2011,** *12*, 1832-1835.
127. Krebs, C.; Matthews, M. L.; Jiang, W.; Bollinger, J. M., Jr., Aurf from streptomyces thioluteus and a possible new family of manganese/iron oxygenases *Biochemistry* **2007,** *46*, 10413-10418.
128. Münck, E., Aspects of ^{57}fe mossbauer spectroscopy. In *Physical methods in bioinorganic chemistry: Spectroscopy and magnetism*, Que, L., Jr., Ed. University Science Books: Sausalito, CA, 2003; pp 287-319.

129. Dong, Y.; Menage, S.; Brennan, B. A.; Elgren, T. E.; Jang, H. G.; Pearce, L. L.; Que, L., Jr., Dioxygen binding to diferrous centers. Models for diiron-oxo proteins. *J. Am. Chem. Soc.* **1993,** *115*, 1851-1859.
130. Dong, Y.; Yan, S.; Young, V. G., Jr; Que, L., Jr, Crystal structure analysis of a synthetic non-heme diiron-o_2 adduct: Insight into the mechanism of oxygen activation. *Angew. Chem. Int. Ed.* **1996,** *35*, 618-620.
131. Zhang, X.; Furutachi, H.; Fujinami, S.; Nagatomo, S.; Maeda, Y.; Watanabe, Y.; Kitagawa, T.; Suzuki, M., Structural and spectroscopic characterization of (μ-hydroxo or μ-oxo)(μ-peroxo)diiron(iii) complexes: Models for peroxo intermediates of non-heme diiron proteins. *J. Am. Chem. Soc.* **2005,** *127*, 826-827.
132. Li, N.; Korboukh, V. K.; Krebs, C.; Bollinger, J. M., Four-electron oxidation of p-hydroxylaminobenzoate to p-nitrobenzoate by a peroxodiferric complex in aurf from *streptomyces thioluteus*. *Proc. Nat. Acad. Sci. U. S. A.* **2010,** *107*, 15722-15727.
133. Chufán, E. E.; Puiu, S. C.; Karlin, K. D., Heme-copper/dioxygen adduct formation, properties, and reactivity. *Acc. Chem. Res.* **2007,** *40*, 563-572.
134. Blaha, G.; Stanley, R. E.; Steitz, T. A., Formation of the first peptide bond: The structure of ef-p bound to the 70s ribosome. *Science* **2009,** *325*, 966-970.
135. Saini, P.; Eyler, D. E.; Green, R.; Dever, T. E., Hypusine-containing protein eif5a promotes translation elongation. *Nature* **2009,** *459*, 118-121.
136. Kim, Y. S.; Kang, K. R.; Wolff, E. C.; Bell, J. K.; McPhie, P.; Park, M. H., Deoxyhypusine hydroxylase is a fe(ii)-dependent, heat-repeat enzyme. Identification of amino acid residues critical for fe(ii) binding catalysis. *J. Biol. Chem.* **2006,** *281*, 13217-13225.
137. Park, M. H.; Cooper, H. L.; Folk, J. E., The biosynthesis of protein-bound hypusine (n epsilon -(4-amino-2- hydroxybutyl)lysine). Lysine as the amino acid precursor and the intermediate role of deoxyhypusine (n epsilon -(4-aminobutyl)lysine). *J. Biol. Chem.* **1982,** *257*, 7217-7222.
138. Ciabatti, R.; Kettenring, J. K.; Winters, G.; Tuan, G.; Zerilli, L.; Cavalleri, B., Ramoplanin (a-16686), a new glycolipodepsipeptide antibiotic. Iii. Structure elucidation. *J. Antibiotics* **1989,** *42*, 254-267.
139. Du, L.; Sanchez, C.; Chen, M.; Edwards, D. J.; Shen, B., The biosynthetic gene cluster for the antitumor drug bleomycin from streptomyces verticillus atcc15003 supporting functional interactions between nonribosomal peptide synthetases and a polyketide synthase. *Chem. Biol.* **2000,** *7*, 623-642.
140. Pootoolal, J.; Thomas, M. G.; Marshall, C. G.; Neu, J. M.; Hubbard, B. K.; Walsh, C. T.; Wright, G. D., Assembling the glycopeptide antibiotic scaffold: The biosynthesis of a47934 from streptomyces toyocaensis nrrl15009. *Proc. Nat. Acad. Sci. U. S. A.* **2002,** *99*, 8962-8967.
141. Chen, H.; Thomas, M. G.; O'Connor, S. E.; Hubbard, B. K.; Burkart, M. D.; Walsh, C. T., Aminoacyl-s-enzyme intermediates in β-hydroxylations and α,β-desaturations of amino acids in peptide antibiotics. *Biochemistry* **2001,** *40*, 11651-11659.
142. Byers, T. L.; Lakanen, J. R.; Coward, J. K.; Pegg, A. E., The role of hypusine depletion in cytostasis induced by s-adenosyl-l-methionine dercarboxylase inhibition: New evidence provided by 1-methylspermidine and 1,12-dimethylspermidine. *Biochem. J.* **1994,** *303*, 363-368.

143. Park, M. H.; Wolff, E. C.; Leea, Y. B.; Folk, J. E., Antiproliferative effects of inhibitors of deoxyhypusine synthase: Inhibition of growth of chinese hamster ovary cells by guanul diamines. *J. Biol. Chem.* **1994,** *269*, 27827-27832.
144. Hanauske-Abel, H. M.; Park, M. H.; Hanauske, A. R.; Popowicz, A. M.; Lalande, M.; Folk, J. E., Inhibition of the g1-s transition of the cell cycle by inhibitors of deoxyhypusine hydroxylation. *Biochim. Biophys. Acta* **1994,** *1221*, 115-124.
145. Clement, P. M. J.; Hanauske-Abel, H. M.; Wolff, E. C.; Kleinman, H. K.; Park, M. H., The antifungal drug ciclopirox inhibits deoxyhypusine and proline hydroxylation, endothelial cell growth and angiogenesis *in vitro*. *Int. J. Cancer.* **2002,** *100*, 491-498.
146. Andrus, L.; Szabo, P.; Grady, R. W.; Hanauske, A.-R.; Huima-Byron, T.; Slowinska, B.; Zagulska, S.; Hanauske-Abel, H. M., Antiretroviral effects of deoxyhypusyl hydroxylase inhibitors: A hypusine-dependent host cell mechanism for replication of human immunodeficiency virus type 1 (hiv-1). *Biochem. Pharmacol.* **1998,** *55*, 1807-1818.
147. Dixon, M., The acceptor specificity of flavins and flavoproteins. I. Techniques for anerobic spectrophotometry. *Biochim. Biophys. Acta* **1971,** *226*, 241-258.
148. Kauffmann, K. E.; Münck, E., Combining mossbauer spectroscopy and magnetometry. In *ACS Symposium on "Spectroscopic Methods in Bioinorganic Chemistry"*, Solomon, E. I.; Hodgson, K., Eds. 1998; pp 16-29.
149. George, G. N.; Pickering, I. J., *Exafspak & edg-fit*. In Stanford Synchrotron Raidation Laboratory, Stanford Linear Accelerator Center, Stanford University; Stanford, CA, 2000.
150. Rehr, J. J.; Mustre de Leon, J.; Zabinsky, S. I.; Albers, R. C., Theoretical x-ray absorption fine structure standards. *J. Am. Chem. Soc.* **1991,** *113*, 5135-5140.
151. Scarrow, R. C.; Trimitsis, M. G.; Buck, C. P.; Grove, G. N.; Cowling, R. A.; Nelson, M. J., X-ray spectroscopy of the iron site in soybean lipoxygenase-1: Changes in coordination upon oxidation or addition of methanol. *Biochemistry* **1994,** *33*, 15023-15035.
152. Ravel, B.; Newville, M., Athena, artemis, hephaestus: Data analysis for x-ray absorption spectroscopy using ifeffit. *J. Synchrotron Rad.* **2005,** *12*, 537-541.
153. Clay, M. D.; Jenney, F. E.; Hagedoorn, P. L.; George, G. N.; Adams, M. W. W.; Johnson, M. K., Spectroscopic studies of *pyrococcus furiosus* superoxide reductase: Implications for active-site structures and the catalytic mechanism. *J. Am. Chem. Soc.* **2002,** *124*, 788-805.
154. Liu, K. E.; Valentine, A. M.; Qiu, D.; Edmondson, D. E.; Appelman, E. H.; Spiro, T. G.; Lippard, S. J., Characterization of a diiron(iii) peroxide intermediate in the reaction cycle of methane monooxygenase hydroxylase from *methylococcus capsulatus* (bath). *J. Am. Chem. Soc.* **1995,** *117*, 4997-4998.
155. Pereira, A. S.; Small, W.; Krebs, C.; Tavares, P.; Edmondson, D. E.; Theil, E. C.; Huynh, B. H., Direct spectroscopic and kinetic evidence for the involvement of a peroxodiferric intermediate during the ferroxidase reaction in fast ferritin mineralization. *Biochemistry* **1998,** *37*, 9871-9876.
156. DeWitt, J. G.; Bentsen, J. G.; Rosenzweig, A. C.; Hedman, B.; Green, J.; Pilkington, S.; Papaefthymiou, G. C.; Dalton, H.; Hodgson, K. O.; Lippard, S. J., X-ray

absorption, mössbauer, and epr studies of the dinuclear iron center in the hydroxylase component of methane monooxygenase. *J. Am. Chem. Soc.* **1991,** *113*, 9219-9235.
157. Roe, A. L.; Schneider, D. J.; Mayer, R. J.; Pyrz, J. W.; Widom, J.; Que, L., Jr., X-ray absorption spectroscopy of iron-tyrosinate proteins. *J. Am. Chem. Soc.* **1984,** *106*, 1676-1681.
158. Shu, L.; Broadwater, J. A.; Achim, C.; Fox, B. G.; Münck, E.; Que, L., Jr., Exafs and mössbauer characterization of the diiron(iii) site in stearoyl-acyl carrier protein δ^9–desaturase. *J. Biol. Inorg. Chem.* **1998,** *3*, 392-400.
159. True, A. E.; Scarrow, R. C.; Randall, C. R.; Holz, R. C.; Que, L., Jr., Exafs studies of uteroferrin and its anion complexes. *J. Am. Chem. Soc.* **1993,** *115*, 4246-4255.
160. Kurtz, D. M., Jr, Oxo- and hydroxo-bridged diiron complexes: A chemical perspective on a biological unit. *Chem. Rev.* **1990,** *90*, 585-606.
161. Gamelin, D. R.; Bominaar, E. L.; Kirk, M. L.; Wieghardt, K.; Solomon, E. I., Excited-state contributions to ground-state properties of mixed-valence dimers: Spectral and electronic-structural studies of $[fe_2(oh)_3(tmtacn)_2]^{2+}$ related to the $[fe_2s_2]^{+}$ active sites of plant-type ferredoxins. *J. Am. Chem. Soc.* **1996,** *118*, 8085-8097.
162. Brunold, T. C.; Tamura, N.; Kitajima, N.; Moro-oka, Y.; Solomon, E. I., Spectroscopic study of $[fe_2(o_2)(obz)_2\{hb(pz')_3\}_2]$: Nature of the μ-1,2 peroxide-fe(iii) bond and its possible relevance to o_2 activation by non-heme iron enzymes. *J. Am. Chem. Soc.* **1998,** *120*, 5674-5690.
163. Liu, Y.; Nesheim, J. C.; Lee, S.-K.; Lipscomb, J. D., Gating effects of component b on oxygen activation by the methane monooxygenase hydroxylase component. *J. Biol. Chem.* **1995,** *270*, 24662-24665.
164. Brennan, B. A.; Chen, Q.; Juarez-Garcia, C.; True, A. E.; O'Connor, C. J.; Que, L., Jr., Models for diiron-oxo proteins: The peroxide adduct of $fe_2(hptb)(oh)(no_3)_4$. *Inorg. Chem.* **1991,** *30*, 1937-1943.
165. Westre, T. E.; Kennepohl, P.; DeWitt, J. G.; Hedman, B.; Hodgson, K. O.; Solomon, E. I., A multiplet analysis of fe k-edge 1s $\rightarrow$ 3d pre-edge features of iron complexes. *J. Am. Chem. Soc.* **1997,** *119*, 6297-6314.
166. Weng, T.-C.; Waldo, G. S.; Penner-Hahn, J. E., A method for normalization of x-ray absorption spectra. *J. Synchrotron Rad.* **2005,** *12*, 506-510.
167. Davydov, R. M.; Ménage, S.; Fontecave, M.; Gräslund, A.; Ehrenberg, A., Mixed-valent μ-oxo-bridged diiron complexes produced by radiolytic reduction at 77 k studied by epr. *J. Biol. Inorg. Chem.* **1997,** *2*, 242-255.
168. Davydov, R. M.; Smieja, J.; Dikanov, S. A.; Zang, Y.; Que Jr, L.; Bowman, M. K., Epr properties of mixed-valent μ-oxo and μ-hydroxo dinuclear iron complexes produced by radiolytic reduction at 77k. *J Biol Inorg Chem* **1999,** *4*, 292-301.
169. Nivorozhkin, A. L.; Anxolabéhère-Mallart, E.; Mialane, P.; Davydov, R.; Guilhem, J.; Cesario, M.; Audière, J.-P.; Girerd, J.-J.; Styring, S.; Schussler, L.; Seris, J.-L., Structure and electrochemical studies of $[(trispicmeen)clfe^{iii}ofe^{iii}cl(trispicmeen)]^{2+}$. Spectroscopic characterization of the mixed-valence $fe^{iii}ofe^{ii}$ form. Relevance to the active site of dinuclear iron-oxo proteins. *Inorg. Chem.* **1997,** *36*, 846-853.
170. MacMurdo, V. L.; Zheng, H.; Que, L., Jr., Model for the cofactor formation reaction of e. Coli ribonucleotide reductase. From a diiron(ii) precursor to an feiiifeiv species via a peroxo intermediate. *Inorg. Chem.* **2000,** *39*, 2254-2255.

171. Xue, G.; De Hont, R.; Münck, E.; Que, L., Jr., Million-fold activation of the [$fe_2(\mu\text{-}o)_2$] diamond core for c-h bond cleavage. *Nat. Chem.* **2010,** *2*, 400-405.
172. Park, J. H.; Dias, C. A. O.; Lee, S. B.; Valentini, S. R.; Sokabe, M.; Fraser, C. S.; Park, M. H., Production of active recombinant eif5a: Reconstitution in e.Coli of eukaryotic hypusine modification of eif5a by its coexpression with modifying enzymes. *Protein Eng., Des. Sel.* **2010,** *24*, 301-309.
173. Park, J.-H.; Wolff, E. C.; Folk, J. E.; Park, M. H., Reversal of the deoxyhypusine synthesis reaction: Generation of spermidine or homospermidine form deoxyhypusine by deoxyhypusine synthase. *J. Biol. Chem.* **2003,** *278*, 32683-32691.
174. Cano, V. S. P.; Medrano, F. J.; Park, M. H.; Valentini, S. R., Evidence for conformational changes in the yeast deoxyhypusine hydroxylase lia1 upon iron displacement from its active site. *Amino Acids* **2010,** *38*, 479-490.
175. Kang, K. R.; Kim, Y. S.; Wolff, E. C.; Park, M. H., Specificity of the deoxyhypusine hydroxylase-eukaryotic translation initiation factor (eif5a) interaction. Identification of amio acid residues of the enzyme required for binding of its substrate, deoxyhypusine-containing eif5a. *J. Biol. Chem.* **2007,** *282*, 8300-8308.
176. Karlsson, A.; Parales, J. V.; Parales, R. E.; Gibson, D. T.; Eklund, H.; Ramaswamy, S., Crystal structure of naphthalene dioxygenase: Side-on binding of dioxygen to iron. *Science* **2003,** *299*, 1039-1042.
177. Roelfes, G.; Vrajmasu, V.; Chen, K.; Ho, R. Y. N.; Rohde, J.-U.; Zondervan, C.; Crois, R. M. l.; Schudde, E. P.; Lutz, M.; Spek, A. L.; Hage, R.; Feringa, B. L.; Mu1nck, E.; Que, L., End-on and side-on peroxo derivatives of non-heme iron complexes with pentadentate ligands: Models for putative intermediates in biological iron/dioxygen chemistry. *Inorg. Chem.* **2003,** *42*, 2639-2653.
178. Koehntop, K. D.; Rohde, J. U.; Costas, M.; Que, L., Jr., Xas characterization of end-on and side-on peroxoiron(iii) complexes of the neutral pentadentate n-donor ligand n-methyl-n,n ',n '-tris(2-pyridylmethyl)ethane-1,2-diamine. *Dalton Trans.* **2004**, 3191-3198.
179. Li, F.; Meier, K. K.; Cranswick, M. A.; Chakrabarti, M.; Van Heuvelen, K. M.; Münck, E.; Que, L., Jr., Characterization of a high-spin non-heme fe^{iii}-ooh intermediate and its quantitative conversion to an fe^{iv}=o complex. *J. Am. Chem. Soc.* **2011,** *133*, 7256-7259.
180. Kitajima, N.; Moro-oka, Y., Copper-dioxygen complexes. Inorganic and bioinorganic perspectives. *Chem. Rev.* **1994,** *94*, 737-757.
181. Mirica, L. M.; Ottenwaelder, X.; Stack, T. D. P., Structure and spectroscopy of copper-dioxygen complexes. *Chem. Rev.* **2004,** *104*, 1013-1046.
182. Ebbesen, T. W.; Levey, G.; Patterson, L. K., Photoreduction of methyl viologen in aqueous neutral solution without additives. *Nature* **1982,** *298*, 545-548.
183. Root, D. E.; Mahroof-Tahir, M.; Karlin, K. D.; Solomon, E. I., Effect of protonation on peroxo-copper bonding: Spectroscopic and electronic structure study of [cu_2((un-o-)(ooh)]$^{2+}$. *Inorg. Chem.* **1998,** *37*, 4838-4848.
184. Mathé, C.; Mattioli, T. A.; Horner, O.; Lombard, M.; Latour, J.-M.; Fontecave, M.; Nivière, V., Identification of iron(iii) peroxo species in the active site of the superoxide reductase sor from desulfoarculus baarsii. *J. Am. Chem. Soc.* **2002,** *124*, 4966-4967.

185. Liu, J.-G.; Ohta, T.; Yamaguchi, S.; Ogura, T.; Sakamoto, S.; Maeda, Y.; Naruta, Y., Spectroscopic characterization of a hydroperoxo–heme intermediate: Conversion of a side-on peroxo to an end-on hydroperoxo complex. *Angew. Chem. Int. Ed.* **2009,** *48*, 9262-9267.
186. Kitajima, N.; Fujisawa, K.; Fujimoto, C.; Morooka, Y.; Hashimoto, S.; Kitagawa, T.; Toriumi, K.; Tatsumi, K.; Nakamura, A., A new model for dioxygen binding in hemocyanin. Synthesis, characterization, and molecular structure of the μ–η^2:H^2-peroxo dinuclear copper(ii) complexes, [cu(hb(3,5-$r_2$pz)$_3$)]$_2$(o_2) (r = ipr and ph). *J. Am. Chem. Soc.* **1992,** *114*, 1277-1291.
187. Ghiladi, R. A.; Hatwell, K. R.; Karlin, K. D.; Huang, H.-w.; Moënne-Loccoz, P.; Krebs, C.; Huynh, B. H.; Marzilli, L. A.; Cotter, R. J.; Kaderli, S.; Zuberbühler, A. D., Dioxygen reactivity of mononuclear heme and copper components yielding a high-spin heme-peroxo-cu complex. *J. Am. Chem. Soc.* **2001,** *123*, 6183-6184.
188. Naruta, Y.; Sasaki, T.; Tani, F.; Tachi, Y.; Kawato, N.; Nakamura, N., Heme-cu complexes as oxygen-activating functional models for the active site of cytochrome c oxidase. *J. Inorg. Biochem.* **2001,** *83*, 239-246.
189. Chishiro, T.; Shimazaki, Y.; Tani, F.; Tachi, Y.; Naruta, Y.; Karasawa, S.; Hayami, S.; Maeda, Y., Isolation and crystal structure of a peroxo-bridged heme–copper complex. *Angew. Chem. Int. Ed.* **2003,** *42*, 2788-2791.
190. Lewis, E. A.; Tolman, W. B., Reactivity of dioxygen-copper systems. *Chem. Rev.* **2004,** *104*, 1047-1076.
191. Chen, H.; Walsh, C. T., Coumarin formation in novobiocin biosynthesis: Beta-hydroxylation of the aminoacyl enzyme tyrosyl-s-novh by a cytochrome p450 novi. *Chem. Biol.* **2001,** *8*, 301-312.
192. Neary, J. M.; Powell, A.; Gordon, L.; Milne, C.; Flett, F.; Wilkinson, B.; Smith, C. P.; Micklefield, J., An asparagine oxygenase (asno) and a 3-hydroxyasparaginyl phosphotransferase (hasp) are involved in the biosynthesis of calcium-dependent lipopeptide antibiotics *Microbiology* **2007,** *153*, 768-776.
193. Strieker, M.; Nolan, E. M.; Walsh, C. T.; Marahiel, M. A., Stereospecific synthesis of threo- and erythro-β-hydroxyglutamic acid during kutzneride biosynthesis. *J. Am. Chem. Soc.* **2009,** *131*, 13523-13530.
194. Sanders-Loehr, J.; Wheeler, W. D.; Shiemke, A. K.; Averill, B. A.; Loehr, T. M., Electronic and raman spectroscopic properties of oxo-bridged dinuclear iron centers in proteins and model compounds. *J. Am. Chem. Soc.* **1989,** *111*, 8084-8093.
195. Zheng, H.; Zang, Y.; Dong, Y.; Young, V. G.; Que, L., Jr., Complexes with fe^{iii2}(μ-o)(μ-oh), fe^{iii2}(μ-o)$_2$, and [fe^{iii3}(μ_2-o)$_3$] cores: Structures, spectroscopy, and core interconversions. *J. Am. Chem. Soc.* **1999,** *121*, 2226-2235.
196. Chow, M. S.; Eser, B. E.; Wilson, S. A.; Hodgson, K. O.; Hedman, B.; Fitzpatrick, P. F.; Solomon, E. I., Spectroscopy and kinetics of wild-type and mutant tyrosine hydroxylase: Mechanistic insight into o2 activation. *J. Am. Chem. Soc.* **2009,** *131*, 7685-7698.
197. Shu, L.; Liu, Y.; Lipscomb, J. D.; Que, L., Jr., X-ray absorption spectroscopic studies of the methane monooxygenase hydroxylase component from methylosinus trichosporium ob3b. *J. Biol. Inorg. Chem.* **1996,** *1*, 297-304.

198. Rudd, J. D.; Sazinsky, M. H.; Merkx, M.; Lippard, S. J.; Hedman, B.; Hodgson, K. O., Determination by x-ray absorption spectroscopy of the fe-fe separation in the oxidized form of the hydroxylase of methane monooxygenase alone and in the presence of mmod. *Inorg. Chem.* **2004,** *43*, 4579-4589.
199. Toussaint, L.; Cuypers, M.; Bertrand, L.; Hue, L.; Romão, C.; Saraiva, L.; Teixeira, M.; Meyer-Klaucke, W.; Feiters, M.; Crichton, R., Comparative fe and zn k-edge x-ray absorption spectroscopic study of the ferroxidase centres of human h-chain ferritin and bacterioferritin from desulfovibrio desulfuricans. *J. Biol. Inorg. Chem.* **2009,** *14*, 35-49.
200. Wang, D.; Farquhar, E. R.; Stubna, A.; Münck, E.; Que, L., Jr., A diiron(iv) complex that cleaves strong c–h and o–h bonds. *Nat. Chem.* **2009,** *1*, 145-150.
201. Bunker, G.; Petersson, L.; Sjöeberg, B. M.; Sahlin, M.; Chance, M.; Chance, B.; Ehrenberg, A., Extended x-ray absorption fine structure studies on the iron-containing subunit of ribonucleotide reductase from *escherichia coli*. *J. Am. Chem. Soc.* **1987,** *26*, 4708-4716.
202. Nordlund, P.; Eklund, H., Structure and function of the escherichia coli ribonucleotide reductase protein r2. *J. Mol. Biol.* **1993,** *232*, 123-164.
203. Riggs-Gelasco, P. J.; Stemmler, T. L.; Penner-Hahn, J. E., Xafs of dinuclear metal sites in proteins and model compounds. *Coord. Chem. Rev.* **1995,** *144*, 245-286.
204. Penner-Hahn, J. E., X-ray absorption spectroscopy in coordination chemistry. *Coord. Chem. Rev.* **1999,** *190-192*, 1101-1123.
205. True, A. E.; Orville, A. M.; Pearce, L. L.; Lipscomb, J. D.; Que, L., Jr., An exafs study of the interaction of substrate with the ferric active site of protocatechuate 3,4-dioxygenase. *Biochemistry* **1990,** *29*, 10847-10854.
206. Andersen, O. A.; Stokka, A. J.; Flatmark, T.; Hough, E., 2.0 å resolution crystal structures of the ternary complexes of human phenylalanine hydroxylase catalytic domain with tetrahydrobiopterin and 3-(2-thienyl)-l-alanine or l-norleucine: Substrate specificity and molecular motions related to substrate binding. *J. Mol. Biol.* **2003,** *333*, 747-757.
207. Dunietz, B. D.; Beachy, M. D.; Cao, Y.; Whittington, D. A.; Lippard, S. J.; Friesner, R. A., Large scale ab initio quantum chemical calculation of the intermediates in the soluble methane monooxygenase catalytic cycle. *J. Am. Chem. Soc.* **2000,** *122*, 2828-2839.
208. Rinaldo, D.; Philipp, D. M.; Lippard, S. J.; Friesner, R. A., Intermediates in dioxygen activation by methane monooxygenase: A qm/mm study. *J. Am. Chem. Soc.* **2007,** *129*, 3135-3147.
209. Xue, G.; Fiedler, A. T.; Martinho, M.; Münck, E.; Que, L., Jr., Insights into the p-to-q conversion in the catalytic cycle of methane monooxygenase from a synthetic model system. *Proc. Nat. Acad. Sci. U. S. A.* **2008,** *105*, 20615-20620.